SCATTEROMETER AND RADIOMETER LAND APPLICATIONS

ESRIN Contract No: 11122/94/I-HGE(SC)
Final Report

Evolution of Near Surface Air Temperature in North Finland
Based on SSM/I Data

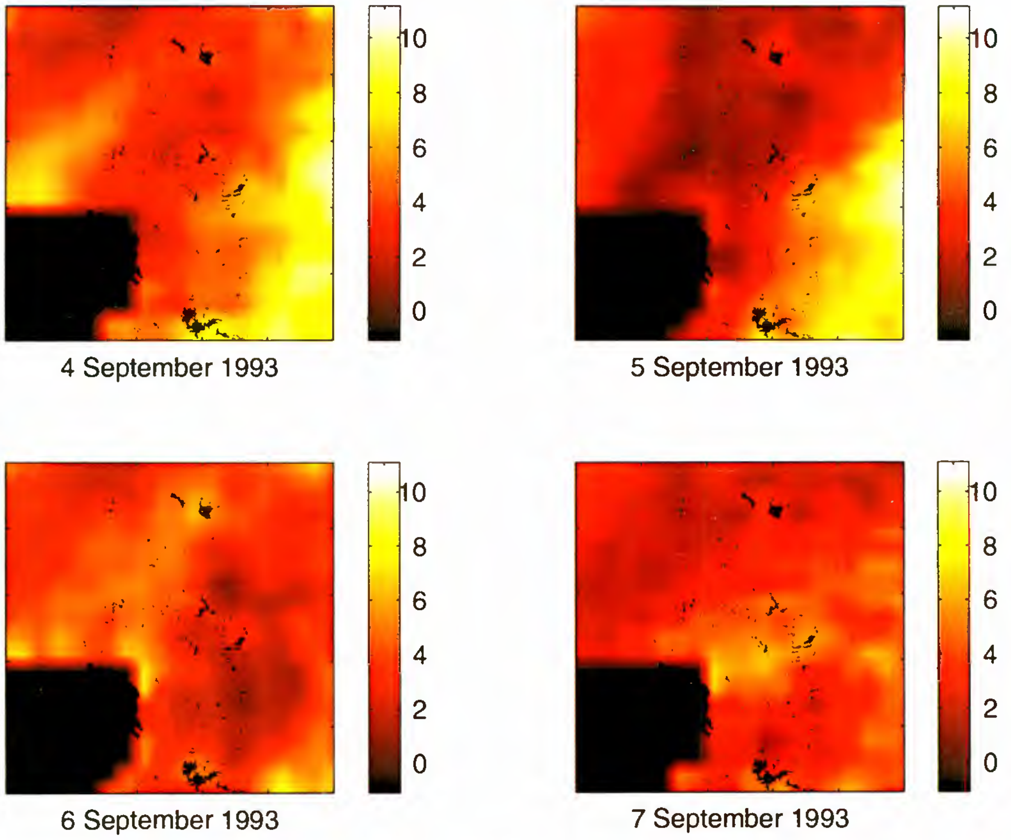

Helsinki University of Technology
Laboratory of Space Technology (HUT)

GEC-Marconi Research Centre (MRC)

Finnish Environment Agency (FEA)

Technical Research Centre of Finland (VTT)

April 1996

Scatterometer and Radiometer Land Applications
Final Report

ESRIN Contract: 11122/94/I-HGE(SC)

Jouni Pulliainen, Jochen Grandell, Martti Hallikainen and Mika Virtanen
Helsinki University of Technology
Laboratory of Space Technology (Finland)

Nicholas Walker
GEC-Marconi Research Centre (UK)

Sari Metsämäki, Jari-Pekka Ikonen and Yrjö Sucksdorff
Finnish Environment Agency

Terhikki Manninen
VTT (Finland)

Principal Investigator:
Martti Hallikainen
Helsinki University of Technology

ESA Technical Management:
Pascal Lecomte
ESA/ESRIN

April 1996

ESA STUDY CONTRACT REPORT SUMMARY PAGE

ESA CONTRACT No:	SUBJECT:		CONTRACTOR:
ESRIN Contract 11122/94/I-HGE	Scatterometer and Radiometer Land Applications		Helsinki University of Technology Laboratory of Space Technology
* ESA CR( )No	* STAR CODE	No of volumes: 1	CONTRACTOR'S REFERENCE

ABSTRACT:

The results obtained in the study of land applications of space-borne scatterometers and radiometers are presented. The investigations have been conducted using data from two microwave instruments: the ERS-1 Wind Scatterometer and the SSM/I radiometer. The potential of these present systems is analyzed and new inversion techniques for various applications are developed. The applicability of these instruments was primarily investigated for the boreal forest zone. The study also emphasizes the investigation of scatterometer image resolution enhancement techniques. The results show that the ERS-1 Wind Scatterometer has good potential for some land applications, including soil frost mapping and detection of soil moisture changes and effects of precipitation. The usefulness of Wind Scatterometer data was found to be poor for retrieval of vegetation biomass. The SSM/I data showed the highest potential for retrieval of surface (air temperature) and considerable potential for mapping sea ice concentration and snow extent/snow water equivalent. For monitoring the seasonal dynamics of vegetation and soil freezing in the boreal forest zone the applicability of SSM/I data was found to be poor. The investigations concerning the ERS-1 Wind Scatterometer spatial resolution enhancement showed that substantial resolution improvement is not possible.

Names of authors:
Jouni Pulliainen, Jochen Grandell, Martti Hallikainen, Mika Virtanen,
Nicholas Walker, Sari Metsämäki, Jari-Pekka Ikonen, Yrjö Sucksdorff and
Terhikki Manninen

** NAME OF ESA STUDY MANAGER	** ESA BUDGET HEADING
Pascal Lecomte DIV: ERS Remote Sensing Exploitation Division DIRECTORATE: ESRIN	60.512

Contents

1 Introduction

This report describes the work conducted in the study: "Scatterometer and Radiometer Land Applications". The aim of the study is to develop, promote and test inversion algorithms for land applications of satellite-borne microwave scatterometer and radiometer. The work is conducted using data from (1) the ESA ERS-1 Wind Scatterometer (WS) and U.S. SSM/I radiometer on-board DMSP satellite. The goal is to analyze the potential of these present systems and to outline the requirements for future systems. The investigations also emphasize the development of scatterometer image resolution enhancement techniques. These methods are important when a coarse resolution scatterometer, such as ERS-1 Wind Scatterometer (ground resolution about 50 km), is used for land applications.

The feasibility of WS and SSM/I data is investigated for various applications which include the monitoring/retrieval of:
- forest/vegetation biomass,
- vegetation extent and land use,
- vegetation type or species,
- vegetation phenological state,
- vegetation seasonal dynamics,
- soil and vegetation moisture,
- soil frost,
- snow cover extent,
- snow water equivalent (snow depth),
- sea ice extent,
- sea ice type and concentration.

The inversion algorithms that are studied and developed include the common statistical regression and classification approaches. However, the priority is in the use and development of methods that employ the physical background of the measurements. With these methods, the inverse problem is solved by seeking an iterative solution for a forward backscattering or emission model. When a multi-channel/instrument/temporal remote sensing data set is available, it is possible to estimate various geophysical target parameters simultaneously.

The use of multi-source data in the retrieval of land surface characteristics is also stressed. The auxliary data can include e.g. land use and precipitation information. These *a priori* information can be obtained by other remote sensing instruments, such as NOAA AVHRR visible/infrared radiometer, or by ground-based *in situ* measurements.

Chapter 2 of the report focuses on the presentation of land areas, land types and data sets that are used in the data analysis and in the development and testing of inversion approaches. The SSM/I, Wind Scatterometer and reference data pre-processing methods are also described. The detailed reference data were obtained for a set of relatively small test areas which were selected from boreal forest, cryosphere, tropical forest and arid/semiarid zones. These areas were used in the detailed data analysis, and in the development and testing of inversion algorithms.

Chapter 3 discuss about current microwave backscattering and emission models applicable for land surface and vegetation. These models are evaluated with concern laid on:

(1) *Applicability for inversion purposes.*
A model should be simple enough, but not oversimplified, in order to be inversely solved.

(2) *General usability in sensitivity analyses.*
The model should cover sufficient parameter ranges. The model parameters should preferably be well known or measurable physical and geometrical properties, and the number of these parameters should be limited. The large number of parameters, especially if these parameters are not well known, make the use of the model somewhat speculative: typically, the model may be fitted into any empirical data, but its prediction capabilities may remain poor.

(3) *Model validation.*
The models used for sensitivity analyses and inversion purposes should be well validated against empirical data. However, this is often an a tight or impossible requirement, since the models are often complex and the experimental validation is a laborious or expensive task.

Chapter 4 describes the semi-empirical forest backscattering model that describes the behavior of ERS-1 Wind Scatterometer measurements. The model-based sensitivities of scatterometer data to various target features are also discussed. Similarly to Chapter 4, Chapter 5 describes the semi-empirical brightness temperature model for SSM/I measurements and sensitivity analyses performed using the model. The brightness temperature model is a combined model that includes the effects of snow-cover, (frozen) soil, forest cover and atmosphere.

Chapters 6 and 7 describe the seasonal behavior of Wind Scatterometer and SSM/I data. The responses to various target parameters (see the list above), as well as the angular response of WS measurements, are also discussed.

The actual development and testing of inversion algorithms are presented in Chapters 8 in for WS data and in Chapter 9 for SSM/I data. The inversion/classification algorithms were developed for the most prominent land applications. These were found to be the monitoring of soil moisture, effect of precipitation and soil/vegetation frost in the case of ERS-1 WS data, and monitoring of surface temperature, sea ice concentration and snow cover properties in the case of SSM/I data.

Chapter 10 presents the results obtained in the investigations of ERS-1 Wind Scatterometer image resolution enhancement. Chapter 11 summarizes the conclusions on the feasibility of SSM/I and Wind Scatterometer in land applications. Also the comparison and combination of SSM/I and WS data with other satellite-borne data, such as NOAA AVHRR data are discussed. Finally, Chapter 12 provides the recommendations for future work.

The prime contractor of the study is Helsinki University of Technology, Laboratory of Space Technology. The investigations were carried out with the following companies and institutes working as subcontractors: GEC-Marconi Research Centre (scatterometer image resolution enhancement), Finnish Environment Agency (reference data supply and comparisons of microwave data with optical/infrared data) and Technical Research Centre of Finland (VTT; scatterometer data pre-processing and scatterometer data analysis).

The following persons have written the contributions to the report:
J. Pulliainen: Chapters 1, 4, 8, 12, Sections 2.1, 6.1, 6.3, 9.1, 11.2, 11.3 and part of Sections 2.4, 3.1, 3.2, 3.3, 7.1, 7.2, 9.3, 11.1;
J. Grandell: Chapter 5, Sections 2.3, 7.3, 9.2, 9.4 and part of Sections 2.4, 3.1, 3.2, 3.3, 7.1, 7.2, 9.3;
M. Virtanen: part of Section 7.1;
N. Walker: Chapter 10;
S. Metsämäki: Section 11.4 and part of Section 2.4;
T. Manninen: Sections 2.2, 6.2 and part of Section 11.1.
The editing of the report was conducted by J. Pulliainen and M. Hallikainen.

2 Test Areas and Data Sets

2.1 General Description of Test Areas and Data

The coverage of ERS-1 Wind Scatterometer and SSM/I data is global, but the ground resolutions of these instruments are relatively poor (ranging from 15 to 50 km for different channels). Hence, these instruments can be primarily used in global or large area applications. However, the development of inversion techniques, testing of algorithms and the sensitivity analyses require the employment of high quality (ground) reference data which do not typically exist for global/large areas. Therefore this study emphasizes the use of detailed reference data obtained for selected test areas.

Reference data

Finnish test area

The main reference data obtained covers the boreal forests of Finland. This data set includes the land use, forest cover, soil type, daily soil moisture, daily weather statistics, soil frost information and snow cover information. Additionally, NOAA AVHRR image series have been obtained for reference.

West Africa test area

Another reference data set covers the forest, semi-arid and desert regions of West Africa. These data includes daily weather statistics, NDVI and land use information.

Sea ice test areas

Sea ice data have been obtained for Northern Baltic Sea.

Reference data for large areas

Reference data for large areas include NOAA AVHRR-based land use/forest cover map of North Europe. Global reference information was obtained for monthly maximum values of NDVI (normalized difference vegetation index), and for desert area extent. This information was obtained through UNEP/GRID-office, Geneva.

2.2 ERS-1 Wind Scatterometer Data Properties and Processing

The scatterometer data was delivered on tapes by the French Processing and Archiving Facility of ESA. Each tape contained all scatterometer data within one month all over the world. To read the tapes and to pick only the data needed (i.e. data over Northern Africa, data over Northern Europe and data over Finland) a suitable software was written in C- language. The data over

Africa was kept in latitudes and longitudes, because the ground truth data was also in those coordinates. The data over Finland and Northern Europe, however, had to be changed into the national metric KKJ-coordinates, because the background information was in these coordinates. Because the Finnish test areas of soil moisture and snow studies were quite small and the ground truth was given for square pixels, scatterometer images over Finland had to be rectified. For this purpose a program was developed using the Mathematica software.

The original scatterometer images consist of 19 x 19 pixels, whose coordinates are explicitly given. They are not parallel to the principal compass points. The size of an individual scatterometer pixels is nominally 50 km x 50 km, but consecutive pixels overlap about 25 km in every direction. The footprint is naturally closer to an ellipse than a rectangle, but in the rectification calculations it is practical to allocate every σ^o value to a single pixel of about 25 km x 25 km. The pixels are not exactly rectangular and they are defined so that the edges of each pixel consist of points that have an equal distance to the nearest pixels.

In principle the comparison of the scatterometer pixels and the ground truth should be done by weighting the ground truth according to the antenna pattern of the beam in question. However, it turned out that in practice this effect is negligible for pure land and pure water areas and very small in mixed pixels (see Section 6.2). The rectification of the scatterometer images produces new images with rectangular pixels that are parallel to the principal compass points. The new pixel values have to be calculated using the original image. There are several approaches to this problem.

One simple method would be to take every new pixel value to be the value of the closest old pixel. This assumption is quite good, if the new pixels are smaller than the old one. In this case it would not be a good method, because the new pixels are the same size as the old ones and the pixels are so large that they seldom cover homogeneous areas. Another simple approach would be to take every new pixel value to be the average of all the old pixels overlapping a circle with a radius of 25 km around the new pixel centre. The average could be weighted with the inverse values of the distances between the old and new pixel centres. The problem of this approach is that the scatterometer orbits change so that images covering the same test sites do not always have exactly the same coordinates. Thus a small change in the coordinates of the original image could produce sudden large changes in the new pixel values (Fig. 2.1). Since the test sites in Finland are very small, sometimes only a few pixels, this effect could produce artifacts in the test data picked from the rectified images. It would not be so easy to detect whether the change in the pixel value is due to a change of orbit or a change of intensity values. If the test sites were as large as the original images these artifacts could be revealed by the surroundings of Figure 2.1. An example, where the new pixel value is obtained as an average of the pixels inside the circle, whose centre is the centre of the new pixel. A small shift of the orbit of the scatterometer may alter the new pixel value radically, if the one of the four pixels shown that is inside both of the circles has a value clearly deviating from those of the other three (or at least from one of the other three pixels). each pixel. Therefore a more complicated method for the rectification of the scatterometer images was chosen.

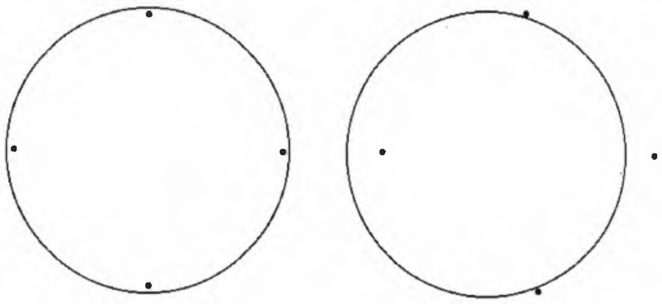

Figure 2.1. An example, where the new pixel value is obtained as an average of the pixels inside the circle, whose centre is the centre of the new pixel. A small shift of the orbit of the scatterometer may alter the new pixel value radically, if the one of the four pixels shown that is inside both of the circles has a value clearly deviating from those of the other three (or at least from one of the other three pixels).

The principle of the rectification procedure chosen is, that the new pixel value is calculated as an average of the old pixels overlapping the new one weighted with the corresponding intersection areas. The basic idea of the rectification is very simple, but in practice the number of different situations to be taken into account is quite large.

The rectification algorithm was at first tested using artificial images. Another test was to use the coordinates of the pixels as the pixel values. If the algorithm worked properly, the new pixel values should roughly equal their coordinates. This was found to occur with a high precision, which also means that the original scatterometer pixels did not deviate from rectangles very much. Some examples of original and rectified images are shown in Figure 2.2. The average and standard deviation values were also calculated for original and rectified images. However, the difference of these statistical parameters of the original and rectified image does not directly tell how well the rectification has been done, because the rectified image does not contain the whole area of all the edge pixels of the original image. But the deviation should not be very large either, if the edges of the original image are not very different from the inner part of it.

Figure 2.3 shows the effect of the rectification on the mean intensity in the images of one month. Table 2.1 reveals that the difference in the mean intensity caused by the rectification is typically smaller than one percent in the images of one month (some 90 images). The corresponding difference in the standard deviation values is only a few percent. The systematic decrease of the standard deviation is natural, because all the new pixels are calculated from the old ones. Thus all the new values are between the old maximum and minimum values. Also local maximum and minimum peaks tend to decrease, because of interpolation. This is the price paid when touching the original scatterometer intensity values.

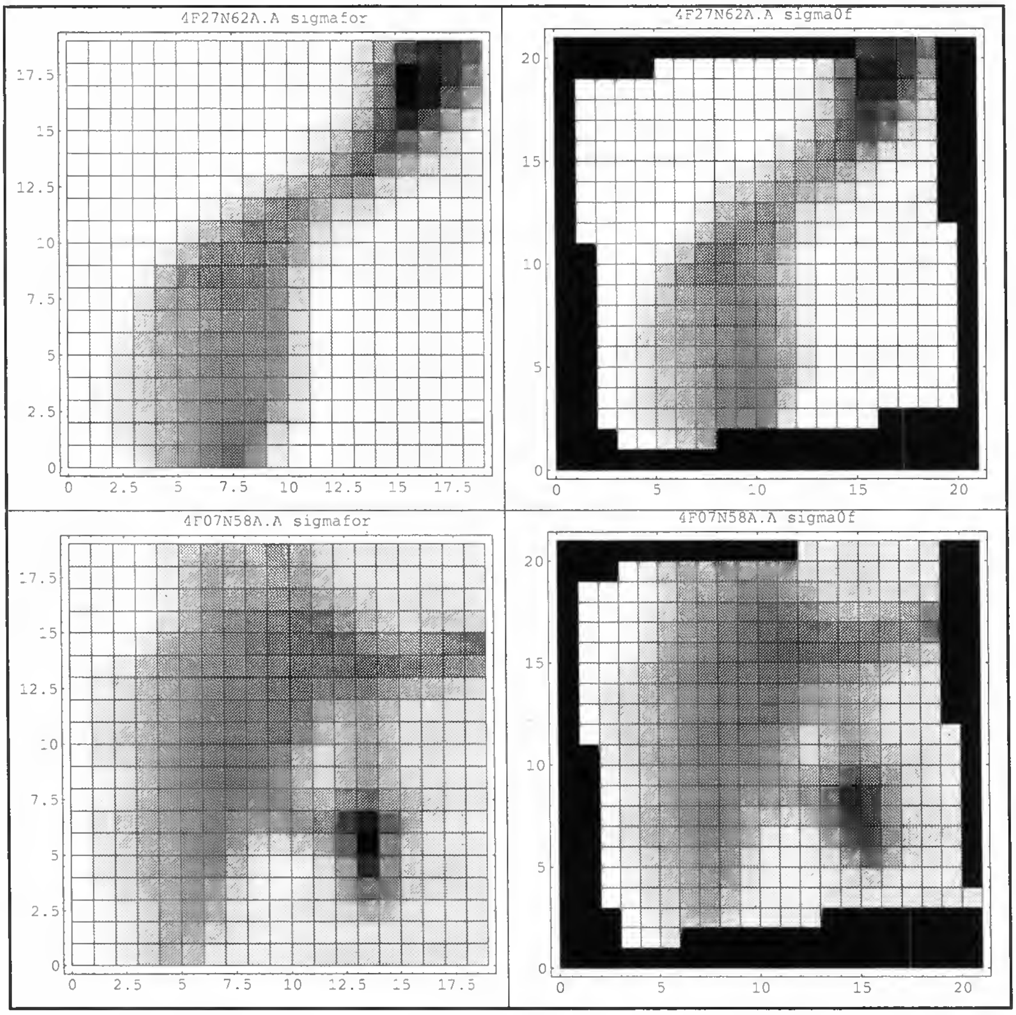

Figure 2.2. Examples of the effect of rectification on the intensity values of the images. On the left hand sides are the original images and on the right hand side the corresponding rectified images. The rectified images cover a slightly smaller area than the originals, because the interpolation was applied only to cases were the new pixel was totally covered by the old ones.

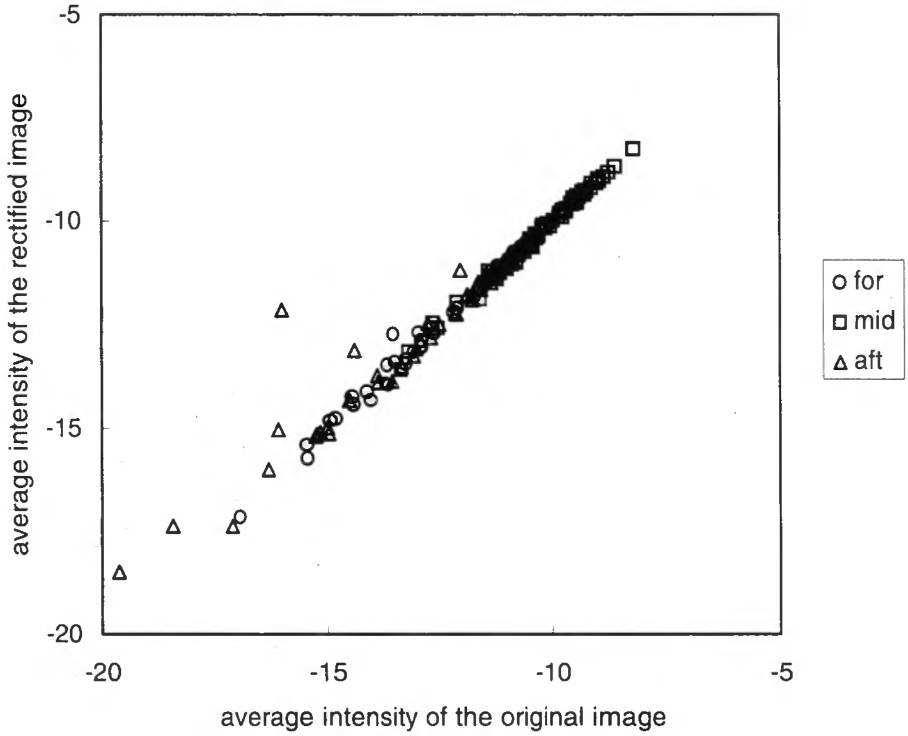

Figure 2.3. The average intensity of original and rectified scatterometer images of June, 1994.

Table 2.1. The median of the difference in the mean intensity and the standard deviation of the intensity of the scatterometer images of June, 1994 caused by the rectification.

	Mean Intensity Difference (rectified - original)			Standard Deviation of Intensity Difference (rectified - original)		
	For	Mid	Aft	For	Mid	Aft
Median (%)	-0.00076	0.0035	-0.0042	-0.048	-0.073	-0.061

2.3 SSM/I Data Properties and Processing

The SSM/I microwave radiometer is a seven channel instrument designed for global sea, land area and atmosphere measurements. The incidence angle employed is 53.1° off nadir. The frequency and polarization combinations of the SSM/I are listed in Table 2.2.

The SSM/I data was acquired from Remote Sensing Systems, California, USA for a 12 month time period, reaching from July 1993 to June 1994. The data was delivered on 12 Exabyte-tapes, each containing 8 files thus making one month of data. The data coverage was chosen to be 100%, i.e. including all data from the F-11 SSM/I instrument from the time period in question.

During each scan, the SSM/I 85 GHz channels are sampled 128 times over a 102.4° arc, thus resulting in 128 V-polarization and 128 H-polarization footprints. Observations at the three lower frequencies are only taken every other scan. Those scans during which the lower frequency channels are sampled together with the higher frequency channels are called "A-scans", and the scans with only higher frequency channels sampled are called "B-scans". During an A-scan, 64 samples of each of the lower channels are collected *(Wentz 1991)*.

The data was first processed from the tapes using a software developed at HUT, although parts of the software source code followed the data delivery. During this first processing, some of the data was skipped from further processing. This data included areas which were in no proximity to the chosen test sites, e.g. the whole southern hemisphere. The data was at this second stage already saved in ASCII-format, thus making the validation process easier.

After the preliminary data processing, the data for Finnish test sites had to undergo a coordinate system change. The original geodetic ϕ, λ coordinates were transferred to the Finnish National Coordinate Grid (KKJ). This transformation includes a Gauss-Krüger projection (transverse cylindrical projection) of geodetic coordinates using central meridian of 27°. The resulting coordinates are in meters, having the north coordinate starting from equator and east coordinate set on 3,500,000 m on central meridian. After transformation, the data was interpolated into the fixed grid using bilinear interpolation in order to make it directly comparable with the reference data, see Figure 2.4. This was only done for the data for Finnish test sites, since the accuracy of the KKJ deteriorates with increasing distance from Finland. The data for African test site use the original coordinate system.

Table 2.2. SSM/I channels and their spatial resolution *(Wentz 1991)*.

Frequency (GHz)	Polarization	3 dB Footprint size (km)	
		Along-track	Cross-track
19.35	vertical	69	43
19.35	horizontal	69	43
22.235	vertical	50	40
37.0	vertical	37	28
37.0	horizontal	37	29
85.5	vertical	15	13
85.5	horizontal	15	13

2.4 Test Area Data Descriptions

Finnish test area

The Finnish test area includes two squared areas presented in Figure 2.4 (referred to as the North and South Finland test areas). The size of both areas is 500 km by 500 km. They embody primarily boreal forests, water areas (Northern Baltic sea and inland lakes) and some agricultural areas. The areas are divided into a fixed 25 km grid for which the satellite-borne microwave instrument data (ERS-1 WS and SSM/I) and the reference data are processed. However, the additional NOAA AVHRR time series are processed for a 1 km grid. Smaller sub-areas have been selected from the two large test areas and a detailed reference data are obtained for these areas using a 5 or 1 km fixed grid, see Figure 2.5.

The NOAA AVHRR-based data set employed in this study includes the following quantities:

- NDVI values
- atmospherically uncorrected surface temperature (band 4)
- atmospherically corrected surface reflectance (band 1)
- atmospherically corrected surface reflectance (band 2).

The AVHRR data set covers the time periods from June 1993 to September 1993, from April 1994 to July 1994, and additionally, selected observation for the winter 1993/1994.

The employed satellite-borne data are summarized below:

ERS-1 Wind Scatterometer data

- interpolation grid size: 25 km
- number of channels: 1
- aerial coverage:
    Northern Finland (400 grid cells)
    Southern Finland (400 grid cells)
- time period:
    from 1 June 1993 to 31 July 1994

SSM/I data

- interpolation grid size: 25 km
- number of channels: 7
- aerial coverage:
    Northern Finland (400 grid cells)
    Southern Finland (400 grid cells)
- time period:
    from 1 July 1993 to 30 June 1994

NOAA AVHRR data

- grid size: 1 km
- number of channels: 4
- aerial coverage:
  Northern Finland (25000 grid cells)
  Southern Finland (25000 grid cells)
- time period:
  selected observations
  from 1 June 1993 to 31 July 1994

The reference data includes (1) daily weather statistics, (2) snow/sea ice cover information, (3) soil moisture information, (4) soil frost information and (5) the percentage values for different land use classes and soil types (71 classes) for each grid point.

Daily weather statistics are based on the measurements at fixed weather stations of the Finnish Meteorological Institute.

Snow cover information is based on the operational *in situ* measurements on fixed test lines scattered around the Finnish test areas. The information includes snow water equivalent and density values. Based on these measurements, the Finnish Environment Agency also generates twice a month a snow cover map presenting the nation wide snow water equivalent information.

The sea ice charts used in the study were acquired from the Finnish Institute of Marine Research. The charts are published daily, but because they are not necessarily updated with any new information as frequently, a cycle of 2 charts per week was chosen. This provides a tool for estimating the feasibility of any tested algorithm to detect changes in the ice conditions. The charts are based on visual observations from ice breakers in the area, reports from commercial vessels and NOAA AVHRR images when the weather permits their use (non cloudy daylight conditions).

The soil moisture reference values (for 0-10 cm top soil layer) are determined for the summer and autumn 1993 using a hydrological model (Deardorff model) that defines the soil/vegetation/atmosphere interaction model. The model employs precipitation information and other meteorological data as input *(Sucksdorff et al. 1992)*. This reference information is only obtained for selected sub-areas. The weather information employed by the model includes such variables as sun radiation, air temperature, wind speed, air humidity and rainfall. The interaction model was used to calculate the surface fluxes, temperatures and moistures for the same area, same times and same resolution as the soil/land use maps. The moisture data include day averages for a 0-10 cm surface layer and for a 0-120 cm root zone. According to several comparisons with measured data (e.g. in Eura- and Loimijoki area) the results are close to real values of soil moisture (relative error from 10% to 20%).

The soil frost information is based on the *in situ* measurements conducted on fixed stations scattered around the two test areas.

The land use/soil information needed for the study is available through the digital land use and soil maps of Finland. The digital land use map was produced by means of a supervised classification using Landsat TM-images from years 1988-90. The whole Finland was covered. The result consists of 62 classes, which includes also different types of forests divided into separate groups according to the stem volume. All classified images were rectified into the Finnish national coordinate system with a ground resolution of 25 m. To separate peatlands from mineral lands, the peatland element from the 1:100000 topographic paper maps was scanned and combined with the land use map. This procedure was applied for agricultural areas as well. The land use map was produced as a collaborative work by several Finnish research institutes, the National Board of Survey being the project coordinator.

The digital soilmap with a resolution of 200 m was produced by scanning the 1:1000000 paper map which was produced by the Geological Survey of Finland in years 1979-81. The scanning was carried out by the Finnish Environment Agency in 1991. Soil map consists of 11 classes. Another digital soilmap with a resolution of 25 m was produced by scanning the 1:100000 paper map. That map, which has 17 classes, was also produced by the Geological Survey of Finland in years 1965-67.

A combination of the land use map (resolution 25 m) and the soil map (resolution 200 m) has been produced for this project. First the number of classes in both maps was reduced by joining some of the classes into a new generalized class. Then a full cartesian product was calculated. As a result, a new map with a resolution of 25 m with 71 classes was obtained. For Porvoo test area, also a combination of the land use map (resolution 25 m) and the soil map (resolution 25 m), has been produced. The result has a resolution of 25 m as well. The combined land use/soil map was used as an input to the statistical calculations for the grids over test areas. For each grid cell, the percentages for each land use/soil class have been calculated.

The employed test areas and the reference data obtained for each grid point of these areas are summarized below:

The large areas:

North Finland test area (size: 500 km by 500 km)
(grid size: 25 km)

- grid cell-wise land use statistics
- grid cell-wise soil type statistics
- grid cell-wise forest cover statistics
- time series for meteorological information (point measurements)
- time series for soil frost depth (point measurements)
- time series for snow cover extent, water equivalent and density

South Finland test area (size: 500 km by 500 km)
(grid size: 25 km)

- grid cell-wise land use statistics
- grid cell-wise soil type statistics
- grid cell-wise forest cover statistics
- time series for meteorological information (point measurements)
- time series for soil frost depth (point measurements)
- time series for snow cover extent, water equivalent and density

and their sub-areas:

Porvoo area (size: 100 km by 100 km)
(grid size: 1 km)

- grid cell-wise time series for soil moisture
- grid cell-wise land use statistics
- grid cell-wise soil type statistics
- grid cell-wise forest cover statistics
- time series for meteorological information

Eurajoki-Loimijoki area (size: 200 km by 100 km)
(grid size: 5 km)

- grid cell-wise time series for soil moisture
- grid cell-wise land use statistics
- grid cell-wise soil type statistics
- grid cell-wise forest cover information
- time series for meteorological information

Lammi area (size: 150 km by 150 km)
(grid size: 5 km)

- grid cell-wise land use statistics
- grid cell-wise soil type statistics
- grid cell-wise forest cover statistics
- time series for meteorological information.

Kajaani area (size: 150 km by 150 km)
(grid size: 5 km)

- grid cell-wise land use statistics
- grid cell-wise soil type statistics
- grid cell-wise forest cover statistics
- time series for meteorological information.

Sodankylä area (size: 100 km by 100 km)
(grid size: 5 km)

- grid cell-wise time series for soil moisture
- grid cell-wise land use statistics
- grid cell-wise soil type statistics
- grid cell-wise forest cover statistics
- time series for meteorological information.

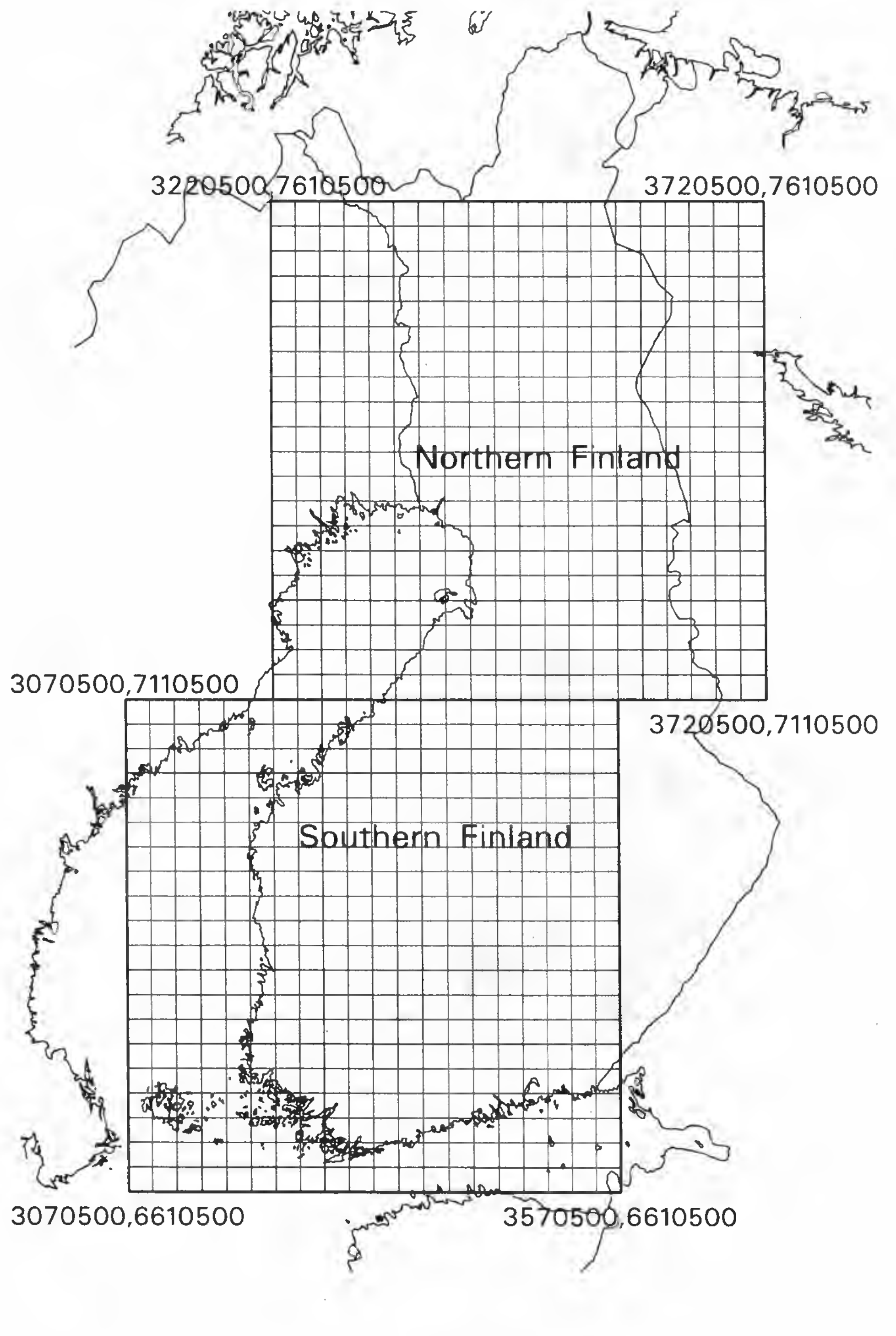

Figure 2.4. Large Finnish test areas with the fixed 25 km grid. Coastal lines, national borders, and major lakes are also shown.

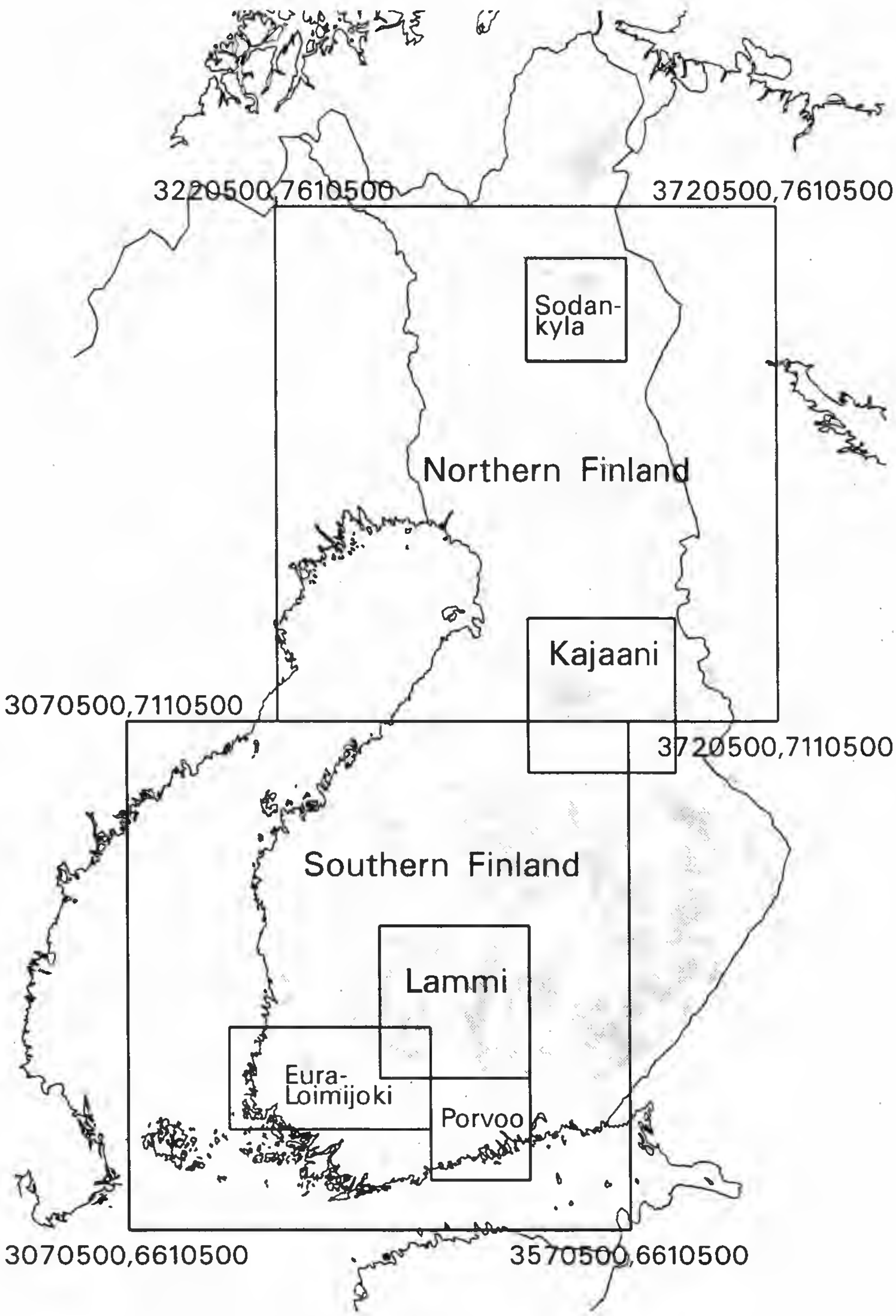

Figure 2.5. Large Finnish test areas and their sub-areas.

Sea ice study areas

The primary sea ice test sites chosen cover most of the northern parts of the Baltic Sea (Gulf of Bothnia). The Gulf is divided into 25 km x 25 km pixels, while carefully avoiding the coastline, see Figure 2.4. The geolocation error of the SSM/I is less than 10 km, and this is the minimum safe distance from the coast. The northern parts of the Gulf of Bothnia is during a normal winter mostly covered with an ice sheet from December to April, and the southern parts usually have some drifting ice throughout that period. The winter of 1993-1994 was relatively cold, and 100% concentrations of sea ice can be expected for most test sites throughout the winter. The reference data include weather information and sea ice cover information (sea ice charts).

West Africa test area

The West Africa test area covers the region between the longitudes E 10° and W 15° and, between the latitudes N 5° and N 20° (tropical forest, savanna and desert areas). The reference data obtained for this area include:

- land use and forest cover information
- time series for meteorological information
- statistics of the monthly maximum vegetation index values.

North Europe test area

The North Europe test area covers the whole European boreal forest zone from Scandinavia to Ural mountains (and northern parts of European mid-latitude mixed forest zone). The reference data for this area includes the NOAA AVHRR-based forest biomass (stem volume) estimates determined separately for coniferous and deciduous species.

3 Review of Microwave Backscattering and Emission Models

The approaches employed in the modeling of microwave backscattering and emission include (1) theoretical, (2) empirical and (3) semi-empirical approaches. Theoretical models are based on the analysis of microwave interaction with the physical constituents of the target, which are defined as statistical parameters. Empirical models are based on the parametrical fitting of mathematical formulas into the obtained experimental data. Semi-empirical models combine both aspects.

Parameters contributing to microwave interaction

The backscattering and emission properties of the target are dependent on the following properties of microwave radiation: frequency, angle of incidence and polarization.

The general characteristics that affect microwave interaction with vegetated terrain are: (1) volumetric vegetation and soil water contents which primarily determine the dielectric properties of the target and (2) vegetation canopy structure (geometry) or surface floor geometry (slope, roughness and correlation length). Additionally, the physical temperature of the medium (water) has an effect on its dielectric properties. An important characteristic is the drop of the dielectric constant of water as the water freezes. The essential factor affecting the microwave interaction is not the absolute value of the dielectric constant, but the contrast between a target structure and its background (e.g. the ratio of the dielectric constant of vegetation to that of air). In addition to the scattering of incident signal, the target absorbs part of the incident power, which, again, depends on the dielectric and geometrical properties of the target. The target structures that are larger than the radar wavelength act primarily as scatterers, while those structures substantially smaller than the wavelength are attenuators (*Kasichke and Christensen 1990*).

Dielectric properties of target

The dielectric properties of soil are well described by semi-empirical mixing models for the frequency range from 1 to 20 GHz (*Dobson et al. 1985, Hallikainen et al. 1985*). *Dobson et al. (1985)* also presented a four component theoretical mixing model for dielectric properties. However, the practical convenience of this approach is inferior to the semi-empirical approach.

The dielectric constant of a vegetation canopy can be found using two different modeling approaches: (1) defining the effective dielectric constant of the continuous vegetation-air mixture, (2) defining the dielectric constant of discrete vegetation particles. The forest canopy is a sparse medium: the effective fractional volume of vegetation is typically only 0.01 - 0.02% of the total volume (*Le Toan et al. 1990*). Empirical models for the continuous dielectric properties of vegetation are given in (*Le Toan et al. 1990*). The dielectric constant of the vegetation is, above all, dependent on the volumetric moisture of the material. *Ulaby and El-Rayes (1987)* presented a Debye-Cole dual-dispersion dielectric model that gives the vegetation dielectric constant as a function of volumetric fraction occupied by water. This model is validated up to 20 GHz. *Schmugge and Jackson (1992)* successfully applied this approach further for frequencies up to

40 GHz. *Mätzler (1994b)* developed a semi-empirical formula for the dielectric constant of leaves for a frequency range from 1 to 100 GHz and found good agreement with modeled and experimental values.

3.1 Theoretical Approaches

The theoretical approaches are divided to surface and volume scattering models. The emission properties of the target are directly connected to scattering properties (*Tsang et al. 1985, Ulaby et al. 1982*). Hence, the presentation of theoretical models can focus to the presentation of scattering models. The backscattering and emission from land surface (soil) are typically treated with surface scattering models in microwave frequencies, whereas the microwave interaction with vegetation canopy is modeled by volume scattering approaches. For such media as snow and sea ice, both the surface and volume scattering models are required depending on the frequency and snow/sea ice type.

<u>Ground surface scattering and emission (bare soil)</u>

The classical surface scattering modeling approaches are the Kirchoff model (KM) and the small (scale field) perturbation method (SPM). The former gives the high frequency solution to the rough surface scattering problem, as the latter gives the low frequency solution. When the wavelength is comparable with the surface roughness both approaches fail (the validity range of these models is restricted by two target parameters: the surface roughness and correlation length). Some new attempts have been recently carried out in order to make more unified techniques, namely the phase perturbation method (PPM), the full wave model (FWM) and the integral equation model (IEM) (*Fung 1994*). However, the theoretical approaches that have been typically employed in practise are the (small scale) field perturbation model and the Kirchoff approximation (*Sun et al. 1991, Chauhan et al. 1991*). However, these classical models have found to agree with experimental observations only under certain conditions. The other methods are not yet in the level of feasible use.

Natural surfaces are typically composite surfaces that consist of *very rough* large scale random structures, such as terrain slopes, and small scale *slightly rough* random structures, such as surface foliage and small rocks or gravel. Both these types scatter microwave signal incoherently since the coherent component is suppressed by the random roughness (*Ruck et al. 1970*). For a very rough surface, the rms-surface roughness is much larger than the wavelength, whereas the roughness is much smaller than the wavelength for a slightly rough surface. The scattering component, caused by the large scale roughness, can be modeled using Kirchoff approximation (this roughness component is typically gently sloping). This scattering component is dominant for backscattering at incidence angles near the nadir (near the nadir the specular reflection from a gently sloping surface also occurs in the direction of backscatter). As the angle of incidence increases, the small scale roughness becomes a more important factor in backscattering (perturbation models are typically applicable for the modeling of this component) (*Ruck et al. 1970*). The total incoherent backscattering from a composite surface can be approximated as a sum of these two components (*Ruck et al. 1970*).

However, typically the ground surface is covered by an irregular layer which can contain litter and/or surface vegetation (or snow). In the case of microwave emission from that kind of surface, the coherent component (coherent transmission across layer boundaries) can be more important than the incoherent component (*Fung 1994*). But in the case of radar backscatter, the incoherent backscattering remains predominant.

A major problem in the employment of theoretical approaches arises from the fact that the classical methods (KM, SPM) cannot describe the scattering for large range of surface roughness, correlation length or incidence angle. The other problem is the restricted information on the surface roughness and correlation length for natural targets.

Vegetation scattering (volume scatter)

The theoretical approaches for vegetation modelling can typically be applied for both the forest and the short vegetation canopies. Canopy structure parameters that are relevant to microwave interaction include such characteristics as tree/plant height, stem/plant density, trunk diameter, branch density and orientation, and leaf/needle density and orientation. These parameters are directly related to the stem volume and the total biomass of a vegetation canopy.

A forest can be generally considered as a three-layer system incorporating the crown layer, trunk layer and soil layer (*Le Toan et al. 1990*). The sensitivity of the backscattering coefficient to these parameters is a function of the microwave frequency, polarization and the angle of incidence. In general, as the frequency increases, towards the X-band, the effect of needles (or leaves) and twigs starts to dominate backscatter instead of the contributions from the stems and forest floor (*Pulliainen and Hallikainen 1992, Mougin et al. 1993*).

Cloud models and other approaches to vegetation scattering modeling

Cloud models are radiative transfer models, in which the vegetation is modeled as a cloud of water droplets (analogously to an atmospheric cloud). The water droplets can be considered to be uniformly or unequally distributed in size. *Attema and Ulaby (1978)* proposed this model for agricultural vegetation canopies. The canopy properties are described by a volume backscattering coefficient and a total attenuation (extinction) coefficient. *Richards et al. (1987)* applied this approach to backscatter from forest at the L-band. In their model the scattering from the foliage is taken into account with the water droplets model, but in addition to that, trunk-ground reflections and forward scattering from crown to ground are considered. The trunk-ground reflection is incorporated using a dihedral corner reflector approach (the trunk acts as a dielectric cylinder). The model requires calibration against empirical measurements. The model applies well to co-polarized signatures, but does not deal adequately with cross-polarization backscattering signatures. *Durden et al. (1989)* and *Sun et al. (1991)* have enlarged this approach to include cross-polarization (full polarimetric) properties by modeling the branches as randomly orientated dielectric cylinders.

Chauhan et al. (1991) have used the distorted Born approximation in modeling backscattering from boreal forests on P-, L- and C-bands. The distorted Born approximation with vegetation modeled as a continuous medium (i.e. random permittivity fluctuations) has been studied by e.g. *Le Toan et al. (1990)*. These models are based on the field approach instead of the radiative transfer approach. The field approach is based on the approximate solutions of Maxwell's equations which define the exact theoretical background of an electromagnetic scattering problem (refer e.g. to (*Tsang et al. 1985*)). In general, the field approach is appropriate for a weakly scattering medium, while the radiative transfer approach treats better such a medium (e.g. trees) where the dielectric properties of the material differ strongly from the air dielectric constant (*Ulaby et al. 1990*).

MIMICS model for vegetation canopy scatter

The MIMICS model (Michigan Microwave Canopy Scattering Model) is a widely employed model for vegetation canopy scattering, especially in the case of forests. A general description of the model is given in *Ulaby et al. (1990)*. The MIMICS model is based on the radiative transfer approach. In this technique, the backscattered signal is expressed in terms of radiation intensities (extinction and phase matrices). The MIMICS model is a three-layer model (crown layer, trunk layer and soil) that treats the scattering material of the canopy as discrete dielectric cylinders. The soil scattering is determined by semi-empirical/theoretical equations. The dielectric cylinders of which the canopy is constructed approximate stems, branches and needles (or leaves). The dielectric properties of these are determined from their volumetric water contents. The frequency range of the model is from 0.5 to 10 GHz.

The MIMICS model has also been implemented as a software package (*Ulaby et al. 1992*). The input parameters of the MIMICS software include the mean values or distributions of the following characteristics:

(a) for the crown layer: height of the layer; length, diameter and orientation of primary and secondary branches; diameter and length (or thickness) of needles (or leaves); and water contents and temperatures of all these particles.

(b) for the trunk layer: height; trunk diameter, density, orientation, temperature and water content.

(c) for the soil layer: soil moisture, temperature, surface roughness, soil type, and possible snow layer characteristics.

The MIMICS model can be applied to any vegetation. The application and model validation reports are given by e.g. *McDonald et al. (1990), McDonald et al. (1991)* and *Hoekman et al. (1992)*. Restrictions of the model include (1) that it only treats flat surfaces, (3) the crown layer is modeled as a single layer, (2) that the second order scattering is not included (i.e. multiple scattering is not included) and (3) the crown layer is modeled as a single layer. The last restriction is avoided with the latest development (MIMICS II) which treats discontinuous vegetation canopies (*McDonald and Ulaby 1993*).

Karam and Fung's model is based on a similar approach to the MIMICS model (*Karam et al. 1992a, Karam et al. 1992b, Fung 1994*). However, this model also incorporates multiple scattering and it can be used with different surface slopes. *Hsu et al. (1992)* also give a description of another analogous radiative transfer model applied to a pine forest.

Modeling approaches for sea ice and snow cover

Sea ice is in most cases covered with a snow layer, which leads to a complex case of a modeling problem. The various layers (snow, sea ice, water) and their interactions should be taken into account when the expected natural behaviour is being modeled. The general case of this kind of modeling consists of a snow layer, an ice layer (both of these layers may be divided into sub-layers) and a water layer. Some approaches found in the literature combine these multi-layer structures into a general model, presented later in this Section.

Modeling of anisotropic layer structure scattering for sea ice

While modeling an anisotropic layer with a random structure, the combined effects of volume and surface scattering must be examined. Most models expect these to be calculated separately. A simple model including both of these has been made using Radiative Transfer Theory for volume scattering in the snow layer, and physical optics model for surface scattering *(Drinkwater and Crocker 1988)*. The physical optics model has been found to predict the VV-polarized backscatter to substantially lower levels than the HH-polarized backscatter at high incidence angles. This behaviour has not been verified by any measurements *(Carlström and Ulander 1993)*. Another approach using the Integral Equation Method (IEM) for surface scattering has been tested, but the results have not proved satisfactory. Apparently the use of a fixed value for the surface roughness is not applicable to sea ice, which has a continuous roughness spectrum *(Manninen 1994)*.

Attempts to solve the electromagnetic wave scattering problem by applying the first-order Born approximation has been made by *Lee and Kong (1985)*. The resulting two-layer model has later been extended to a three-layer model to include the snow layer. Some experimental comparison has been made, but the results obtained have required some parameter fitting *(Borgeaud et al. 1986)*.

The three-layer model mentioned above has been improved by using the strong fluctuation theory, and by computing the bistatic scattering coefficients and emissivities using the wave scattering theory in conjunction with the Born approximation *(Lin et al. 1987)*. No comparison to experimental passive data has been found in the literature, but some limited results when compared to actively sensed data do exist. However, some of the needed parameters have been estimated *(Lin et al. 1987)*.

The full wave solutions for surface scattering have been extended to a nonuniform multi-layered structure with an unlimited number of layers *(Bahar 1988)*. The full wave theory permits very complicated structure, but it has not yet been successfully applied to sea ice. Only a simple case of a two-layer structure with plane boundaries and homogeneous permittivities has been so far presented in the literature.

General models usually combine a surface scattering and a volume scattering model, and the interaction between the different scattering mechanisms are dealt with in various manners and in some cases even neglected. For example *Carlström and Ulander (1993)* have used an approach where they have modified the scattering model proposed by *Kim et al. (1985)* and neglected the interactions. The volume scattering is modeled by the water cloud model *(Attema and Ulaby 1978)*, and the surface scattering by the Integral Equation Method (IEM). Another approach by *Tjuatja et al. (1992)* uses the radiative transfer model, which is modified in a way that the phase matrix accounts for both non-Rayleigh particle size and close spacing between scatterers. The above mentioned IEM model is included for surface scattering. The authors have tested their model with a reference to some limited experimental data sets, and the results are somewhat encouraging for bare saline ice types. The snow covered problem and a problem with a continuous roughness spectrum has not been dealt with in a satisfactory manner.

Modeling of scattering from a snow layer

Most of the sea ice models presented above are three-layered models, thus including the snow layer. The same methods and models may be used for a single snow layer with a ground layer beneath. For example the radiative transfer approach has been shown to give a reasonably good correlation to experimental results if calculated as a function of incidence angle *(Kong and Shin 1979)*. Due to overestimating the scattering effect, the radiative transfer equation gives much too low values when calculated as a function of snow water equivalent *(Chang et al. 1987, Pulliainen et al. 1990)*. According to these results the radiative transfer model, when applied to scattering from a snow layer, is only suitable to frequencies below 30 GHz which is not enough for snow modeling purposes.

The strong fluctuation theory *(Stogryn 1986)* has been shown to apply reasonably well for large snow water equivalents. Likewise, the radiative wave theory *(Tsang 1987)* seems promising since it does not overestimate scattering effects. This approach is however more mathematically complicated than the rather simple radiative transfer theory, making it less attractive to be used. Both of these models lack experimental comparisons, and have still not been widely tested and verified. Some comparisons of strong fluctuation approach with experimental data are presented in *(Weise 1996)*. These comparisons showed considerable differences between the model predictions and experimental values.

3.2 Empirical and Semi-Empirical Approaches

Backscattering from soil

The Michigan empirical model proposed by *Oh et al. (1992)* is a well validated model that can be used for L-, C- and X-bands for the angle of incidence range from 20° to 70° at VV, HH and cross polarizations. The valid range of surface roughness and volumetric soil moisture is defined by:

$0.1<ks<6.0$,
$2.6<kl<19.7$ and
$0.09<mv<0.31$,

where k is the wave number, l surface correlation length and mv is the volumetric soil moisture.

The model overcomes the problems evident with theoretical approaches which fail to predict that large parameter value ranges, especially the wide incidence angle range *(Oh et al. 1992)*.

The model parameters include:

- frequency,
- rms soil surface height (roughness),
- angle of incidence,
- soil dielectric constant (which is, most of all related to the volumetric soil moisture).

Backscattering from forests

Semi-empirical model for boreal forests

The backscattering model developed at the HUT for conifer-dominated boreal forests describes the forest canopy volume backscattering and extinction properties as a function of forest biomass (stem volume) and vegetation volumetric moisture (*Pulliainen 1994, Pulliainen et al. 1994*). The model is based on the employment of airborne profiling scatterometer data obtained by the HUTSCAT instrument for C- and X-bands. The polarization combinations are VV, VH, HV and HH. The model has been employed jointly with the Michigan soil backscattering model (*Oh et al. 1992*) in the analyses of forest backscattering contributions, sensitivities to various target parameters and in the development of inversion approaches for ERS-1 SAR data. Currently, the model is well validated for the conditions of Finland.

The restrictions of the model include the fact that the it basically treats only 23° angle of incidence. The experimental measurements for large forest areas were conducted using this angle of incidence. The model can be used for angles different from 23° when the angular effects in canopy extinction and volume backscattering coefficients are incorporated by theoretical considerations, e.g. from MIMICS simulations. However, the model validation against experimental data for other angles of incidence is quite limited.

The model parameters include:

- forest biomass (stem volume),
- angle of incidence,
- rms ground surface roughness,
- forest canopy volumetric moisture,
- volumetric soil moisture.

Emission from vegetation

The model by *Kerr and Njoku (1990)* has been employed in the Nimbus-7 SMMR data analysis. The model takes into account the following parameters:

- sensor parameters (viewing angle, ground resolution, frequency, polarization),
- atmospheric conditions,
- soil surface parameters:
  moisture, roughness and temperature,
- vegetation characteristics:
  temperature, water content, single-scattering albedo, structure and percent coverage.

The most severe restriction with the model is the description of surface emission (surface reflectivity). The expressions for surface reflectivity employed by *Kerr and Njoku (1990)* are only validated for frequencies from 1 to 10 GHz.

Semi-empirical model for vegetation effects in land surface emissivity

Schmugge and Jackson (1992) applied the dual dispersion model for vegetation dielectric constant (*Ulaby and El-Rayes 1987*) in the determination of plant canopy absorption properties in the frequency range from 1 to 40 GHz. The results obtained show good agreement with the empirical data. The semi-empirical model by *Mätzler (1994b)* may be used for enlarging these approaches to frequencies up to 100 GHz.

Snow and sea ice

Semi-empirical models for sea ice

The major problem with empirical studies of sea ice backscatter is the lack of adequate ground truth, i.e. measurements with all or most of the contributing parameters recorded for reference. These data include surface roughness, ice temperature, ice thickness, ice salinity, ice thickness and the same parameters for the overlaying snow cover. Currently the available data sets make it possible to detect ice from a surrounding open sea, but for classification purposes the models are far too simple. The complicated nature of the media (e.g. time variance) also limits the validity of any straight-forward model *(Pulliainen et al. 1990)*.

Semi-empirical models for snow

Semi-empirical models should be able to estimate the emissivity of a snowpack with given parameters, but should also include the effect of vegetation canopies. *Stiles and Ulaby (1980)* have derived a simple equation for the brightness temperature of a snow-covered ground, but it does not include a vegetation factor. Another model which is here referred to as the HUT model *(Hallikainen and Jääskeläinen 1988)* is based on the radiative transfer model where multiple scattering is dealt with an empirical constant factor. The dielectric and extinction properties of the target are considered with formulas given in *(Hallikainen et al. 1987, Mätzler 1987, Hallikainen et al. 1986)*. The model has already been shown to agree well when compared to experimental results with refrozen snow *(Grandell and Hallikainen 1994)*. A model by *Hallikainen (1984)* sums the factors contributing to the emission from the ground and the snowpack, but includes a new factor describing the emission contribution from the vegetation. Extensive experimental data sets are described e.g. in *(Mätzler 1994a)*.

Atmospheric effects

The atmospheric attenuation and emission effects on a satellite-borne measurement have to be considered when the frequency exceeds the C-band, as in the case of SSM/I radiometer measurements. At the micro- and millimeter wave frequencies, the influence of atmosphere can be modeled by the radiative transfer approach. A well validated model for the determination of the absorption coefficients of atmosphere at the whole frequency range of SSM/I is the MPM-model (*Liebe 1989*). A simpler model, which is more uncertain at higher frequencies (85 GHz), is given by *Ulaby et al. (1981)*. The employment of these models require detailed information on atmospheric conditions: pressure profile, temperature profile and cloud conditions.

The models by *Liebe (1989)* and *Ulaby et. al (1981)* are unpractical for inversion purposes. Hence, in the case of inversion of satellite-borne microwave radiometer data, simplified models and/or statistical values for the atmospheric transmissivity have to be employed. These models and approaches are discussed e.g. in (*Bernard 1988, Aschbacher 1989, Pulliainen et al. 1990, Kerr and Njoku 1990, Pulliainen et al. 1993*).

3.3 Summary: Comparison of Models

Constraints of current models

The basic problem with the vegetation scattering (and emission) models arises from the complexity of the target. Hence the applied theoretical models are also complex (a large number of input parameters). The more accurately the model includes the physical features of the target, the larger is the number of parameters needed. Nevertheless, the mean values and distributions of these parameters are often poorly known (e.g. the variations of moisture contents in different parts of trees). The model validation is mostly based on comparisons to the total backscattering coefficient even though the models deal with separate bidirectional scattering contributions from different scattering mechanisms. How accurately these contributions determined by the model correspond to the real values is not well known.

Even though the theoretical models are complex systems they always include some simplifications about canopy and surface structure, and thus the models are restricted to certain input parameter ranges (e.g. frequency range, look angle range, surface curvature range or certain tree species). For example, the MIMICS model treats scatterers as homogeneous dielectric cylinders, even though the plant tissue can be significantly inhomogeneous material (e.g. trunks of some conifer tree species). The lower the employed microwave frequency is, the more severe these problems are as the penetration depth into the woody tissue is higher (of course, in the extreme case when e.g. the trunk radius is much smaller than the wavelength, the modeling becomes an easier task). Also the shape of vegetation structures (e.g. branches or leafs) can be far from the cylindrical shape assumed in the MIMICS model. Hence the characterization of cylinders that should correspond to the real canopy structure can be a difficult task. These problems may be, at least partially, overcome when the models are compared or calibrated against experimental data.

The particular problem with the theoretical models for surface and layered media (the case of soil, snow cover or sea ice scattering/emission) arises from the crucial need of information on surface roughness and correlation length. These parameters are typically modelled by constant average values even though the surface may have a continuous roughness spectrum (e.g. the case of sea ice (*Manninen 1994*)). This makes the employment of theoretical models somewhat speculative. Moreover, the general knowledge on surface roughness of natural targets is limited.

Empirical models typically have a substantially smaller number of parameters than theoretical models. Thus they can be more reliable, but they are more restricted to those conditions under which they have been developed. Semi-empirical models can basically combine benefits of both modeling approaches. However, one problem in the model development has been the lack of data by which the different scattering mechanisms (or any of them) could have been distinguished from each other. This has restricted the model validation, and the development of empirical or semi-empirical models.

Validity of present models

Target dielectric properties

The dielectric properties of soil are well described for the frequencies below 20 GHz. The semi-empirical mixing model by *Dobson et al. (1985)* describes the soil permittivity using easily measurable and well defined physical parameters while the detailed theoretical mixing models require a large set of difficulty measurable characteristics. The problem is that the models are not validated for the frequencies higher than 20 GHz. The most reliable description for the dielectric properties of vegetation canopy are given by the dual-dispersion model (*Ulaby and El-Rayes 1987*). This model has been successfully applied in frequencies up to 40 GHz even though the model development was conducted using frequencies below 20 GHz (*Schmugge and Jackson 1992*). New development in the modelling of vegetation dielectric constant includes a semi-empirical model by *Mätzler (1994b).*

Soil backscattering and emission models

The classical theoretical approaches (Kirchoff model and small perturbation model) for surface scattering and emission fail to work for a large range of surface roughness, frequency and angle of incidence. The most recent theoretical approach, the integral equation model (IEM), applies better for a large parameter range. However, the key target parameters employed in IEM are the surface roughness and correlation length, which are often poorly known or cannot be treated with constant values. The empirical backscattering model by *Oh et al. (1992)* fo L-, C- and X-bands describes the soil backscattering properties with higher reliability than the current theoretical approaches. The empirical models for soil emissivity can be applied moderately for frequencies below 10 GHz. For higher frequencies their appliance is hypothetical. Hence, the only possible models for soil surface emissivity at the frequencies of SSM/I are the theoretical approaches, even though their applicability is also speculative. Since the wavelength at SSM/I frequencies is short or about equal compared to the typical soil surface roughness, the use of small perturbation model is negligible. The employment of the other classical approach, the Kirchhoff model (physical optics approximation), is more justified.

Vegetation canopy scattering and emission models

The MIMICS model is currently the most extensively validated theoretical approach for vegetation canopy scattering. The models developed e.g. by *Karam and Fung (1992, 1994)* are not compared against empirical data in that extent as the MIMICS model. The problem with the MIMICS approach arises from the complexity of the model (large number of poorly measurable parameters). This makes the model inadequate to be used without support from experimental data. The well validated semi-empirical model by *Pulliainen (1994)* employs definitions similar to the MIMICS model for describing the boreal forest backscattering properties and hence, it can be used in conjunction with the MIMICS model.

The absorption and emission properties of vegetation canopies are, at least, moderately described for frequencies up to 40 GHz, especially in the case of short vegetation (*Kerr and Njoku 1990, Schmugge and Jackson 1992*). Moreover, some empirical data sets can well be used for the frequencies up to 90 GHz (*Kurvonen 1994*).

Snow and sea ice models

Approximations made during model development limits their use for extensive estimation of the expected backscatter. For example the Kirchhoff and Small Perturbation Method (SPM) require the surface to be either rough or smooth with respect to the wavelength used, and the traditional radiative transfer model is not well suited for a dense media for which the volume fraction of scatterers is more than a few percent. The Integral Equation Model (IEM) is not suitable for a surface with a continuous surface roughness, although some good results have been obtained using limited data sets. The frequency ranges for the models are usually well below 20 GHz.

Selected backscattering and emission models

The following models were selected to be employed further in investigations, i.e. in the analysis of land surface backscattering and emission properties and in the development of inversion algorithms. The selection criterion was their feasibility for implementation within the project framework.

Target dielectric properties

Dual dispersion model for vegetation (*Ulaby and El-Rayes 1987*)
(with the adoption by *Schmugge and Jackson (1992)*)

Semi-empirical dielectric mixing model for soil (*Dobson et al. 1985*)

Soil backscattering models

Michigan empirical model (*Oh et al. 1992*)

Theoretical vegetation canopy scattering models

Michigan microwave canopy scattering model (MIMICS) (*Ulaby et al. 1990*)

Semi-empirical volume backscattering and emission models

Cloud model (basic first-order radiative transfer approach) (*Attema and Ulaby 1978*)

Semi-empirical forest backscattering models

Semi-empirical model for boreal forests (*Pulliainen et al. 1994*)

Theoretical surface emission/scattering models for soil and snow/ice cover

Kirchoff model (*Ulaby et al. 1982*)

Semi-empirical soil and surface vegetation emission models

Semi-empirical emission model for semiarid land surfaces (*Kerr and Njoku 1990*)
Semi-empirical model for vegetation effects in land surface emissivity
(*Schmugge and Jackson 1992*)

Snow cover emission models

HUT model for dry snow (*Hallikainen and Jääskeläinen 1988*)

Atmospheric effects

MPM-model (*Liebe 1989*)

Since the applicable models do not describe the backscattering/emission properties of all various targets and all relevant microwave frequencies and, since their validation is sometimes inadequate, experimental data sets had to be used additionally (e.g. in the considerations of forest canopy in microwave emission analyses).

4 A Semi-Empirical Backscattering Model for ERS-1 Wind Scatterometer Measurements

4.1 Forest Backscattering Model Formulation

The semi-empirical backscattering model employed in these investigations describes the forest backscattering contributions as a function of quantitative forest characteristics, such as stem volume (forest biomass), soil moisture and vegetation canopy moisture. The model is based on the use of airborne C- and X-band high-resolution ranging scatterometer data in the estimation of forest canopy volume backscattering and extinction coefficients (and the level of forest floor backscatter). These parameters are the bulk properties that can be applied in the basic radiative transfer equation for determining the backscattering coefficient measured by a space-borne radar.

The semi-empirical model was developed by using airborne HUTSCAT scatterometer (*Hallikainen et al. 1993*) data from Finnish boreal forests (conifer dominated forests). The original model was developed for a constant angle of incidence (23° off nadir corresponding the ERS-1 SAR incidence angle), but recently the model has been enlarged to cover a angular range from 20° to 60°. Detailed descriptions of the modeling approach are given in (*Pulliainen et al. 1993, Pulliainen 1994, Pulliainen et al. 1994*).

The backscattering coefficient of forest land σ^o can be written as

$$\sigma^o = \sigma^o_V + \sigma^o_g \tag{4.1}$$

where

σ^o_V = backscattering coefficient of the forest canopy

σ^o_g = backscattering contribution from the ground (forest floor).

These two contributions can be determined directly from the high-resolution ranging HUTSCAT measurements. σ^o_g can be divided to the contributions of soil backscatter and trunk-ground reflection (which cannot be directly distinguished in profiling radar measurements):

$$\sigma^o_g = t^2 \cdot (\sigma^o_s + \sigma^o_{dihed}) \tag{4.2}$$

where

σ^o_s = backscattering coefficient of forest floor

t = forest canopy transmissivity

σ^o_{dihed} = backscattering coefficient contribution caused by trunk-ground dihedral corner reflector effect.

The canopy transmissivity as a function of forest stem volume can be determined by comparing $t^2 \cdot \sigma_g^o$ (ground backscattering contribution) of areas with a wide range of stem volumes with each other. The semi-empirical model used here was developed applying this approach for a large forest area (HUTSCAT data from the Teijo test area for 23° angle of incidence) (*Pulliainen et al. 1994, Pulliainen 1994*). The effects of soil and canopy moisture variations, as well as the dependence on the angle of incidence, have been incorporated into the modeling approach using well known models (*Oh et al. 1992, Ulaby et al. 1982, Attema and Ulaby 1978*). The changes in vegetation and soil moisture are the dominant actual causes to seasonal and diurnal changes of σ^o, in addition to freeze/thaw effects, seasonal defoliation and snow cover effects.

Since the backscattering contribution of soil (forest floor) σ_s^o cannot be distinguished from that of the trunk-ground reflection σ_{dihed}^o in a scatterometer measurement, σ_{dihed}^o can be only evaluated through a theoretical consideration. The theoretical concept used is the physical optics approximation for a lossy dielectric cylinder perpendicularly above a rough plane (*Pulliainen et al. 1994, Pulliainen 1994*).

The forest canopy backscattering contribution can be written in terms of the stem volume as

$$\sigma_V^o = \frac{C}{-2 \cdot a_1} \cdot \frac{\cos\theta}{\cos\theta_{ref}} \cdot \left[1 - e^{2 \cdot a_1 \cdot V \cdot \cos\theta_{ref}/\cos\theta}\right] \tag{4.3}$$

where

C = empirical coefficient for canopy backscatter [ha/m^3]
a_1 = empirical coefficient for canopy extinction [ha/m^3]
V = forest stem volume [m^3/ha]
θ = angle of incidence
θ_{ref} = 23° reference angle of incidence
(used in the HUTSCAT experiments).

The empirical values obtained in dry summer conditions for the coefficients above for 5.4 GHz, VV polarization are (in the case of Finnish boreal forests):
$C = 9.68 \cdot 10^{-4}$ m^3/ha and
$a_1 = -2.78 \cdot 10^{-3}$ m^3/ha (*Pulliainen et al. 1994*).

The extinction coefficient a_1 can be assumed to be linearly related to the volumetric canopy moisture, while the change of C can be assumed to be related to the square of the change in volumetric moisture (*Ulaby et al. 1982*):

$$C = k_1 \cdot m_{v,v}^2 \tag{4.4}$$

and

$$a_1 = k_2 \cdot m_{v,v}, \tag{4.5}$$

The forest stem volume V (in m^3/ha) can be approximately converted into the total dry biomass of trees (in tons/ha) by multiplying the stem volume by 0.6 (*Häme et al. 1992*).

4.2 Response to Forest Biomass

Figure 4.1 shows the radar response to forest stem volume (biomass) at various angles of incidence and soil moistures. The results have been calculated using the semi-empirical backscattering model described in Section 4.1. The parameter values employed correspond the typical conditions of Finnish boreal forests on summer: the soil moisture varies from 10 to 25%, vegetation moisture has its nominal value corresponding to dry summer conditions and the effective soil surface roughness is 1.2 cm (this surface roughness value has been determined in previous investigations, refer to (*Pulliainen 1994*)).

Figure 4.1 demonstrates that the C-band radar response to forest biomass at small incidence angles can change from positive to negative depending on soil moisture. For high angles of incidence the response is always positive and also, the sensitivity of σ^o to stem volume is higher than at smaller angles of incidence. When the stem volume is higher than about 150 - 200 m^3/ha (biomasses from 90 to 120 tons/ha), the C-band response to stem volume is saturated.

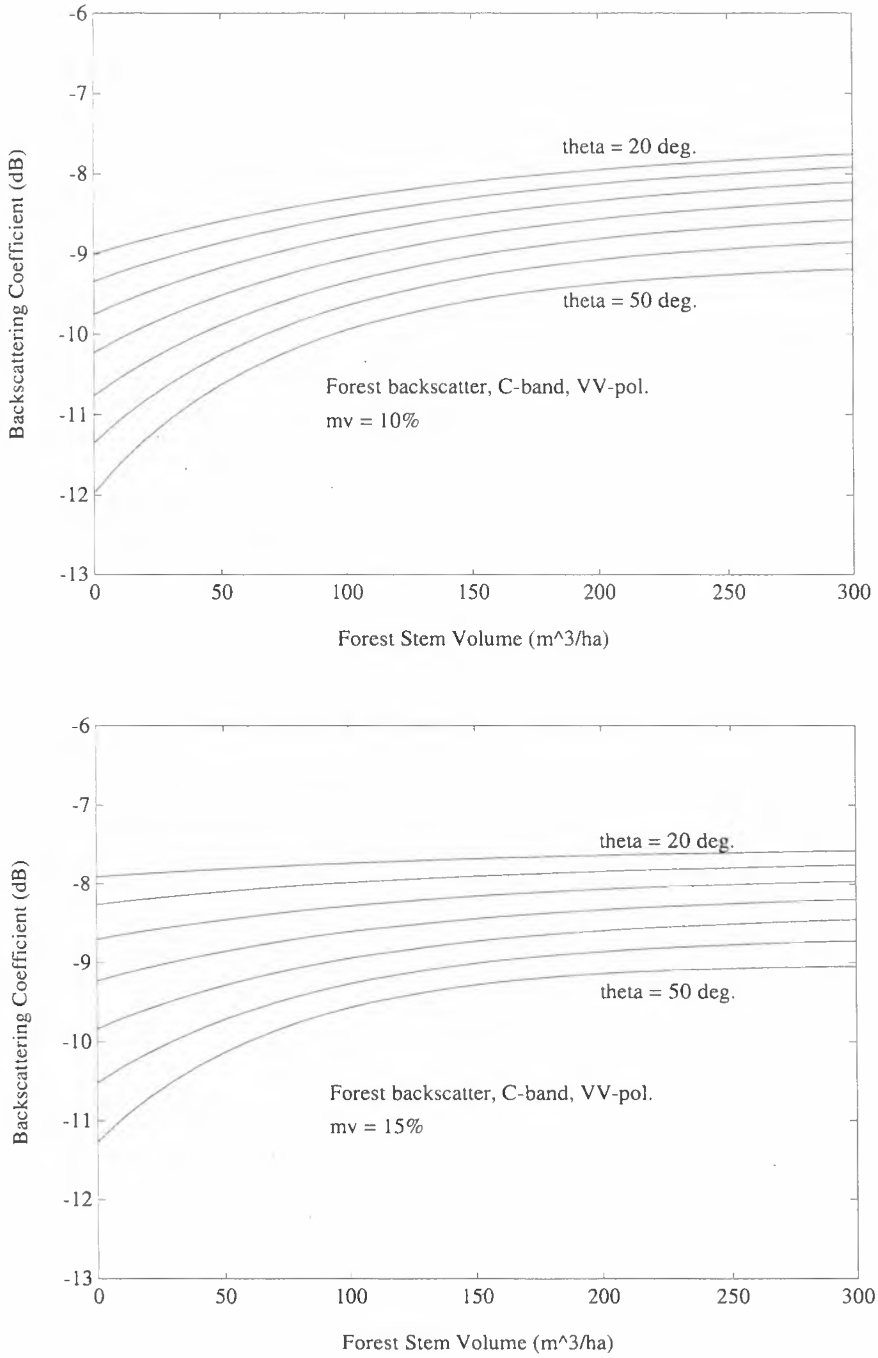

Figure 4.1. Modeled behavior of forest backscatter (boreal forests) as a function of forest stem volume (biomass) with varying angle of incidence (5^o interval). Different figures show the response for various volumetric soil moisture.

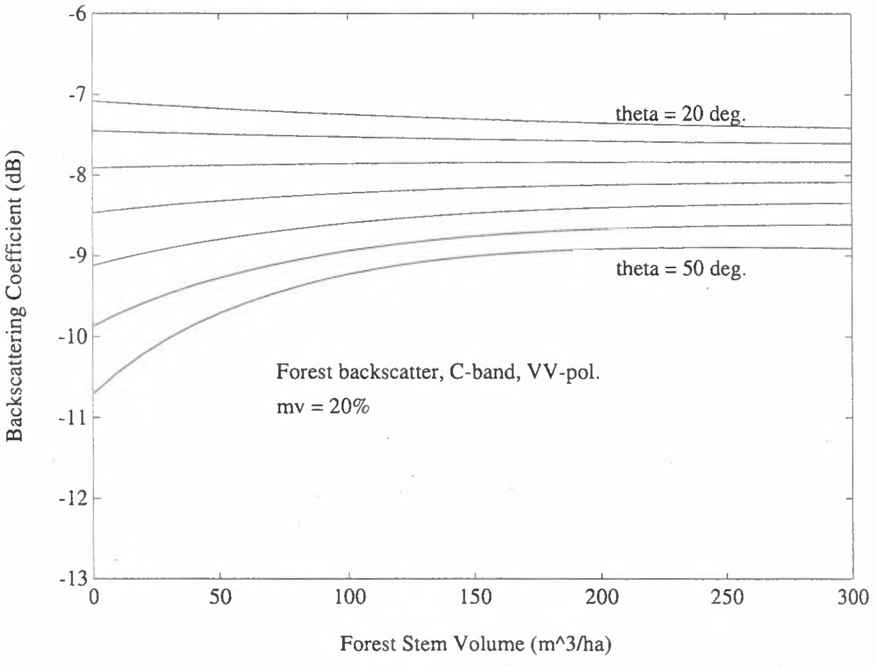

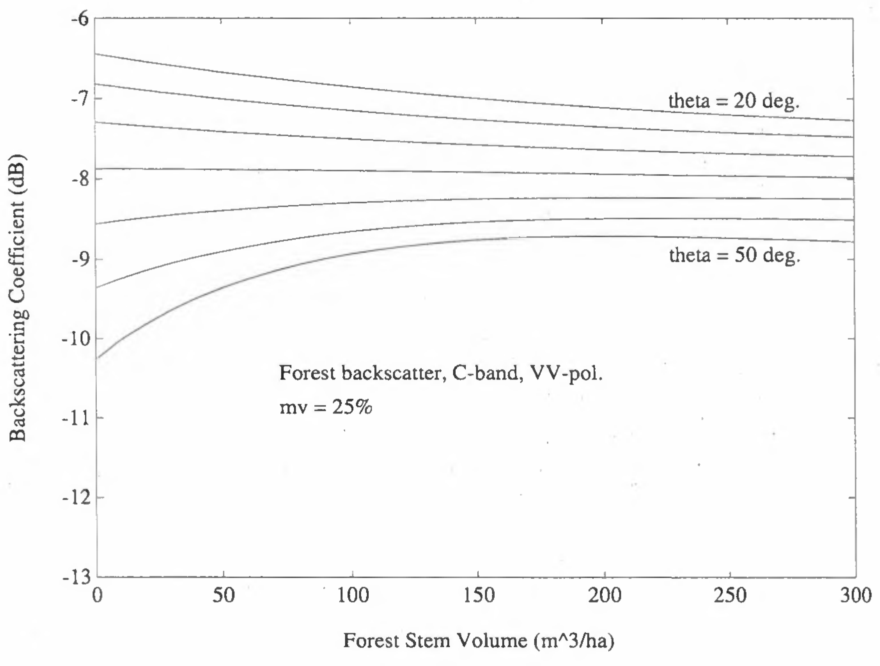

Figure 4.1 Continued.

4.3 Effect of Incidence Angle

The behavior of C-band σ^o as a function of the angle of incidence is depicted in Figure 4.2. As in the case of Figure 4.1, the model parameters have been selected according to boreal forest characteristics. The forest stem volume is varying at 10 m^3/ha steps from 0 to 300 m^3/ha (biomass of 180 tons/ha). The results show that, for VV polarization, the level of backscatter decreases monotonically as the angle of incidence increases. For HH, polarization, the behavior appears to be slightly different due to the influence of trunk-ground reflection. As discussed in Section 4.1, the effect trunk-ground reflection is considered through a theoretical approach. Since validation data for high incidence angles were not available, the predicted magnitude of trunk-ground reflection at high angles of incidence is somewhat speculative (hence the increase in HH polarized σ^o at incidence angles higher than 45° shown in Figure 4.2 is hypothetical).

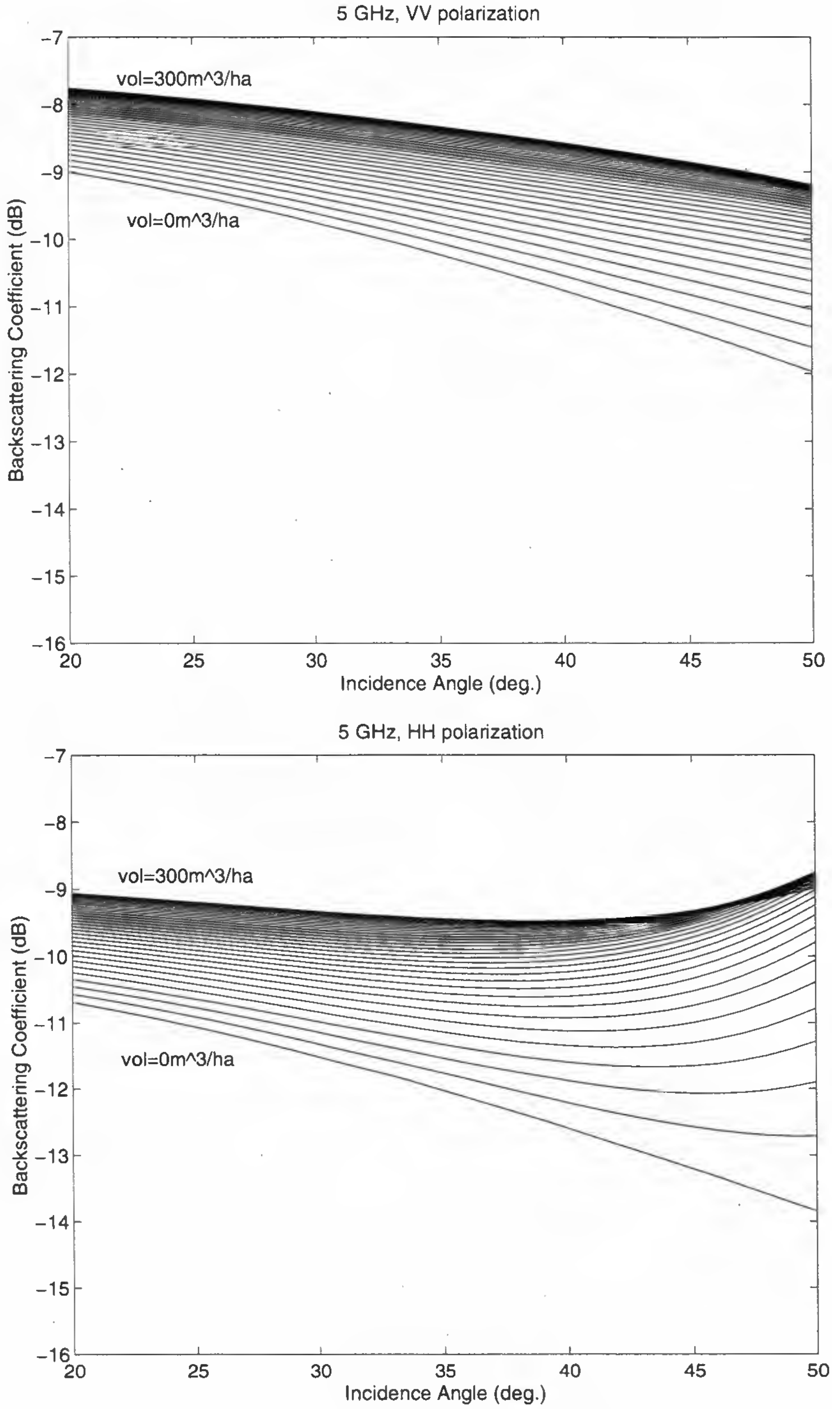

Figure 4.2. Modeled C-band backscattering coefficient as a function of the angle of incidence for various forest stem volumes at $10m^3/ha$ interval. The response for HH polarization is shown for comparison. The volumetric soil moisture is 10%.

4.4 Response to Soil and Vegetation Moisture

During summer, the changes of σ^o in forested areas are caused by the changes in soil and vegetation moisture. The magnitudes of these changes are presented in Figures 4.3 and 4.4 for C-band, VV polarization, as the forest stem volume is 67 m^3/ha.

Figure 4.3 shows that the variations in soil moisture cause the higher effect on σ^o, the lower is the angle of incidence. Evidently, the effect of variations in vegetation canopy moisture is opposite to that, as depicted in Figure 4.4. For typical boreal forests, the influence of soil moisture variations is significantly higher than that of vegetation moisture variations. The volumetric soil moisture of mineral soil varies typically from about 6 to 25%. In cases of clay or peat soil, much higher moisture values are possible. The ±11% relative change range used in Figure 4.4 represents a typical maximum moisture change interval of woody tissue according to literature sources (*Kramer and Kozlowski 1979*).

Figures 4.3 and 4.4 also show how the angular response of Wind Scatterometer measurements changes as the level of soil moisture or vegetation moisture changes. This occurs due to the partially transparent forest canopy layer. The transmissivity of forest canopy as a function of the angle of incidence is presented below in Figure 4.9 corresponding to parameter values used in Figures 4.3 and 4.4 (for a forest with a stem volume of 67 m^3/ha).

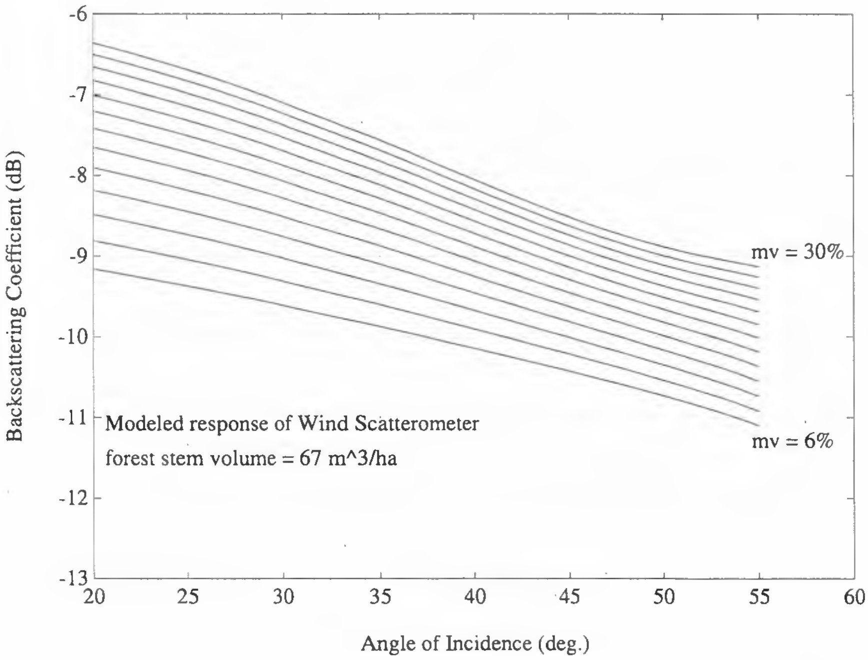

Figure 4.3. Modeled behavior of forest backscatter (boreal forests) as a function of the angle of incidence with varying volumetric soil moisture.

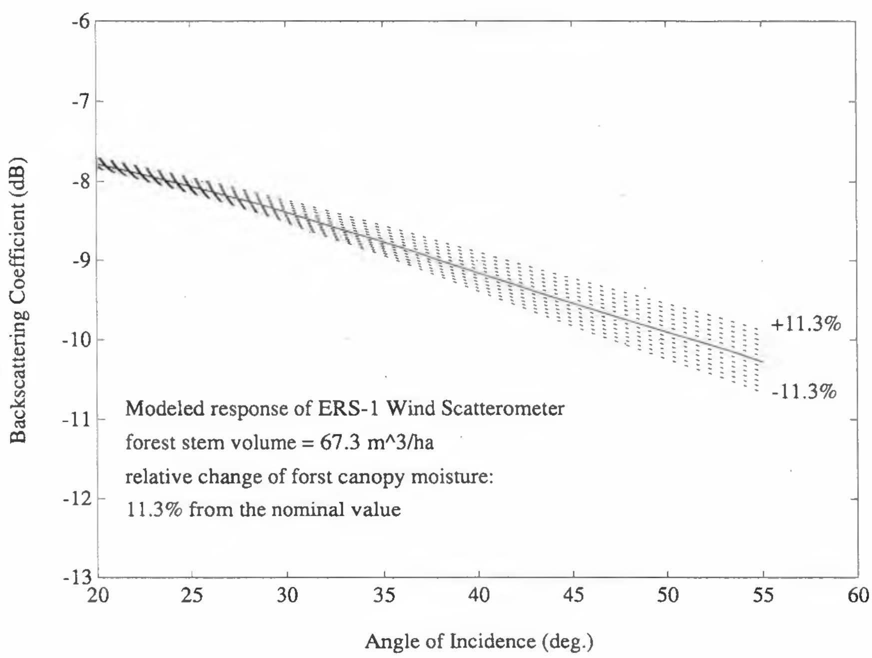

Figure 4.4. Modeled behavior of forest backscatter (boreal forests) as a function of the angle of incidence. Different volumetric forest canopy moistures are at 1.9% relative change interval from the nominal value corresponding to dry summer conditions (assumed to be 53%).

4.5 Snow Cover Effects

Since the current theoretical or empirical modeling approaches do not describe appropriately the behavior of backscatter under different snow cover conditions, the presentation of seasonal snow cover effects has to be based on the analysis of experimental data. The experimental results discussed here are obtained from airborne campaigns conducted using the HUTSCAT instrument, and from ERS-1 SAR data analysis. The results are obtained for C-band, VV polarization at the incidence angle of 23°. These experiments are discussed in detail in (*Jääskeläinen 1993, Jääskeläinen et al. 1993, Pulliainen 1994*).

HUTSCAT-based investigations

Examples of the multi-temporal HUTSCAT results from the Sodankylä test area, Northern Finland, are depicted in Figures 4.5 and 4.6. Figure 4.5 shows the temporal change of the backscattering coefficient for various stem volumes at 5 GHz, VV polarization. The temporal variation of bare ground backscattering (deforested areas) is presented in Figure 4.6.

The freezing of the ground decreases the bare ground results about 3 dB, which corresponds well to the ERS-1 SAR observations of Alaskan and Finnish boreal forests. Figure 4.5 (fall and spring characteristics) indicates that the behavior of canopy backscatter is analogous to that of soil, as the temperature decreases below freezing point (a 3 dB drop has been observed for canopy backscattering contribution only (*Jääskeläinen 1993*), which corresponds to the drop depicted for pine-III class in Figure 4.5). In the mid-winter case response to stem volume is low, which is primarily caused by the relatively high level of backscatter from the dry snow layer.

The highest correlation to stem volume has been observed in the case of a wet snow layer. In the case of wet snow the level of backscatter from the forest floor can be significantly lower than the backscattering level from the canopy. This phenomenon probably occurs (1) due to the high signal attenuation caused by the wet snow and (2) due to the low level of backscatter on the air-snow boundary (evidently the level of specular reflection can be significant but in the case of a smooth wet snow layer it does not occur to the direction of backscatter).

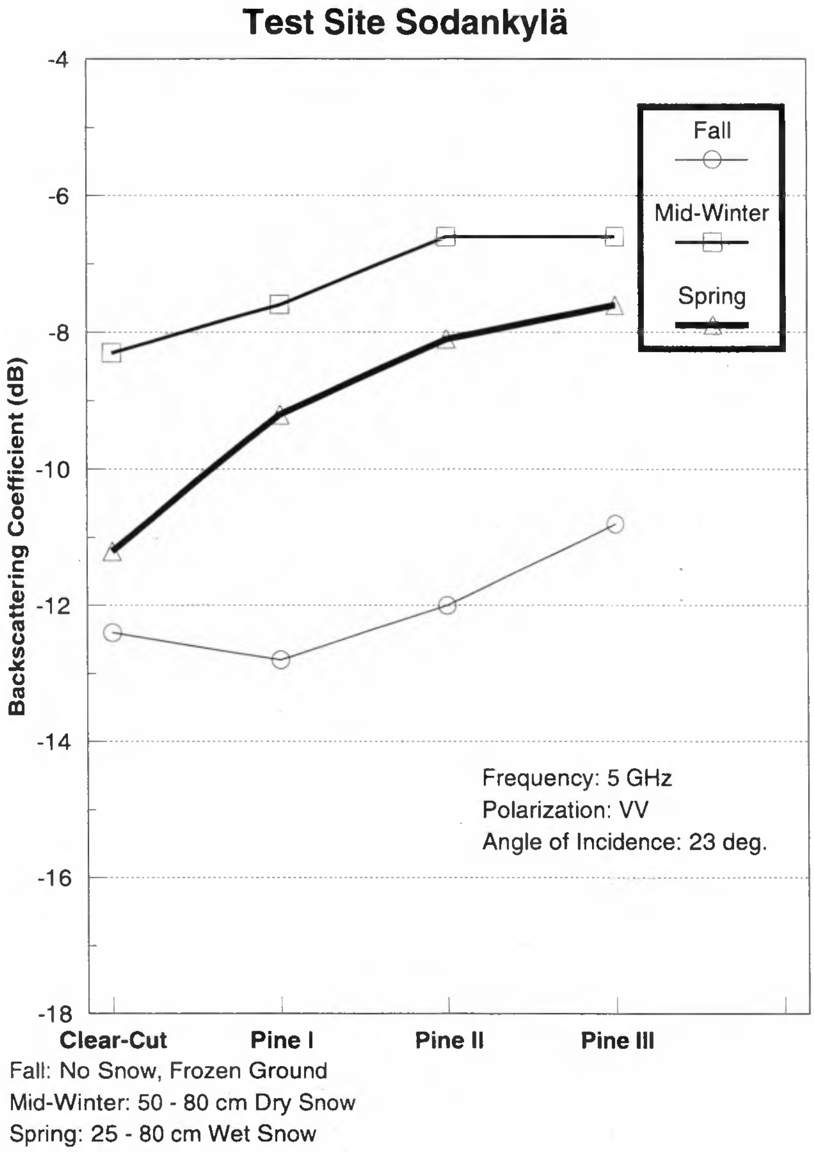

Figure 4.5. Backscattering coefficient for 5 GHz, VV polarization obtained for Sodankylä pine forest test lines. Different stem volume classes are: 0-50 m^3/ha (I), 50-100 m^3/ha (II), and 100-150 m^3/ha (III) (Jääskeläinen et al. 1993).

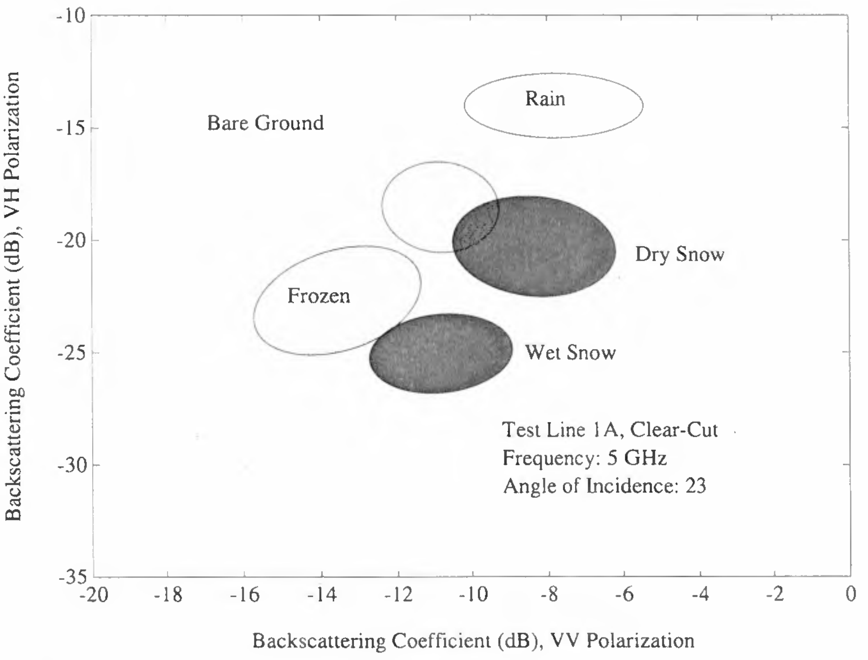

Figure 4.6. Temporal variations of VV and VH polarization results for C-band bare ground (clear-cut areas) and snow-covered bare ground (Jääskeläinen 1993). The ellipses presented contain 95% of the data points. The gray ellipses depict the snow-free conditions.

ERS-1 SAR-based investigations

In addition to scatterometer measurements, the C-band radar response to snow cover conditions has been studied using ERS-1 SAR data from the test areas of Sodankylä (Northern Finland) and Porvoo (Southern Finland). The high spatial resolution of ERS-1 SAR enables the investigation of backscattering properties as a function of such parameters as forest stem volume (biomass). Figure 4.7 depicts the ERS-1 SAR response (imaging hour, 11 am) of the Sodankylä test area for five cases. The results are shown as a function of the stem volume. Curves (a) - (c) are the summer time responses, and curves (d) and (e) present the winter time behavior.

For curve (a) the weather was non-rainy, but heavy rain (30 mm) and moderate rain (9.9 mm) occurred three and two days prior to the imaging. Hence the soil moisture can be assumed to be high, but in contrast the vegetation moisture can be assumed to have stayed at normal values. For curve (b) moderate rainfall (17 mm) occurred during image acquisition day (and light rain prior to the image acquisition day). For curve (c) heavy rain (30 mm) occurred during the image acquisition day (and light rain prior to the image acquisition day). For curves (d) and (e) the ground was covered by thick snow layer (curve (d): dry snow, snow water equivalent 140 mm, temperature -16°C, and curve (e): wet snow, snow water equivalent 140 mm, temperature +4.5°C). The winter time results for wet snow cover show the highest correlation to stem volume similarly to the HUTSCAT-results discussed above. The freezing of the ground decreases the level of backscatter about 2-3 dB compared to curve (a) of Figure 4.7. This decrease is slightly smaller than those observed in the HUTSCAT measurements (discussed above).

Figure 4.8 shows the seasonal response of ERS-1 data in the Porvoo test area (for three separate sub-areas). the effects of soil freezing and snow cover are clearly visible. The data shown covers the period from June 1993 to March 1994. Figure 4.8 also shows the temperature and cumulative precipitation information for the Porvoo test area for comparison.

The results of Figure 4.8 show the behavior of average σ^o for each area. Measurement dates from 30 to 159 (preceding point B) present the σ^o values for summer and autumn, i.e. observations in snow-free and unfrozen soil conditions. At point A (24 July 1993), a substantial precipitation occurred during the image acquisition and hence, the drop of σ^o is evident due to the rain attenuation. At point B (25 November 1994), the ground was frozen, which causes a 2 to 3.5 dB decrease in the backscattering coefficient compared to unfrozen soil cases (dates 30-159 in Figure 4.8). The temporal variations in the results for summer and autumn are caused by the changes in canopy and soil moisture. The ERS-1 SAR images used were obtained either in the morning (acquisition time about 9.30) or in the evening (acquisition time about 20.10), The correlation between the imaging hour and σ^o is negligible.

Dates 178 - 220 (preceding point C) in Figure 4.8 show the results for frozen ground that is covered by a thin dry snow layer which has only a marginal effect on the backscatter level (snow water equivalent is from 5 to 30 mm). At point C (15 January 1994), the air temperature was again over 0°C, and concurrently, rain accumulated water in the snow cover. This caused a relatively high level of σ^o. After point C, the temperature decreases and dry snow depth gradually increases. First, refreezing of wet snow decreased the level of backscatter. After that, accumulation of dry snow increased the level of σ^o (snow water equivalent increases from 40 to 60 mm). This is due to the increased volume backscatter in new dry snow. However, after date 247 (2 February 1994) considerable snow falls did not occur before March and thus, the aging of dry snow decreases the level of backscatter. The results clearly show that the variation of ERS-1 SAR-derived σ^o in winter conditions (snow-covered ground) is much smaller than in summer conditions if no thawing/refreezing events occur.

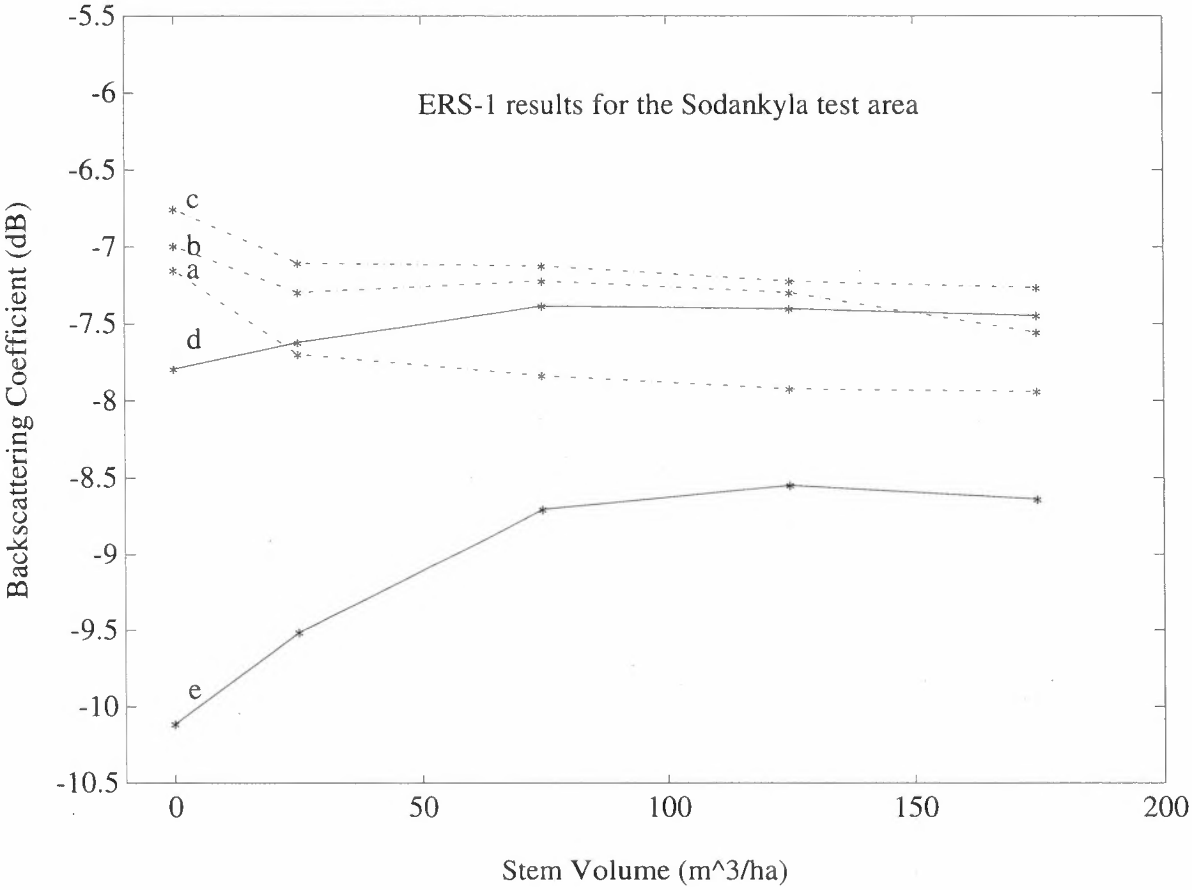

Figure 4.7. ERS-1 SAR results for the Sodankylä test area in summer (temperature well above 0oC) and winter conditions. Curves (a) - (c) are the summer time responses. Curve (a) was obtained on 24 June 1992; curve (b) 18 September 1992; and curve (c) 29 July 1992. Curves (d) (20 January 1993) and (e) (1 May 1992) show the winter time responses for dry and wet snow-cover, respectively. The results are presented for clear-cut areas (V=0m3/ha) and four stem volume classes: 0 - 50 m3/ha, 50 - 100 m3/ha, 100 - 150 m3/ha, and 150 - 200 m3/ha (Pulliainen 1994).

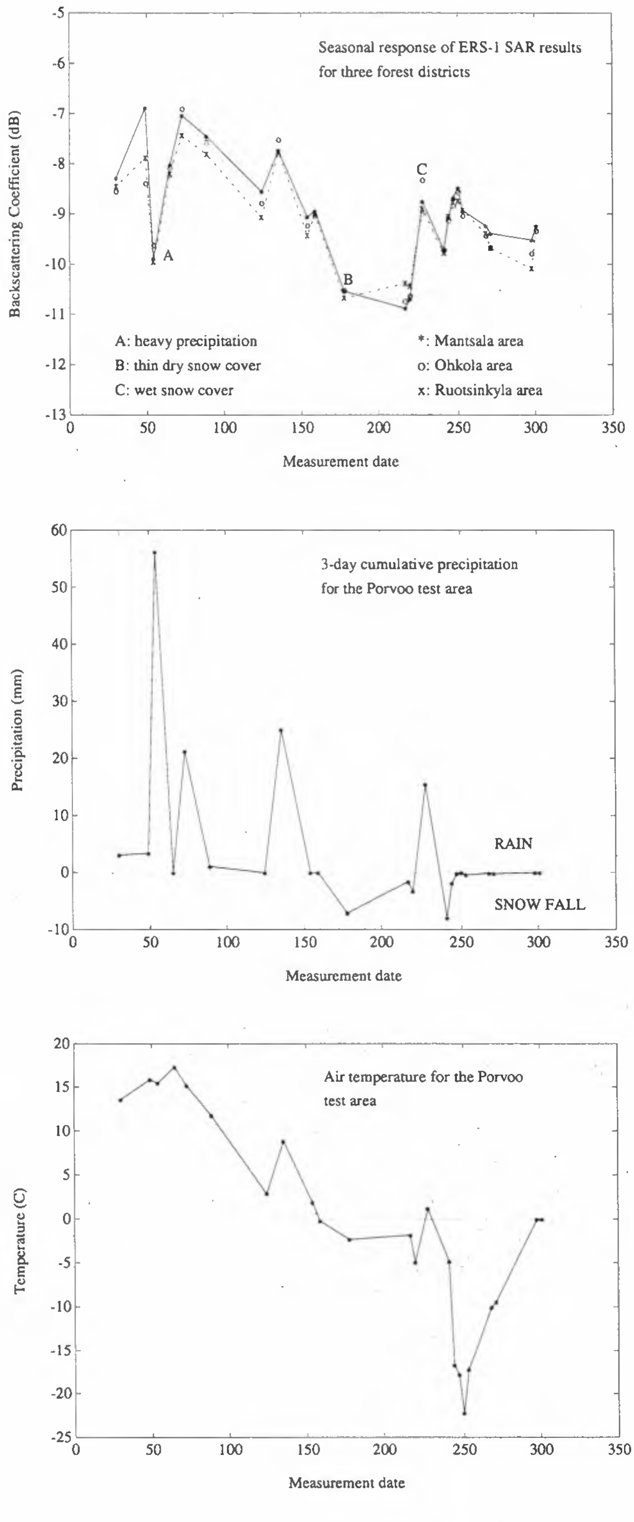

Figure 4.8. Seasonal behavior of ERS-1 SAR observations of the Porvoo test area for three forest districts. The average σ^o values for each forest district are shown. The responses for summer and autumn conditions are given by measurement dates 30-159 and those for winter conditions by dates 178-301. Date 1 is the 1st of June 1993.

Summary

The overall conclusions from the snow cover backscattering experiments can be summarized as:

- the effect of a thin dry snow layer on C-band σ^o is negligible. This is due to the fact that the relative dielectric constant of dry snow is near one (*Hallikainen et al. 1986*). In this case, the backscatter is effected by the underlaying frozen soil (which causes a low level of σ^o). This is also clearly detectable in Wind Scatterometer results discussed in Chapter 6. In forested areas, the correlation of σ^o with the forest stem volume is (at least slightly) positive.

- the increase of (new) dry snow layer slightly increases σ^o due to the increased volume backscatter in new dry snow. The aging of snow layer can decrease the level of backscatter. The melting and refreezing of snow cause major changes in backscatter. In forested areas, the correlation of σ^o with the forest stem volume can be positive or negative (or near zero).

- in the case of wet snow the level of backscatter can have the lowest values. But σ^o values higher than those observed in the case of dry snow are also possible (see Figure 4.8). In forested areas, the correlation of σ^o with the forest stem volume is positive (the highest positive correlations are observed in this case, see Figures 4.5 and 4.7).

4.6 Applicability of the Semi-Empirical Backscattering Model

The analyses presented in (*Pulliainen et al. 1994, Pulliainen 1994*) show that the model applies well for conifer-dominated boreal forests in conditions of Finland for the 23° angle of incidence. The following discussion evaluates the model applicability for different geographical zones and for a wider angular range.

Angular validity

The assumption made in Equation (4.3) is that the volume backscattering coefficient C and extinction coefficient a_1 do not vary as a function of the angle of incidence. The feasibility of this assumption can be evaluated against (1) theoretical forest backscattering model predictions and (2) reference measurements.

The comparisons of semi-empirical model-based canopy backscattering contribution σ^o_V with theoretical model predictions, which are either (a) obtained by MIMICS software test runs or (b) given in literature, refer to e.g. (*Wang et al. 1993*), show quite similar angular responses. This indicates that the angular effects are treated satisfactorily in Equation (4.3). On the other hand, the validity of the semi-empirical model can be tested against experimental data. This is shown in Figure 4.9. In this case, the model-based forest canopy transmissivity is compared with independent HUTSCAT-based predictions obtained for two angles of incidence at the Ruotsinkylä test site (*Hyyppä 1994*).

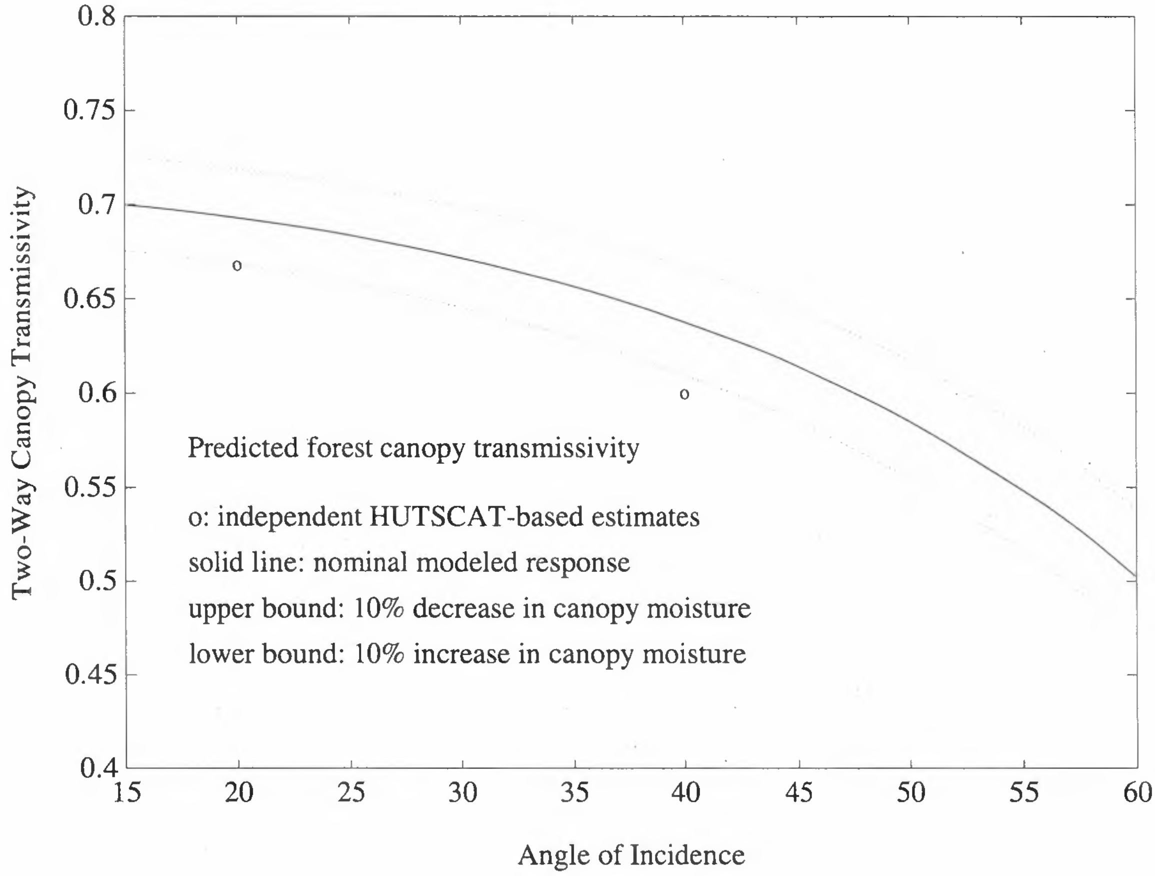

Figure 4.9. Comparison of the semi-empirical model-based forest canopy transmissivity with independent HUTSCAT-based estimates in the case of Finnish boreal forests. The forest stem volume is 67 m^3/ha. The nominal response corresponds to dry summer conditions.

Geographical validity

The semi-empirical model parameters, a_1 and C in Equations (4.3) - (4.5), have been determined in the case of conifer-dominated Finnish boreal forests where the dominant species are Scots pine and Norway spruce. However, the other conifer species in boreal forests of Eurasia and North America are quite similar to these species. Hence, the presented parameter values should be approximately applicable for other conifer-dominated boreal forest types (boreal forests compose the largest forested areas on Earth).

For other vegetation zones, such as tropical forests, the model parameters are not applicable. However, the model formulation given in Equations (4.1) - (4.5) does apply (at least approximately). Typically, the above ground woody biomass in southern forests (tropical and mid-latitude evergreen deciduous forests) is much higher than in boreal forests. For example, the average stem volume in Southern Finland has only a value of about 100 m^3/ha (corresponding the total dry biomass of 60 tons/ha), whereas the stem volume in southern forests may be over ten times higher. Therefore, the extinction of forest canopy is often high in southern forests, and Equation (4.3) diminishes into

$$\begin{aligned} \sigma_V^o &\approx \frac{\sigma_V}{2 \cdot \kappa} \cdot \cos\theta \\ &= \gamma_c \cdot \cos\theta \end{aligned} \tag{4.6}$$

where

σ_V = canopy volume backscattering coefficient
κ = canopy extinction coefficient
γ_c = canopy bistatic scattering coefficient.

According to Equations (4.3) - (4.5) γ_c is linearly related to changes in canopy volumetric moisture. In the case of tropical rain forests, the volumetric canopy moisture does not change significantly with time and hence, γ_c is a (nearly) constant coefficient.

5 A Semi-Empirical Emission Model for SSM/I Measurements

5.1 Formulation of a Combined Model for Snow Cover, Soil, Forest Canopy and Atmospheric Effects

Snow model (HUT model)

The HUT snow model is based on the radiative transfer equation consisting of several components: 1) emission contribution from the ground, 2) emission contribution from the snow layer and 3) emission contribution from the atmosphere. The total brightness temperature observed in space is

$$
\begin{aligned}
T_B = T_{Bg,total}t &+ T_{B,atmos}\uparrow \\
&+ T_{B,atmos}\downarrow(1 - T_{Bg,total}/T_s)t \\
&+ 2.7t^2(1 - T_{Bg,total})/T_s)
\end{aligned}
\tag{5.1}
$$

where

$T_{Bg,total}$ = total emission contribution from the ground surface layer,

T_s = surface temperature (approximated by snow temperature),

t = atmospheric transmissivity,

$T_{B,atmos}\uparrow$ = up-welling atmospheric emission,

$T_{B,atmos}\downarrow$ = down-welling atmospheric emission.

The formulas for different terms of Equation (5.1) are given in the following paragraphs.

Total emission contribution from ground surface layer $T_{Bg,total}$

The total observed (modeled) brightness temperature contribution of ground surface layer without a forest canopy attenuation is

$$T_{Bg,total} = T_{Bg} + T_{Bs}. \tag{5.2}$$

where

T_{Bg} = emission contribution from the ground (soil) surface,

T_{Bs} = emission contribution from the snow layer.

The formulas for T_{Bg} and T_{Bs} are given in the following. When snow emission model is applied for forested areas the effect of forest canopy must be considered by modifying the value of $T_{Bg,total}$. This is also discussed later in this Section.

<u>Emission contribution from the ground</u> T_{Bg}

Measured values of emissivity from a frozen ground at several frequencies are used as a database to provide the emission contribution from the ground. Where exact values for SSM/I frequencies have not been found, interpolated values have been used. This approach was considered feasible, since the snow layer is the main contributor for the resulting total emissivity.

Table 5.1. Measured emissivity values of a frozen ground for several frequencies and polarizations (*Mätzler 1994*).

Channel	4.9H	10.4H	21H	35H	94H	4.9V	10.4V	21V	35V	94V
Frozen soil	0.891	0.952	0.950	0.950	0.938	0.939	0.957	0.957	0.951	0.950

When the emissivity values are known, the power reflection coefficient for the snow-ground boundary can be obtained from

$$\Gamma_2 = 1 - e_g, \tag{5.3}$$

where

e_g = emissivity of the ground.

The reflectivity of the snow-air boundary is obtained from (*Choudhury 1979*)

$$\Gamma_1 = 1 - \mathrm{T}_1 S_1, \tag{5.4}$$

where

T_1 = Fresnel power transmission coefficient of the snow-air boundary,

S_1 = surface roughness factor.

The surface roughness factor is obtained from

$$S_1 = e^{-(2k_0 s \cos\theta)^2}, \tag{5.5}$$

where

θ = angle of incidence,

k_0 = wave number,

s = effective rms height of the snow surface fluctuation (in meters).

Thus, the emission contribution from the ground layer just below the snow-air boundary can be formulated as

$$T_{Bg-} = e_g T_g \left[\frac{1}{L_e} + q\left(\frac{1}{L_a} - \frac{1}{L_e} \right) \right], \tag{5.6}$$

where

T_g = temperature of the ground surface (K),

L_a = attenuation due to absorption,

L_e = total attenuation (extinction),

q = fraction of brightness temperature due to multiple scattering (= 0.70 empirical factor used in this study).

With the multiple reflections between the boundaries included, and some simplifications made (*Pulliainen et al. 1990*) the equation for the ground emitted radiation can formulated as

$$T_{Bg} = T_{Bg-}(1-\Gamma_1)\left(\frac{1}{1-\frac{\Gamma_1\Gamma_2}{L_e^2}} \right) + qT_{Bg-}(1-\Gamma_1)\Gamma_1\Gamma_2\left(\frac{1}{L_a^2} - \frac{1}{L_e^2} \right)\left(\frac{1}{1-q\Gamma_1\Gamma_2\left(\frac{1}{L_a^2}-\frac{1}{L_e^2} \right)} \right), \tag{5.7}$$

<u>Emission contribution from the snow layer</u> T_{Bs}

Emission from the snow layer is divided into two components, up-welling and down-welling radiation. Most of the radiation observed above (e.g. space) is in fact originated from the snow layer, therefore attention should be drawn to the formulation of the snow module of the total emissivity. A few examples of the penetration depth for snow for various volumetric water contents are shown in Figure 5.1. However, the present snow model is not designed for wet snow, instead it assumes that the volumetric water content is equal to zero and applies the formulas given by *(Hallikainen et al. 1987, Mätzler 1987, Hallikainen et al. 1986)* for snow permittivity and extinction considerations. The curves for wet snow presented in Figure 5.1 have been obtained from empirical equations by *Hallikainen et al. (1986)*. The calculated results show a reasonably good fit to reported measurements in other papers (*Eppler et al. 1992*). According to these results and Figure 5.1, it is evident that even very small volumetric water contents seem to effectively mask the underlying soil layer, and the effect is even more severe for the SSM/I frequencies (19 to 85 GHz). Usually mid-winter snow may be regarded as dry (new or refrozen snow).

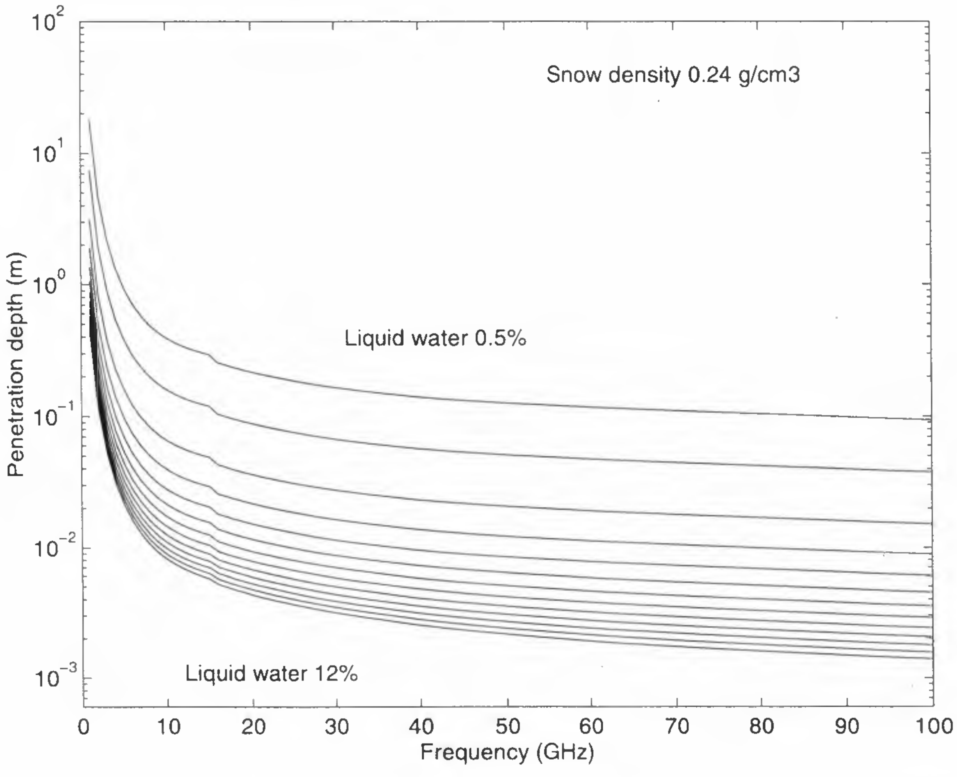

Figure 5.1. Calculated penetration depths (m) in snow when the volumetric water content varies from 0.5% to 12%.

A full description of the original snow module can be found in (*Pulliainen et al. 1990*) and only modified equations are presented in this report.

As in the case of emission from the ground layer, the up-ward emitted radiation just below the snow-air boundary may be expressed as

$$T_{Bs\uparrow -} \quad = \quad T_s \frac{\kappa_{am}}{\kappa_{em}}\left(1 - \frac{1}{L_e}\right) \quad + \quad qT_s\left(1 - \frac{1}{L_a} - \frac{\kappa_{am}}{\kappa_{em}}\left(1 - \frac{1}{L_e}\right)\right), \tag{5.8}$$

where

T_s = snow temperature (K),

κ_{am} = absorption coefficient,

κ_{em} = extinction coefficient.

κ_{em} is determined by equations given in *(Hallikainen et al. 1987)*. κ_{am} is calculated from the snow dielectric constant using the formulas given by *Mätzler (1987)* and *Hallikainen et al. (1986)* for the permittivity of dry snow. If all the multiple reflections are accounted for, the resulting equation after a few simplifications (binomial series) can be formulated as

$$T_{Bs}\uparrow = T_{Bs}\uparrow_{-}(1-\Gamma_1)\left(\frac{1}{1-\frac{\Gamma_1\Gamma_2}{L_e^2}}\right) + qT_{Bs}\uparrow_{-}(1-\Gamma_1)\Gamma_1\Gamma_2\left(\frac{\Gamma_1\Gamma_2\left(\frac{1}{L_a^2}-\frac{1}{L_e^2}\right)}{1-q\Gamma_1\Gamma_2\left(\frac{1}{L_a^2}-\frac{1}{L_e^2}\right)}\right). \tag{5.9}$$

A similar expression can be formulated for the down-ward emitted and back reflected radiation:

$$T_{Bs}\downarrow = T_{Bs}\downarrow_{-}\frac{(1-\Gamma_1)\Gamma_2}{L_e}\left(\frac{1}{1-\frac{\Gamma_1\Gamma_2}{L_e^2}}\right) + qT_{Bs}\downarrow_{-}(1-\Gamma_1)\Gamma_2\left(\frac{1}{L_a}-\frac{1}{L_e}\right)\left(\frac{1}{1-q\Gamma_1\Gamma_2\left(\frac{1}{L_a^2}-\frac{1}{L_e^2}\right)}\right). \tag{5.10}$$

With these equations, the total emission contribution from the snow layer is obtained from:

$$T_{Bs} \quad = \quad T_{Bs}\uparrow \quad + \quad T_{Bs}\downarrow. \tag{5.11}$$

Effect of a forest canopy

The transmissivity of a forest canopy may be modeled as a function of frequency and forest stem volume. This approach is made possible by extensive radiometric measurements of the Finnish boreal forests conducted at the Sodankylä test site in Northern Finland (*Kurvonen 1994*). Using the results obtained by these measurements, an empirical model has been formulated to account for the variability of the forest transmissivity. The transmissivity may be expressed as:

$$t_f \quad = \quad c_1 \cdot e^{\lambda_1 \cdot Vol} + c_2 \cdot e^{\lambda_2 \cdot Vol}, \tag{5.12}$$

where

$$c_1 = 0.8867 \cdot e^{-0.00291 \cdot f} + 0.1133 \cdot e^{-0.3905 \cdot f}, \tag{5.13}$$

$$c_2 = 0.1523 \cdot e^{0.007949 \cdot f} - 0.1523 \cdot e^{-1.262 \cdot f}, \tag{5.14}$$

$$\lambda_1 = 0.0006166 \cdot e^{0.0107 \cdot f} - 0.001617 \cdot e^{-1.319 \cdot f}, \tag{5.15}$$

$$\lambda_2 = 0.08156 \cdot e^{0.0005923 \cdot f} - 0.03156 \cdot e^{-0.9956 \cdot f}, \tag{5.16}$$

f = Frequency (GHz),

Vol = Stem volume (m^3/ha).

A few examples of the transmissivity curves are shown in Figure 5.2 ranging from a frequency of 10 GHz to 100 GHz.

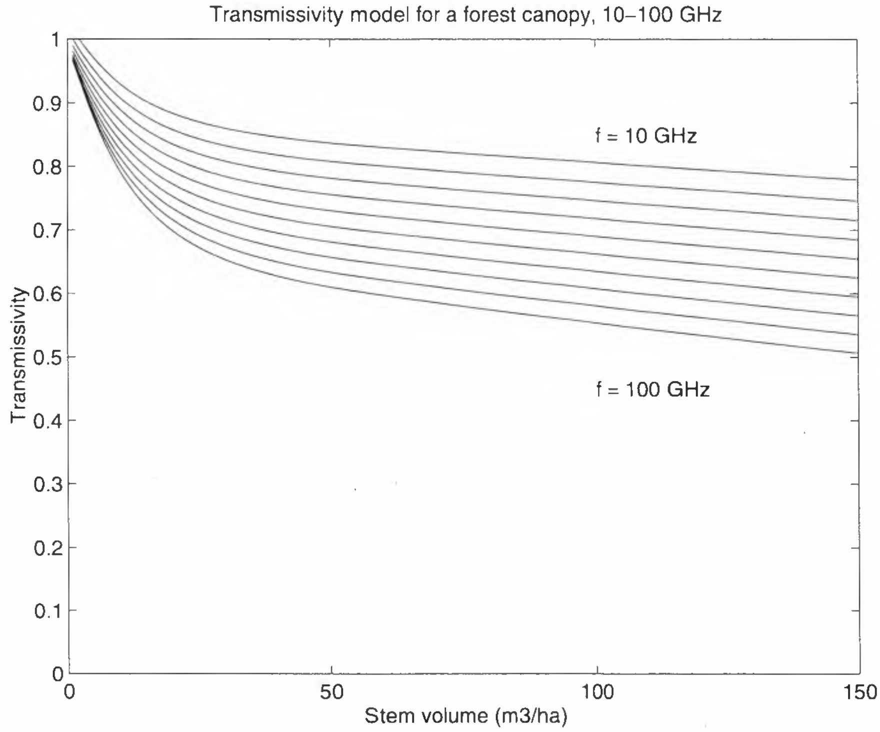

Figure 5.2. Transmissivity of a forest canopy modeled as a homogeneous attenuator based on empirical data.

With the known transmissivity (and attenuation) values of the forest canopy, the brightness temperature of a forested area is defined as

$$T_{B,land} = C_{forest}\left(T_{Bg,total}t_f + T_{forest}(1-t_f)\left(1+\left(1-\frac{T_{Bg,total}}{T_{forest}}\right)t_f\right)\right) \qquad (5.17)$$

$$+ \quad (1-C_{forest})T_{Bg,total},$$

where

$T_{Bg,total}$ = total brightness temperature of surface (Equation (5.2)),

T_{forest} = physical temperature of the forest (K),

C_{forest} = fraction of forest cover within a pixel,

t_f = forest canopy transmissivity.

In the case of forested areas, $T_{B,land}$ given by Equation (5.17) replaces $T_{Bg,total}$-term in Equation (5.1).

<u>*Atmospheric emission contributions and transmissivity*</u> $T_{B,atmos}\uparrow$, $T_{B,atmos}\downarrow$ and t

The atmosphere is modeled by using a statistical approach, where the transmissivity of the atmosphere at the ith SSM/I channel is obtained from a statistical principal component model:

$$t_i(\gamma) = \left[(t_P^0)_i + (t_P^1)_i\gamma\right]^{1.0681}, \tag{5.18}$$

where γ is a scalar variable. t_P^0 and t_P^1 are the zero-order and the first order principal components of atmospheric transmissivity for different SSM/I channels:

$$t_P^0 = (0.9211 \quad 0.9211 \quad 0.8326 \quad 0.8624 \quad 0.8624 \quad 0.6656 \quad 0.6656)^T \tag{5.19}$$

$$t_P^1 = (0.2069 \quad 0.2069 \quad 0.4642 \quad 0.2746 \quad 0.2746 \quad 0.8163 \quad 0.8163)^T \tag{5.20}$$

The exponent correction factor in Equation (5.18) arises from the fact that the principal component model (*Pulliainen et al. 1993*) is determined for the angle of incidence of 50°, whereas the angle of incidence in SSM/I measurements is 53.1°.

With the transmissivity values known, the up- and downwelling radiation from the atmosphere can be obtained by using the equations given in (*Aschbacher 1989*). These provide the approximate atmospheric profile factors $\alpha_\uparrow$ and $\alpha_\downarrow$ in order to determine the effective up- and down-welling brightness temperatures in Equation (5.1).

up-welling radiation: $$T_{B,atmos}\uparrow = \alpha_\uparrow T_s(1-t) \tag{5.21}$$

downwelling radiation: $$T_{B,atmos}\downarrow = \alpha_\downarrow T_s(1-t) \tag{5.22}$$

where

$$\alpha_\uparrow = -0.073t^2 + 0.101t + 0.918, \tag{5.23}$$

$$\alpha_\downarrow = -0.035t^2 + 0.014t + 0.967, \tag{5.24}$$

T_s = surface temperature (K),

t = atmospheric transmissivity.

5.2 Formulation of a Combined Model for Sea Ice

Modeling of sea ice has been found to be an extremely complicated task, and a feasible physical model does not currently exist (refer to Chapter 3). The inner structure of the ice layer and the continuous surface roughness of the ice-snow (or ice-air) boundary are the main causes of difficulties when modeling is concerned.

The approach chosen for the model developed in this study was to derive a semi-empirical model similar to the HUT snow model presented in section 5.1. The emission from an area equal to an SSM/I pixel (25 km x 25 km test sites chosen for this study) can be divided to several sources: 1) contribution from the sea water, 2) contribution from the ice layer, 3) contribution from the snow layer and 4) contribution from the atmosphere.

In order to take into account the non-uniformly distributed snow layer on the ice surface, a factor describing the fraction of ice covered with snow is used by the model.

Emission contribution from the sea water

The emission from the sea surface can be divided into the contribution from a specular surface and the contribution of a wind disturbed surface

$$T_{B,sea} = T_{B,specular} + \Delta T_{B,wind}, \tag{5.25}$$

where

$T_{B,specular}$ = brightness temperature of a specular sea surface,

$\Delta T_{B,wind}$ = increase of brightness temperature due to wind roughened sea surface.

The emissivity (and brightness temperature) for a specular sea surface may be calculated from physical (or semi-empirical) models as the dielectric properties for saline sea water are well understood. Thus, the emissivity and brightness temperature of a calm sea surface are defined by

$$T_{B,specular} = T_{sea}e_p(f,\theta) = T_{sea}(1-\Gamma_p(f,\theta)), \tag{5.26}$$

where

T_{sea} = physical temperature of the sea surface (K).

The power (Fresnel) reflection coefficients $\Gamma_p(f,\theta)$ in Equation (5.26) for vertical and horizontal polarizations are defined by

for horizontal polarization

$$\Gamma_h(f,\theta) = \left|\frac{\cos\theta - \sqrt{\varepsilon_w - \sin^2\theta}}{\cos\theta + \sqrt{\varepsilon_w - \sin^2\theta}}\right|^2, \tag{5.27}$$

for vertical polarization

$$\Gamma_h(f,\theta) = \left|\frac{\varepsilon_w\cos\theta - \sqrt{\varepsilon_w - \sin^2\theta}}{\varepsilon_w\cos\theta + \sqrt{\varepsilon_w - \sin^2\theta}}\right|^2, \tag{5.28}$$

where

ε_w = relative complex dielectric constant of water.

The dielectric model for ε_w is a function of frequency, temperature and salinity. Furthermore, salinity is a function of several independent parameters such as relaxation time of water molecules and ionic conductivity of water. The formal presentation of these equations for the dielectric model used in this study are found in (*Stogryn 1971*).

The increase of brightness temperature due to wind has been investigated by several authors, but there are no suitable physical models currently available to describe this behavior. However, by using an empirical model presented by (*Schluessel and Luthardt 1991*) and extending this to the whole frequency range, a feasible model for the wind roughened sea can be derived. The wind factor in Equation (5.25) can be expressed as:

vertical polarization: $$\Delta T_{B,wind} = \sqrt{W(a + b e^{c\theta})f}, \tag{5.29}$$

horizonal polarization: $$\Delta T_{B,wind} = \sqrt{W(d + e\theta^2)f}, \tag{5.30}$$

where

W = wind speed (m/s),

f = frequency in GHz,

a = 0.117 K s m^{-1},

b = -0.00209 K s m^{-1},

c = 0.0732 deg^{-1},

d = 0.115 K s m^{-1},

e = 0.000038 deg^{-2}.

Emission contribution from the ice layer

As shown in Figure 5.1, the penetration depth of radiation at SSM/I frequencies can easily decrease to a value of only few centimetres. This is due to liquid water included in the mixture of ice and air (dry snow), thus forming various states of wet snow. Therefore the masking effect of the snow layer seriously reduces the effect of the sea ice component to the total apparent brightness temperature. For some purposes this might be considered useful, as the modeling of sea ice has proven to be an immensely difficult task due to the structural variations of the ice layer. For example, surface characterisation of ice is difficult due to the continuous spectrum of the surface roughness (*Manninen 1994*). Due to these difficulties in physical modeling of sea ice, the approach using empirical emissivity values for various sea ice types was chosen.

Navigation in the Baltic Sea during winter time is seriously hampered by growing and deforming ice, especially in the northern parts of the sea (Gulf of Bothnia). Ice breakers are used in order to keep the fairways open for commercial navigation. Sea ice types in the Baltic Sea can be divided into four subgroups according to their potential risk for winter navigation: 1) open water, 2) new ice, 3) level ice and 4) deformed or compact ice. All of these classes may be further divided into subclasses, but that is less important when winter navigation is concerned. Of these classes, new ice and level ice are usually breakable for ice breakers (and for all IA Super ice certified commercial ships) but in extreme conditions the level ice may reach a nearly 100 cm thickness, which would require the assistance of a high-powered ice breaker. As a general rule, thinner forms of level ice (10-30 cm) form no threat to ships usually navigating in winter conditions. However, the class of deformed and compact ice (4) is usually avoided even by ice breakers if possible. This ice is formed from wind-crushed level ice, and may form ridges of several meters in thickness.

The emissivity values used for the sea ice model were taken from (*Eppler et al. 1992*) which is a wide collection of measurements by several authors, and include a great variety of ice classes. However, the measurements have been made for Arctic ice, thus special concern had to be taken when selecting the proper ice types to be used. The possible role of snow (as included in the reported emissivity values) was a first limiting factor. The difference of the structure of level and compact ice as compared to various Arctic ice classes formed another criteria for the selection process.

Snow: As a snow module is included separately in the developed sea ice model, no snow contribution should be included in the emissivities chosen for new and level ice. These ice types in the Baltic Sea usually have a uniform and relatively homogeneous snow layer throughout the winter, and may reach thicknesses of 50-70 cm. Measured emissivity values of First Year Ice were chosen to represent the new and level ice classes of the Baltic Sea, as they showed to be very close to that of the level ice measured in the Baltic Sea, with a modeled snow layer covering the surface.

Structure: Deformed ice such as compact ice in the Baltic Sea, or multi-year ice in the Arctic, differ greatly from level and new ice classes due to their surface properties, including also a large-scale surface roughness component. Snow in these areas is seldom uniformly distributed, and mainly concentrated between ice blocks. As multi-year ice in the Arctic is characterised by annual and even daily melt-freeze cycles, a dry form of multi-year ice was chosen to represent a typical compact ice class in the Baltic Sea.

The values chosen to represent the various ice classes in the Baltic Sea are shown in Table 5.2. Results obtained from airborne radiometric measurements of Baltic Sea ice (*Kurvonen 1994b*) show that the emissivity values chosen fit relatively well to observed data. No exact comparison can be made, though, since the snow cover contributions to the measured brightness temperatures have not been extracted. Direct use of these airborne measurements was not possible, since the reported snow cover information is inadequate for a modeling purpose.

Table 5.2. Measured emissivity values chosen to represent the Baltic Sea ice types of importance (for winter navigation) (*Eppler et al. 1992*).

Channel	19V	19HV	22V	37V	37H	85V	85H
Level Ice (First Year Ice Values)	0.941	0.888	0.960	0.955	0.913	0.926	0.886
Compact Ice (Summer Frozen Multi-Year Ice Values)	0.960	0.920	0.950	0.898	0.833	0.728	0.678

Emission contribution from the snow layer

The parts of the HUT snow model describing the emission from the snow layer are used for determining the effect of the snow layer above ice. The snow-ground boundary equations (reflectivity) appearing in the snow model have been modified to be used with a snow-ice boundary. In addition, a variable between 0 and 1 has been introduced to account for the part of ice within a pixel which is covered/uncovered with snow. Otherwise the snow module of the sea ice model is identical to the HUT snow model presented in Section 5.1.

Emission contribution from the atmosphere

An emission module similar to that of the HUT snow model was used to model the emission from the atmosphere.

Total observed (modeled) brightness temperature

When all the model modules defined, the total brightness temperature from the surface (water, ice, snow) for each frequency and polarization is obtained from

$$T_{B,surface} = C_{lev}T_{B,lev} \quad + \quad C_{com}T_{B,com} \quad + \quad (1 - C_{lev} - C_{com})T_{B,w}, \tag{5.31}$$

where

$$T_{B,lev} = R_{lev}(e_{lev}T_{lev} + T_{Bs,lev}) \quad + \quad (1 - R_{lev})e_{lev}T_{lev}, \tag{5.32}$$

$$T_{B,com} = R_{com}(e_{com}T_{com} + T_{Bs,com}) \quad + \quad (1 - R_{com})e_{com}T_{com}, \tag{5.33}$$

$T_{B,lev}$ = brightness temperature of level ice

$T_{B,com}$ = brightness temperature of compact ice

$T_{B,w}$ = brightness temperature of open water

$T_{Bs,lev}$ = brightness temperature of a snow layer above level ice

$T_{Bs,com}$ = brightness temperature of a snow layer above compact ice

T_{lev}	=	physical temperature of level ice (K)
T_{com}	=	physical temperature of level ice (K)
e_{lev}	=	emissivity of level ice (from Table 5.2)
e_{com}	=	emissivity of compact ice (from Table 5.2)
C_{lev}	=	level ice concentration
C_{com}	=	compact ice concentration
R_{lev}	=	fraction of level ice covered with snow
R_{com}	=	fraction of compact ice covered with snow

With these equations (ice, water, snow, atmosphere) and the radiative transfer equation, the total observed brightness temperature in space can be obtained, in similar way to the HUT snow model.

5.3 Effects of Various Target Characteristics on Modelled Winter-Time SSM/I Data

The sensitivity of the HUT snow model (presented in Section 5.1) to various target parameters was investigated by varying one parameter while keeping others constant. A suitable interval was chosen for each of the parameters. The constant values of the parameters and their intervals during the sensitivity study of the parameter in question are presented in Table 5.3.

Table 5.3. Constant values and the intervals for the target parameters during the sensitivity study of the HUT model.

Parameter	Constant value	Change interval
Snow water equivalent	100 mm	25 mm
Snow density	0.240 g/cm^3	0.05 g/cm^3
Grain size	0.8 mm	0.1 mm
Surface roughness	0.0 mm	0.2 mm
Forest coverage	60 %	10 %
Stem volume	50 m^3/ha	20 m^3/ha

The plots showing the behavior of the model with respect to the variable parameters are shown in Figures 5.3 to 5.8.

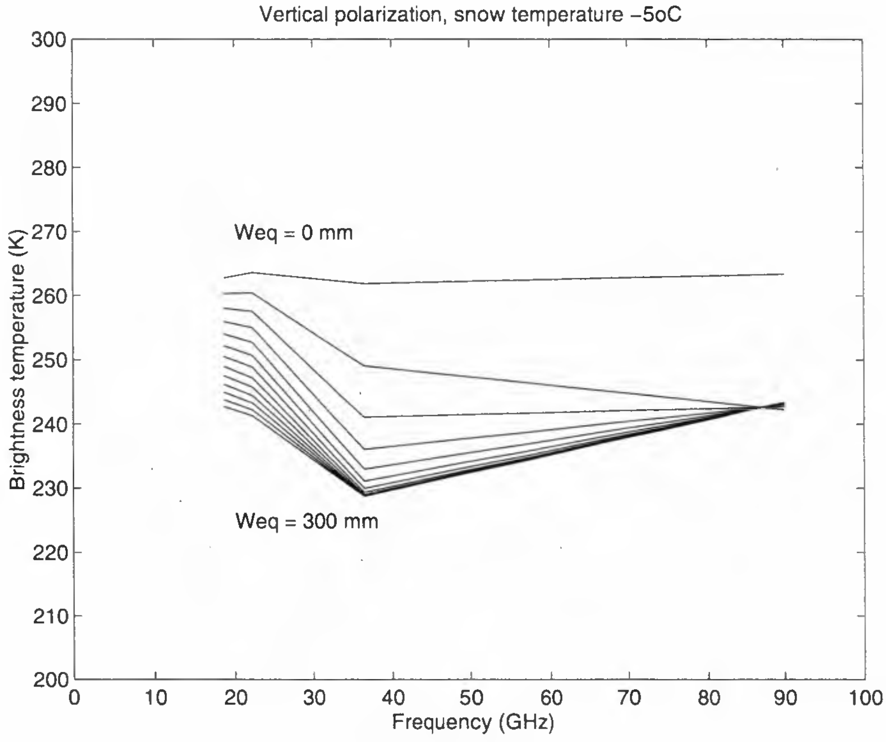

Figure 5.3. Snow model behavior for vertical polarization as a function of frequency and snow water equivalent (mm).

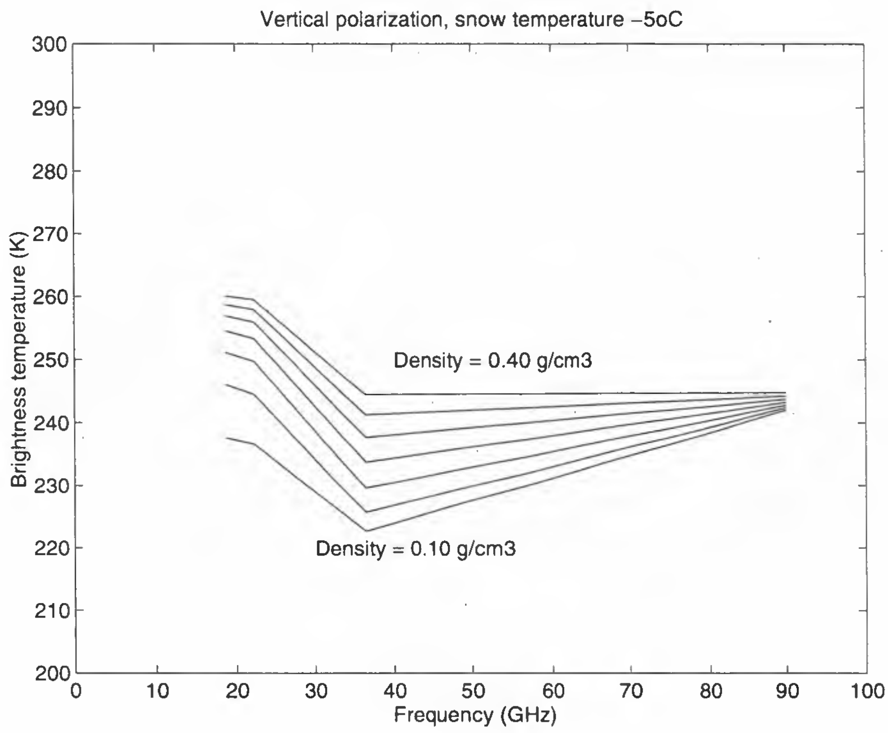

Figure 5.4. Snow model behavior for vertical polarization as a function of frequency and snow density (g/cm3).

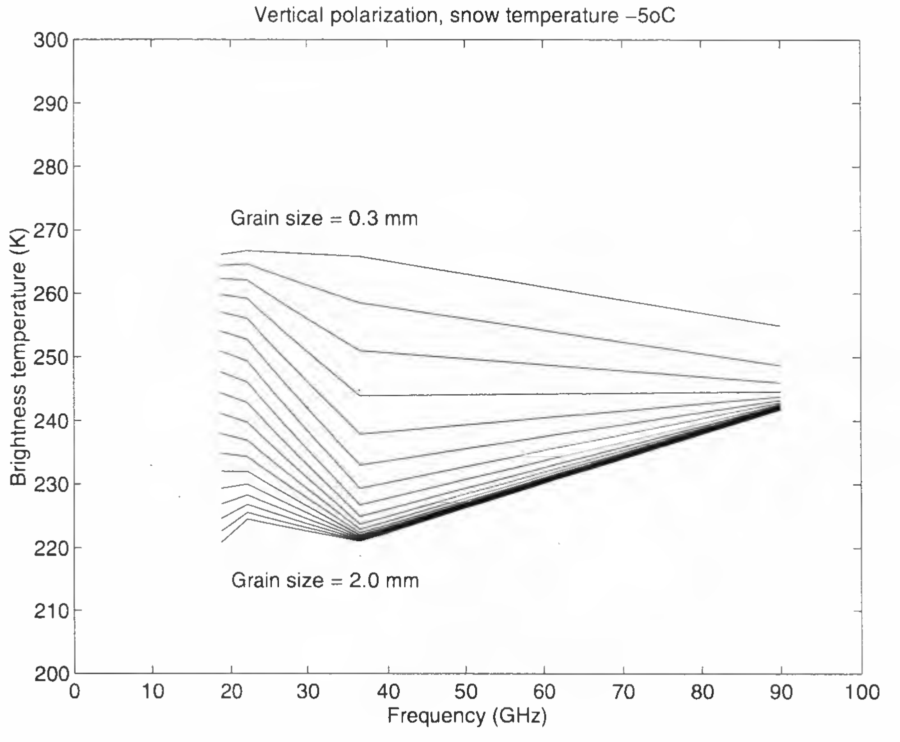

Figure 5.5. Snow model behavior for vertical polarization as a function of frequency and snow grain size (mm).

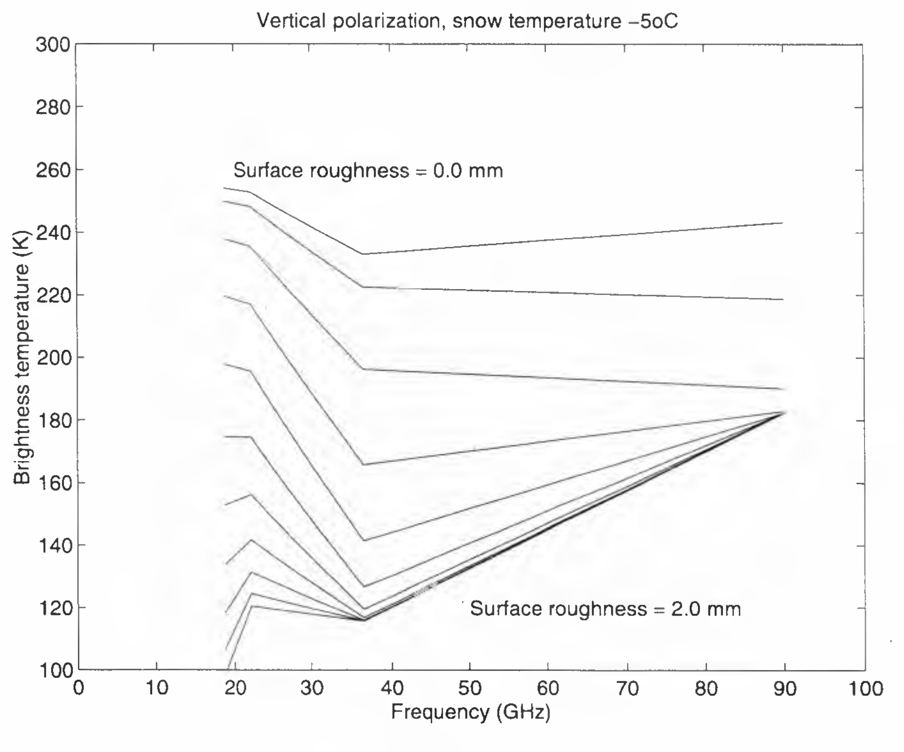

Figure 5.6. Snow model behavior for vertical polarization as a function of frequency and surface roughness (mm).

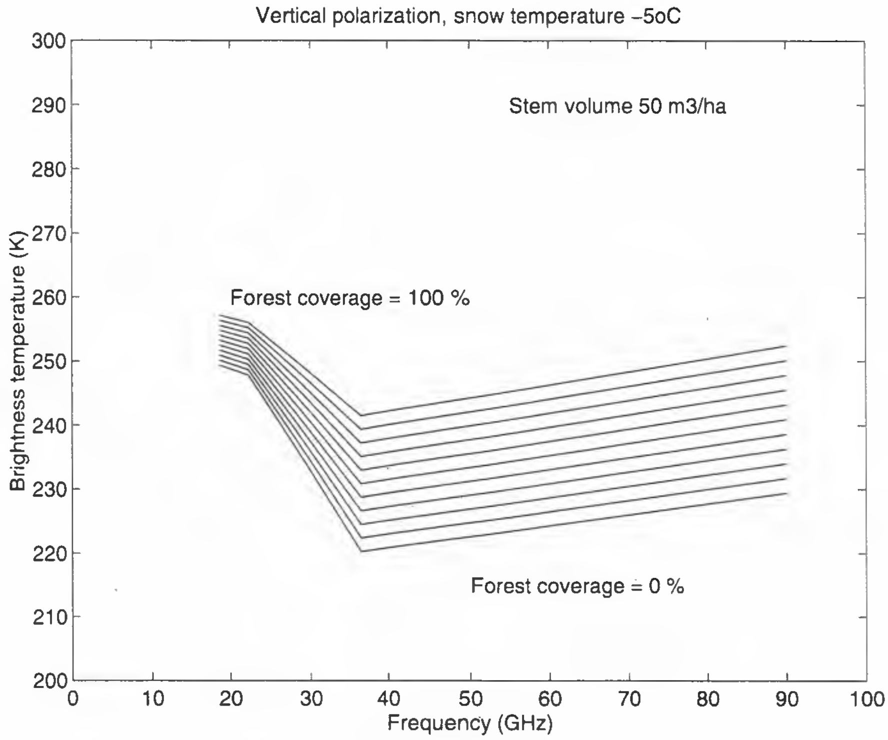

Figure 5.7. Snow model behavior for vertical polarization as a function of frequency and forest coverage (%).

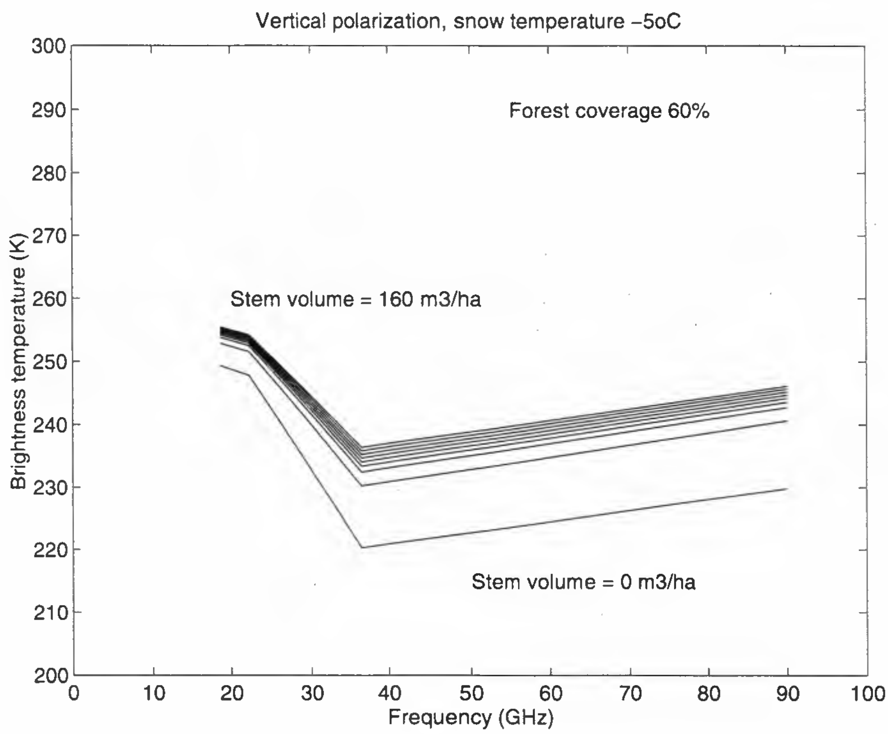

Figure 5.8. Snow model behavior for vertical polarization as a function of frequency and forest stem volume (m3/ha).

6 Behavior of Wind Scatterometer Data and Comparison with Model Predictions

6.1 Seasonal Behavior of ERS-1 Wind Scatterometer Data

Characteristics of Wind Scatterometer data

Since the ERS-1 Wind Scatterometer data products are highly averaged, the effect of radar speckle is minimal in Wind Scatterometer images, on contrary to ERS-1 SAR images. In the data processing, the transmitted pulses are averaged corresponding to the ground resolution of about 50 km. However, the data products are processed for a 25 km grid size. The effect speckle on the standard deviation of pixel-wise measurements (in decibels) can be evaluated by (*Pulliainen 1994*):

$$std_{\sigma^o(dB)} = \frac{10}{\sqrt{N}\ln 10} = 0.27dB \tag{6.1}$$

where
$N \approx 256$, the number of independent samples (number of pulses for a 50 x 50 km area).

The value obtained by Equation (6.1) can be compared with the stability analyses conducted for ERS-1 Wind Scatterometer data, see e.g. (*Amand 1994*). In these analyses, the stability of the instrument has been investigated by analyzing short and long term time series obtained for tropical rain forests which compose a relatively stable reference target. These investigations have shown short term random fluctuations that have a standard deviation of 0.30 dB (which correspond well the value obtained in Equation (6.1)). The long term oscillations have shown a maximum amplitude within 0.4 dB. All these figures of merit indicate that the relative accuracy of ERS-1 Wind Scatterometer is very high even for a single measurement pixel (about 0.14 dB or even better).

The absolute calibration characteristics of Wind Scatterometer data are discussed later in this Section and in Section 6.3.

Variations caused by weather conditions

Figure 6.1 shows an example of ERS-1 Wind Scatterometer data time series obtained for Finnish boreal forests. The average responses of aft-beam measurements for two angular ranges are shown. Each data point in Figure 6.1 presents the mean value of σ^o calculated from the results of 89 grid cells. The grid cell-wise results were determined for the South Finland test area. Since the Wind scatterometer measurements did not cover all pixels (grid cells) on every occasion, the amount of pixels (from which the average is calculated) varies for different data points.

The pixels used in this investigation were selected using the following criteria in order to have a homogeneous pixel set:

- the percentage of open water areas < 20% and
- the percentage of fields < 20% and
- the percentage open swamps < 20% and
- the percentage of other open areas < 20% and
- the sum of all these contributions < 25%.

The outcome was that the chosen set of 89 grid cells has the following average properties:

- percentage of forest areas: 82%
- average stem volume in land areas: 73 m^3/ha (total dry biomass of 44 tons/ha (*Häme et al. 1992*).

The variations observed in average σ^o values presented in Figure 6.1 are primarily caused by changes in soil moisture, vegetation canopy moisture and by the freezing of soil and vegetation in late October and November. The temperature decreases below the freezing point around day 150 (in the late October) which causes a drop of about 3 dB in σ^o. In the beginning of November, the temperature is for a short period above 0°C, which probably causes the local peak visible in Figure 6.1 for days no. 155-160.

The amplitude of variation in Figure 6.1 is about 4 dB (the behavior is also similar for the other antenna beams). When the temperature is above freezing point the amplitude is about 2 dB, and as the temperature is below freezing point the variations in σ^o appear to be smaller. These oscillations in average values are quite large when compared with variations observed in grid cell-wise σ^o values of individual days. The standard deviations of daily pixel-wise results were calculated separately for each antenna beam and for four incidence angle ranges (20°-30°,30°-40°,40°-50° and 50°-60°). The average standard deviations of these daily pixel-wise σ^o values are:

- fore-beam: 0.30 dB
- aft-beam: 0.33 dB
- mid-beam: 0.36 dB.

These deviations include the effects of radar speckle and the variations in target pixel characteristics, i.e. the grid cell-wise differences in soil and vegetation moisture and the differences in land use and forest cover (the 89 grid cells employed are scattered to an area sized 350 km by 400 km). Hence, the standard deviation values obtained are relative low when compared with the variation characteristics discussed above. A possible explanation is that the variability of grid cell-wise results is also reduced due to the resampling conducted for Wind Scatterometer data (interpolation into a fixed grid described in Section 2.2).

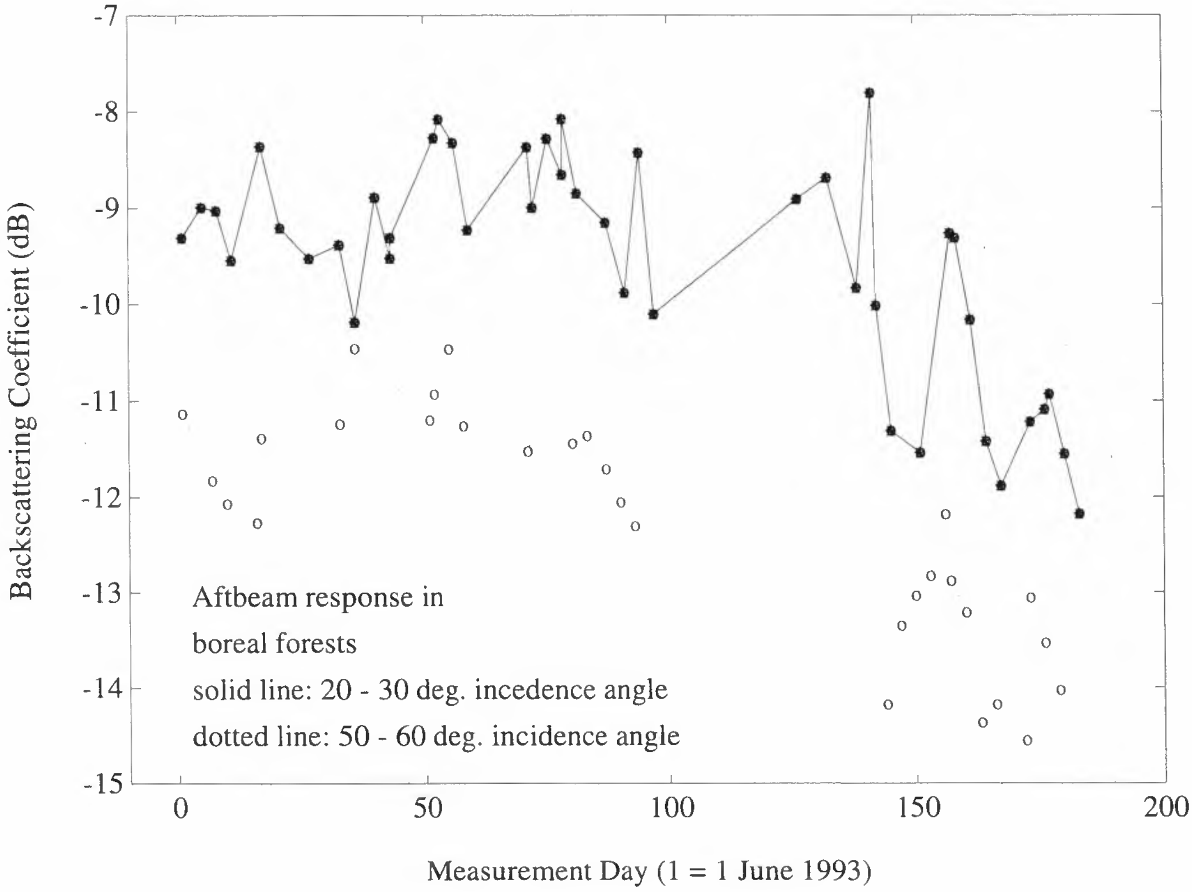

Figure 6.1. Seasonal behavior of ERS-1 Wind Scatterometer measurements in boreal forests. The time period is from the beginning of June to end of November 1993. The ground is partially covered by a thin snow layer in the late October and November (roughly from day no. 150 onwards).

Angular response of WS data in forested areas

The angular response of Wind Scatterometer measurements of boreal forests has been investigated using the same set of grid cells as above (89 fixed pixels from the South Finland test area representing heavily forested areas). Figures 6.2 and 6.3 present the results obtained using averaged values of two short time periods for which the Wind Scatterometer data have shown fairly constant values. The averaging was performed for four angular ranges (20°-30°,30°-40°,40°-50° and 50°-60°) using pixel-wise values of both time periods. In Figure 6.2, the aft- and forebeam responses with second degree polynomial fittings are shown. The corresponding mid-beam responses with appropriate polynomial fittings (and aft- and forebeam data points) are depicted in Figure 6.3.

Figures 6.2 and 6.3 indicate that the calibration differences between different antenna beams are small (cannot be distinguished from these results). Moreover, Figures 6.2 and 6.3 show that the angular response of Wind Scatterometer measurements appears to vary with time in the case of boreal forests. According to Figure 6.2, the decline of σ^o is about 2.15 dB for the data from 1, 5 and 8 June 1993 as the angle of incidence increases from 27° to 53°. For the data set of 22, 23 and 26 July, the decline is about 2.75 dB, respectively. This difference is probably caused by the differences in soil and canopy moisture (these aspects are also discussed in Sections 4.4 and 6.3).

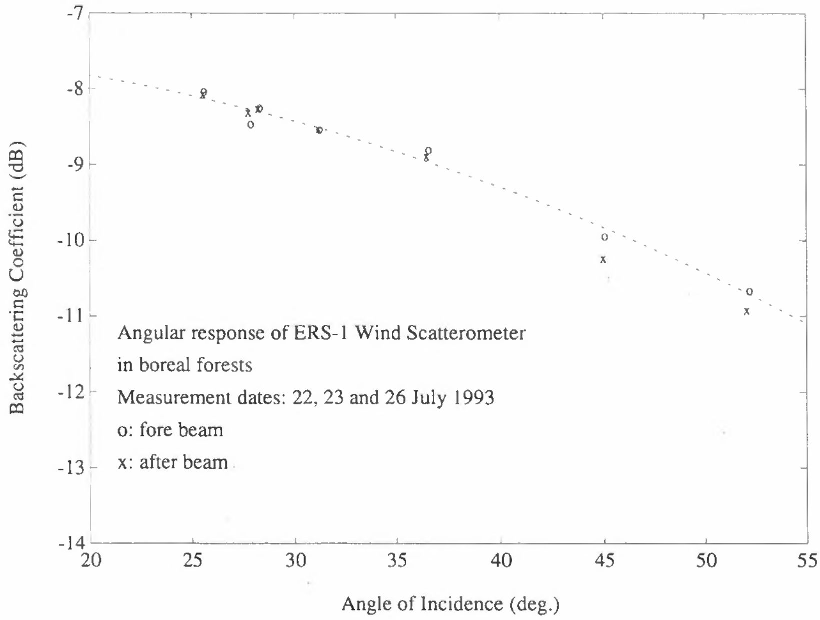

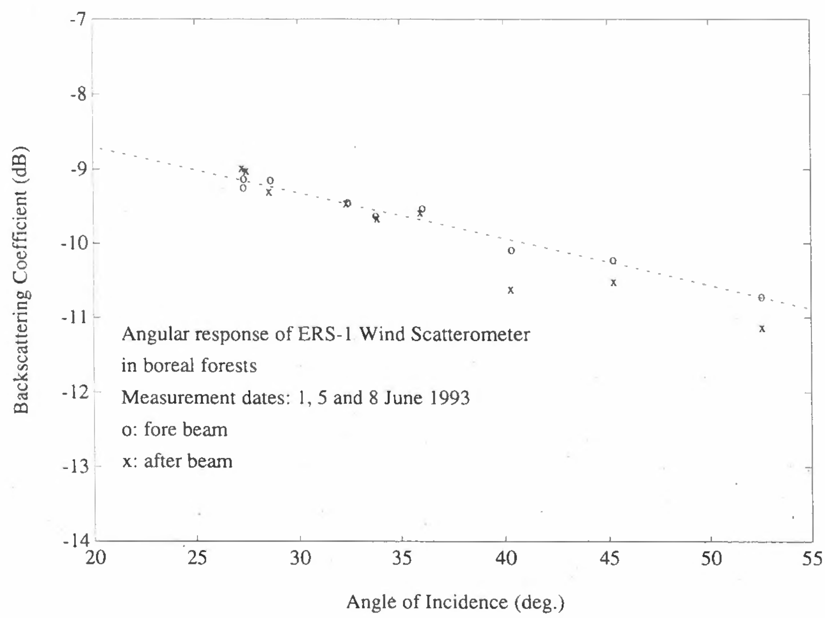

Figure 6.2. Observed behavior of ERS-1 Wind Scatterometer measurements (fore-beam and aft-beam) as a function of the angle of incidence for two time periods. The depicted values show the average response observed for a set of 89 grid cells of the South Finland test area. The second degree polynomial fittings are also shown:
Above: response for 22, 23 and 26 July 1993
Below: response for 1, 5 and 8 June 1993.

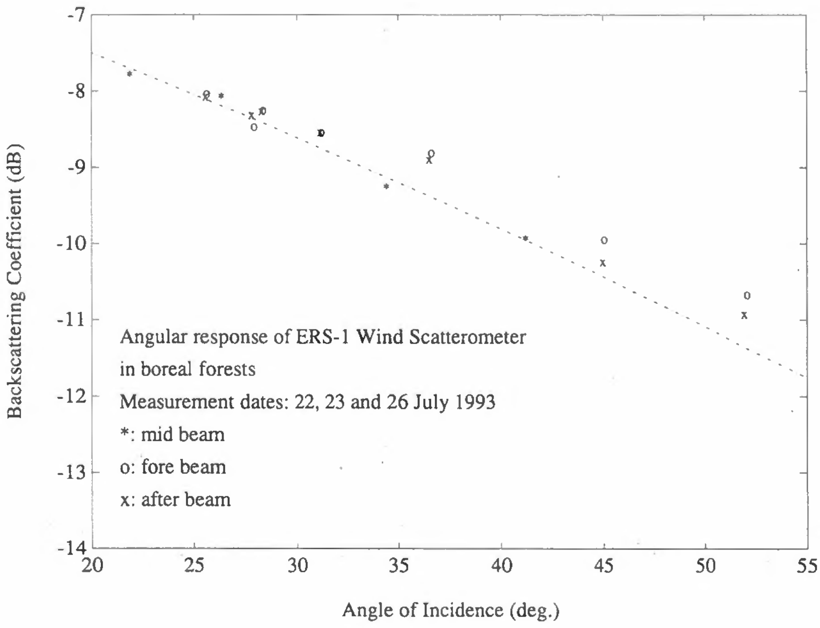

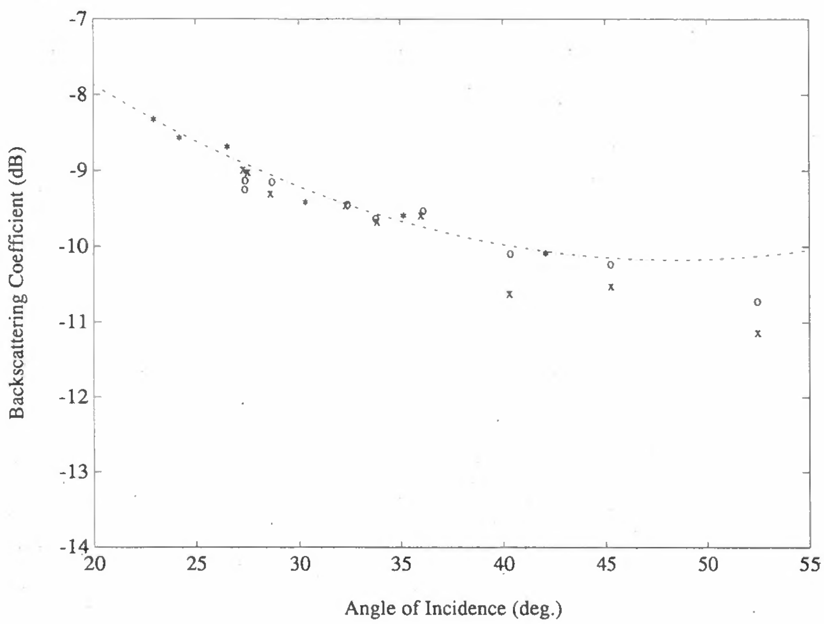

Figure 6.3. Observed behavior of ERS-1 Wind Scatterometer measurements (fore-beam, aft-beam and mid-beam) as a function of the angle of incidence for two time periods. The depicted values show the average response observed for a set of 89 grid cells of the South Finland test area. The second degree polynomial fittings for mid-beam results are also shown.
Above: response for 22, 23 and 26 July 1993
Below: response for 1, 5 and 8 June 1993.

6.2 Effects of Various Target Characteristics on Wind Scatterometer Data

Coniferous and deciduous biomass mosaics based on NOAA/AVHRR images and a regression multi-channel vegetation model *(Häme et al. 1994)* were used as background information in investigating the sensitivity of the ERS-1 wind scatterometer to biomass. This mosaic covers the whole Northern Europe from Scandinavia to Ural mountains (Fig. 6.4). The coniferous biomass values are more reliable than the deciduous biomass values, since the ground truth used in developing the vegetation model was taken from Finnish forest inventory values and Finnish forests are mostly coniferous. The biomass values of Western Russia are slightly underestimated by the model, because the forest structure there is very heterogeneous.

The comparison of the wind scatterometer intensity and the biomass parameters are carried out both for Finland and for the whole Northern Europe. The results of Finland should in principle be better, because the biomass data is more reliable. On the other hand Finland is a rather small area to be used for wind scatterometer analysis. The use of the whole Northern Europe as a test area should then be statistically better justified, because the number of pixels involved is so much larger.

The scatterometer pixels are so large (diameter 50 km), that it is not desirable to touch their values by any rectification process. The scatterometer data is actually not image data, because the incidence angle varies radically from one end to the other inside the image. Each scatterometer pixel is happily enough provided with coordinate values. Thus in this research the scatterometer data was split into individual pixels each having its own incidence angle, look angle and coordinates. Data of ascending and descending passes was kept apart. Because the biomass mosaics were based on summer images (May 1990 - June 1993), most of which are taken in June, the scatterometer data to be used was chosen to be that of June 1993. It consisted of 55 images each having data for the three beams. Thus the number of pixels included in the research was 55 x 3 x 361 = 59565. The comparison of the wind scatterometer and biomass data was carried out using the scatterometer pixel coordinates. Statistical parameters (mean, median, standard deviation, skewness and kurtosis) of coniferous and deciduous biomass were calculated for each scatterometer pixel using the coniferous and deciduous biomass mosaics (Fig. 6.5). Also the percentage of water subpixels and percentage of land subpixels with zero biomass in the scatterometer pixels were registered. All NOAA subpixels inside the scatterometer pixels were taken into account using the same weight in the statistical calculations. A more accurate result would be obtained taking into account the antenna characteristics of the wind scatterometer, but the calculation time of the data set was already now considerable. Moreover the difference between test results obtained using the two methods had no significance in practice. Because the data set is so large, a closer examination was done only for a few incidence angle values. To be able to compare the results of for-, mid- and aft-beam, most of the incidence angle values were chosen to be such that they exist for all the three beams. The incidence angle values used were 25.1°, 25.2°, 34.2°, 34.3°, 34.4°, 45.5°, 45.6°, 56.7°, 56.8°, 56.9° for for- and aft-beams and 18.1°, 18.2°, 25.3°, 34.9°, 45.4° for mid-beam.

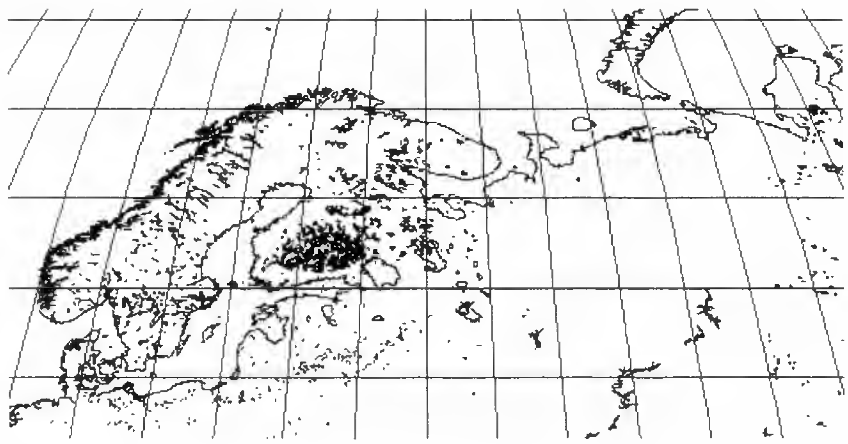

Figure 6.4. The area covered by the biomass mosaics based on NOAA/AVHRR images (Häme et al. 1994).

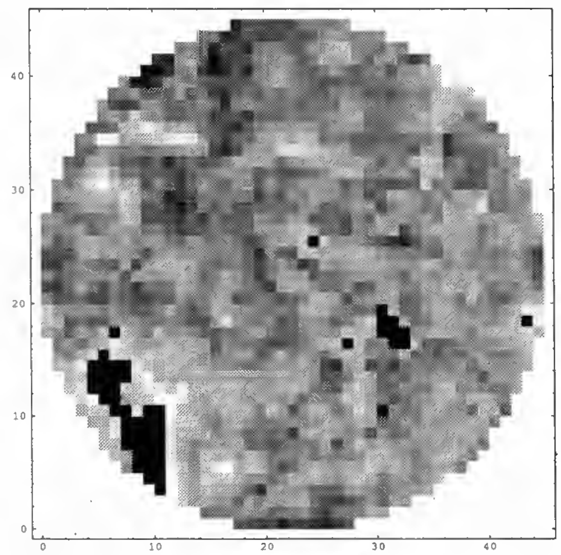

Figure 6.5. Variation of boreal coniferous biomass quantity inside a scatterometer pixel in Southern Finland. The individual biomass values of each 1.1km x 1.1km sub-pixel are taken from the coniferous biomass mosaic calculated from a NOAA/AVHRR mosaic in VTT (Häme et al. 1994). The black area is either water or land with zero biomass. The graylevel increases with increasing biomass. The largest biomass value is 234 m^3/ha.

The effect of water area percentage inside the scatterometer pixels on the backscattered intensity in summer conditions is shown in Figures 6.6 - 6.9 for several incidence angle values. Obviously the water area percentage dominates the signal in most cases. The intensity increases with increasing water percentage, when the incidence angle is about 18°. The intensity decreases with increasing water percentage, when the incidence angle is larger than 25°. Almost no systematic water percentage dependence exists for the incidence angle 25°. All the three beams and the ascending and descending passes behave similarly.

The larger scatter of the intensity values with high water area percentage is probably mostly caused by the wind effect present in large water areas. The wind increases the backscattering from water notably when the water area percentage is above 90. The reason for the very low intensities also characteristic for large water area percentages is not so easy to understand. It is true that June is typically a very calm month, but the smaller water areas should be at least as calm as the larger areas. In principle the antenna pattern should be taken into account when calculating the reference biomass values using the 1.1 km resolution biomass mosaics. However, the difference between ordinary averaging of the biomass values and weighted averaging based on the 3dB-level of the antenna patterns turned out to be smaller than 10 % (Fig. 6.10). Moreover the effect of the weigths is the smallest for pure water and pure land areas, which were only used in this study.

The smallest intensities obtained in the open water areas are situated in the Barents Sea (Figs. 6.11 - 6.13). The very low values occur on several days, but not always in the same places. The backscattering varies very systematically over the whole areas in questions. Moreover, the sorted σ^o values cover the whole variation range uniformly. Thus the very low values (< -35 dB) are not caused by individual defective pixels. Yet it is hard to believe that one could have back-scattering values smaller than -35 dB in the middle of a large sea area even for rather small incidence angles. Moreover it is not very probable that it would be so much calmer in the middle of the sea than closer to the coast. Especially when these low values are obtained in an area of about 5 x 10 pixels, which is about 125 km x 250 km. It seems that the very low intensities are an artifact not caused by any physical phenomenon. Similarly it is possible that some of the lowest intensities over land areas are erroneous, but they do not show up, because the variation range over land is so small.

In principle this dominant water effect should exist also for other targets having typically higher intensities than calm water. One example is naturally sea ice. If one could get good cloudless mosaics of sea ice covered areas, it would be possible to check, how well the discrimination of ice and open water would function using the scatterometer intensities of large incidence angles. One indication supporting this possibility is the fact that the discrimination of ice and open water in ERS-1 SAR images (incidence angle 23°) using only intensity values is not possible. This not only because of completely smooth new ice, which appears black.

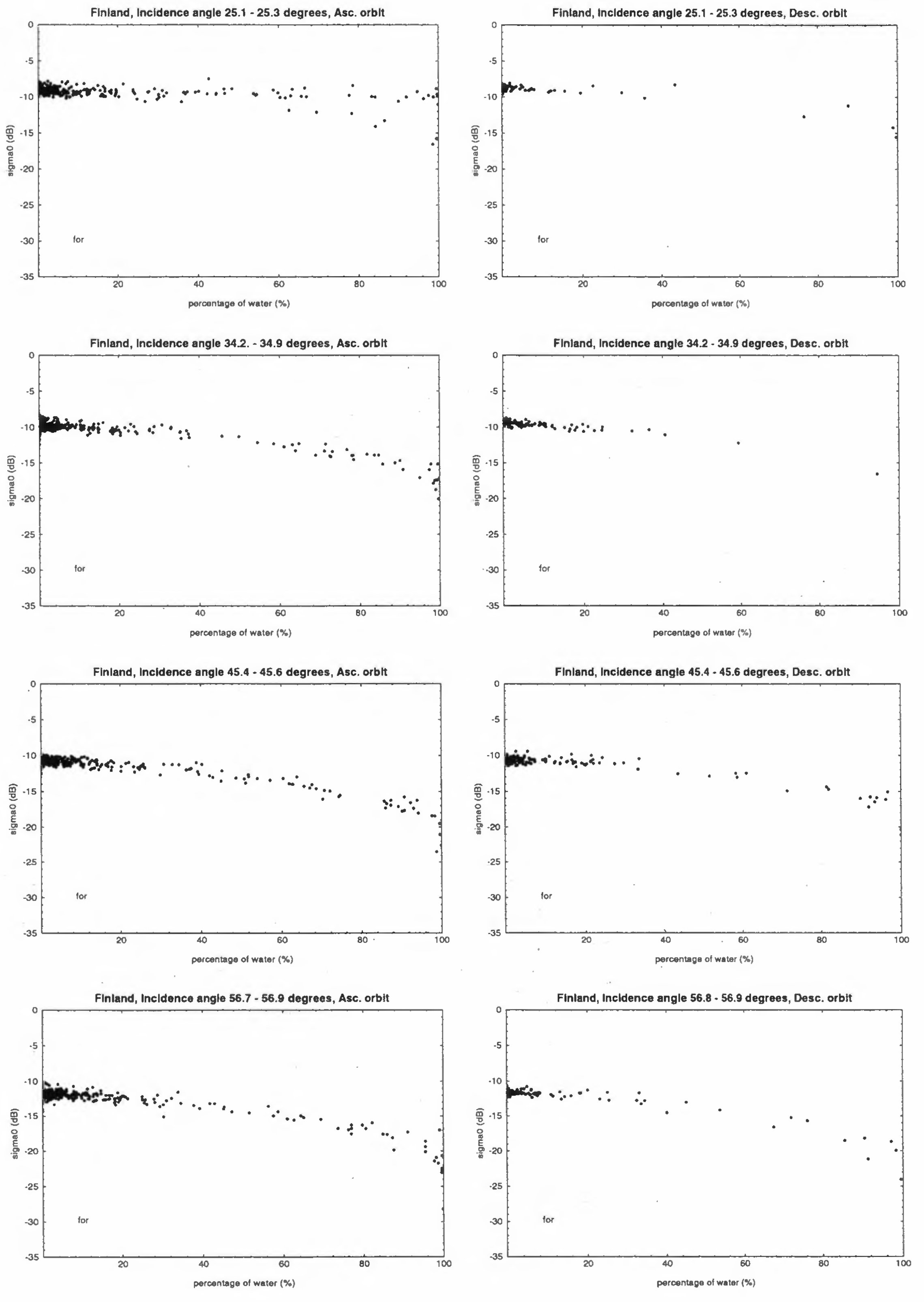

Figure 6.6. The effect of water sub-pixel percentage in the scatterometer pixel on the fore-beam back-scattered intensity in Finland.

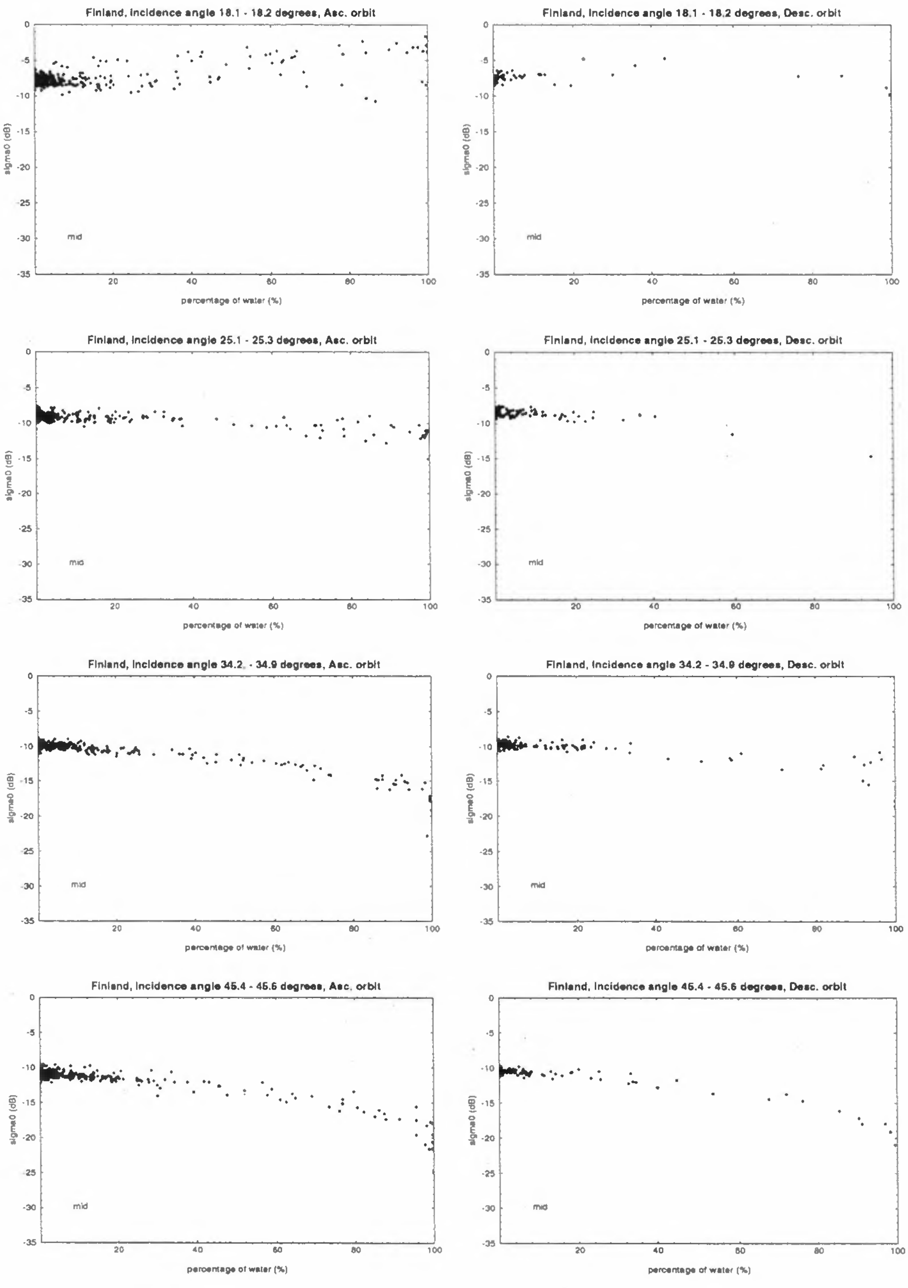

Figure 6.7. The effect of water sub-pixel percentage in the scatterometer pixel on the mid-beam back-scattered intensity in Finland.

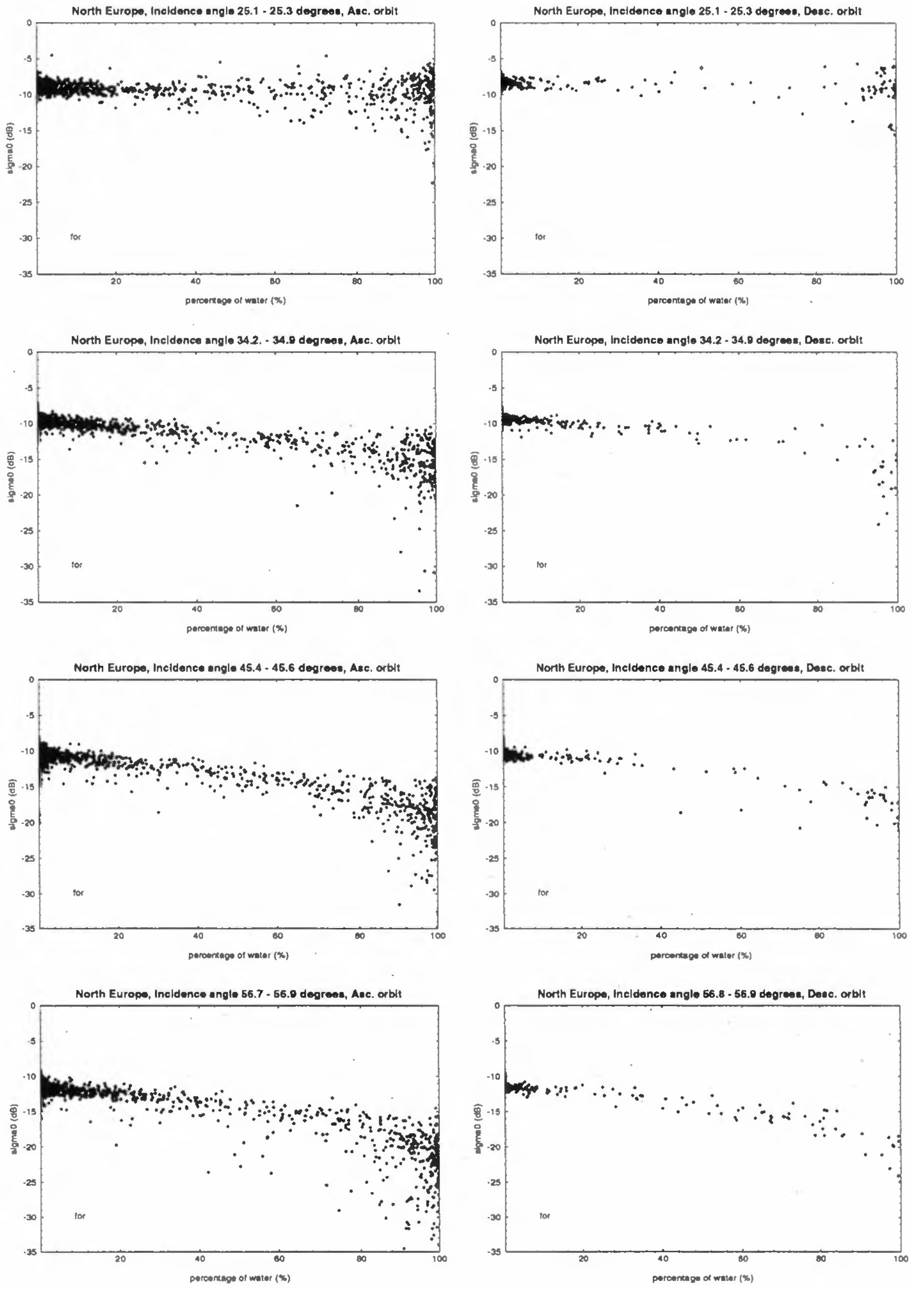

Figure 6.8. The effect of water sub-pixel percentage in the scatterometer pixel on the fore-beam back-scattered intensity in Northern Europe.

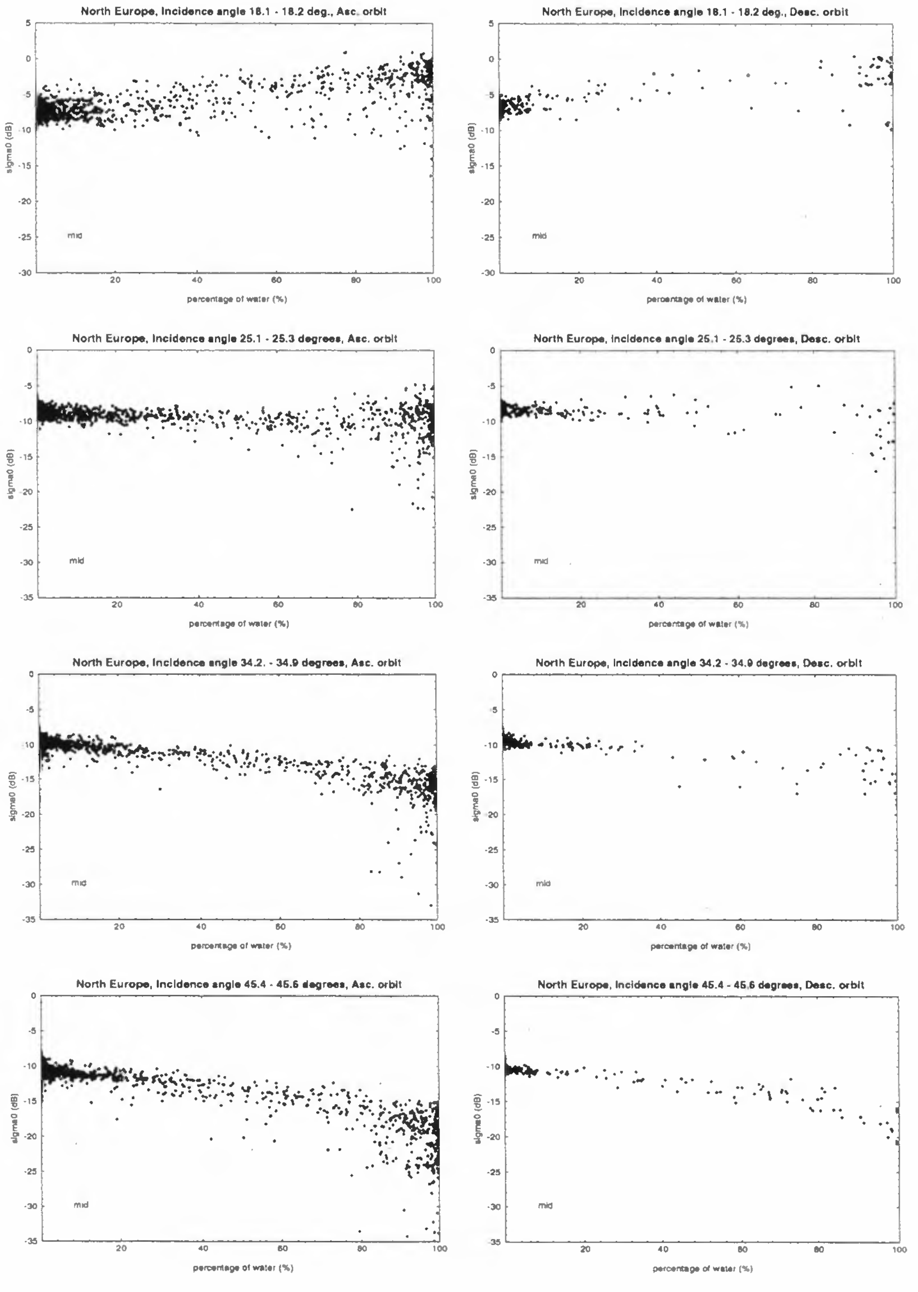

Figure 6.9. The effect of water sub-pixel percentage in the scatterometer pixel on the mid-beam back-scattered intensity in Northern Europe.

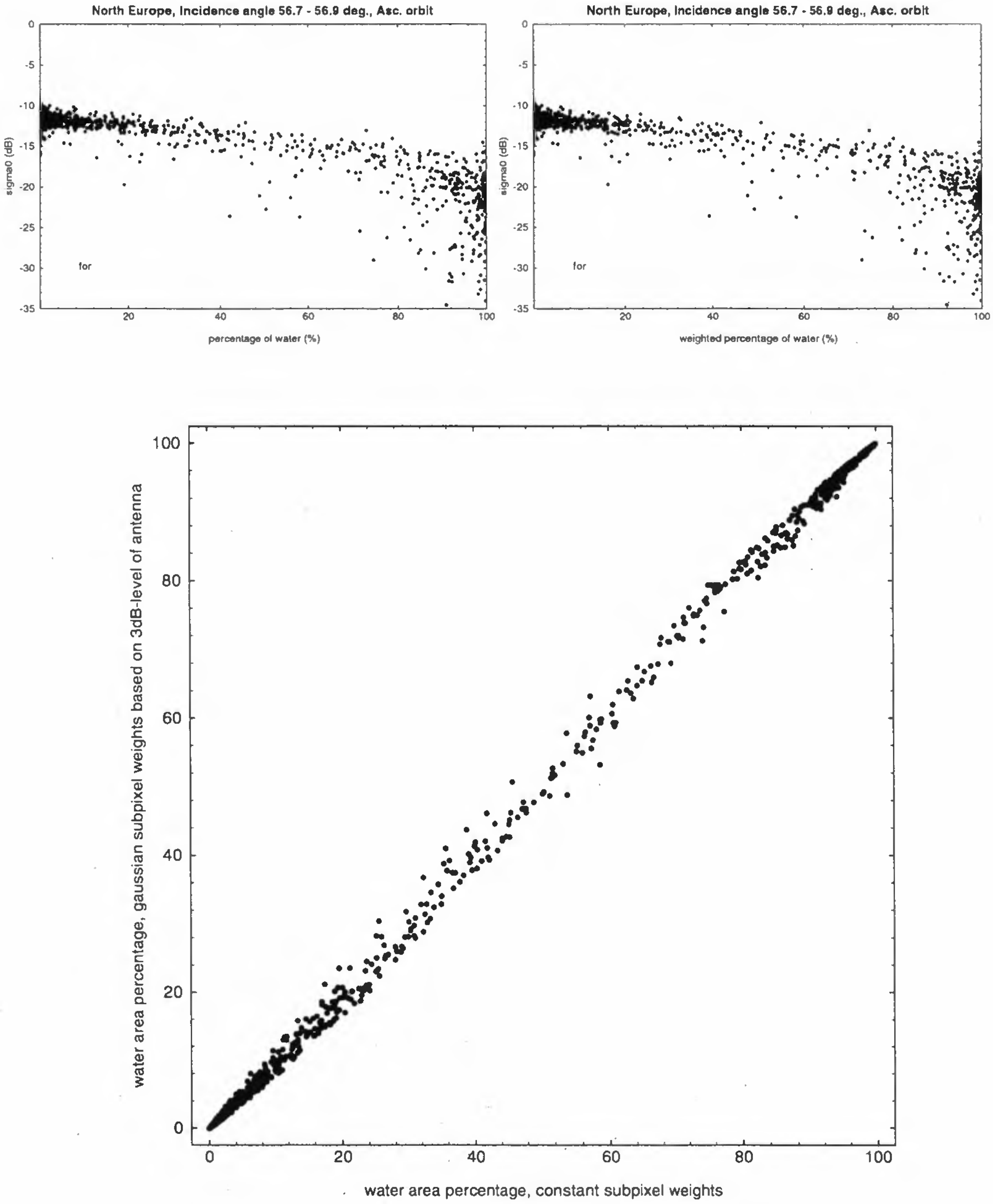

Figure 6.10. The effect of water subpixel percentage in the scatterometer pixel on the fore-beam backscattered intensity of ascending orbit in Northern Europe. Also the relationship between the average water area percentage obtained using constant weights and the Gaussian weights of the fore-beam antenna is shown.

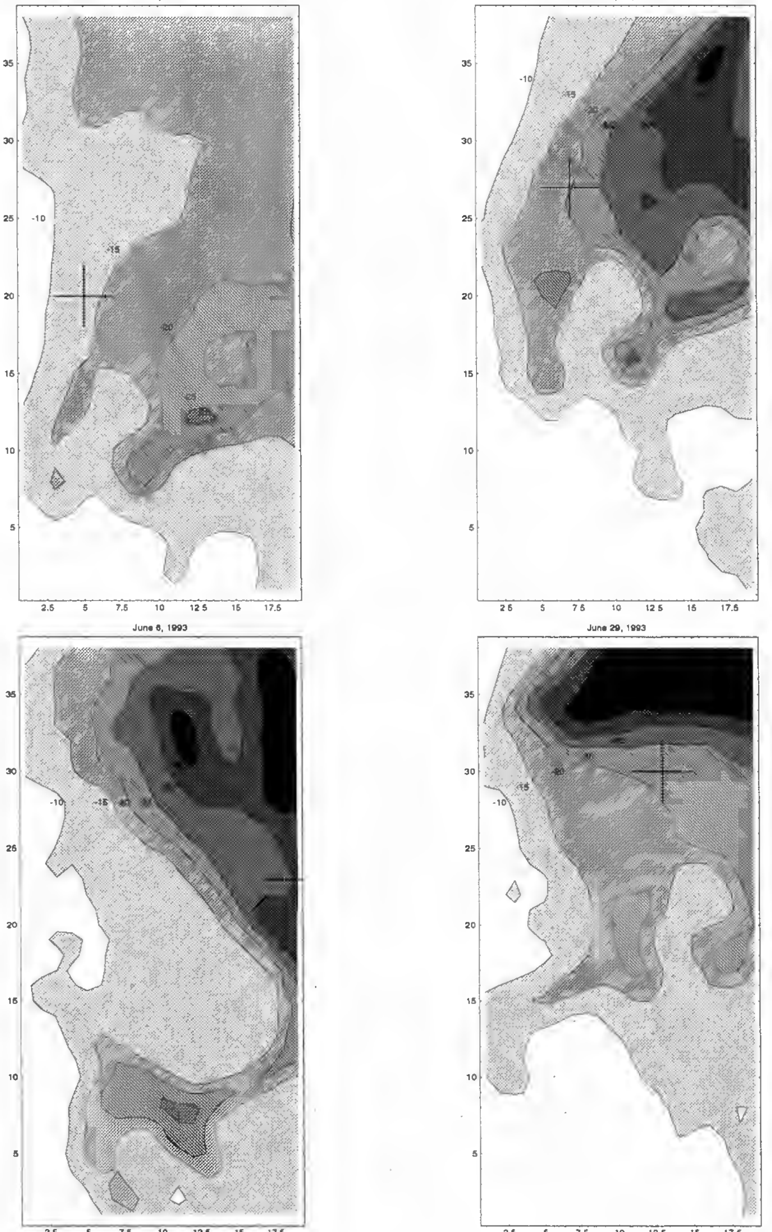

Figure 6.13. Intensity contours of the four scatterometer fore-beam image pairs in the Barents Sea of Figure 6.12. The incidence angle varies from left to right in the range 25.2° - 56.8°. The cross corresponds to the mark in the map of and Figure 6.11.

To avoid the dominant effect of water, the data used for the biomass studies should be chosen so that the water area percentage is smaller than 10 %. If the incidence angle used is about 25°, the water percentage can be 50 % before serious water bias is notable. In this study only pixels with no water subpixels were used. This reduced greatly the number of pixels in the Finnish test area, because there are 60000 lakes in Finland and large archipelagos near Turku and Vaasa, the former consisting of about 30000 islands. The Northern Europe data set was not so strongly fragmented.

The dependence of the backscattered intensity on the mean total biomass in summer conditions is shown for various incidence angles in Figures 6.14 - 6.17. The for- and aft-beam results are practically taken identical. The mid-beam intensity seems to be very slightly higher than that of the for- and aft-beams. The ascending and descending orbit results are similar. The data set of Finland corresponds to areas of rather low biomass values. The minimum intensity values are probably due to dry forests showing first the increase of intensity with increasing biomass and above 20 ... 40 m^3/ha the saturation of the intensity value. The opposite behaviour of the maximum values of the intensity with increasing can be caused by several effects and is studied more closely later. The results of the Finnish and Northern Europe data sets are consistent, which supports the reliability of the Northern Europe data set.

The dependence of the backscattered intensity on the purely coniferous and purely deciduous biomass in summer is shown in Figures 6.18 - 6.19 for Northern Europe. The percentage of the other type of biomass is kept below 10 % in this test data. The results for Finland are similar, but the number of purely deciduous biomass pixels is too small to permit any further analysis. On the contrary the purely coniferous biomass pixels of Northern Europe are mostly situated in the test area of Finland. Clearly there is no distinct difference in the coniferous and deciduous biomass behaviour. This is natural, since the resolution of the scatterometer data is so modest. Although the scatterometer pixels can be very heterogeneous (Fig. 6.5), the standard deviation, the skewness and the kurtosis coefficient of the biomass in the scatterometer pixel do not seem to be correlated with the backscattered intensity. This is not so surprising after all, because the intensity is not very sensitive to the mean value of the biomass either. Basically the scatterometer intensity of purely coniferous and purely deciduous biomass behaves similarly as the intensity of the total biomass. Also the effect of incidence angle is the same. Therefore only one example is shown corresponding to each of the statistical parameters (Figs. 6.18 and 6.19).

All the biomass analyses have been carried out so that the percentage of subpixels with zero biomass is indicated. However, it seems to have no effect on the interdependence of backscattered intensity and biomass. It is not so surprising, since the standard deviation did not have any effect either. Also the percentage of the minority type biomass has no effect in summer conditions: the pixels with no coniferous or deciduous biomass are not distinguished from those including 10% of minority type biomass.

Because the scatterometer is most sensitive to low biomass values, special attention has been paid to these cases. Figures 6.20 and 6.21 and the map of Fig. 6.4 show the areas having the smallest mean biomass values. Naturally they are situated in the northernmost part of the data set. The percentage of subpixels with zero biomass in the scatterometer pixels was checked also.

The areas having a large percentage of zero biomass subpixels correspond to coastal areas (especially mining districts like Kola or Vorkuta) and mountainous areas (Ural). The other low biomass areas represent then tundra, swamp etc.

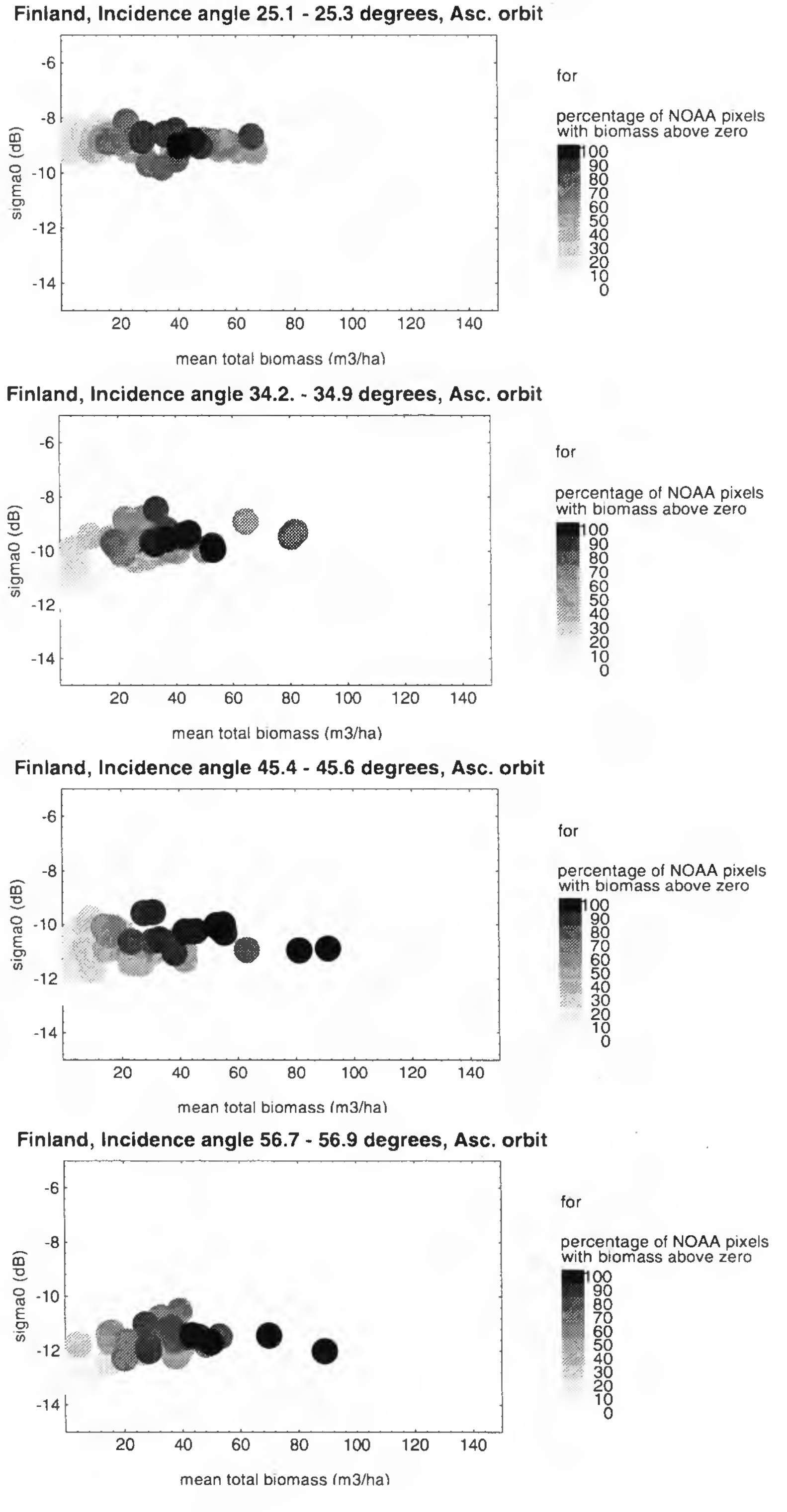

Figure 6.14. The relationship of the mean total biomass (both coniferous and deciduous together) and the back-scattered intensity of fore-beam in Finland. The percentage of the sub-pixels with nonzero biomass value is indicated with the graylevel of the markers.

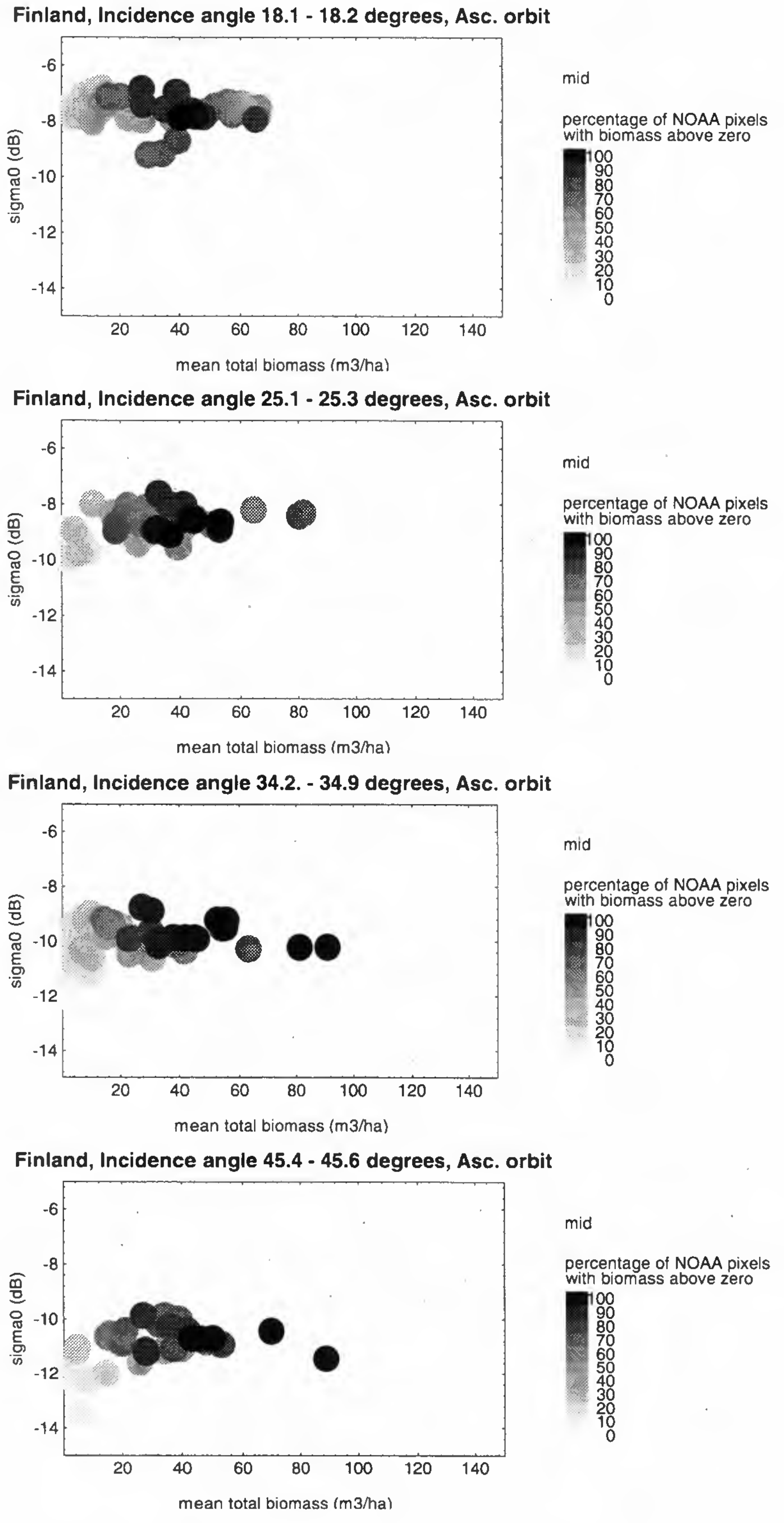

Figure 6.15. The relationship of the mean total biomass (both coniferous and deciduous together) and the back-scattered intensity of mid-beam in Finland. The percentage of the sub-pixels with nonzero biomass value is indicated with the graylevel of the markers.

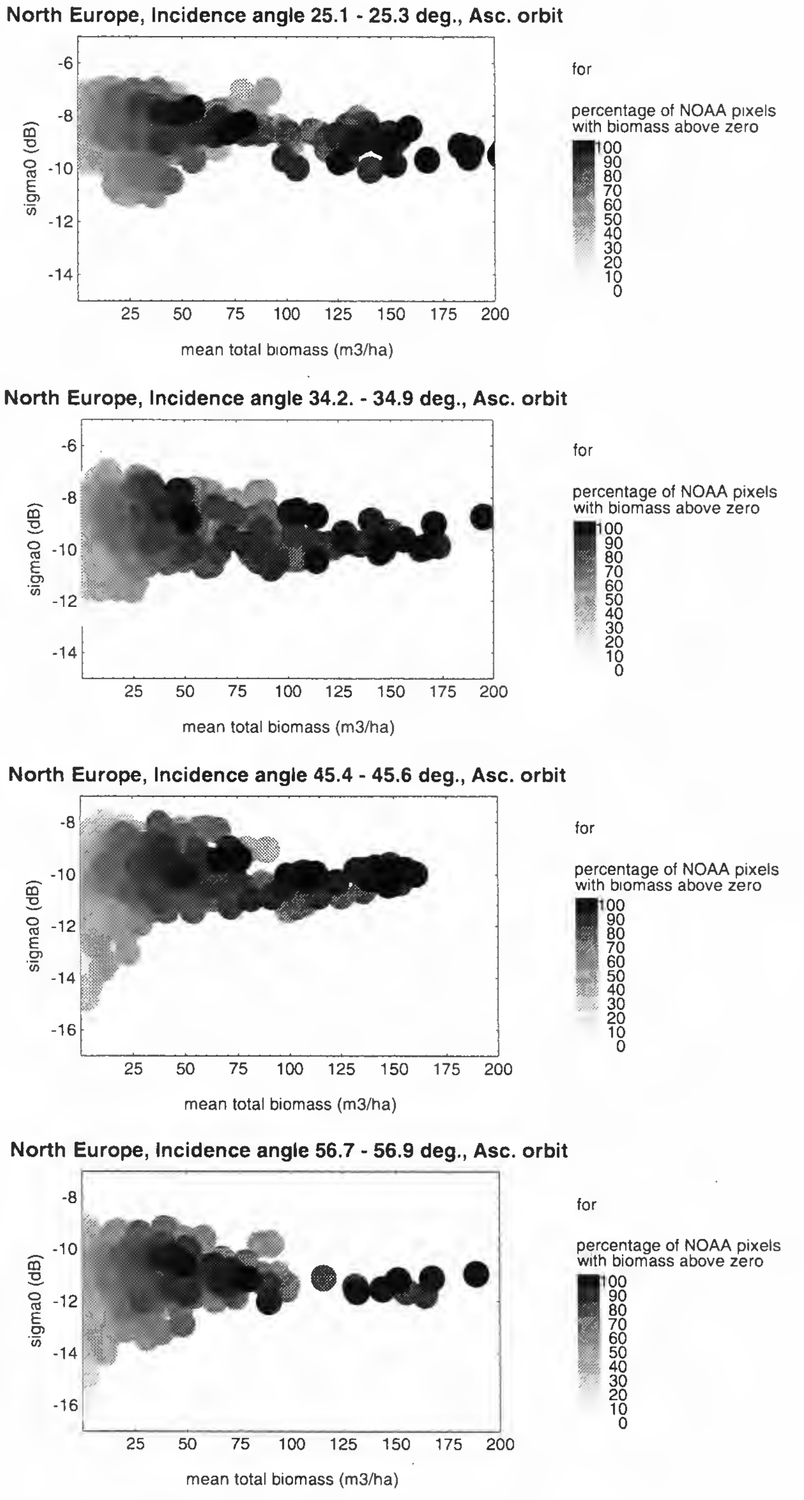

Figure 6.16. The relationship of the mean total biomass (both coniferous and deciduous together) and the back-scattered intensity of fore-beam in Northern Europe. The percentage of the sub-pixels with nonzero biomass value is indicated with the graylevel of the markers.

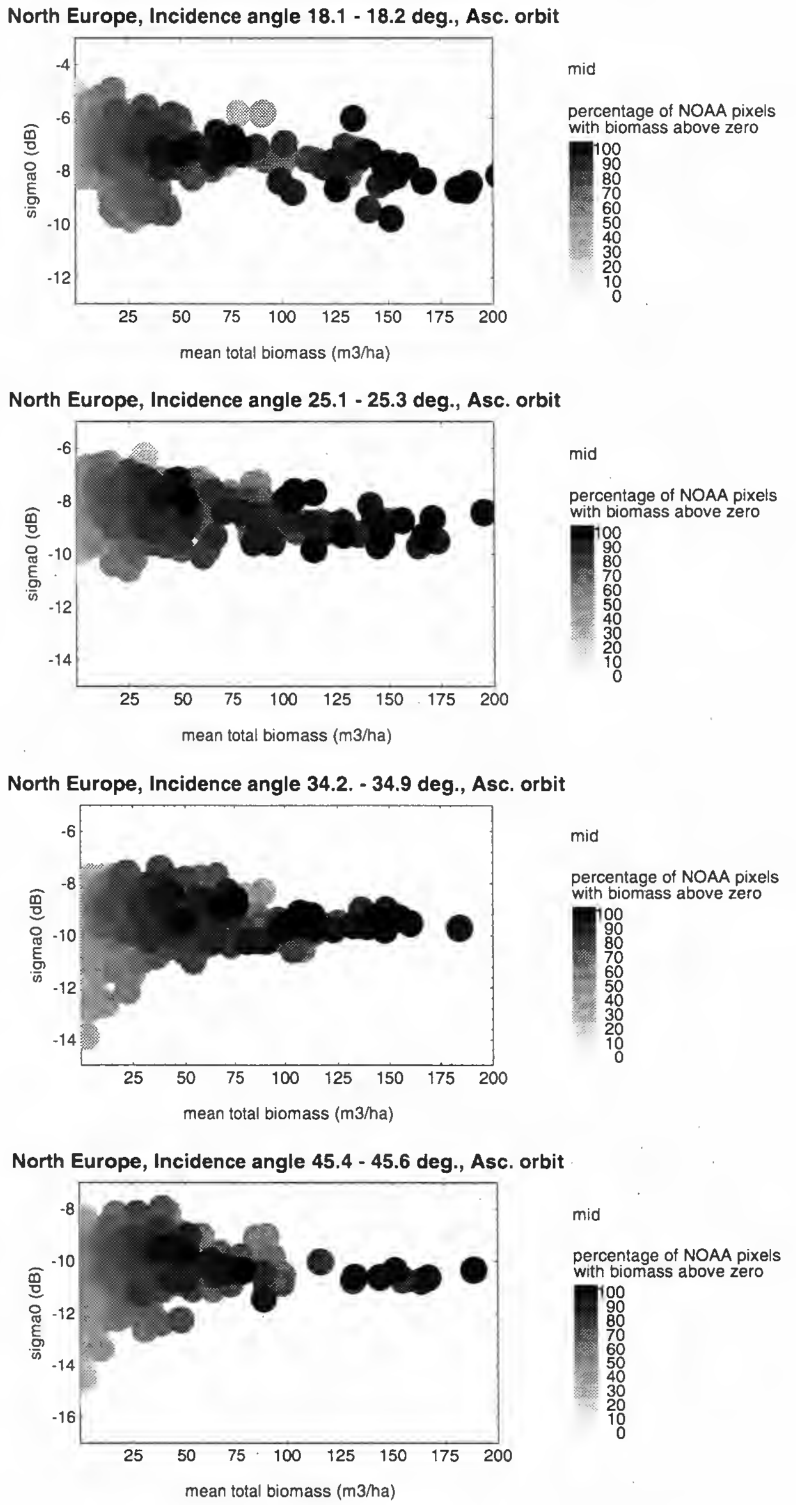

Figure 6.17. The relationship of the mean total biomass (both coniferous and deciduous together) and the back-scattered intensity of mid-beam in Northern Europe. The percentage of the sub-pixels with nonzero biomass value is indicated with the graylevel of the markers.

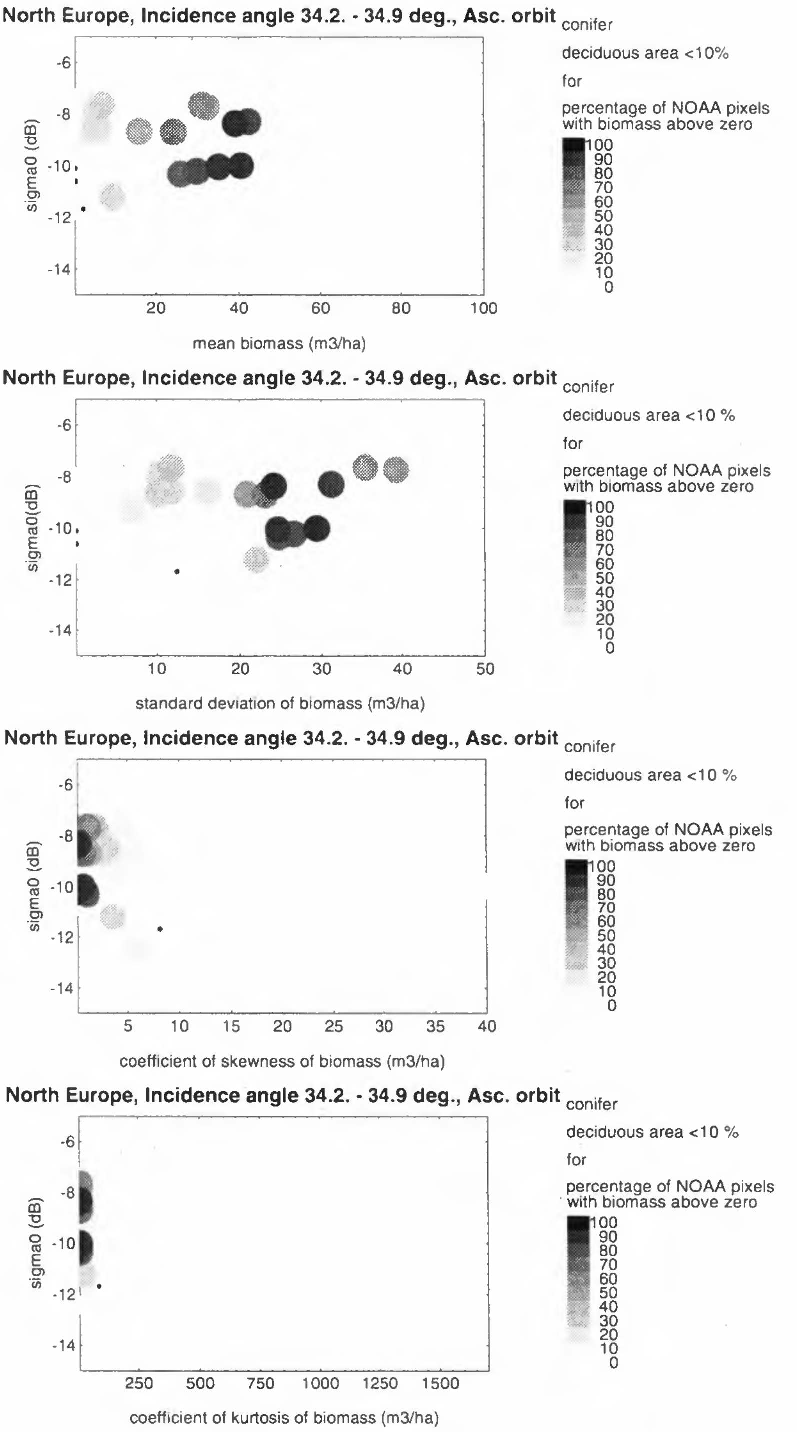

Figure 6.18. The relationship of the backscattered intensity and the mean, standard deviation, skewness and kurtosis coefficient values of the coniferous biomass in the scatterometer pixels in Northern Europe. The percentage of sub-pixels with nonzero deciduous biomass is below 10%. The graylevel of the markers indicate the percentage of sub-pixels with nonzero biomass. The points in the center of the markers show the values that correspond to a case of no deciduous biomass.

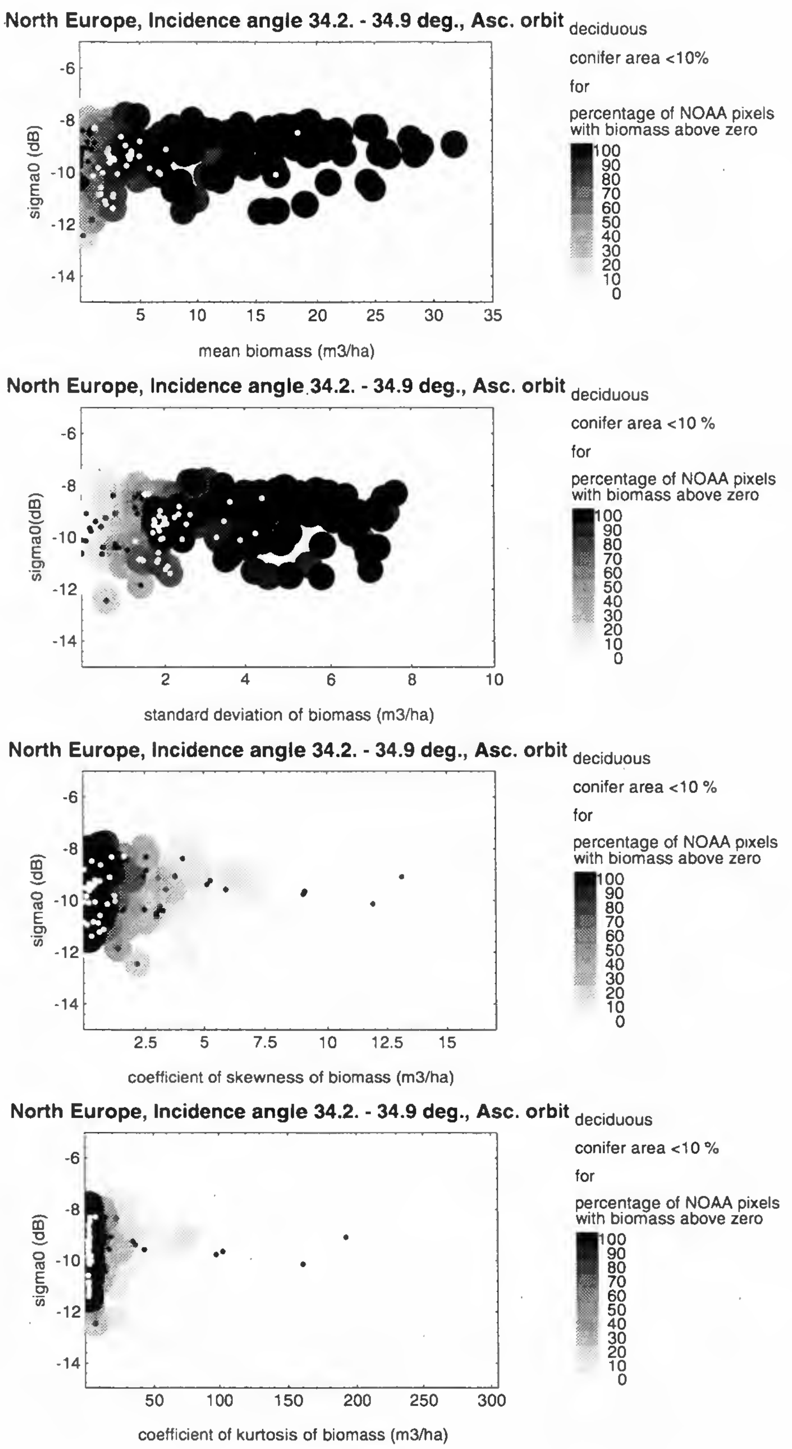

Figure 6.19. The relationship of the backscattered intensity and the mean, standard deviation, skewness and kurtosis coefficient values of the deciduous biomass in the scatterometer pixels in Northern Europe. The percentage of sub-pixels with nonzero coniferous biomass is below 10%. The graylevel of the markers indicate the percentage of sub-pixels with nonzero biomass. The points in the center of the markers show the values that correspond to a case of no coniferous biomass.

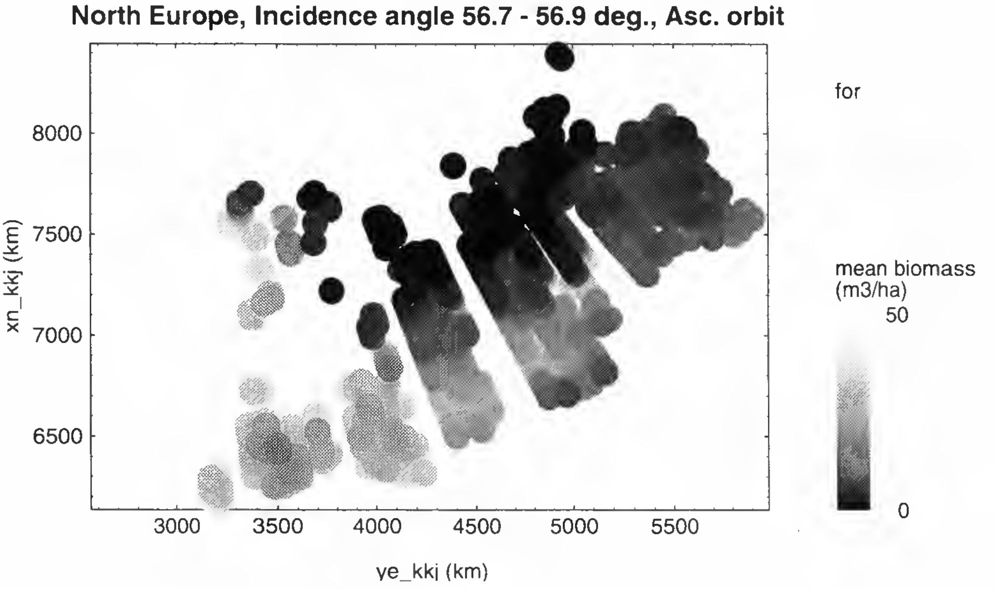

Figure 6.20. An example of the location of low biomass areas in the data set used. The coordinates used here are taken from the fore-beam data of incidence angles 56.7° - 56.9°. The points have been plotted in the order of decreasing biomass value. Mean biomass values greater than 50 m^3/ha are white.

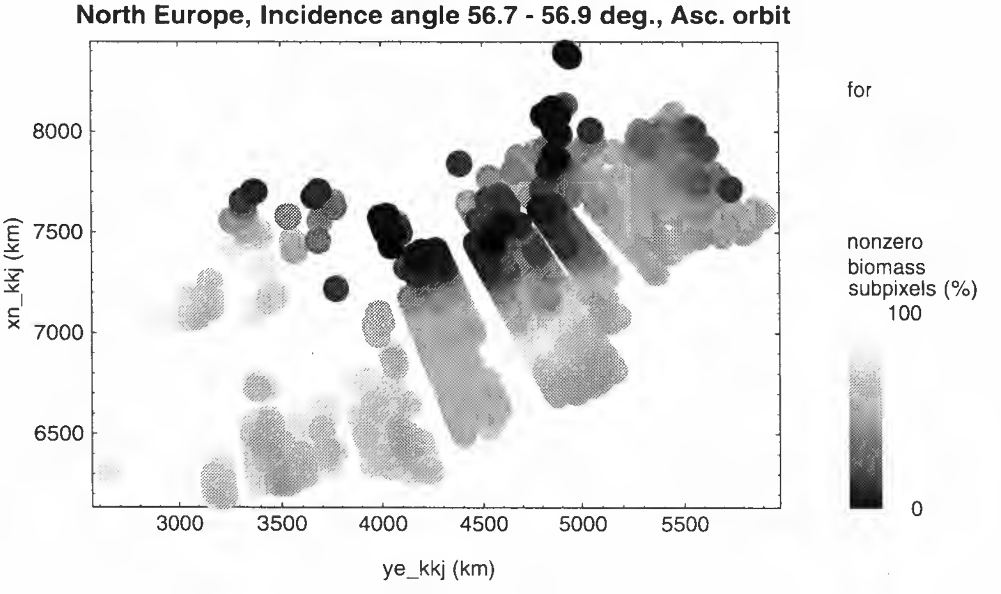

Figure 6.21. An example of the location of areas with a small percentage of nonzero biomass subpixels in scatterometer pixel in the data set used. The coordinates used here are taken from the fore-beam data of incidence angles 56.7° - 56.9°. The points have been plotted in the order of decreasing percentage of nonzero biomass subpixels.

The relationship between the mean biomass and the percentage of nonzero biomass subpixels is naturally monotonously positive, but the scatter is quite large (Figs. 6.22 - 6.23). The lowest backscattering values correspond to cases, when the mean biomass value is small and most of the subpixels have zero biomass (Fig. 6.22). These places are close to the coast or mining areas (Vorkuta). However, the highest backscattering values do not have a clear dependence on the mean biomass (Fig. 6.23, Figs. 6.14 - 6.17). The highest intensities corresponding to lowest biomass values were in this data set in the Ural mountains. This is understandable, since a rough surface topography increases backscattering. Precipitation and soil moisture also increase the backscattering *(Pulliainen 1994)*. Since no ground truth existed on the soil moisture of the whole Northern Europe, it is not possible to check its influence, but it is quite certain that during June 1993, it rained at least once in the whole Northern Europe. Thus at least some of the high intensities corresponding the low biomass values can be allocated to soil moisture and precipitation.

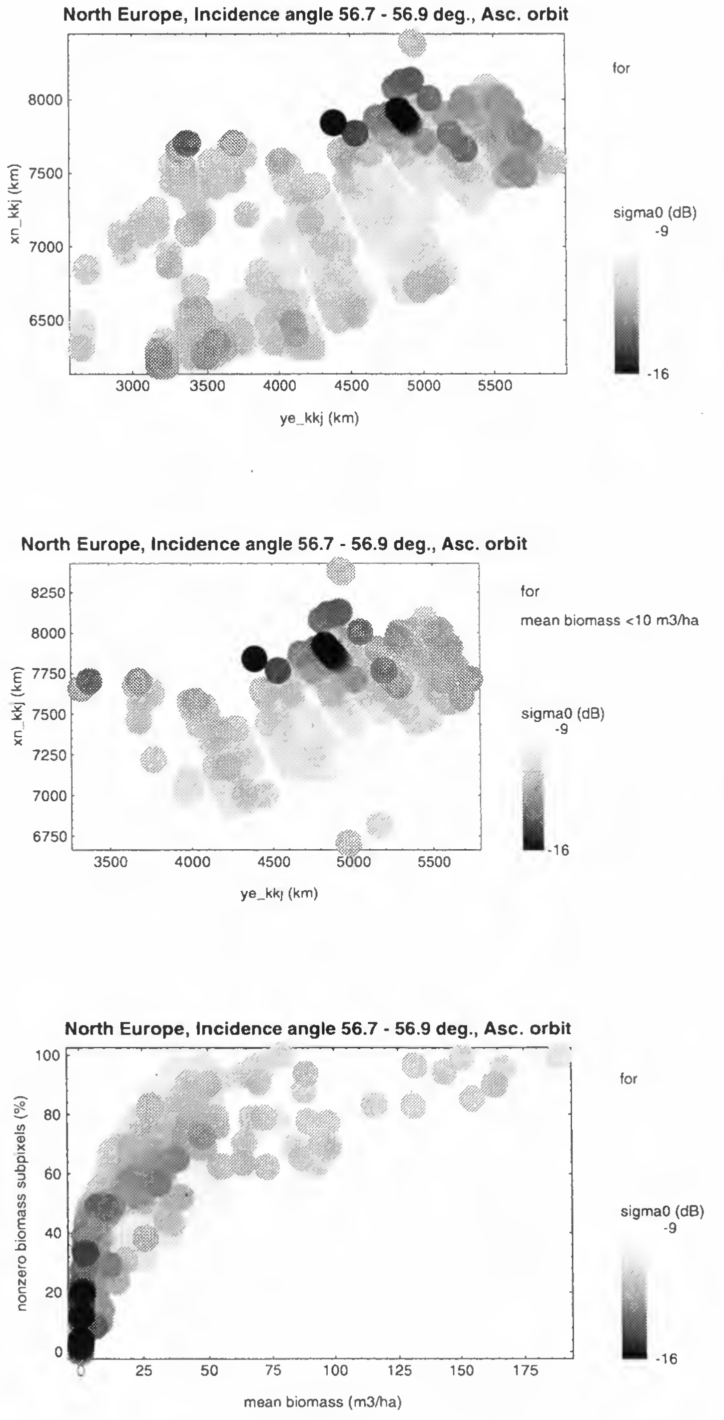

Figure 6.22. The areas of low backscattered intensities for all the data used and for low biomass cases. The relationship between the mean biomass, the percentage of nonzero biomass subpixels and the backscattered low intensities is also shown. The points are plotted in the order of decreasing intensity.

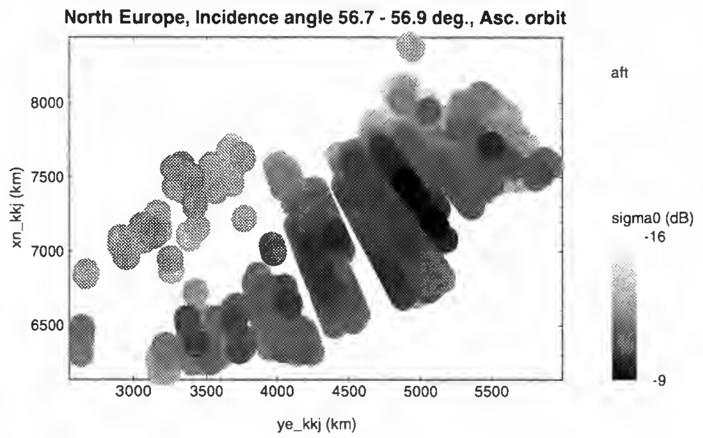

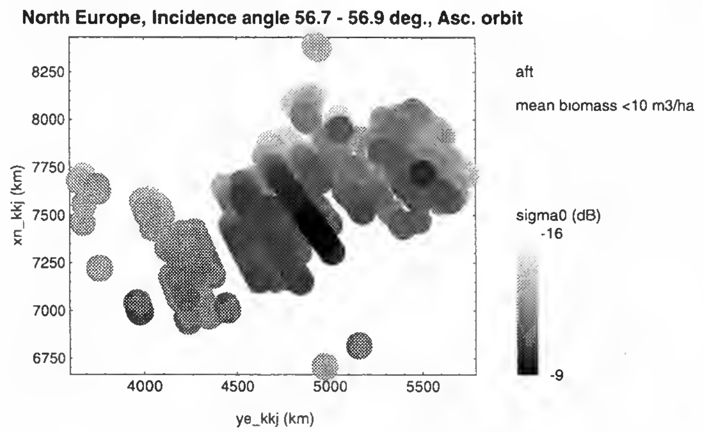

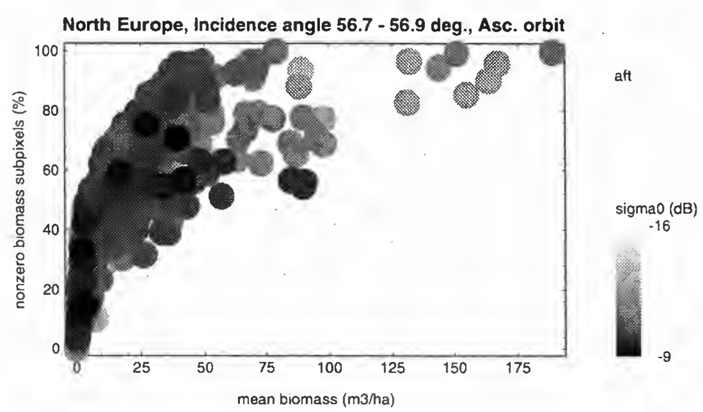

Figure 6.23. The areas of high backscattered intensities for all the data used and for low biomass cases. The relationship between the mean biomass, the percentage of nonzero biomass subpixels and the backscattered high intensities is also shown. The points are plotted in the order of increasing intensity.

6.3 Comparison of Wind Scatterometer Data with Model Predictions

The ERS-1 Wind Scatterometer measures each image cell with three separate antenna beams nearly simultaneously. Moreover, the angle of incidence is different for different antenna beams. Hence, it is possible to compare pixel-wise Wind Scatterometer measurements with the model predictions. This is shown in Figure 6.24 for a single grid cell (interpolated pixel) of the Porvoo test area. Figure 6.24 shows the measured values for different antenna beams and the model fittings. The semi-empirical backscattering model described in Section 4.1 has been fitted into the Wind Scatterometer data by choosing a soil moisture value that minimizes the mean squared difference between the model and data points (refer to Figure 4.3). The effects of water and land areas have been taken into account separately in the model (the total backscatter has been modeled as a sum of these two contributions). In land areas, the assumption has been that forest cover is homogeneous (the average stem volume value calculated for the total land area). The level of backscatter of water areas is evaluated from the σ^o values observed simultaneously for open sea. However, the fraction of water is small in the case of Figure 6.24: 2% in the pixel under study, and from 1 to 14% in its nine neighbouring pixels (grid cells).

The systematic (calibration) difference between the semi-empirical backscattering model and Wind Scatterometer data has been assumed to be 1.3 dB. This value was evaluated from the comparisons of ERS-1 SAR-based σ^o with the ERS-1 Wind Scatterometer-based σ^o values obtained for heavily forested areas at incidence angles from 20° to 30° (the systematic difference between ERS-1 SAR data and the semi-empirical backscattering model is known (*Pulliainen 1994*)). These two cases are shown in Figures 6.1 and 4.8. On the other hand, the calibration difference can be evaluated by analyzing the behavior of bias in the soil moisture estimation results. This aspect is discussed in Section 8.1.

The Porvoo test area grid cell (pixel # 293) for which the results of Figure 6.24 were determined has the following properties (in parenthesis are the range of these characteristics in neighbouring pixels):

- percentage of water areas: 2% (1% - 14%)
- percentage of forest areas: 61% (62% - 77%)
- percentage of field areas: 35% (17% - 28%)
- average forest stem volume in land areas: 67 m^3/ha (75 m^3/ha - 102 m^3/ha).

Figure 6.24 shows the model fittings for three occasions: 10 June, 6 July and 1 September 1993. The solid lines depict the model fittings including the contribution of water areas. Since the effect of water is separately considered for different antenna beams, each antenna beam has a slightly different behavior. Only the fitting obtained for mid-beam is depicted. The 1.3 dB calibration difference is summed to Wind Scatterometer data points. The soil moisture estimation discussed in Chapter 8 is conducted using the same method as in the case of Figure 6.24.

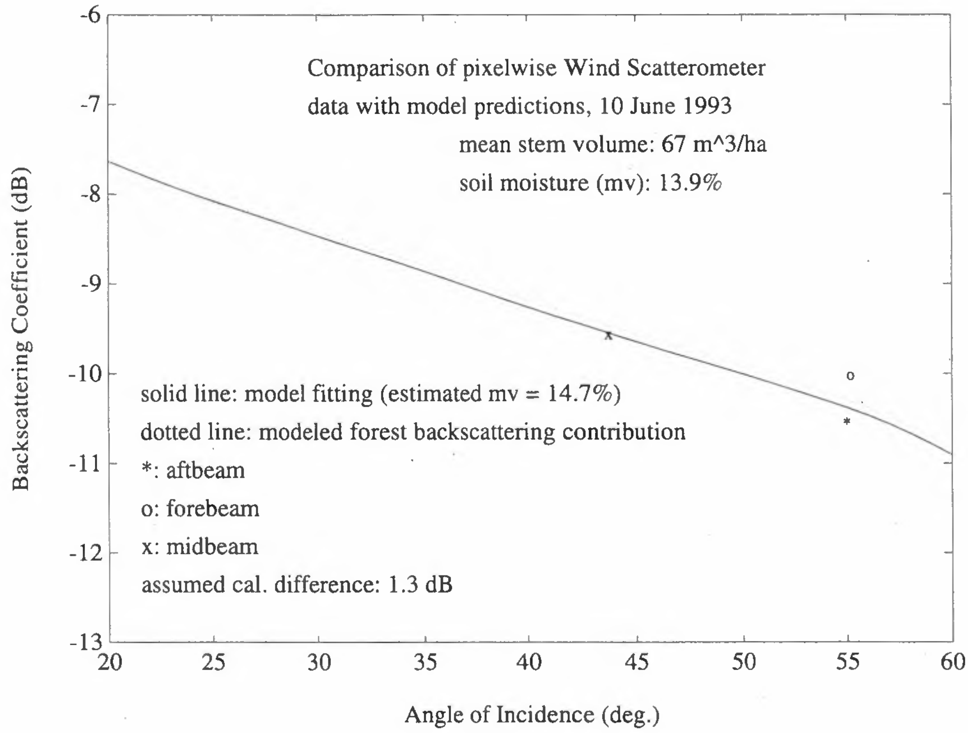

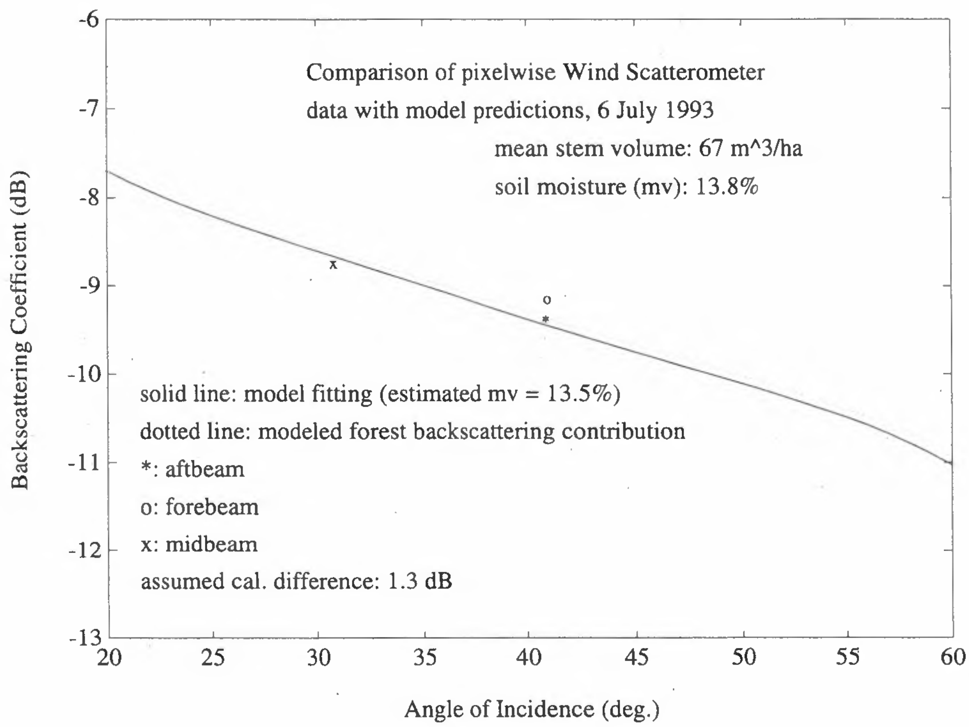

Figure 6.24. Comparison of pixel-wise ERS-1 Wind Scatterometer data with the semi-empirical forest backscattering model for three occasions (pixel # 293 of the Southern Finland test area). The third case is in the following page.

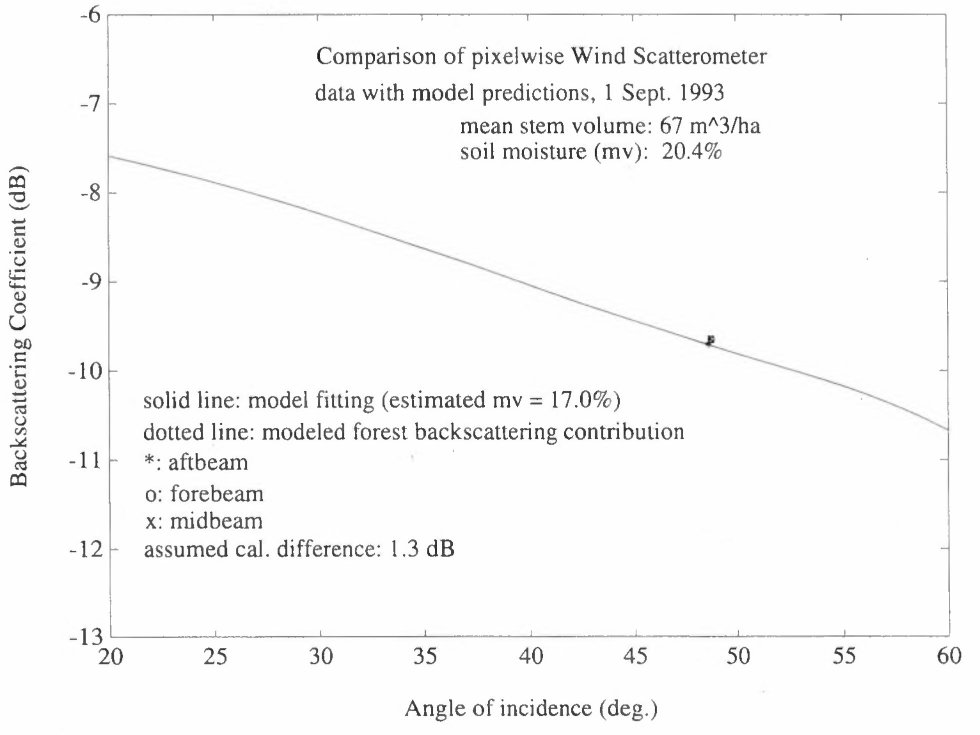

Figure 6.24 continued.

7 Behavior of SSM/I Data and Comparison with Model Predictions

7.1 Seasonal Behavior of SSM/I Data

Seasonal behavior of SSM/I data in Finnish test areas

The seasonal behaviour of SSM/I data for the Finnish test areas was investigated by plotting brightness temperature time series for a few test sites. This was conducted for the test sites in Northern and Southern Finland as well as for a test site located in the Baltic Sea. The results are presented in Figures 7.1 to 7.9.

Land test sites (Southern/Northern Finland)

Figures 7.1 to 7.3 show the seasonal behavior of SSM/I data for a test site in Southern Finland, and Figures 7.4 to 7.6 for a test site in Northern Finland. The decrease of brightness temperatures during winter (appearance of snow) is noticeable for all channels. For southern test sites, the decrease is approximately 20K, 40K and 40K for the 19, 37 and 85 GHz channels, respectively. However, the simultaneous decrease in the physical temperature has to be eliminated in order to unveil the effect of snow cover. It must also be noted that a part of the drop in the 85 GHz level is due to a dry and cold season, thus decreasing the atmospheric contribution to apparent brightness temperatures.

The most evident difference between Northern and Southern Finland results is the length of the snow period, which is usually few months longer in Northern Finland.

Baltic Sea test site

Figures 7.7 to 7.9 which show the seasonal behaviour for a sea ice test site, clearly manage to demonstrate the differences between the various polarizations and the relationship between the used frequency and the apparent brightness temperature.

The 19 GHz channels give the proportionally largest response to increasing fraction of sea ice which is demonstrated when ice has started to appear in the middle of December. The response is saturated approximately to 70K for vertical polarization and to 100K for horizontal polarization. For the 37 GHz channels, the response is slightly smaller, although the apparent brightness temperature still increases with 40K and 80K, vertical and horizontal polarizations, respectively.

For the 85 GHz channels, such a behaviour in the brightness temperature as a function of appearing ice is not as easily detectable. No actual change can be noticed for the vertical polarization, but the temporal variations for the horizontal channel seem to decrease when ice is present, and the brightness temperature level also seems to increase slightly, approximately 20K. This is probably due to the fact that the fraction of water (waves) is decreasing.

As the measured apparent temperature of the SSM/I is composed of surface and atmosphere related contributions, it is also clear that the atmospheric effects are more disturbing at higher frequency channels (such as 85 GHz). As a lower atmospheric transmissivity leads to a greater contribution from the atmosphere, the effect of the instable atmosphere on 85 GHz measurements is proportionally greater than on 19 or 37 GHz measurements. This is also a reason for the larger variation in the 85 GHz brightness temperatures in Figure 7.9 and a probable reason for the relatively weak response to appearing ice.

Figures 7.7, 7.8 and 7.9 also demonstrate the fact that vertically polarized channels are less affected by wind conditions at the incidence angle of the SSM/I.

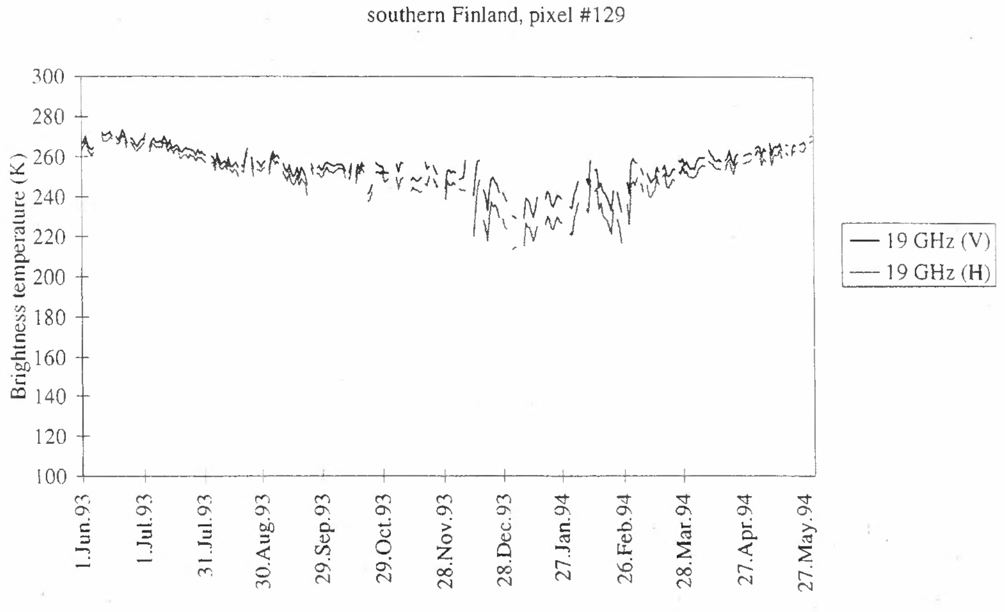

Figure 7.1. The seasonal behaviour of SSM/I data for a test site located in Southern Finland (pixel # 129). Both 19 GHz channels (vertical and horizontal) are included.

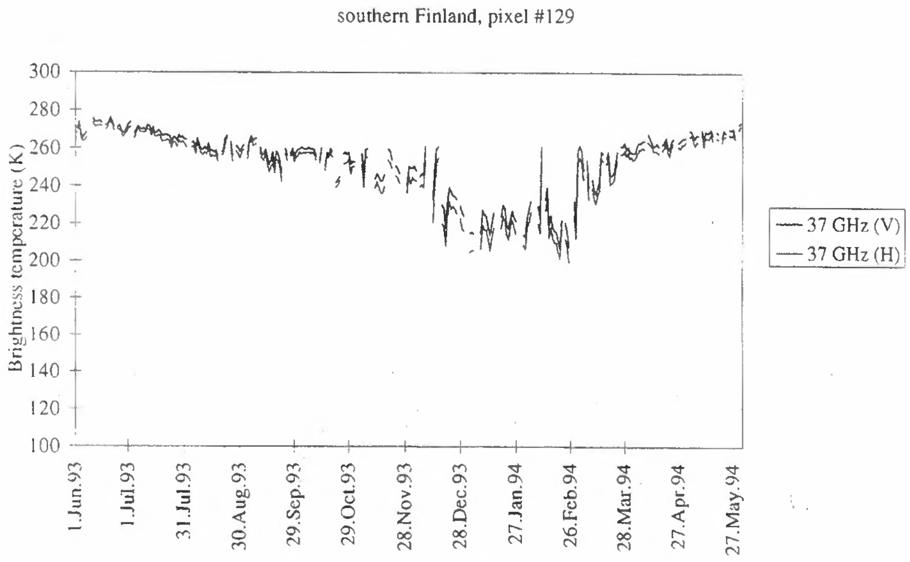

Figure 7.2. The seasonal behaviour of SSM/I data for a test site located in Southern Finland (pixel # 129). Both 37 GHz channels (vertical and horizontal) are included.

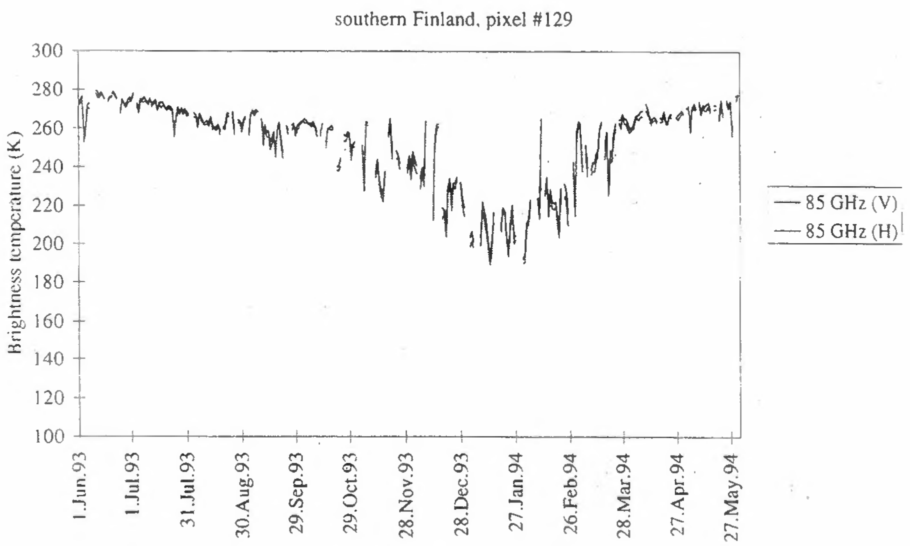

Figure 7.3. The seasonal behaviour of SSM/I data for a test site located in Southern Finland (pixel # 129). Both 85 GHz channels (vertical and horizontal) are included.

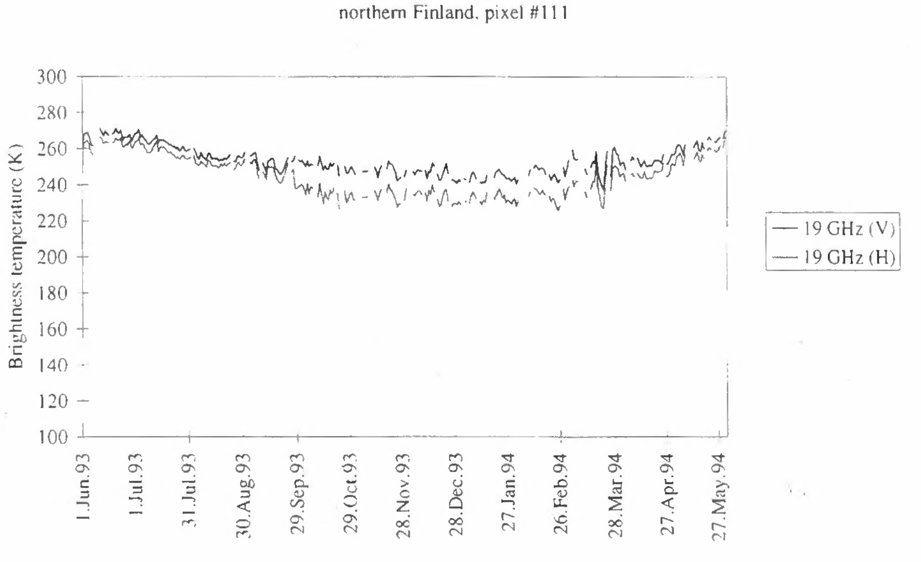

Figure 7.4. The seasonal behaviour of SSM/I data for a test site located in Northern Finland (pixel # 111). Both 19 GHz channels (vertical and horizontal) are included.

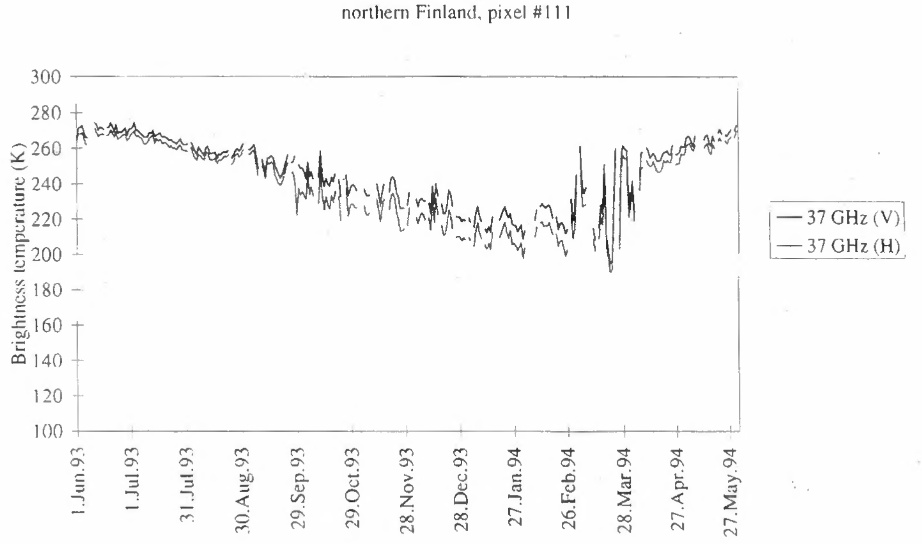

Figure 7.5. The seasonal behaviour of SSM/I data for a test site located in Northern Finland (pixel # 111). Both 37 GHz channels (vertical and horizontal) are included.

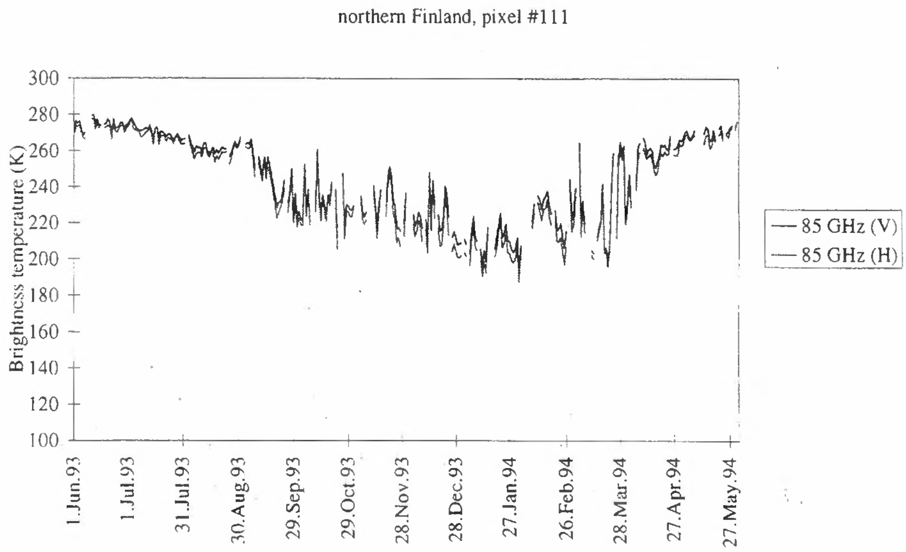

Figure 7.6. The seasonal behaviour of SSM/I data for a test site located in Northern Finland (pixel # 111). Both 85 GHz channels (vertical and horizontal) are included.

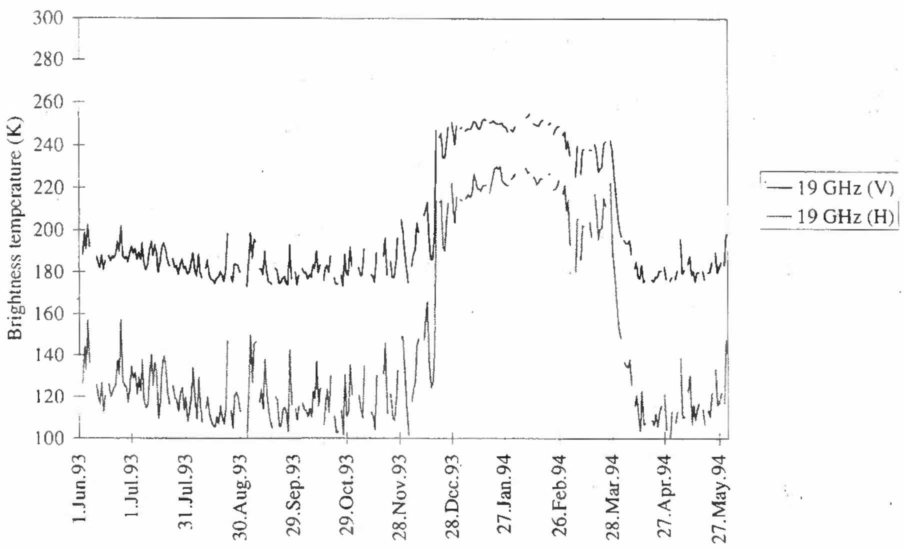

Figure 7.7. The seasonal behaviour of SSM/I data for a test site located in the Baltic Sea (pixel # 364). Both 19 GHz channels (vertical and horizontal) are included.

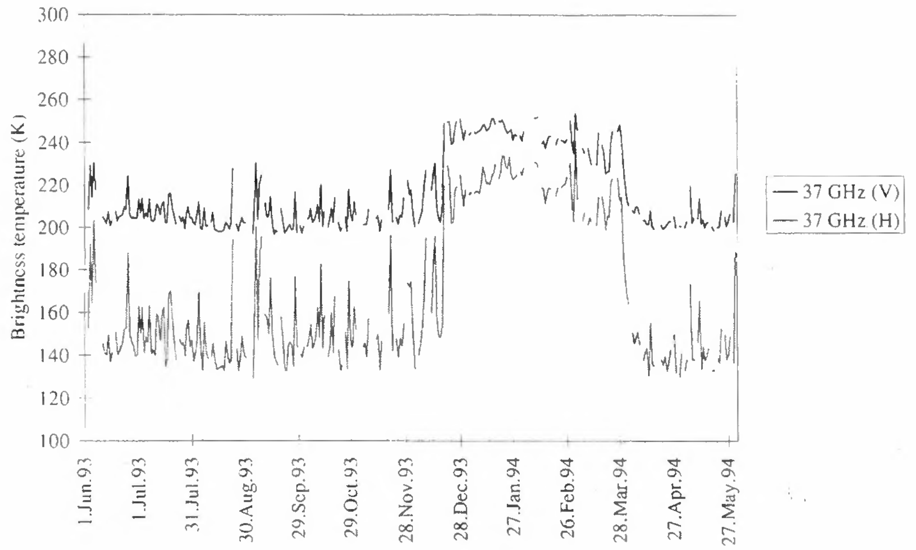

Figure 7.8. The seasonal behaviour of SSM/I data for a test site located in the Baltic Sea (pixel # 364). Both 37 GHz channels (vertical and horizontal) are included.

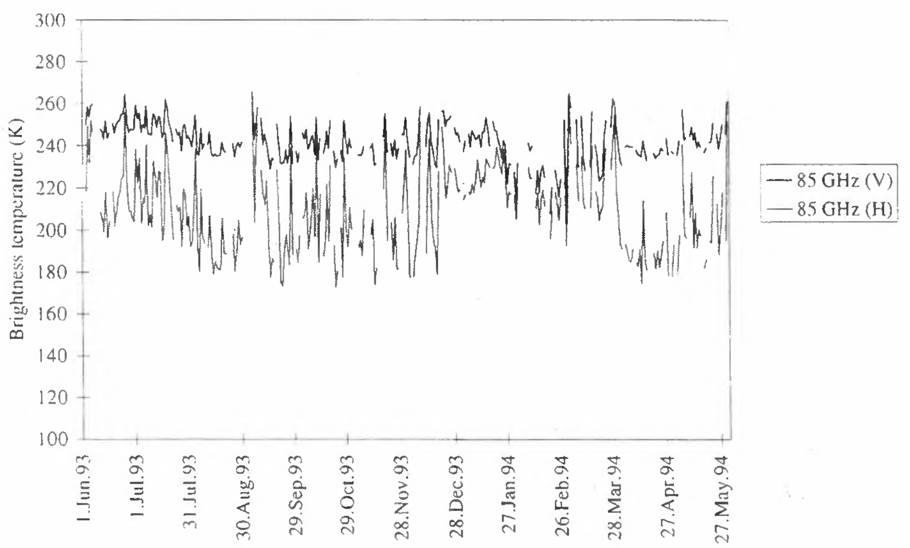

Figure 7.9. The seasonal behaviour of SSM/I data for a test site located in the Baltic Sea (pixel # 364). Both 85 GHz channels (vertical and horizontal) are included.

Seasonal behavior of SSM/I data in African test areas

Figures 7.10 - 7.13 show the observed correlation between the two-day cumulative precipitation and the apparent emissivity in the African test area. The results are shown for all SSM/I channels using night/morning measurements. The results are determined for three land use categories: tropical forest, grassland (savanna) and desert. The apparent emissivity e_{ap} presented in the figures is the atmospherically uncorrected emissivity:

$$e_{ap} = \frac{T_b}{T_{phys}}, \tag{7.1}$$

where

T_b = brightness temperature for a certain channel measured by the SSM/I instrument

T_{ap} = ground-based physical temperature (air temperature at the height of 2 m).

The results in Figures 7.10 - 7.13 are determined for a one year period (from July 1993 to June 1994). Each data point represents a daily average of e_{ap} for a large land area of a certain land use category. The sizes of land areas used in averaging are roughly:

desert area: 400 km by 400 km,
grassland area: 300 km by 400 km,
forest area: 2000 km by 400 km.

Figures 7.14 - 7.16 show that the apparent emissivity is quite insensitive to precipitation for all land use categories and for all channels. The results obtained also show that the apparent emissivity (evidently as well the true surface emissivity) of a certain land use category has a relatively constant value throughout the year. However, the brightness temperature measured by the SSM/I instrument appear to be highly correlated with the physical temperature (air temperature at ground level). The results also show that the vegetated areas can be distinguished from unvegetated areas in the case of H polarized 19 and 37 GHz channels (this was observed only in the case of night/morning time results, not in the case of day time measurements).

Figures 7.14 - 7.16 show the seasonal behavior of polarization ratio for 19 GHz and 37 GHz channels using the night/morning measurements. The polarization ratio PR is defined as

$$PR = \frac{T_{b,V} - T_{b,H}}{T_{b,V} + T_{b,H}}, \tag{7.2}$$

where

$T_{b,V}$ = brightness temperature for a certain frequency at vertical polarization

$T_{b,H}$ = brightness temperature for a certain frequency at horizontal polarization.

A clear conclusion from Figures 7.14, 7.15 and 7.16 is that the polarization ratio of 19 GHz and 37 GHz channels can be used for land use classification. Especially in the case of 19 GHz, the three different land use categories are well distinguishable through a time period from January to June. The 85 GHz channels appear to be quite useless also for that application also.

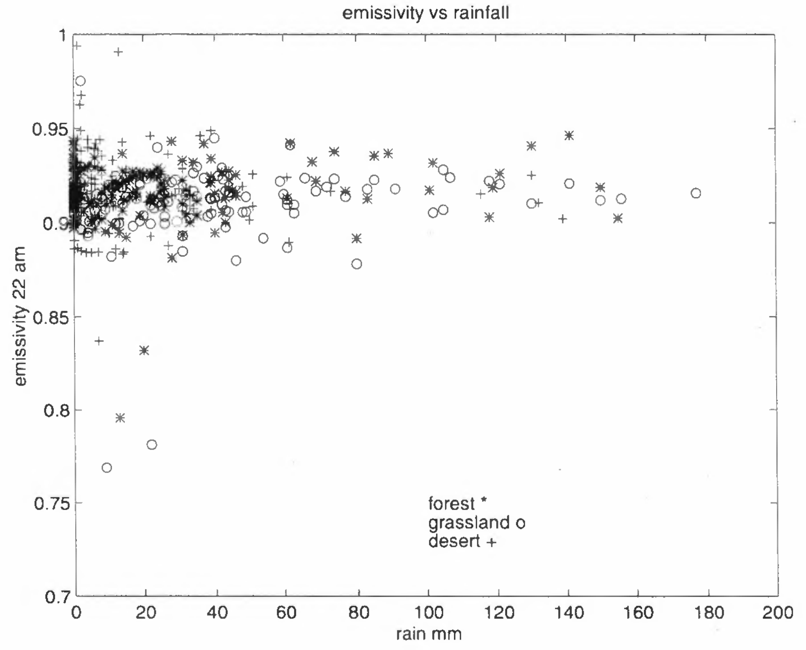

Figure 7.10. Apparent emissivity in African test areas as a function of two-day cumulative precipitation at 22 GHz. The results are shown for different land-use categories.

(a)

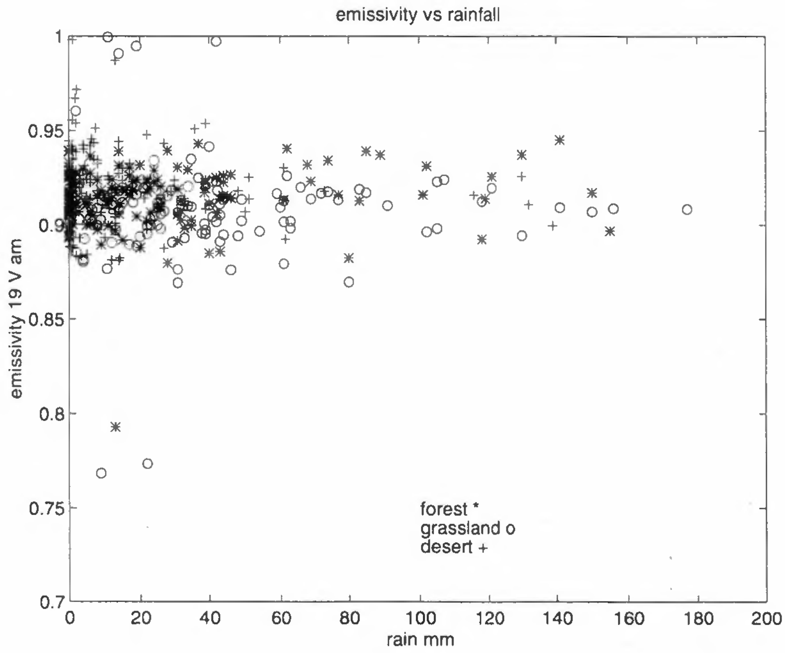

(b)

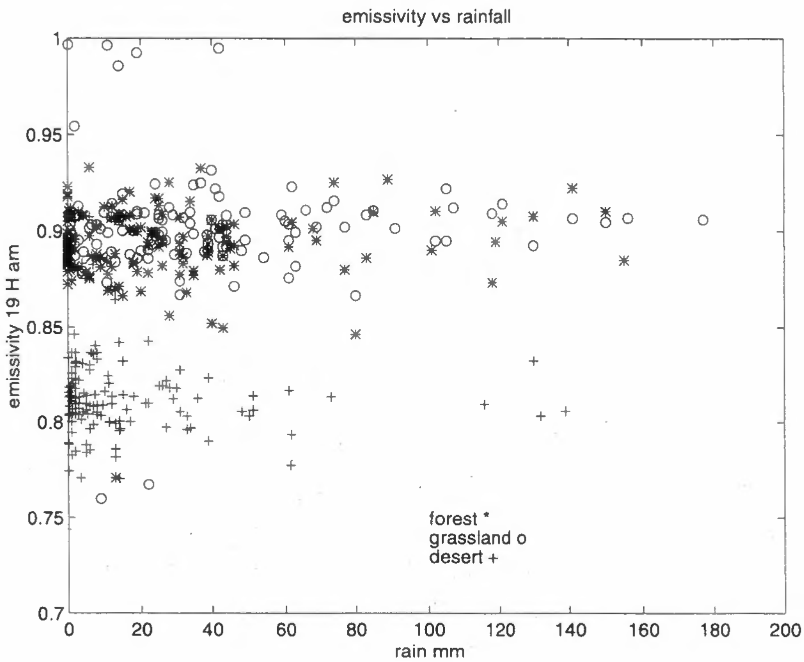

Figure 7.11. Apparent emissivity in African test areas as a function of two-day cumulative precipitation at 19 GHz. The results are shown for different land-use categories.
(a): results for vertical polarization.
(b): results for horizontal polarization.

(a)

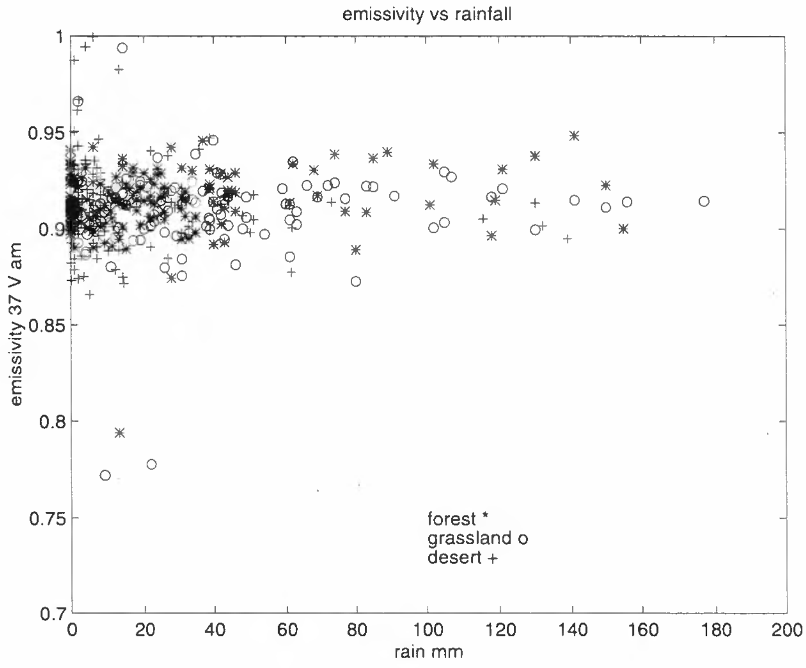

(b)

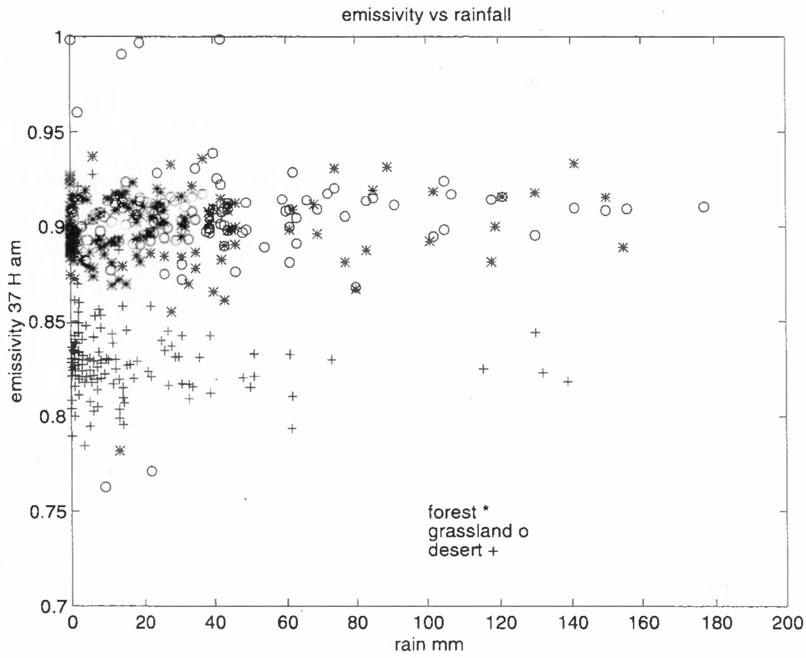

Figure 7.12. Apparent emissivity in African test areas as a function of two-day cumulative precipitation at 37 GHz. The results are shown for different land-use categories.
(a): results for vertical polarization.
(b): results for horizontal polarization.

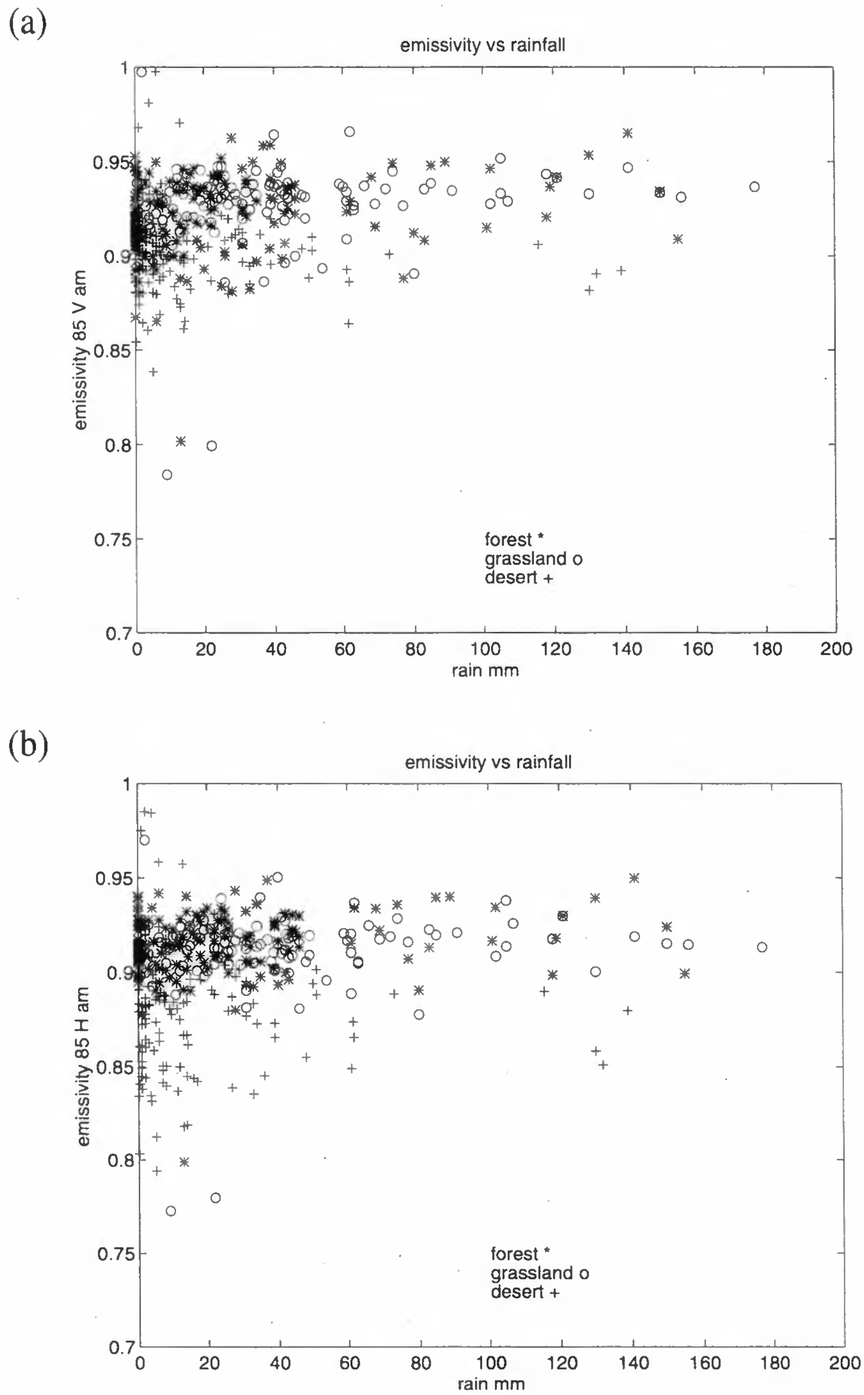

Figure 7.13. Apparent emissivity in African test areas as a function of two-day cumulative precipitation at 37 GHz. The results are shown for different land-use categories.
(a): results for vertical polarization.
(b): results for horizontal polarization.

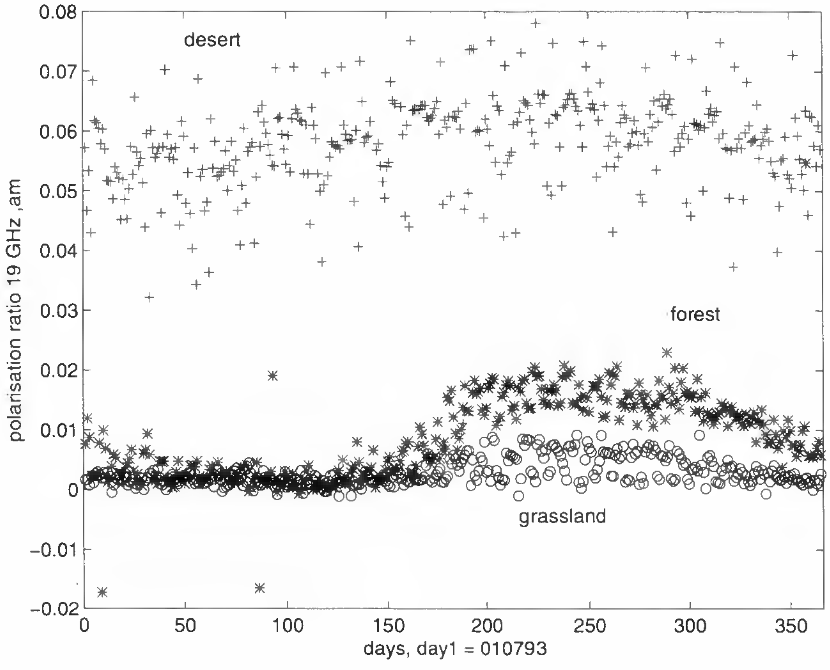

Figure 7.14. Seasonal behavior of polarization ratio (V-H)/(V+H) at 19 GHz.

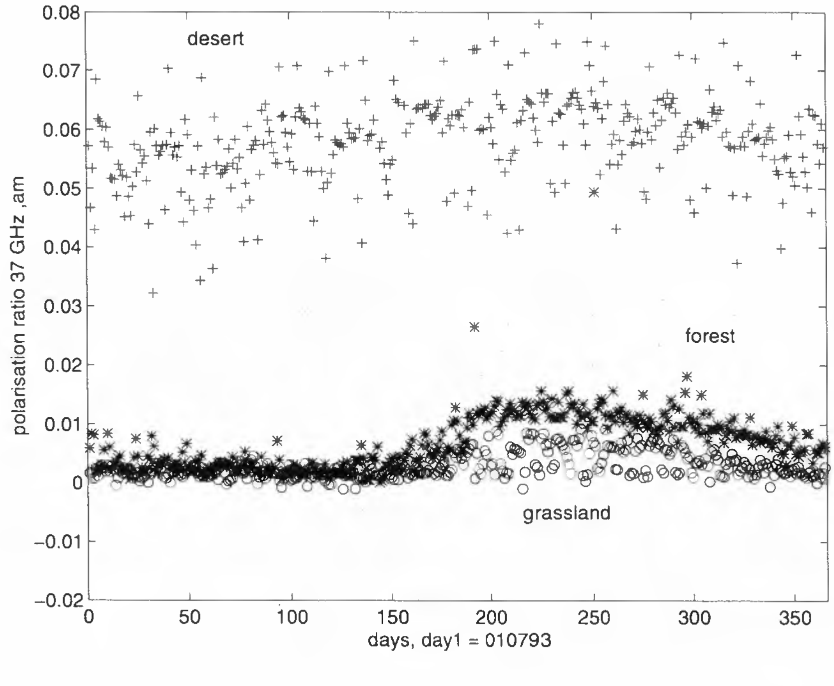

Figure 7.15. Seasonal behavior of polarization ratio (V-H)/(V+H) at 37 GHz.

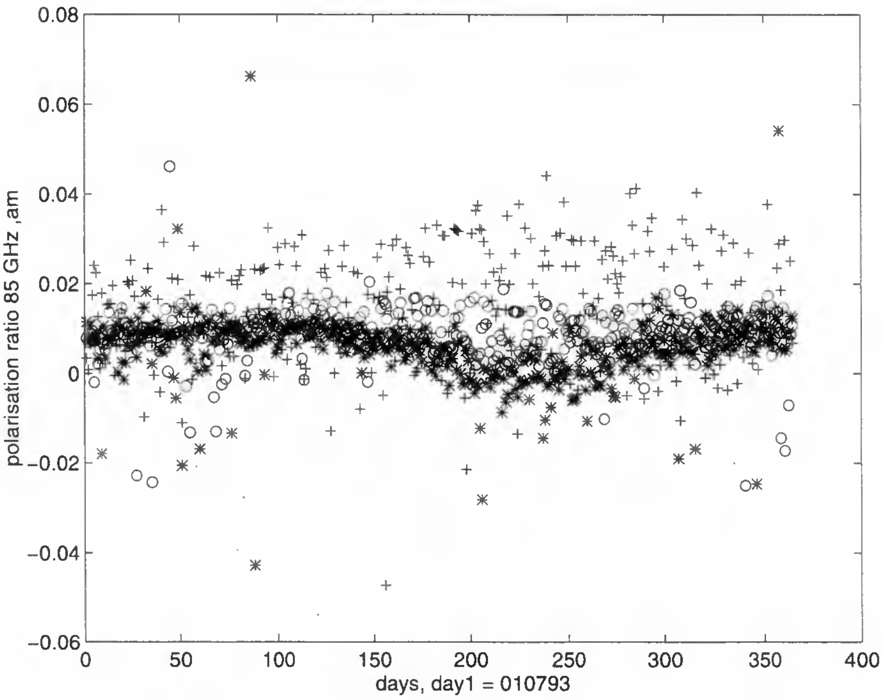

Figure 7.16. Seasonal behavior of polarization ratio (V-H)/(V+H) at 85 GHz.

7.2 Effects of Various Target Characteristics on SSM/I Data

<u>Variations caused by weather conditions during snow free conditions</u>

The sensitivity of microwave emission to atmospheric moisture (water vapour) increases rapidly with increasing frequency, and weather related disturbances have been found to be severe at the higher SSM/I channels (85 GHz vertical and horizontal). These effects may be demonstrated by time series similar to those presented in Section 7.1. In order to unveil the atmospheric effects, the apparent emissivities (Equation (7.1)) observed by the instrument have been calculated by using the average temperature data for the individual test sites acquired from the Finnish Meteorological Institute. The resulting emissivities for 19 GHz (V/H) and 85 GHz (V/H) for a southern test site are presented in Figures 7.17 and 7.18. The test site employed (grid cell #330 of the South Finland test area) consists of forests (69%), agricultural areas (22%) and lakes (7%).

The Figures show that for those time periods, in which the 19 GHz emissivities are quite stable (snow free periods, unfrozen ground), the 85 GHz emissivities show disturbances caused by atmospheric instability. During a shorter period from the middle of January 1994 to the end of March 1994 there is a great drop in the apparent emissivity of the 85 GHz channels (Figure 7.18). This is due to a very cold period, resulting in a dry atmosphere and a consequent drop in the atmospheric component of the apparent brightness temperature. It is evident that some atmospheric correction procedures are needed in order to use the 85 GHz data.

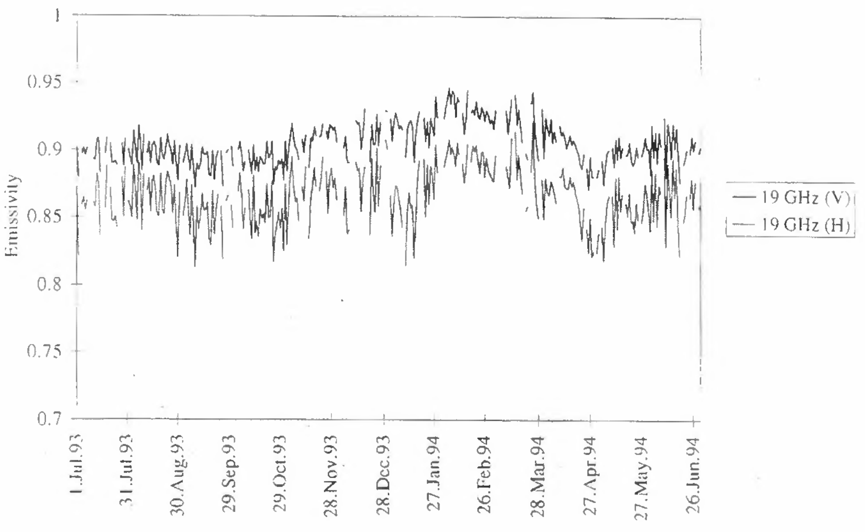

Figure 7.17. The apparent emissivities for 19 GHz channels (vertical and horizontal polarization). The test site is located in Southern Finland (pixel # 330). The emissivities have been calculated by using the average temperature data for the pixel.

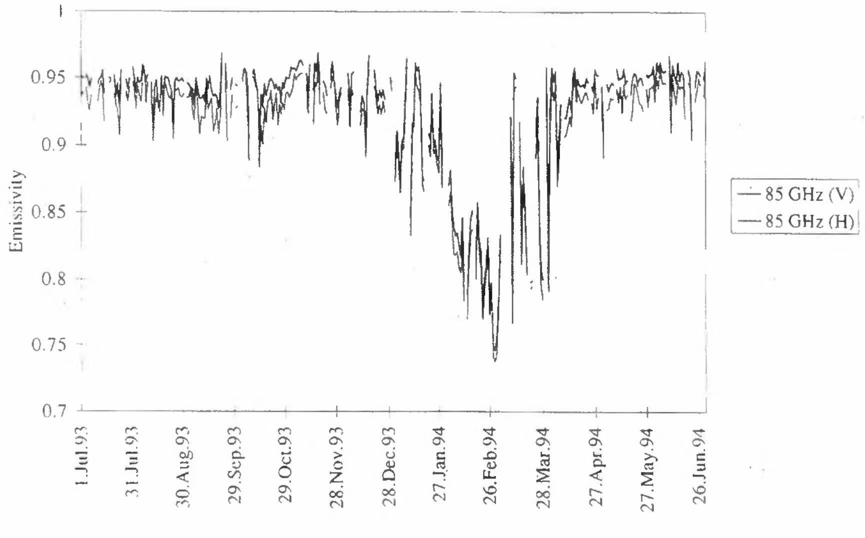

Figure 7.18. The apparent emissivities for 85 GHz channels (vertical and horizontal polarization). The test site is located in Southern Finland (pixel # 330). The emissivities been calculated by using the average temperature data for the pixel.

Effects of snow cover and soil freezing

Snow cover

As Finland is mostly heavily forested (average forest coverage 66 %), is it difficult to find an area of 25 km x 25 km consisting mostly of open areas, if open waters (lakes) are excluded. In order to study the effect of accumulating snow cover, an area located right outside the coast of northern Finland (near the city of Oulu) was chosen. This area is during winter time mostly covered by thick level ice (solid ice up to 100 cm), and the ice situation does usually not change in this area before the end of May. As the winter of 1993-1994 was colder than usual, this course of action was acceptable.

The temperature data (diurnal average temperatures) for Oulu were used in order to calculate the apparent emissivity of the test site. The results are presented in Figure 7.19 for the 19 GHz channels, in Figure 7.20 for the 37 GHz channels and in Figure 7.21 for the 85 GHz channels.

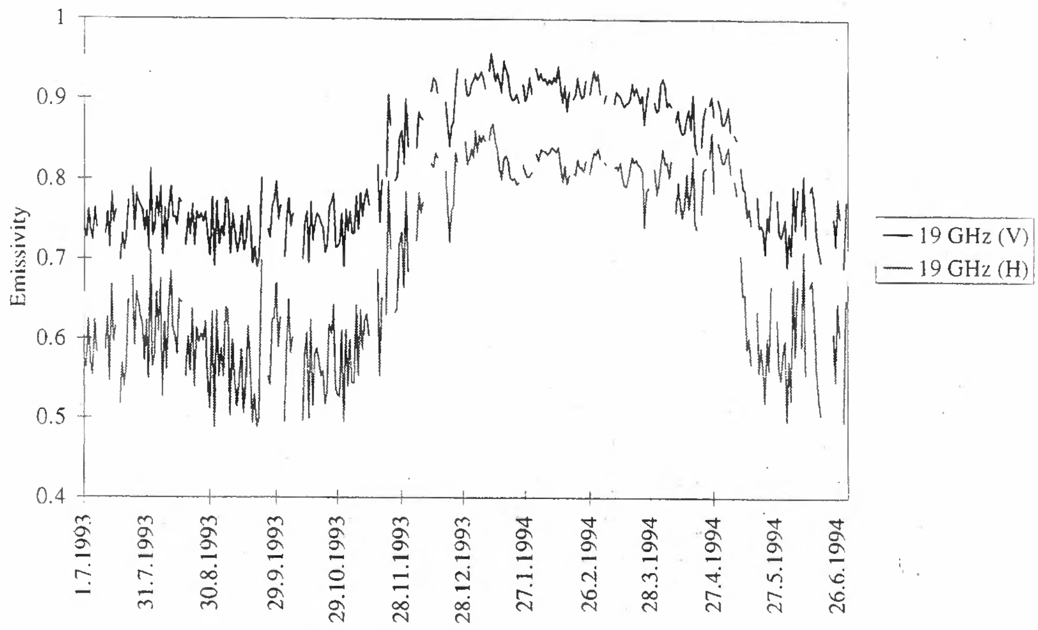

Figure 7.19. The apparent emissivity right outside the coastline of Northern Finland. The results for 19 GHz channels (vertical and horizontal) are included.

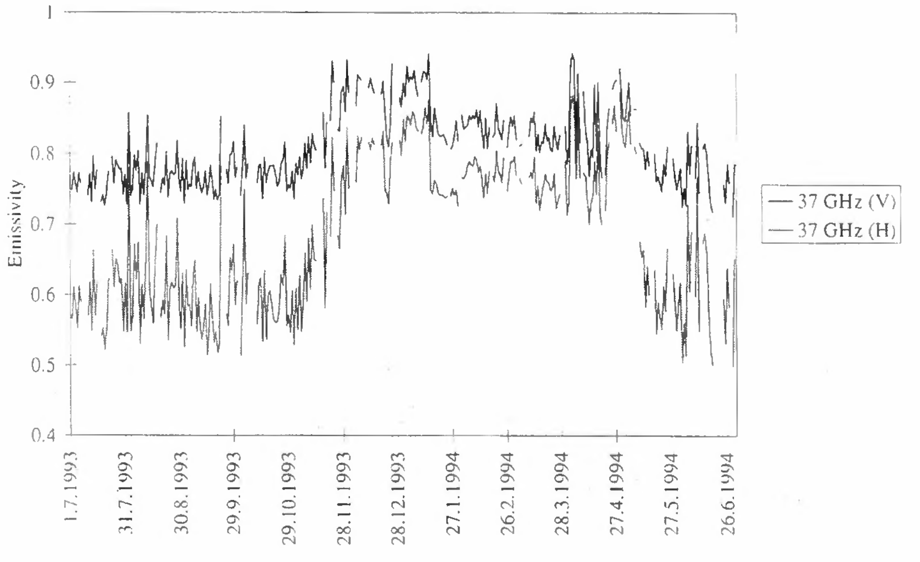

Figure 7.20. The apparent emissivity right outside the coastline of Northern Finland. The results for 37 GHz channels (vertical and horizontal) are included.

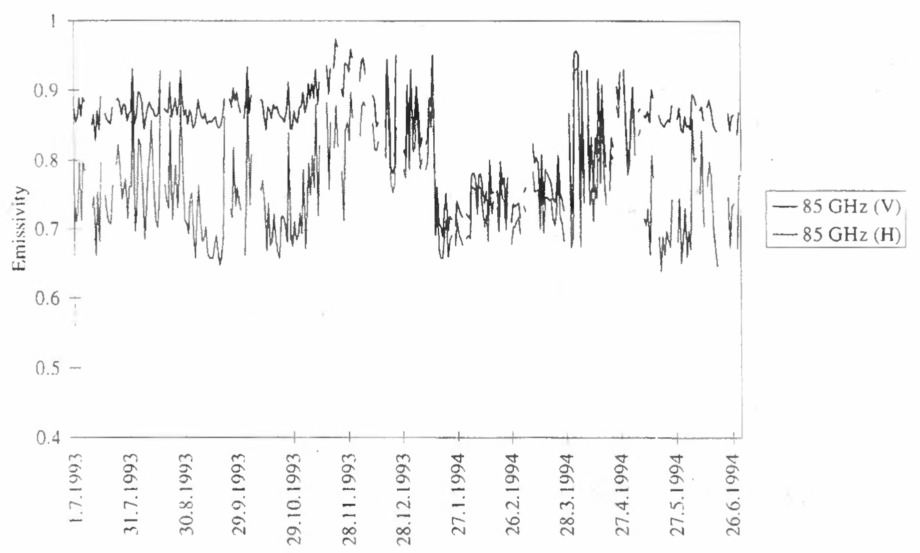

Figure 7.21. The apparent emissivity right outside the coastline of Northern Finland. The results for 85 GHz channels (vertical and horizontal) are included.

Soil freezing

It has been previously reported that soil freezing is clearly detectable from passive microwave signatures (*Mätzler 1994*). The cold winter of 1993-1994 leads to slight problems when soil freezing is investigated. The period of frozen ground, but without a snow cover is usually very short. This period should be extracted from the time series data.

Figures 7.22 to 7.26 show the seasonal response for a test area in southern Finland, with the emissivities calculated from average diurnal temperatures. The first figures (Figure 7.22 and 7.23) show the seasonal response for the whole one year period, and in the second pair of figures (Figures 7.25 and 7.26) the period showing the soil freezing juncture has been extracted from Figures 7.22 and 7.23. The average diurnal temperature for the test site is shown in Figure 7.24.

The results show that there may occur a slight increase in the emissivity values when soil freezing has taken place, although the increase is not as large as that reported in (*Mätzler 1994*) (approximately +0.05 in emissivity values). This is probably due to the fact that the test sites employed in this study represent heavily forested areas.

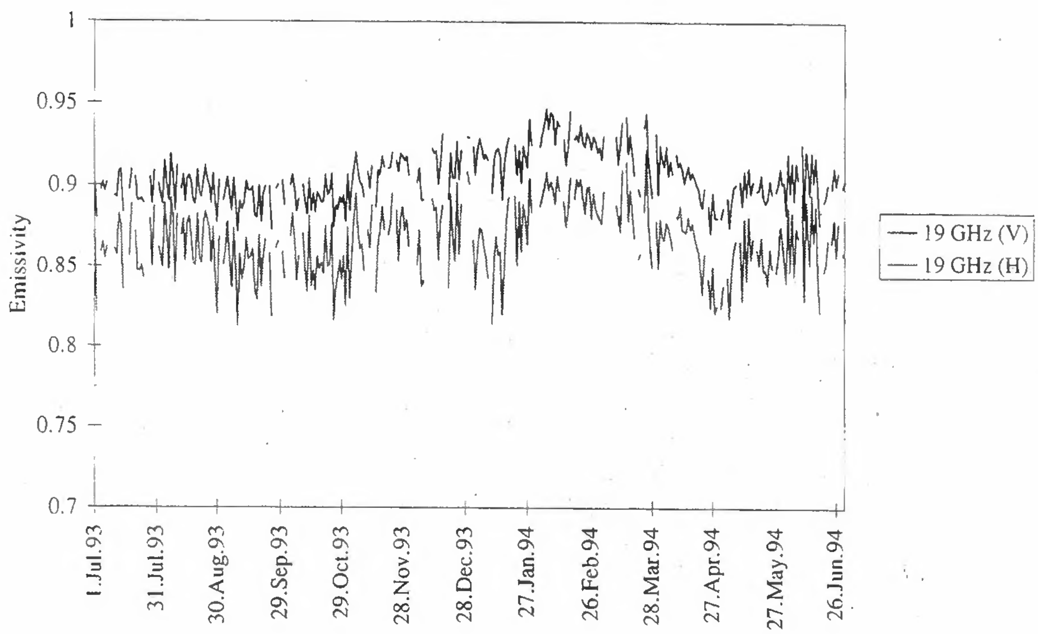

Figure 7.22. Seasonal response for a southern test site (pixel #330), showing the apparent emissivities calculated using average diurnal temperature data. Both 19 GHz channels are included.

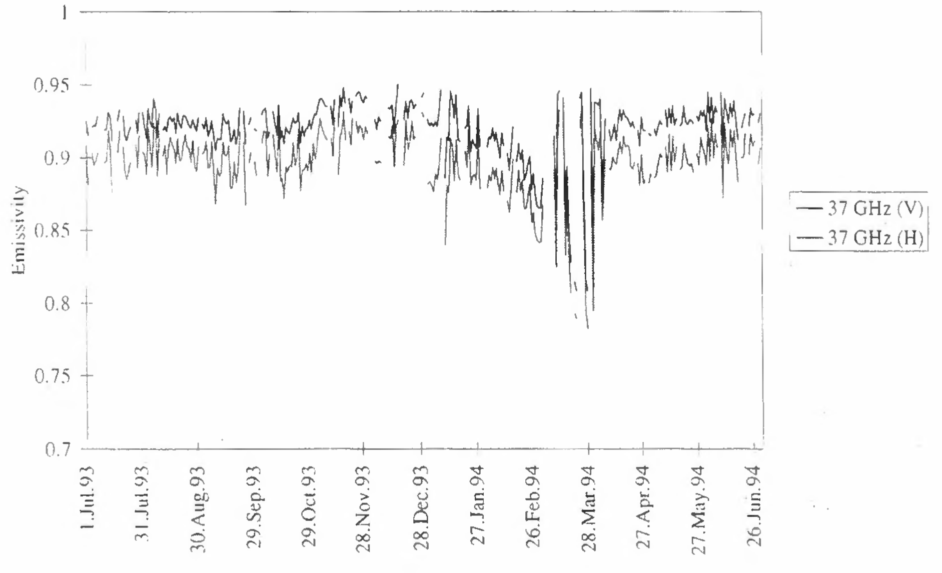

Figure 7.23. Seasonal response for a southern test site (pixel #330), showing the apparent emissivities at 37 GHz calculated using average diurnal temperature data.

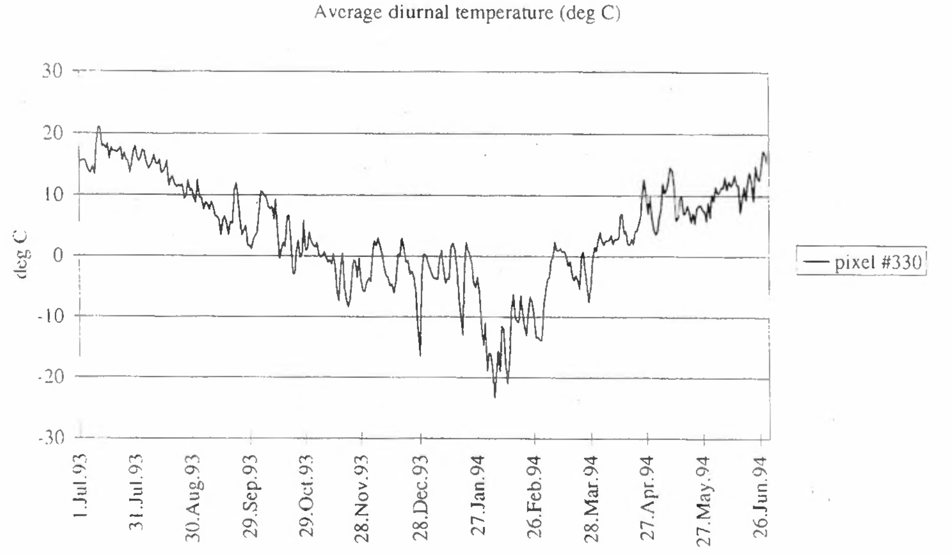

Figure 7.24. Average diurnal temperatures for test site #330 (Southern Finland).

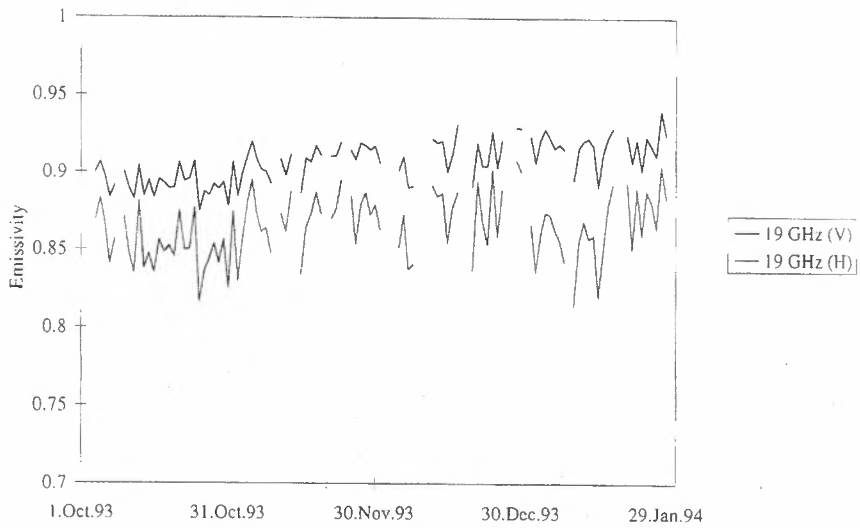

Figure 7.25. Seasonal response for a southern test site (pixel #330), showing the apparent emissivities calculated using average diurnal temperature data. The period with soil freezing occurring has been extracted from Figure 7.22. Both 19 GHz channels are included.

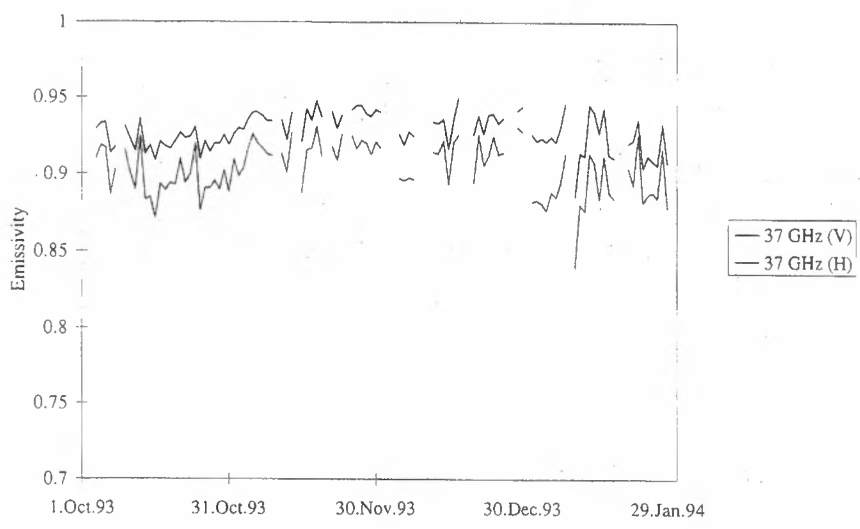

Figure 7.26. Seasonal response for a southern test site (pixel #330), showing the apparent emissivities calculated using average diurnal temperature data. The period with soil freezing occurring has been extracted from Figure 7.23. Both 37 GHz channels are included.

Effect of different land use categories

The effect of different land use categories on the seasonal response was investigated by using the digital land use data available for the study. Using this reference information, all test sites (pixels) falling in a certain land use category could be picked up and grouped together. The main categories of interest were the forested areas, of which three groups were formed according to their forest cover percentage: 25-50%, 50-75% and 75-100%. A few representative days of the study period of 1993-1994 were selected for the seasonal response study. This was conducted separately for the northern and southern main test sites (500 km x 500 km).

The results are presented in Figures 7.27 to 7.35. Only the results for northern test sites have been included as the results for northern vs. southern test sites are highly analogious. For each time period and forest cover percentage group represented, there are three figures included (19, 37 and 85 GHz channels).

The results show that the increasing forest coverage seems to increase the measured brightness temperature for all SSM/I channels. For example, for the 19 GHz channels, the increase from the 25-50% to 75-100% category during a snow free measurement (9 July 1993) is approximately 15 K. It can be also noted from the figures that appearance of snow decreases the measured brightness temperature for the 37 GHz channels, which is, of course, expected due to increased level of scatter.

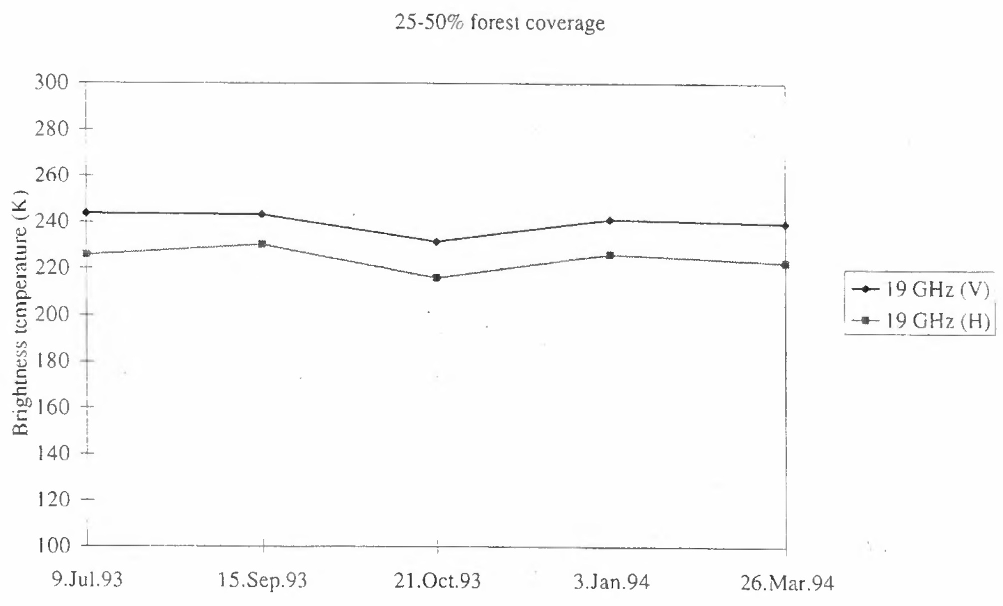

Figure 7.27. Seasonal response of the 19 GHz channels for all North Finland test area pixels with a forest coverage of 25-50%.

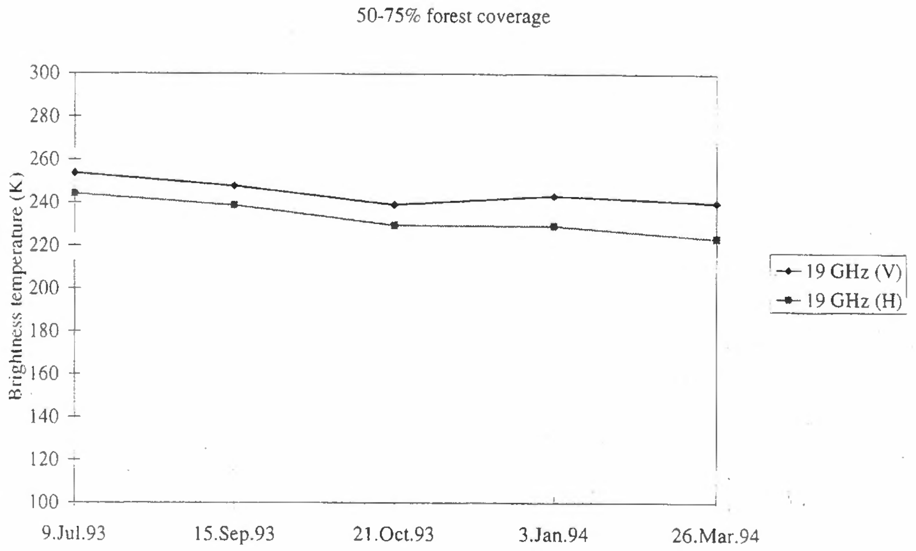

Figure 7.28. Seasonal response of the 19 GHz channels for all North Finland test area pixels with a forest coverage of 50-75%.

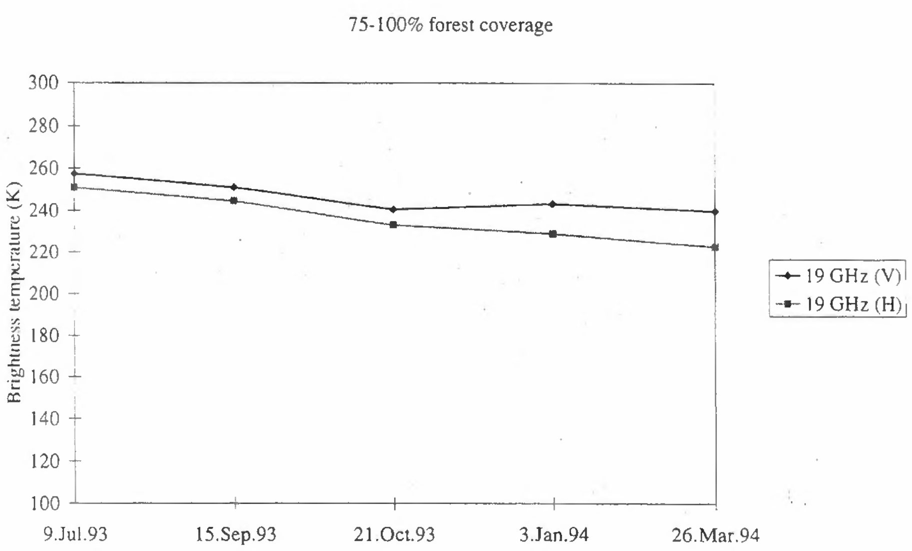

Figure 7.29. Seasonal response of the 19 GHz channels for all North Finland test area pixels with a forest coverage of 75-100%.

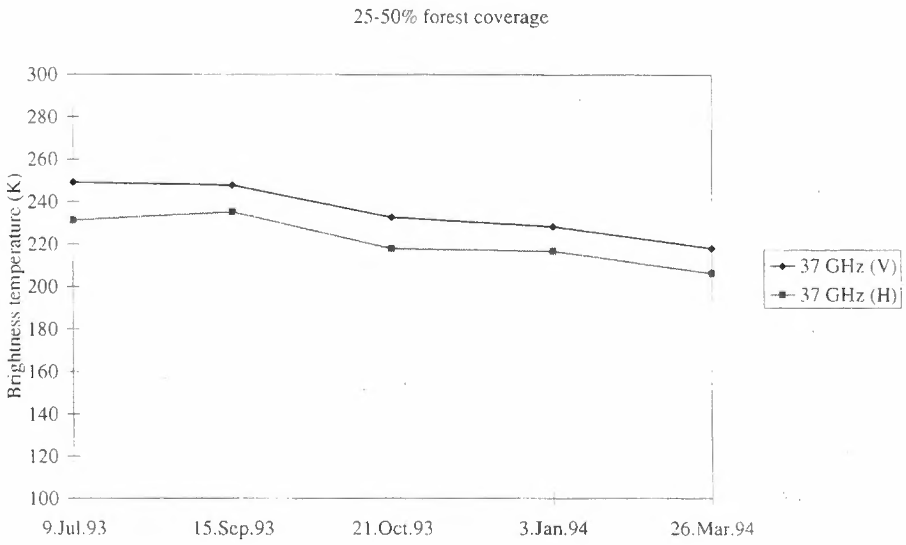

Figure 7.30. Seasonal response of the 37 GHz channels for all North Finland test area pixels with a forest coverage of 25-50%.

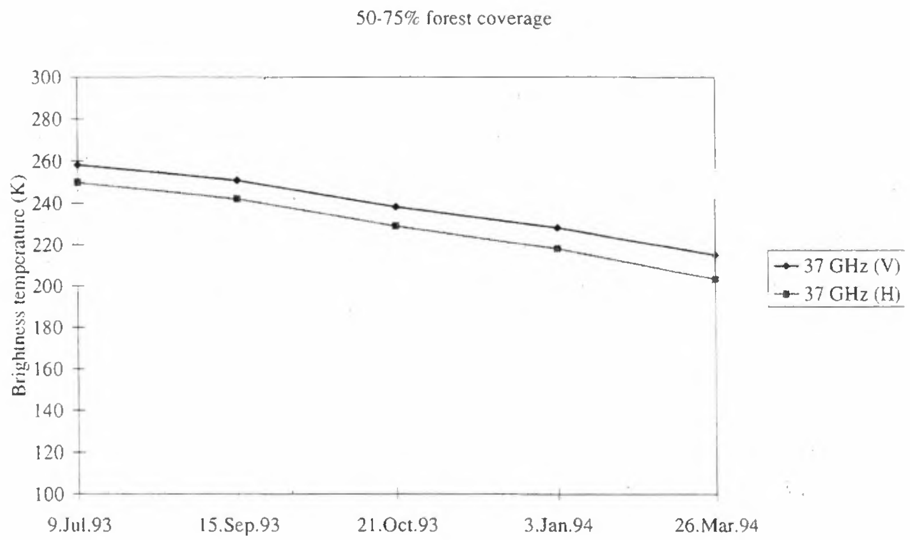

Figure 7.31. Seasonal response of the 37 GHz channels for all North Finland test area pixels with a forest coverage of 50-75%.

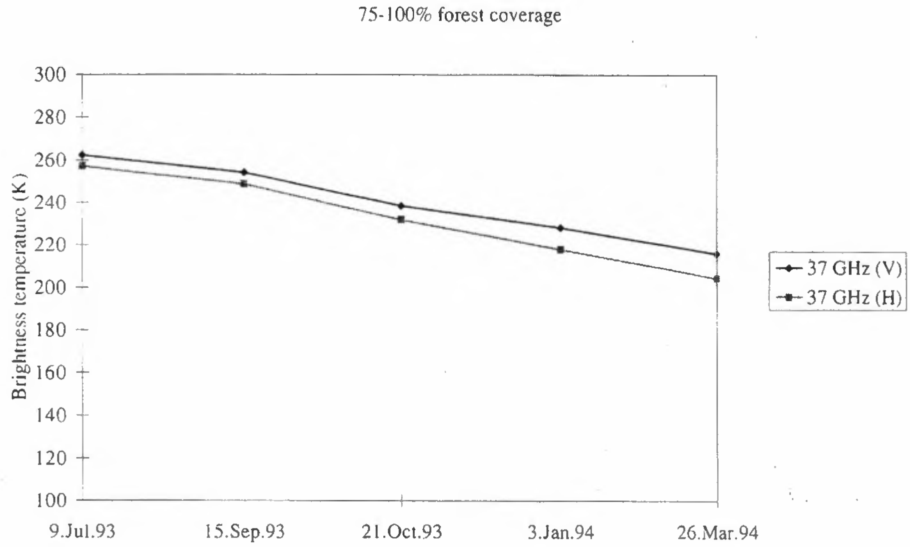

Figure 7.32. Seasonal response of the 37 GHz channels for all North Finland test area pixels with a forest coverage of 75-100%.

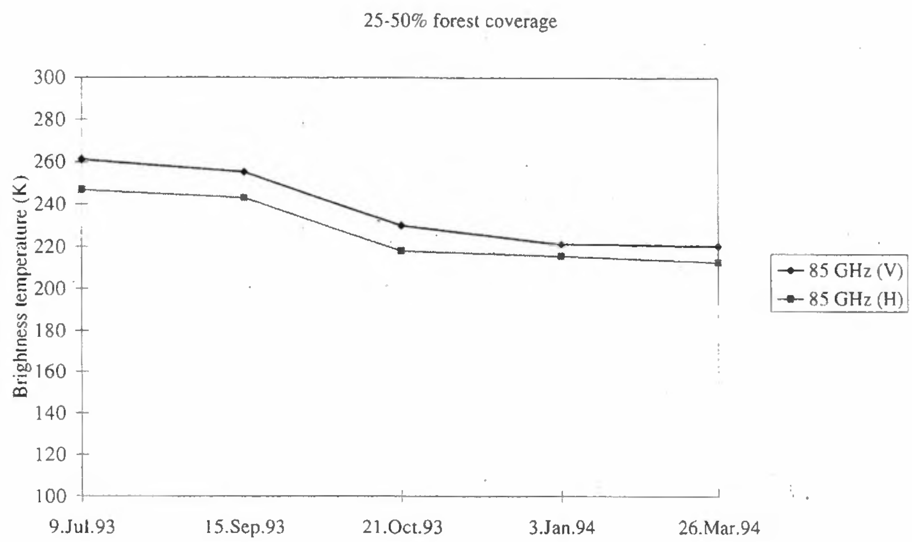

Figure 7.33. Seasonal response of the 85 GHz channels for all North Finland test area pixels with a forest coverage of 25-50%.

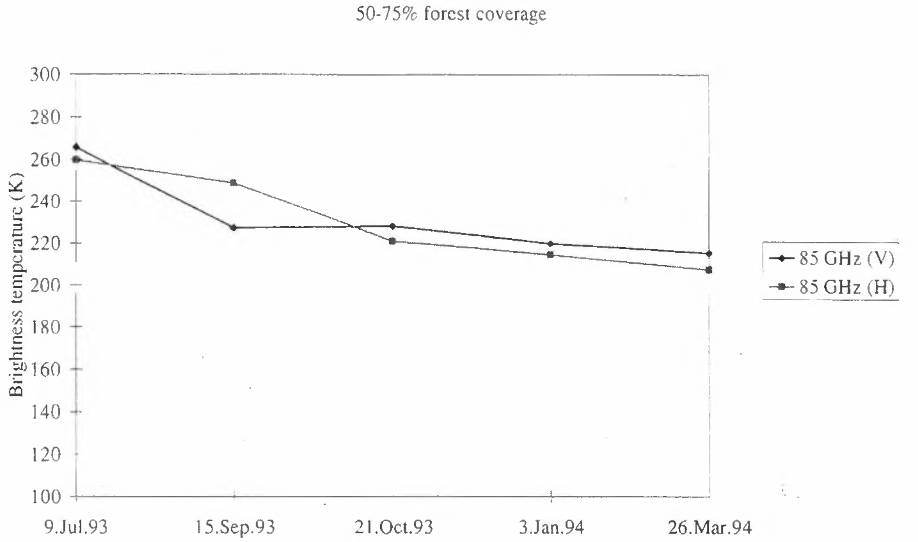

Figure 7.34. Seasonal response of the 85 GHz channels for all North Finland test area pixels with a forest coverage of 50-75%.

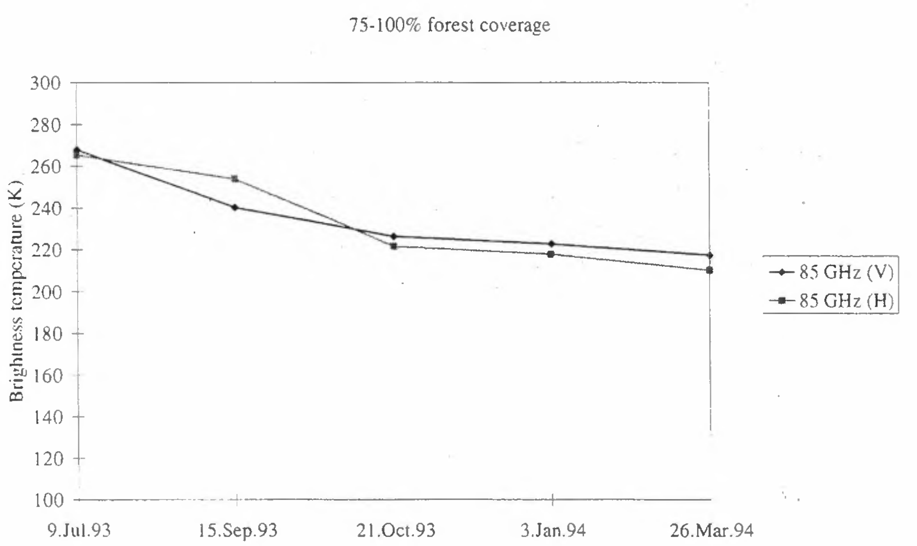

Figure 7.35. Seasonal response of the 85 GHz channels for all North Finland test area pixels with a forest coverage of 75-100%.

Response to forest biomass

A similar approach as in the previous section was used, but the land types were divided in two groups according to their average forest biomass (0-50 m^3/ha and 50-100 m^3/ha). Since the individual test sites are rather large (25 km x 25 km) it is impossible to get a large variance in forest biomass. With airborne measurements it is possible to carefully choose small test sites with homogeneous land types. Even test sites with a forest biomass from 150 up to 300 m^3/ha have been used for these measurements (*Kurvonen 1994*). The results obtained in these investigations are discussed in detail in Section 7.3.

The results are presented in Figures 7.36 to 7.41, with two forest biomass categories included for each SSM/I channel.

The obtained results show that there is no notable change in the brightness temperatures between the two forest biomass categories (0-50m^3 and 50-100m^3) during different seasonal conditions (summer, fall, early winter, mid-winter). This is partially explained by the large and thus inhomogeneous test sites, even if average forest biomass values have been used.

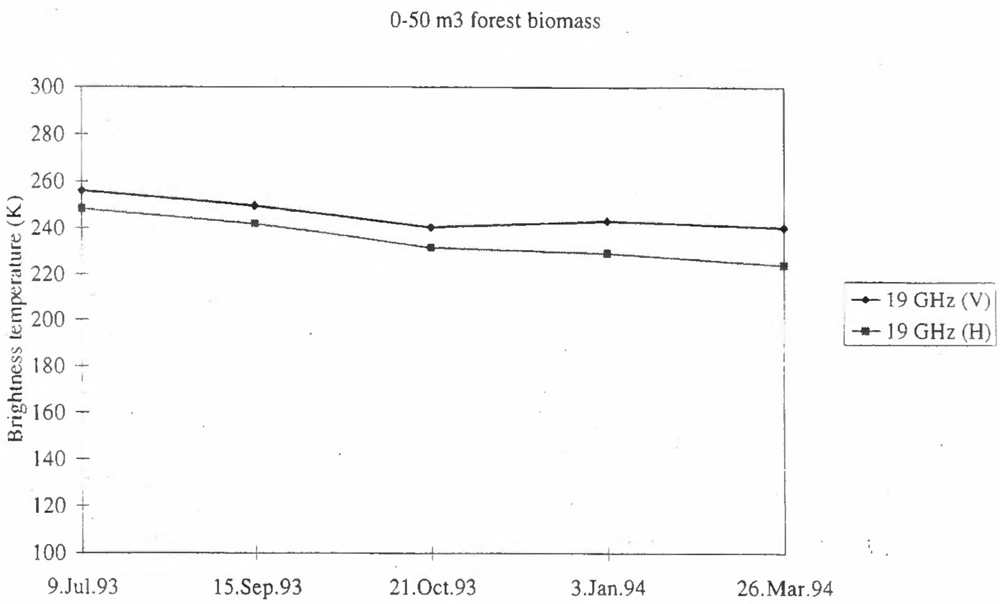

Figure 7.36. Seasonal response of the 19 GHz channels for areas with a forest biomass of 0-50 m^3/ha.

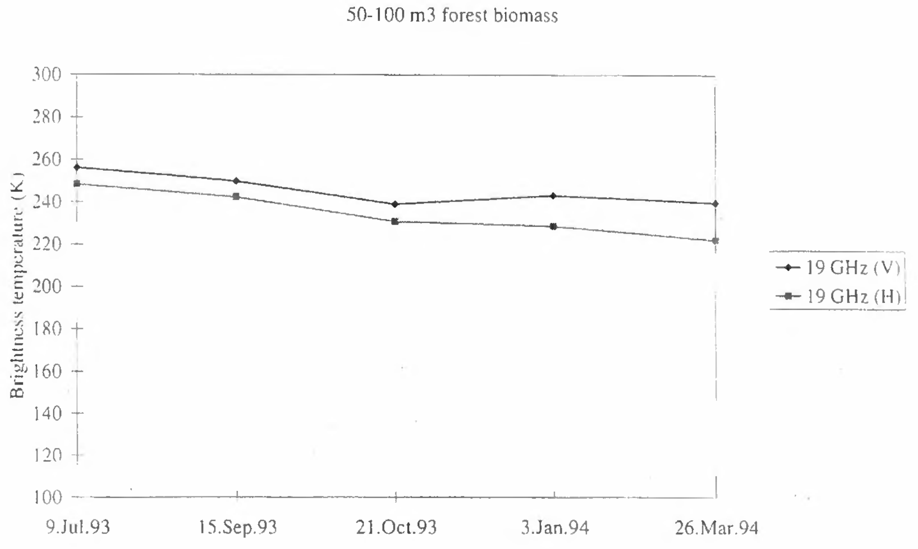

Figure 7.37. Seasonal response of the 19 GHz channels for areas with a forest biomass of 50-100 m^3/ha.

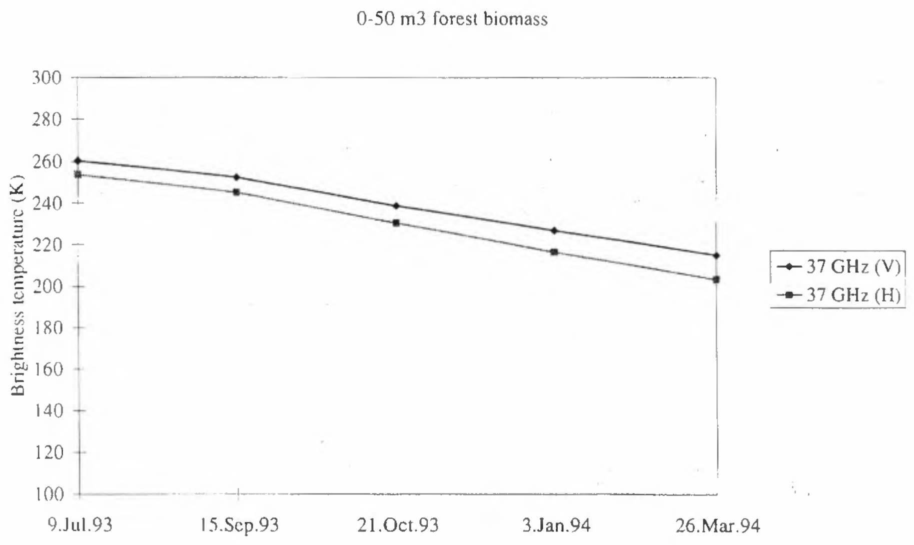

Figure 7.38. Seasonal response of the 37 GHz channels for areas with a forest biomass of 0-50 m^3/ha.

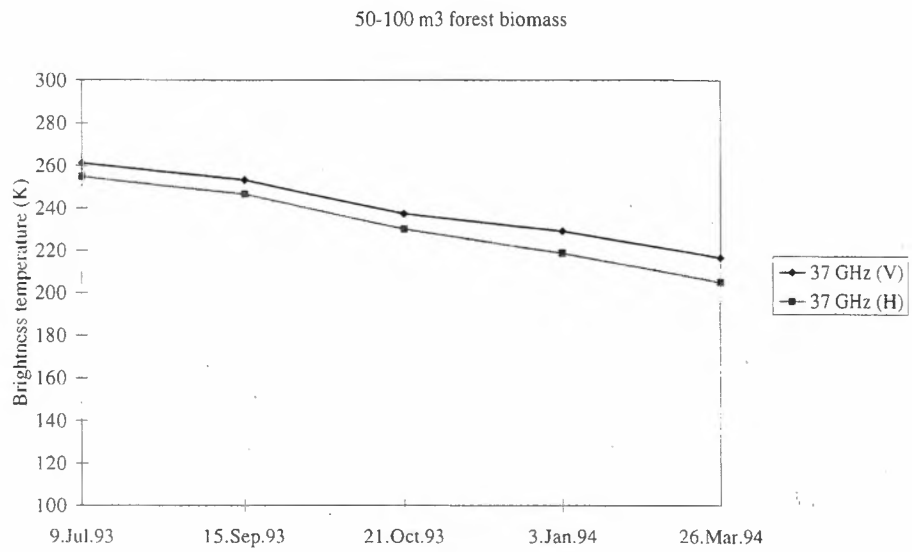

Figure 7.39. Seasonal response of the 37 GHz channels for areas with a forest biomass of 50-100 m^3/ha.

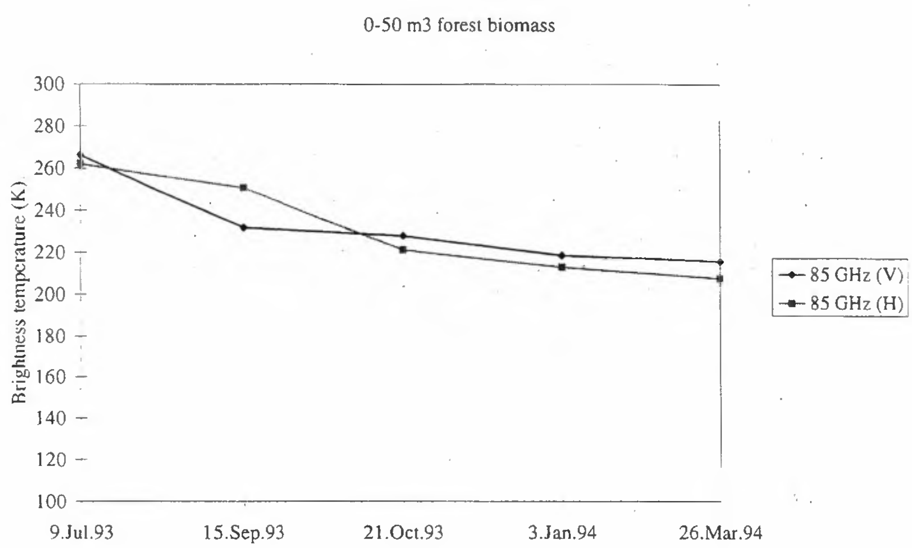

Figure 7.40. Seasonal response of the 85 GHz channels for areas with a forest biomass of 0-50 m^3/ha.

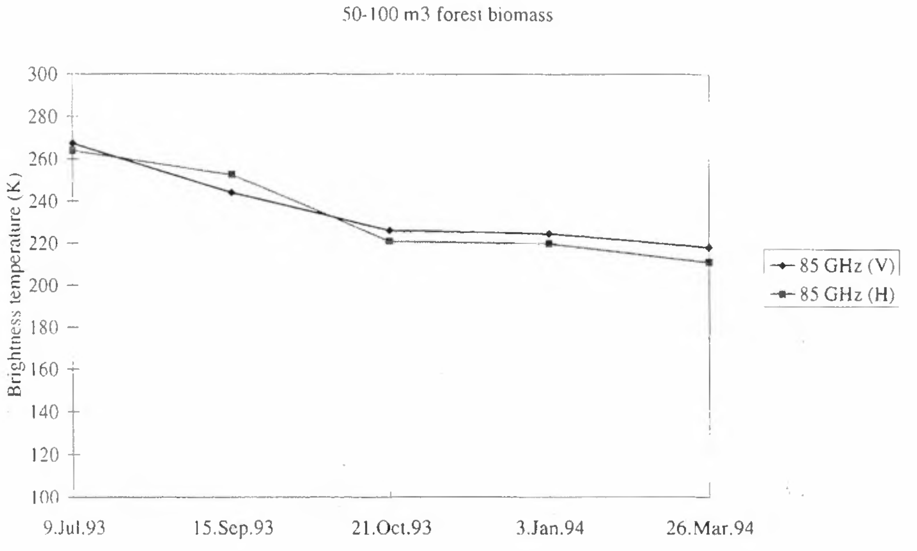

Figure 7.41. Seasonal response of the 85 GHz channels for areas with a forest biomass of 50-100 m^3/ha.

Response to physical temperature

The investigations discussed above showed that the effect of forest biomass (or stem volume) is negligible in the SSM/I measurements, what applies both for the summer-time and winter-time data. In contrast to that, the land use category has a considerable effect. A possible explanation is that since the range of variation in the stem volume (or biomass) is low for the 25 km by 25 km grid cells employed in the analysis (whereas the variation in land use can be high), the SSM/I data does not allow the investigation of the correlation between the emissivity and biomass.

The comparison of SSM/I brightness temperatures with varying environmental parameters shows that the physical temperature is the dominant effecting factor. This is evident especially with the summer/autumn data (snow free conditions) as Table 7.1 indicates. Table 7.1 presents the correlation coefficient between the summer/autumn-time brightness temperatures and the physical temperature for three grid cells (for July, August and September 1993). The reference temperature employed in the analysis is the average daily air temperature at the ground level, not the actual physical temperature of the target at the moment of imaging. Table 7.1 shows that the correlation with the physical temperature is very high for 19, 22 and 37 GHz channels. For 85 GHz channels the correlation is significantly lower, probably due to the atmospheric disturbances. The results also indicate that the higher is the fraction of forest cover, the higher is the correlation of brightness temperature with the physical temperature.

The effect of other varying physical parameters can be observed in Figure 7.42 in which the daily behavior of apparent emissivity is presented together with a scatter plot that shows the relation between the physical temperature and the SSM/I-based brightness temperature. The apparent emissivity e_{ap} is defined here as an atmospherically uncorrected target emissivity given by Equation (7.1).

Figure 7.42 depicts the response of SSM/I measurements to physical temperature at 37 GHz, V polarization for pixel #249 of the South Finland test area (refer to Table 7.1). The results are only depicted for this channel, but the behavior is similar for the other channels also (except that the correlation is not that high for 85 GHz channels). The results show (1) that the correlation with the physical temperature is high and (2) that the correlation with the weather-dependent varying characteristics, such as the soil moisture and precipitation, is marginal. This remark is also supported by the fact that negligible correlation was found between the precipitation or modelled soil moistures against brightness temperatures or apparent emissivities. Thus, the emissivity of land surface appears to be a fairly constant value. This observation led to the development of the temperature retrieval approach discussed below in Section 9.1. Even though the emissivity is a constant value in a certain location, it appears to vary geographically from one location to another. This is depicted in Figure 7.43 which shows similar results as Figure 7.42 for a total of 32 pixels located in the South Finland test area. Figures 7.42 and 7.43 imply that the variation in land surface emissivity from one pixel to another is mainly due to the land cover differences.

Figure 7.44 shows, similarly to Figure 7.42b, the behavior of apparent emissivity of a single grid cell, but now for the whole one year period. These results clearly indicate the major effect of snow cover. As the snow cover starts to form around day #100, the emissivity starts to decrease. Throughout the snow period the apparent emissivity remains in low values changing due to variations in (1) the amount of snow and (2) snow cover physical properties.

Table 7.1. Correlation between the SSM/I-based brightness temperature and the physical temperature (air temperature at ground) for three pixels of the South Finland test area.

Channel	Correlation Coefficient (r)		
Pixel Forest Cover Fraction (%)	#290 54	#249 68	#133 90
19V	0.93	0.93	0.95
19H	0.90	0.90	0.93
22V	0.95	0.94	0.95
37V	0.95	0.94	0.94
37H	0.91	0.91	0.92
85V	0.86	0.80	0.83
85H	0.76	0.79	0.83

(a)

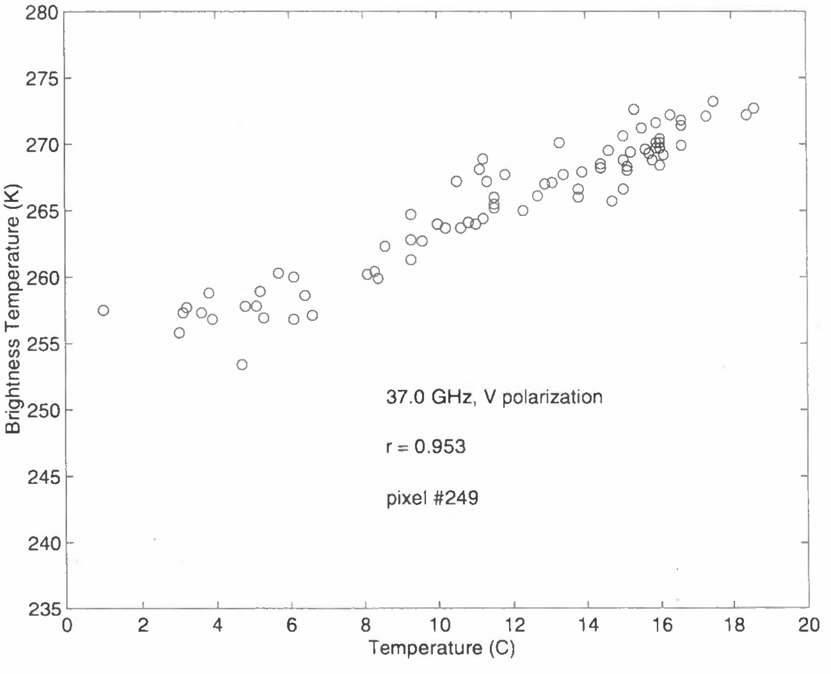

(b)

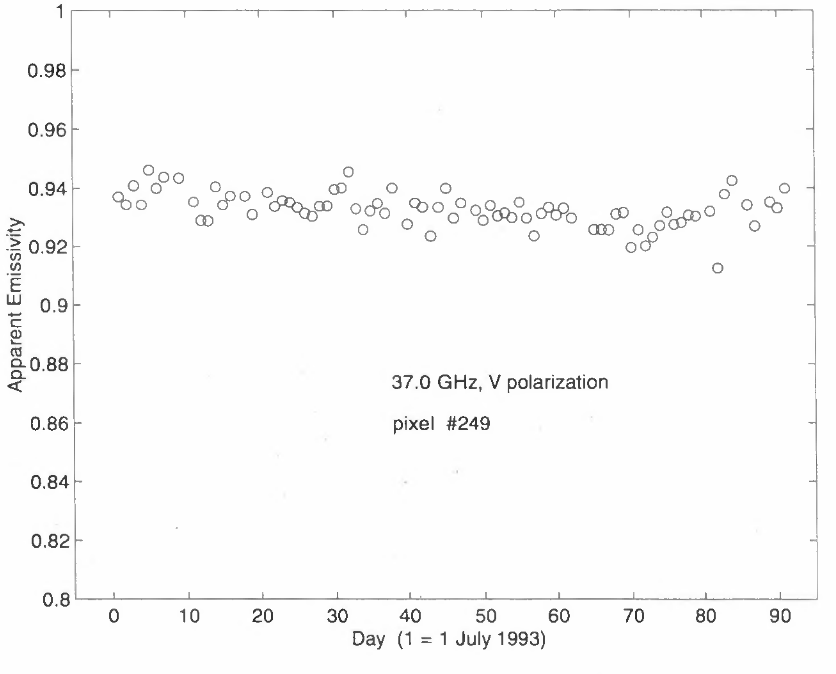

Figure 7.42. (a) Behavior of brightness temperature at 37 GHz, V polarization as a function of temperature for July, August and September 1993. The results are depicted for a single pixel using interpolated SSM/I data (#249 of the South Finland test area). The results for night/morning time (from 0.00 am to 9.00 am.) are presented. The reference temperature is the mean daily air temperature at ground. For day-time results the correlation of SSM/I results with the physical temperature is somewhat lower.
(b) Apparent emissivity at 37 GHz, V polarization as a function of time for the same pixel.

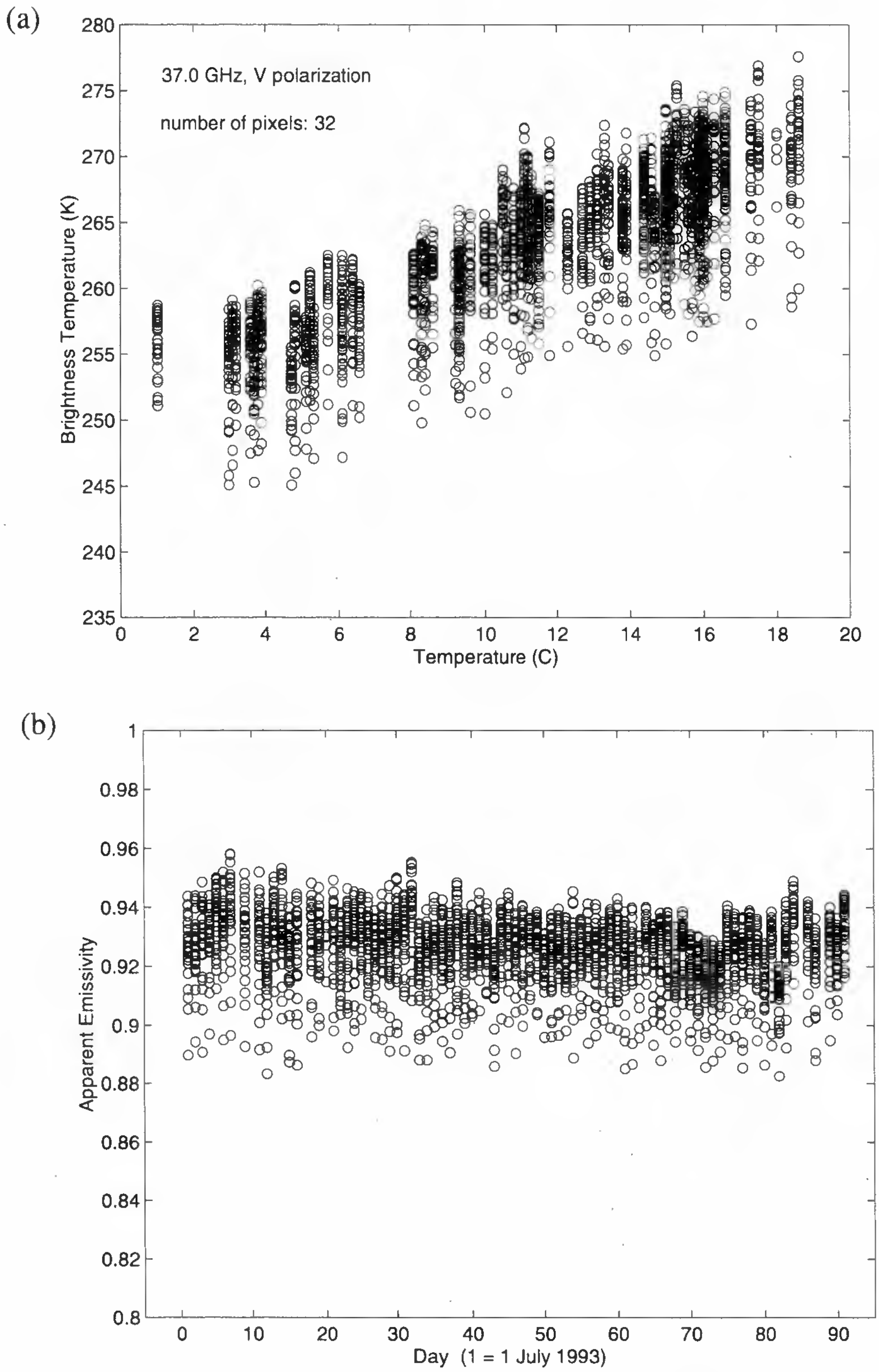

Figure 7.43. (a) Behavior of brightness temperature at 37 GHz, V polarization as a function of temperature for July, August and September 1993 for 32 pixels of the South Finland test area. (b) Apparent emissivity at 37 GHz, V polarization as a function of time for the 32 pixel-set.

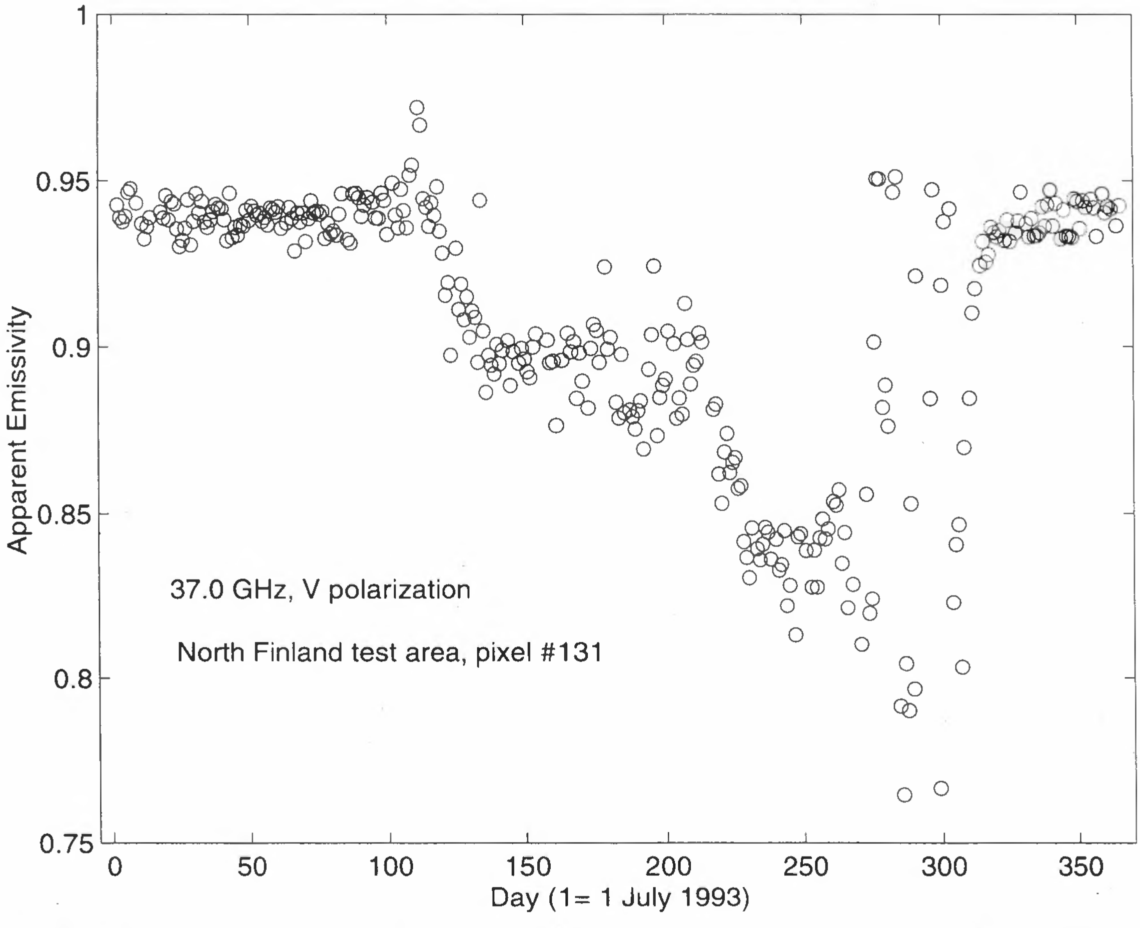

Figure 7.44. Apparent emissivity at 37 GHz, V polarization for a one year period in the North Finland test area, pixel #131.

7.3 Comparison of SSM/I Data with Model Predictions

Atmospheric effects

The atmospheric part of the apparent brightness temperature predicted by the HUT snow model has been considered using statistical atmospheric transmissivity values. With this approach ten transmissivities referring to a certain probability in Finnish circumstances are used. Using these transmissivity values, ten apparent brightness temperature values can be calculated by the model.

In Figures 7.45 to 7.50, these modeled results are plotted together with the measured SSM/I brightness temperatures for the 19, 37 and 85 GHz channels. The HUT model predictions are calculated employing ground-based snow water equivalent and snow density values. The results are determined for grid cell #111 of the North Finland test area (79% forest coverage). It is evident from the results that the atmospheric effects are most severe for the 85 GHz channels, which can be seen both from the modeled results and measured data. The transmissivity values used refer to 15%, 55% and 95% probabilities. The percentages mean the time when the transmissivities exceed this certain value. An estimate for the water vapour content of the 15% atmosphere is 0.8 g/cm^2, for 55% atmosphere 1.2 g/cm^2 and for 95% atmosphere 3.3 g/cm^2.

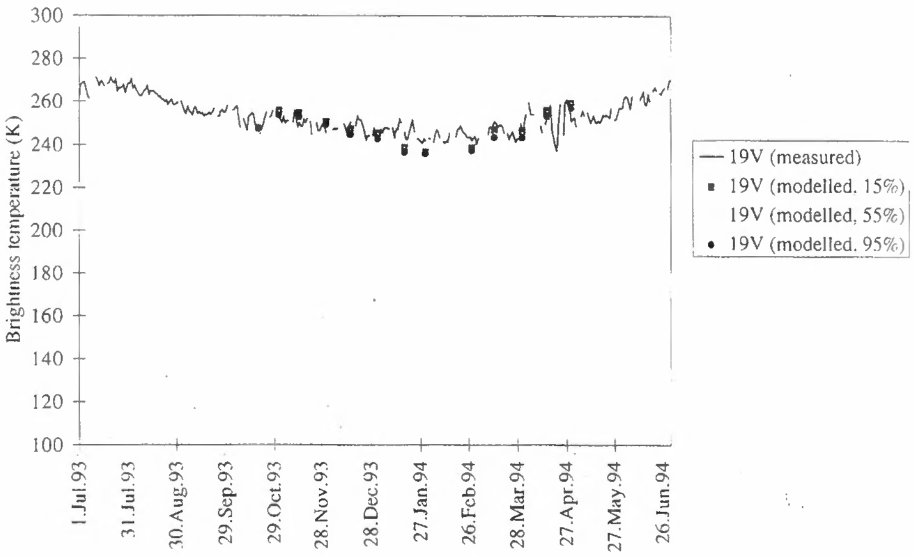

Figure 7.45. Comparison of HUT-model with the measured SSM/I data (grid cell #111 of the North Finland test area). The results are for 19 GHz (vertical polarization).

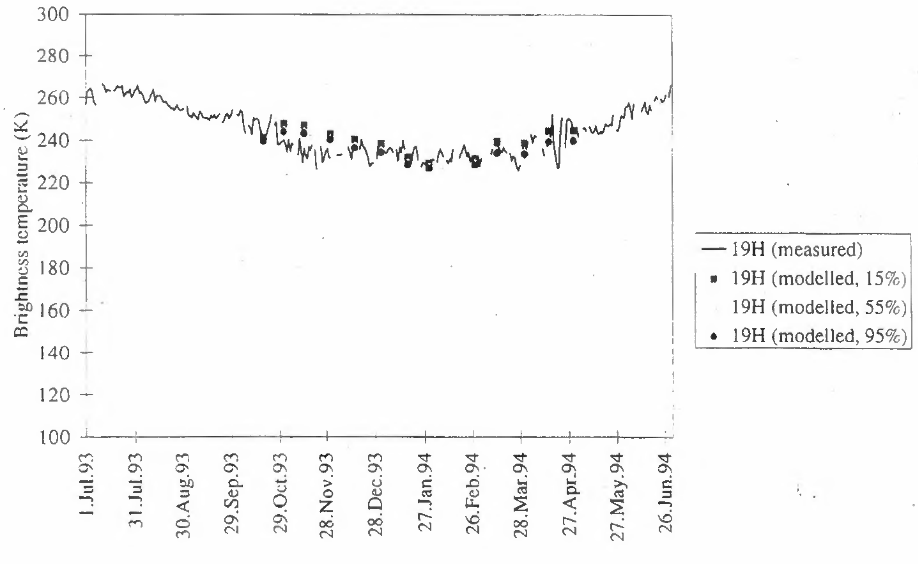

Figure 7.46. Comparison of HUT-model with the measured SSM/I data (grid cell #111 of the North Finland test area). The results are for 19 GHz (horizontal polarization).

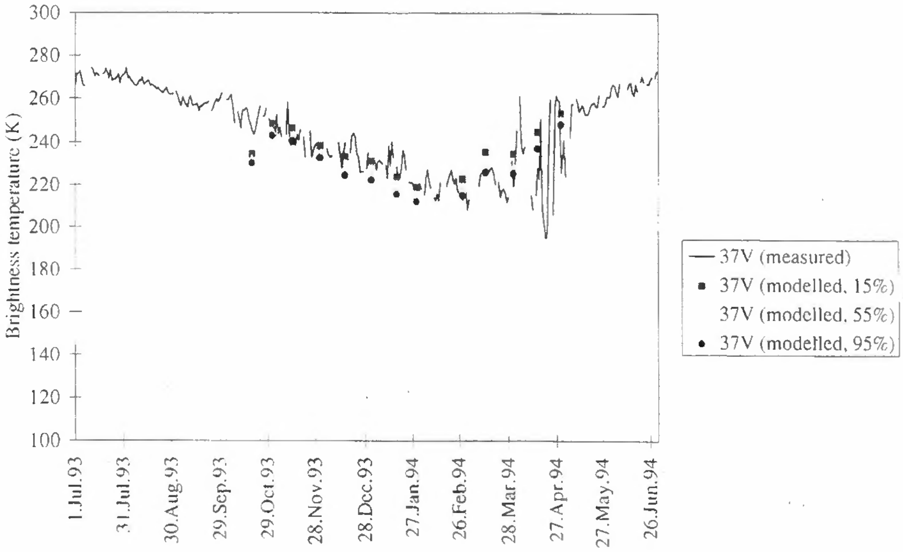

Figure 7.47. Comparison of HUT-model with the measured SSM/I data (grid cell #111 of the North Finland test area). The results are for 37 GHz (vertical polarization).

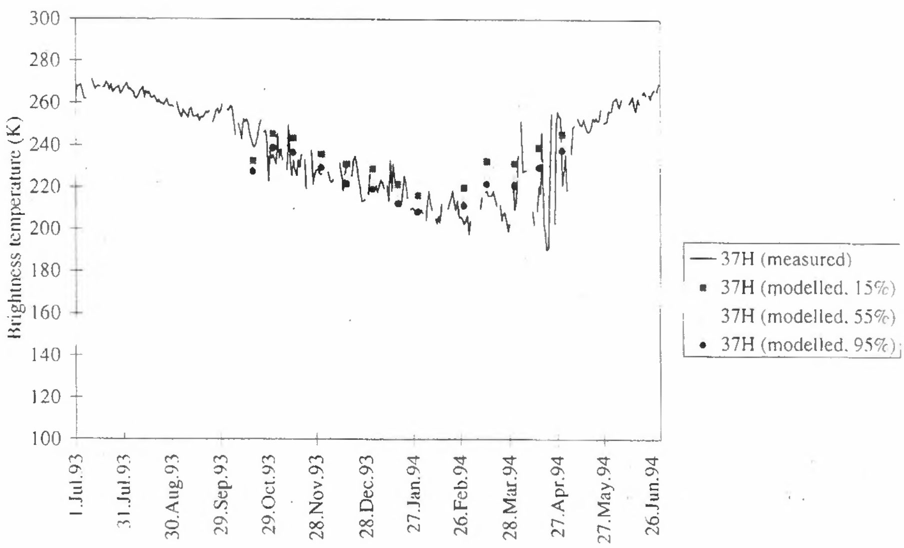

Figure 7.48. Comparison of HUT-model with the measured SSM/I data (grid cell #111 of the North Finland test area). The results are for 37 GHz (horizontal polarization).

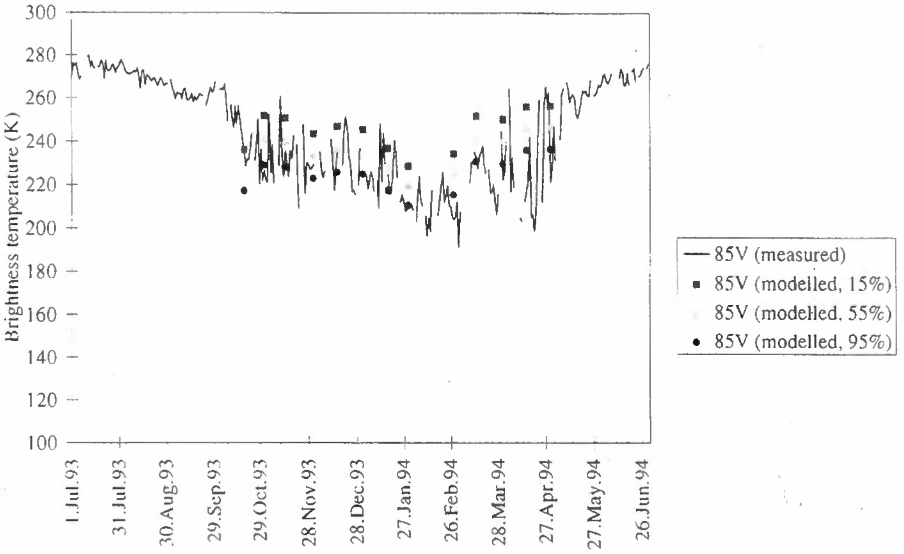

Figure 7.49. Comparison of HUT-model with the measured SSM/I data (grid cell #111 of the North Finland test area). The results are for 85 GHz (vertical polarization).

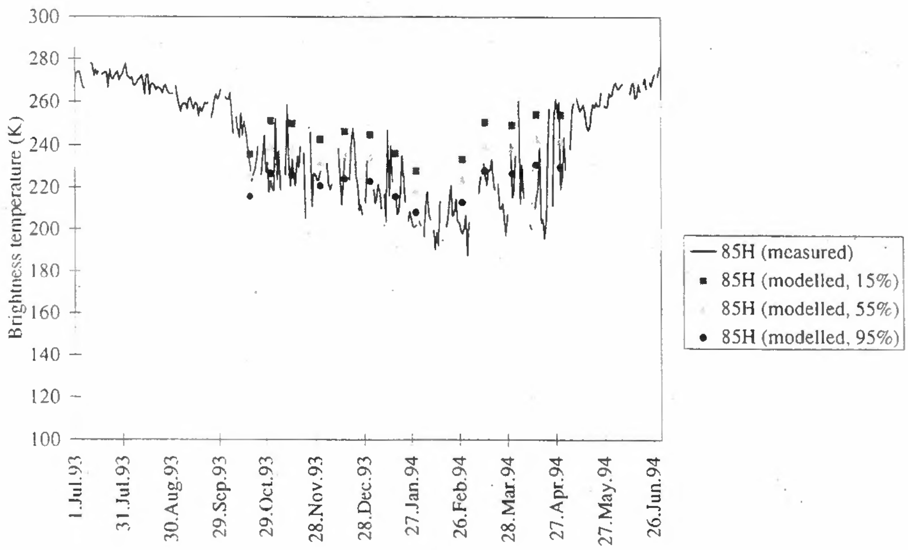

Figure 7.50. Comparison of HUT-model with the measured SSM/I data (grid cell #111 of the North Finland test area). The results are for 85 GHz (horizontal polarization).

Response to forest biomass

The behavior of the HUT snow model as a function of forest biomass was not investigated by modeling for various forest biomass classes as the results of Section 7.2 showed that for satellite borne measurements there is no correlation between seasonal behavior and forest biomass. This is due to the large, relatively heterogeneous test sites when compared to smaller, homogeneous measurements lines used in airborne measurement campaigns. Results obtained from airborne measurements are presented in Figures 7.51 to 7.52, showing the attenuation behavior of forest canopy for three forest biomass classes, i.e. 0-50 m^3/ha, 50-100 m^3/ha and 100-150 m^3/ha.

The results show that the change of brightness temperature increases to nearly 60K for 94 Ghz (vertical polarization) results for a mid-winter measurement. The change seems to saturate to a forest biomass of 50-100m^3/ha, therefore the use of only two forest biomass classes in Section 7.2 for satellite borne measurements should not have any influence on the results.

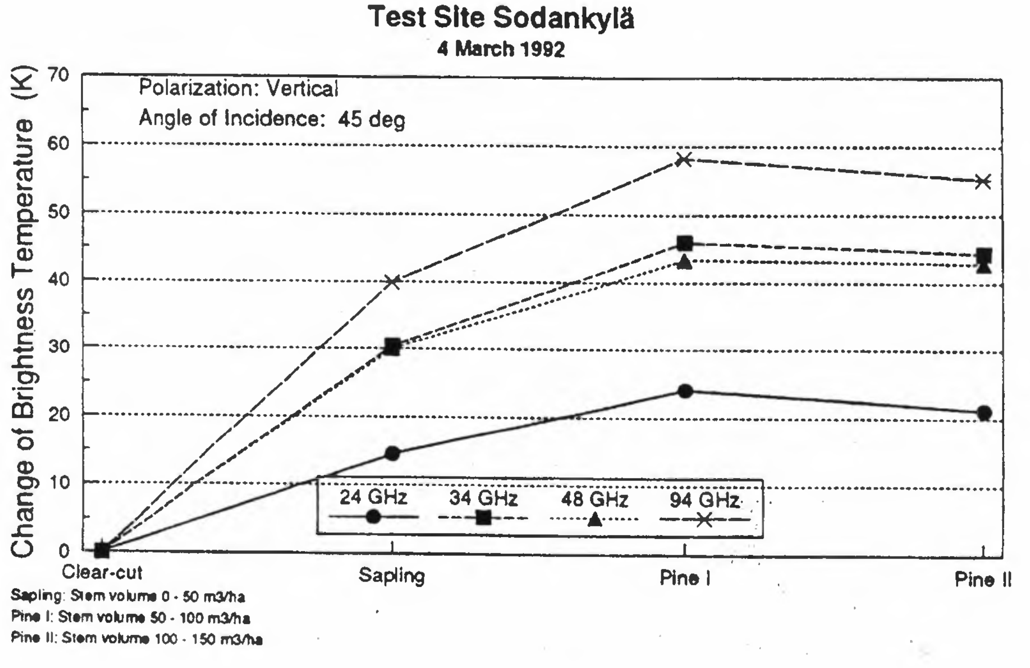

Figure 7.51. Change of brightness temperature obtained from airborne measurements as a function of forest vegetation on 4 March 1992 (Kurvonen 1994).

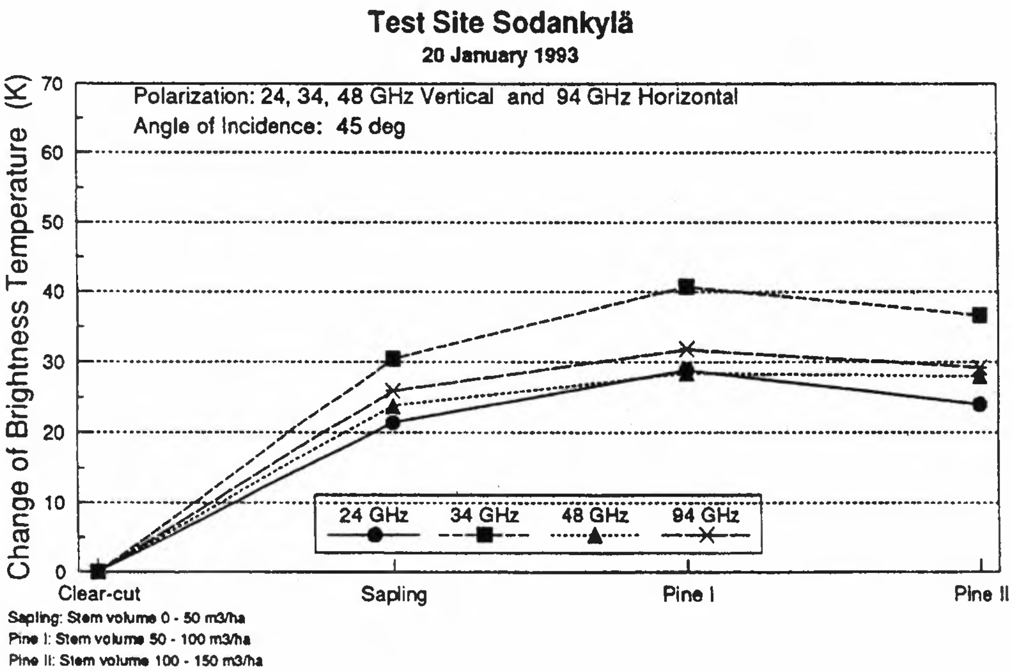

Figure 7.52. Change of brightness temperature obtained from airborne measurements as a function of forest vegetation on 20 January 1993 (Kurvonen, 1994).

Snow cover effects

The effect of snow cover was studied by comparing modeled results with SSM/I observations for two test sites that had large differences in snow cover, but about the same values for other ground parameters (forest biomass, forest coverage etc.). This analysis was performed for the winter of 1993 - 1994. The other test site (grid cell) was selected from the North Finland test area and the other from the South Finland test area. For simplicity, the northern test site was chosen to be the same which was used above (grid cell #111), and for which the results are presented in Figures 7.45 to 7.50. The southern test site was chosen in a way that its forest coverage/biomass would be equal to this northern test site. Thus, grid cell #330 from the South Finland test area was used for this comparison.

Modeled results for the southern test site using this approach are presented in Figures 7.53 to 7.58 using the 55% atmosphere. Snow water equivalent values ranged from 0 to 78 mm at the southern test site, and from 0 to 172 mm at the northern test site.

When compared to results presented in Figures 7.45 to 7.50, the modeled results for southern test sites do not follow as well the measured data as for northern test sites. There may be several reasons for this behavior. For example, as the snow layer decreases, the effect of surface scattering becomes more important. However, during the modeling calculations, the surface parameters are kept constant.

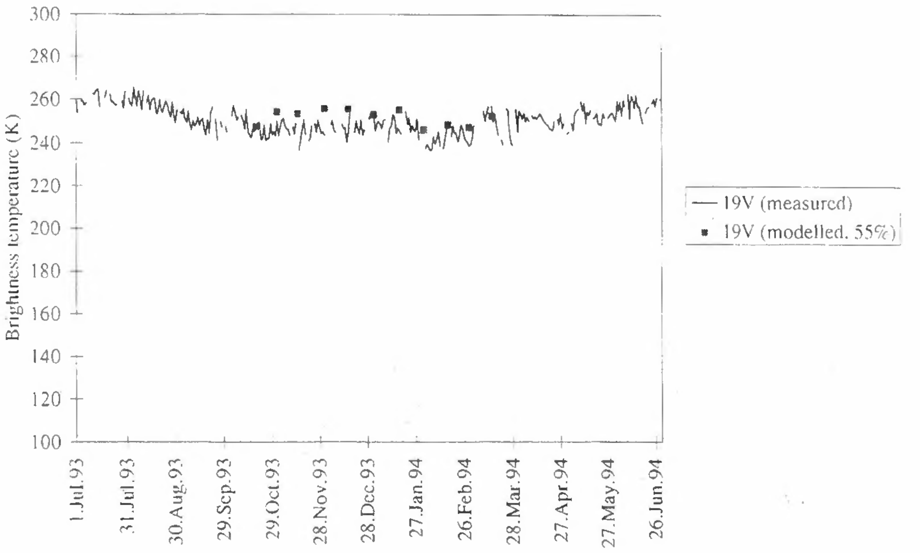

Figure 7.53. Modeled SSM/I brightness temperatures for a test site in Southern Finland (#330). The 19 GHz vertical channel is included.

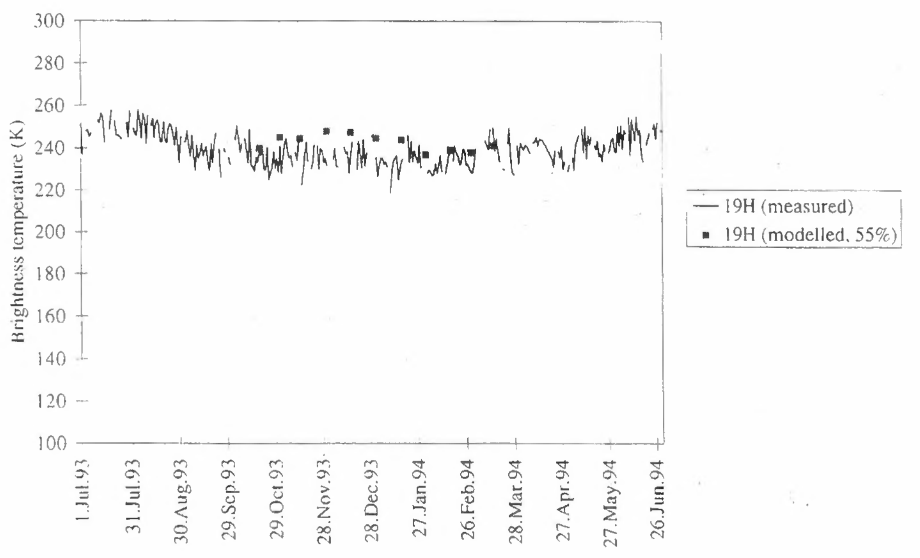

Figure 7.54. Modeled SSM/I brightness temperatures for a test site in Southern Finland (#330). The 19 GHz horizontal channel is included.

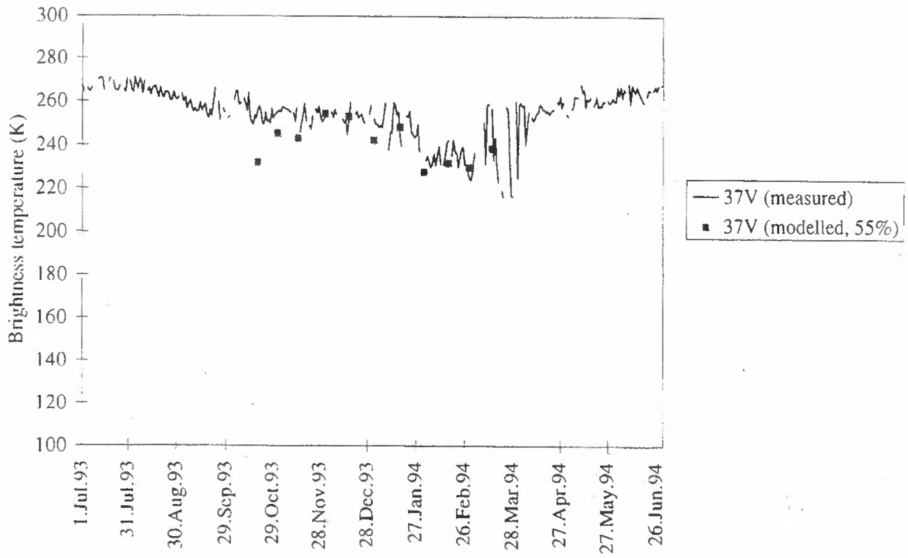

Figure 7.55. Modeled SSM/I brightness temperatures for a test site in Southern Finland (#330). The 37 GHz vertical channel is included.

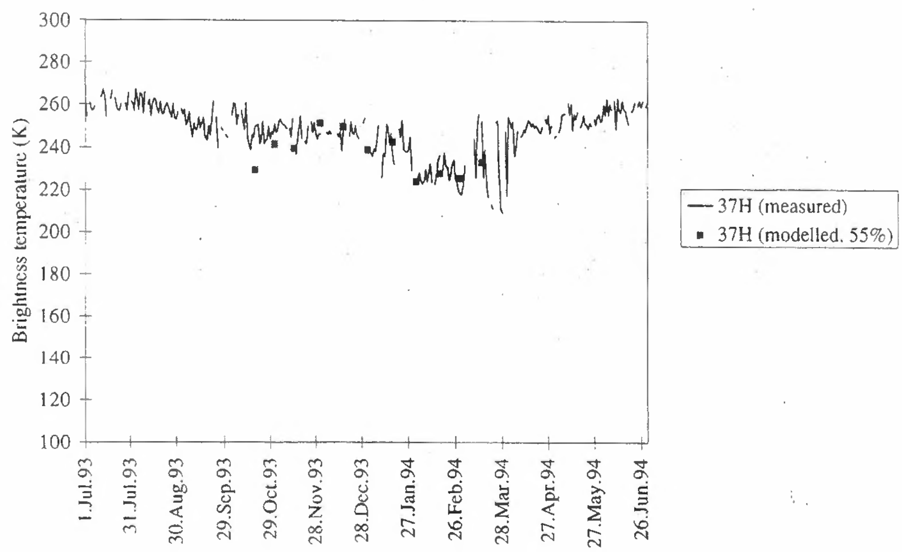

Figure 7.56. Modeled SSM/I brightness temperatures for a test site in Southern Finland (#330). The 37 GHz horizontal channel is included.

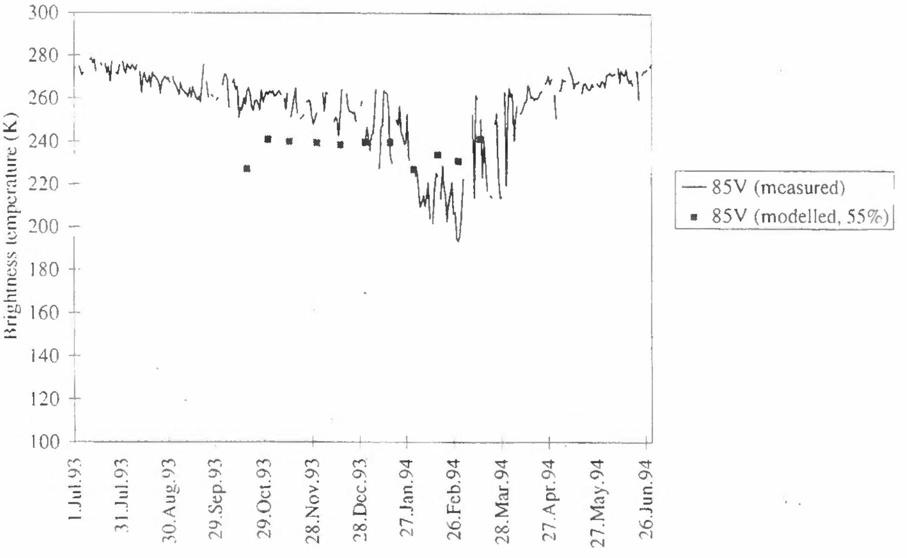

Figure 7.57. Modeled SSM/I brightness temperatures for a test site in Southern Finland (#330). The 85 GHz vertical channel is included.

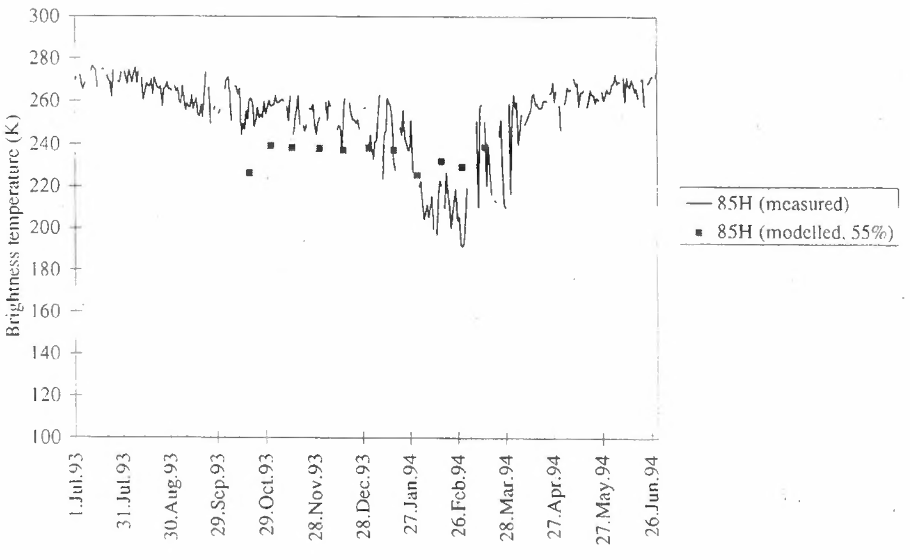

Figure 7.58. Modeled SSM/I brightness temperatures for a test site in Southern Finland (#330). The 85 GHz vertical channel is included.

Effect of different land use categories

The effect of land use categories (mainly forested areas vs. open areas) on the modeled brightness temperatures are investigated next. Only two classes were used as distinction to Section 7.2 where three classes were used. These two classes were distinguished by their forest coverage per cent to test sites with 0-50% and 50-100% forest coverages. The first category is represented by pixel #12 (forest coverage 43%) and the second by grid cell #111 (forest coverage 79%), both located in the North Finland test area. The results are presented in Figures 7.59 to 7.64 for grid cell #12 (43% forest coverage) using the 55% atmosphere. The results for grid cell #111 (79% forest coverage) are shown in Figures 7.45 to 7.50.

The results show that there is no significant difference when the results in Figures 7.59 to 7.64 are compared to those in Figures 7.45 to 7.50 which represent the higher forest coverage (79%) results. It may be therefore concluded that forest coverage or land use does not have a significant effect on the performance of the HUT model.

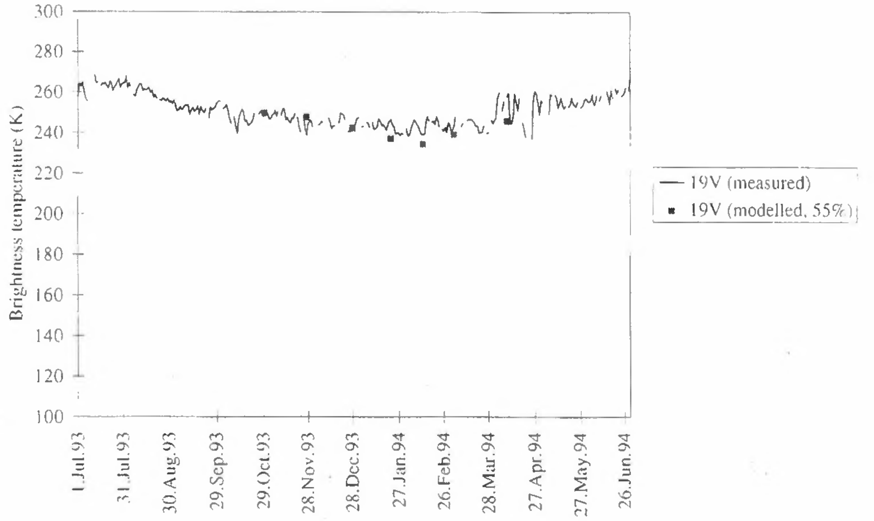

Figure 7.59. Modeled SSM/I brightness temperatures compared to measured values for a test site with a forest coverage of 43% (grid cell #12 of the South Finland test area). The results for 19 GHz (vertical polarization) are included.

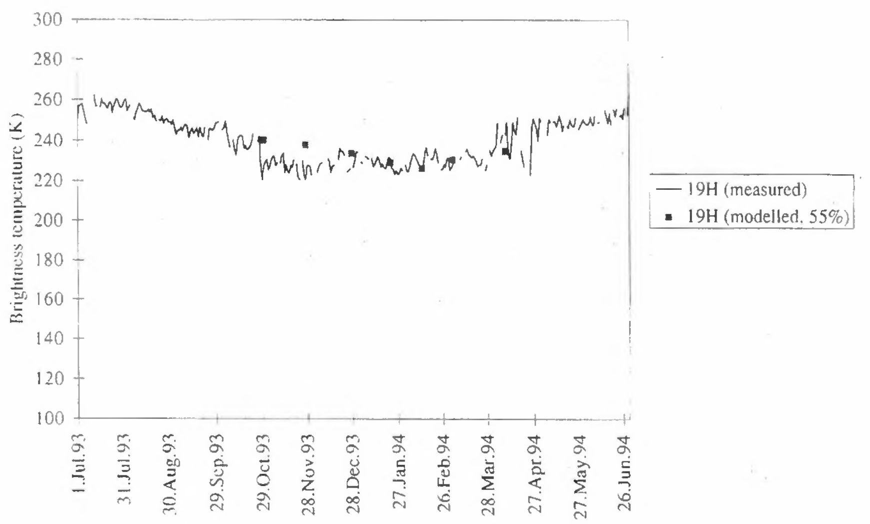

Figure 7.60. Modeled SSM/I brightness temperatures compared to measured values for a test site with a forest coverage of 43% (grid cell #12 of the South Finland test area). The results for 19 GHz (horizontal polarization) are included.

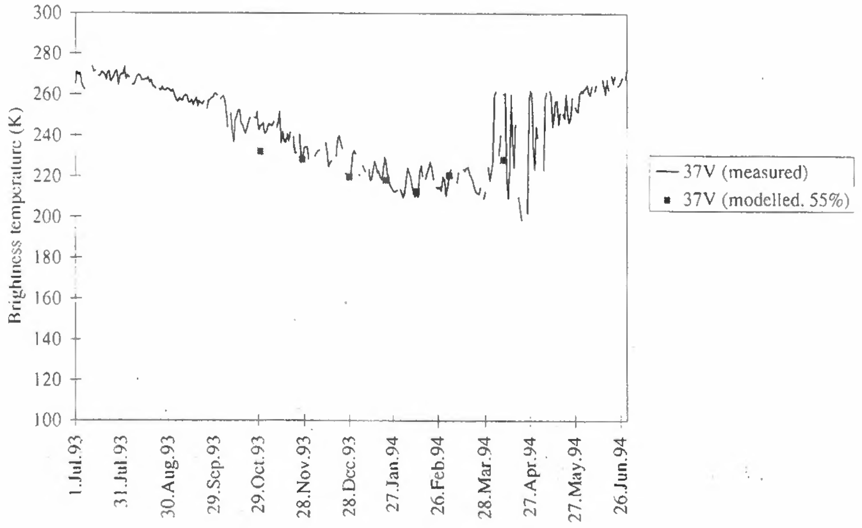

Figure 7.61. Modeled SSM/I brightness temperatures compared to measured values for a test site with a forest coverage of 43% (grid cell #12 of the South Finland test area). The results for 37 GHz (vertical polarization) are included.

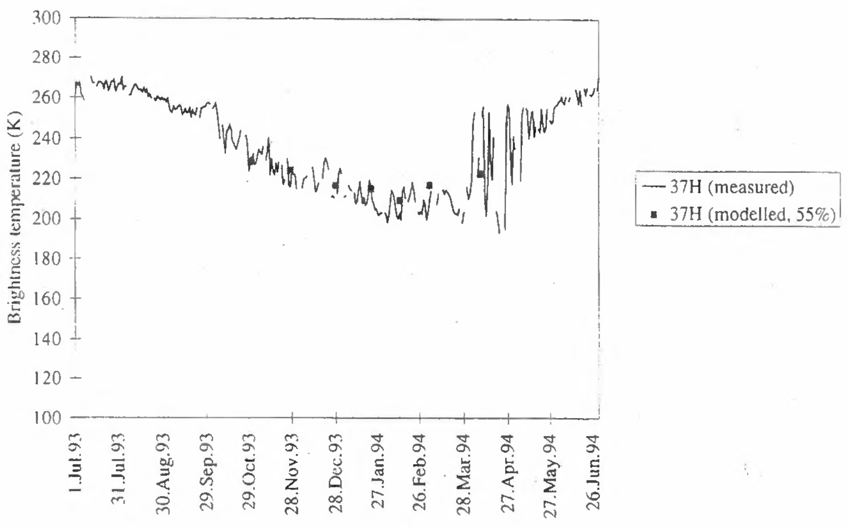

Figure 7.62. Modeled SSM/I brightness temperatures compared to measured values for a test site with a forest coverage of 43% (grid cell #12 of the South Finland test area). The results for 37 GHz (horizontal polarization) are included.

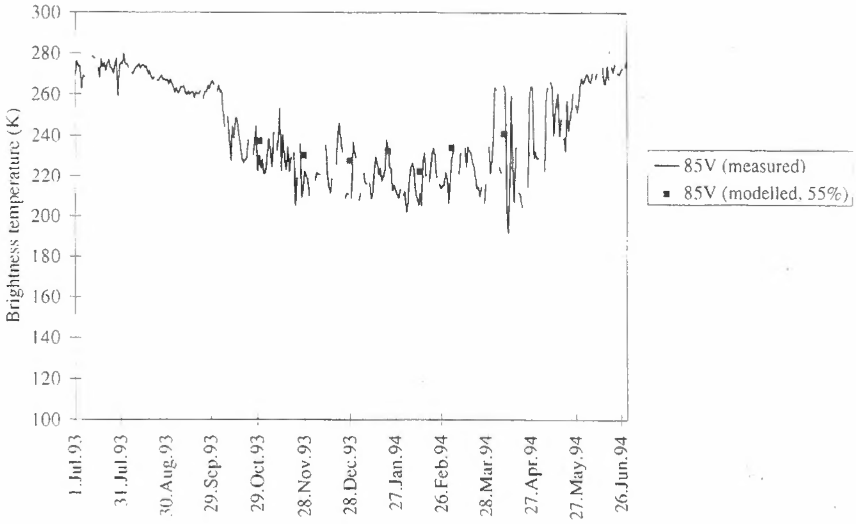

Figure 7.63. Modeled SSM/I brightness temperatures compared to measured values for a test site with a forest coverage of 43% (grid cell #12 of the South Finland test area). The results for 85 GHz (vertical polarization) are included.

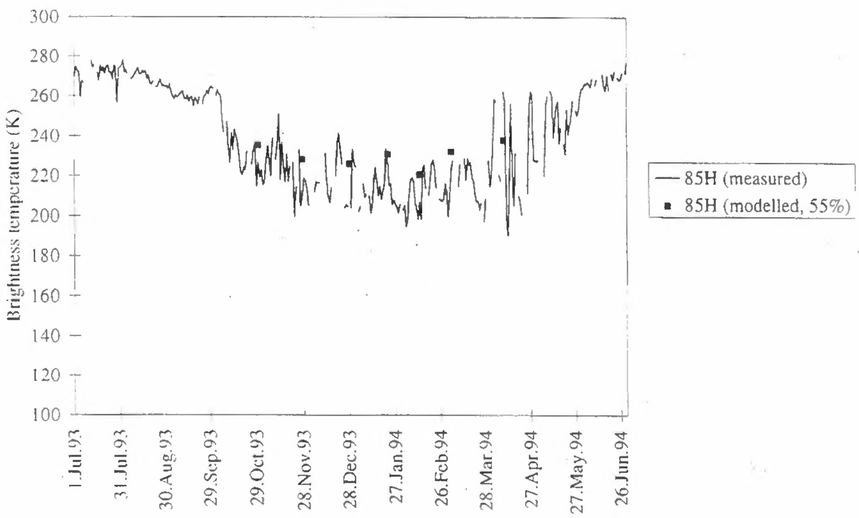

Figure 7.64. Modeled SSM/I brightness temperatures compared to measured values for a test site with a forest coverage of 43% (grid cell #12 of the South Finland test area). The results for 85 GHz (horizontal polarization) are included.

Comparison of SSM/I data with sea ice emission model

Figures 7.65 and 7.66 show the behavior of the sea surface emission module for various wind speeds. The modeled emission is compared to experimental values (grid cell #8 of the south Finland test area, summer period) in order to demonstrate the feasibility of the model module under open sea conditions.

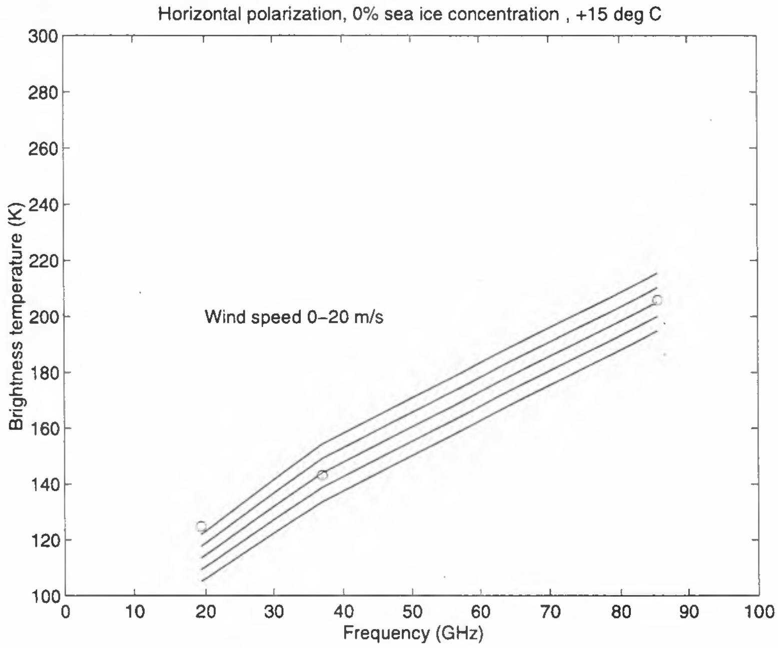

Figure 7.65. Results modeled with the sea surface model module for vertical polarization. Modeled results are shown with a solid line and SSM/I measurements with circles.

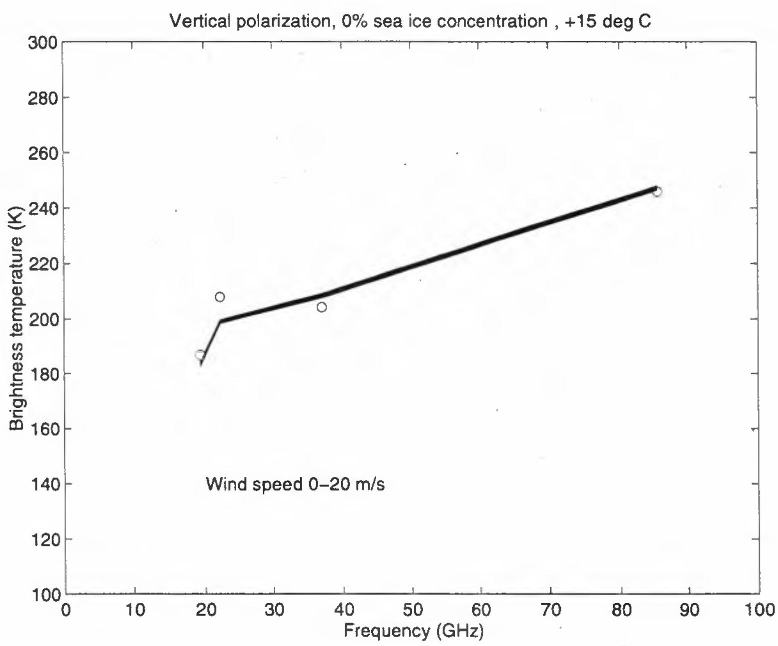

Figure 7.66. Results modeled with the sea surface model module for horizontal polarization. Modeled results are shown with a solid line and SSM/I measurements with circles.

8 Retrieval Algorithms for ERS-1 Wind Scatterometer Data

8.1 Estimation of Soil Moisture and Effects of Precipitation

Inversion method

The inversion technique employed is based on the idea of searching the maximum likelihood inverse solution for the semi-empirical forest backscattering model (described in Section 4.1) in the case of ERS-1 Wind Scatterometer measurements interpolated into a fixed 25 by 25 km grid. The inversion method employs the (nearly) simultaneous three-beam results, and it requires the land-use and forest cover information as *a priori* data. The current implemented inversion algorithm is a two-stage procedure that first estimates the soil moisture for a single grid cell using WS-based σ^o-values from this specific pixel. At the second stage, the soil moisture is re-estimated by considering the effects of neighbouring pixels also.

The inversion technique is a maximum likelihood method in which a inverse solution for a semi-empirical forest backscattering model is searched using (nearly) simultaneous aft-, fore- and mid-beam Wind Scatterometer data. The land use information is employed as *a priori* data.

The inverse problem is to find the solution which maximises the following conditional probability:

$$p\left(\overline{\sigma^o} \mid (V, \bar{\theta}, m_{v,v}, m_{v,s}, c)\right) = \tag{8.1}$$

$$B_1 \cdot \exp\left(-\sum_{i=1}^{3} \frac{1}{2\sigma_i^2} \{ c_i \cdot [(1-f_w) \cdot [\sigma_V^o(V, \theta_i, m_{v,v}) + t^2(V, \theta_i, m_{v,v}) \cdot \sigma_g^o(\theta_i, m_{v,s})] \;+\; f_w \sigma_w^o(\theta_i)] \;-\; \sigma_i^o \}^2 \right),$$

where

$\overline{\sigma^o}$ = $((\sigma^o)_1, (\sigma^o)_2, (\sigma^o)_3)$, vector containing grid cell-wise interpolated backscattering coefficients (mid-, aft- and fore-beams)
V = average forest stem volume (of land areas) of the grid cell
θ = angle of incidence
$m_{v,v}$ = average volumetric canopy moisture
$m_{v,s}$ = average volumetric soil moisture (mean value for all land areas)
B_1 = norming constant
f_w = fraction of water areas (lakes and sea)
σ_i = standard deviation of σ^o for the ith antenna beam
c_i = calibration constant due to the systematic and random difference between the model and ERS-1 WS data for the ith antenna beam
σ_V^o = modeled forest canopy backscattering contribution (refer to section 4.1)

t	= modeled forest canopy transmissivity (refer to section 4.1)
σ_g^o	= modeled soil backscattering contribution (refer to section 4.1)
σ_w^o	= assumed backscattering coefficient of water areas (refer to Section 6.3).

In order to estimate $m_{v,s}$ for a single pixel, Equation (8.1) yields the following iteration problem which is the first stage of the inversion algorithm (first order iteration):

$$\text{Minimize} \quad \sum_{i=1}^{3} \frac{1}{2\sigma_i^2}\{c \cdot (1-f_w) \cdot [\sigma_V^o(V,\theta_i,m_{v,v}) + t^2(V,\theta_i,m_{v,v}) \cdot \sigma_g^o(\theta_i,m_{v,s})] \; + \; c \cdot f_w \cdot \sigma_w^o(\theta_i) \; - \; \sigma_i^o\}^2$$

$$+ \; \frac{1}{2\lambda_c^2}(c-\hat{c})^2 \; + \; \frac{1}{2\lambda_{m_{v,v}}^2}(m_{v,v} - \hat{m}_{v,v})^2, \tag{8.2}$$

where

$\lambda_{m_{v,v}}$	= standard deviation of volumetric canopy moisture
$\hat{m}_{v,v}$	= average value of volumetric canopy moisture
λ_c	= standard deviation of ERS-1 WS calibration accuracy (assumed to be 0.1 dB)
$\hat{c}$	= systematic difference between the backscattering model (refer to section 4.1) and ERS-1 WS-based σ^o (assumed to be 1.3 dB for all channels).

The iteration results presented in this Chapter are calculated using σ^o values given in decibels (in practise the employment of plane σ^o values does not make any significant difference).

The second stage of the algorithm (second order iteration) takes into account the influence of neighbouring pixels by an appropriate $\cos^2$-weighting (according to antenna beam characteristics). The soil moisture estimates obtained according to Equation (8.2) for the eight pixels that surround the actual pixel under study are used to refit the backscattering model into the observations. Now, the soil moisture of the pixel under study $m_{v,s,1}$ is the only unknown parameter:

Minimize (8.3).

$$\sum_{i=1}^{3}\left\{\sum_{k=1}^{9} n_k \cdot \{c \cdot (1-f_{w,k}) \cdot [\sigma_V^o(V_k,\theta_{i,k},m_{v,v,k}) + t^2(V_k,\theta_{i,k},m_{v,v,k}) \cdot \sigma_g^o(\theta_{i,k},m_{v,s,k})] \; + \; c \cdot f_{w,k} \cdot \sigma_w^o(\theta_{i,k})\} \; - \; \sigma_i^o\right\}^2,$$

where

n_k	= weighting value for the pixel (grid cell) under study and its neighbouring pixels.

The weighting values for different square-sized grid cells have been determined by assuming that the ground projection of every antenna beam is $\cos^2$-shaped and has a 3 dB beam width of 47 km. Thus, the following weighting values n_k are obtained:

$n_1 = 0.32$ for the interpolated pixel under study,

$n_{2...5} = 0.13$ for the nearest neighbouring pixels,

$n_{6...9} = 0.04$ for the farthest neighbouring pixels.

If the retrieval errors obtained in the first order iteration are (on average) unbiased, the second order iteration convergates (on average) towards the correct value. This is shown in the following.

Let the soil moisture retrieval error in the first order iteration be ε_1' for the pixel under investigation and $\varepsilon_2', \varepsilon_3', \ldots \varepsilon_9'$ for its neighbouring pixels. Hence, we can rewrite the term to be minimized in order to estimate $m_{v,s,1}$ in the second order iteration (Equation (8.3)) as (for a single antenna beam for simplicity):

$$\left\{\left[n_1\sigma^o_{model,1}(m_{v,s,1}) + \sum_{k=2}^{9} n_k\sigma^o_{model,k}(m_{v,s,k}+\varepsilon_k')\right] - \sigma^o\right\}^2. \tag{8.4}$$

Thus, the error in the modelled backscattering coefficient $\Delta\sigma^o_{model,k}$ is

$$\Delta\sigma^o_{model,k} = \sigma^o_{model,k}(m_{v,s,k}+\varepsilon_k') - \sigma^o_{model,k}(m_{v,s,k}) \tag{8.5}$$

and Equation (8.4) can be rewritten as:

$$\left\{\left[n_1\sigma^o_{model,1}(m_{v,s,1}) + \sum_{k=2}^{9} n_k(\sigma^o_{model,k}(m_{v,s,k}) + \Delta\sigma^o_{model,k})\right] - \sigma^o\right\}^2. \tag{8.6}$$

If the following criterion is valid (for a small change interval, refer to Figure 4.3)

$$\frac{d\sigma^o_{model}(m_{v,s,k})}{dm_{v,s,k}} \approx constant \tag{8.7}$$

$$\Rightarrow \quad \Delta\sigma^o_{model,k} \approx constant \cdot \varepsilon_k' \tag{8.8}$$

Now, if $<\varepsilon_k'> = 0$ for $k = 1...9$ (i.e. the retrieval error is unbiased) $\Rightarrow \; <\Delta\sigma^o_{model,k}> \approx 0$

$$\Rightarrow \quad <\sum_{k=2}^{9} n_k\Delta\sigma^o_{model,k}> \approx 0 \tag{8.9}$$

which implies that the second order iteration should on average convergate towards the right value on the condition that the retrieval bias is zero.

Testing of second order iteration

The inversion method was first tested for a small data set in order to find out wether the second order iteration can possibly improve the estimation accuracy compared to first order iteration. Since the inversion calculation requires considerable computing efforts, the algorithm testing for a more extensive data set was only conducted for the first order iteration procedure. This is described later in this Section.

Figure 8.1 shows the preliminary results obtained in the soil moisture estimation using ERS-1 Wind Scatterometer data. The soil moisture estimates were determined according to Equations (8.2) and (8.3) using mid-, fore- and aft-beam data from a single scatterometer measurement together with the semi-empirical forest backscattering model. Both the first and second order soil moisture estimates were calculated. The *a priori* information employed was the average forest cover and land use information for each 25 by 25 km grid cell (WS pixel). The reference soil moisture values were determined by the hydrological model (refer to Section 2.4).

The inversion testing was conducted using the data of summer 1993 of the Porvoo test area, Southern Finland. Unfortunately, the Porvoo test area was not well covered by the Wind Scatterometer. Hence, applicable data were only available for six occasions for the time period from June to the beginning of September 1993. The (interpolated) WS results for nine fixed grid cells of the Porvoo area were employed (the grid cells on coastline and sea were excluded). Since the data was not available for all grid cells for all occasions, the total amount of data points in Figure 8.1 was limited to 24. For comparison, Figure 8.2 shows the hydrological model-based temporal behavior of the soil moisture and the average WS-based estimates obtained for six separate occasions.

The results obtained correspond quite well the reference soil moisture values, except for one point for which the estimation error appears to be over 30%-units (July 28). However, in this case the reference value may be too low due to the inaccuracies in the timing of incident precipitation. The precipitation characteristics for each grid cell (total diurnal amount) have been interpolated from the data from fixed weather stations. Hence, inaccuracies in the exact timing of rain fall are evident. The typical overall relative error in reference soil moisture values is 10% to 20% (refer to Section 2.4).

The rms-retrieval errors and the retrieval biases obtained are listed in Table 8.1. The retrieval errors indicate that the second order iteration (effects of neighbouring pixels are included) may improve the estimation accuracy. However, the testing was conducted using a small data set. Hence, solid conclusions cannot be made. Moreover, the testing should have been done using original uninterpolated Wind scatterometer data. As discussed above, the worst case estimate may have been obtained in conditions where the reference prediction has failed. Therefore, Table 8.1 also shows the retrieval errors when the worst case is neglected. The most severe problem in the inversion appears to be the influence of open water areas. The inversion inaccuracies are the highest for those pixels which have the largest water areas (or which have large water areas in neighbouring pixels). The level of backscatter of water areas was determined by analyzing the backscattering coefficients obtained simultaneously for open sea. This analysis enabled the estimation of angular behavior of backscatter of open water. However, since the wave shapes differ on lakes and coastal regions from those of open sea, this approach can only give rough estimates.

The magnitude of estimation bias depends on the value of the calibration difference ($\hat{c}$ in Equation (8.2)). When this systematic difference between the applied backscattering model and Wind Scatterometer data is evaluated correctly, the retrieval bias should approach zero (especially, if a large set of independent estimates are considered). The biases listed in Table 8.1 show quite low values. This indicates that the assumed 1.3 dB calibration difference is near the correct value.

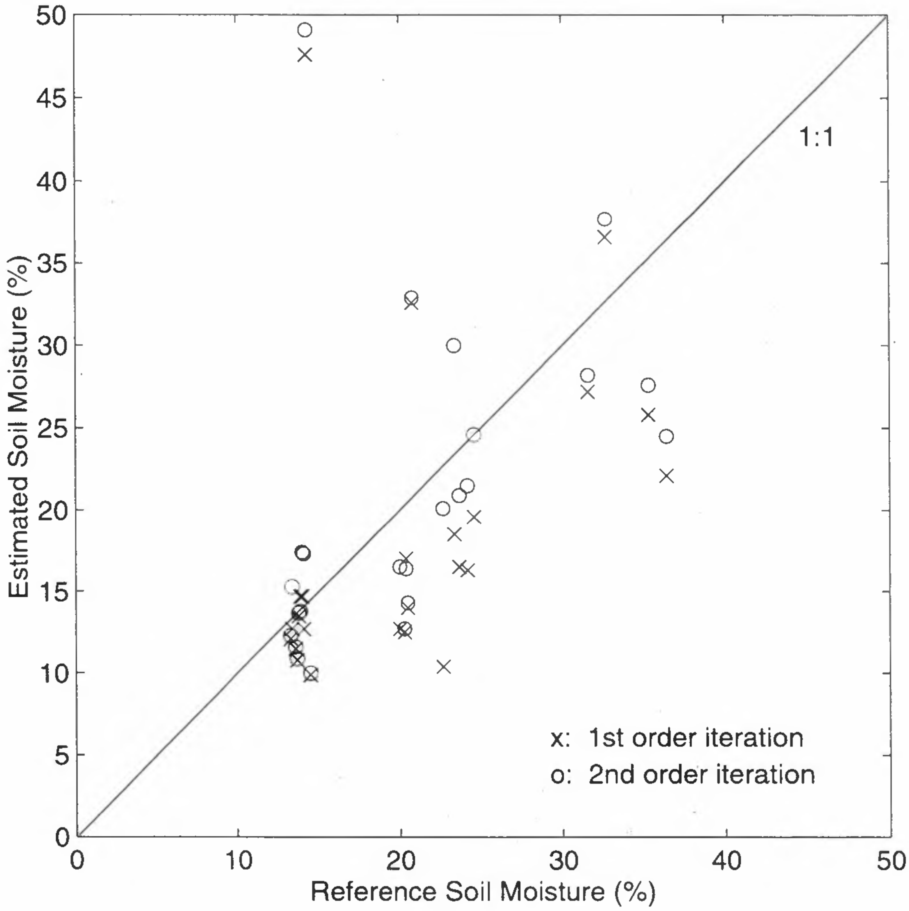

Figure 8.1. ERS-1 Wind Scatterometer-based soil moisture estimation results for the Porvoo test area. The reference values are hydrological model-based predictions.

Table 8.1. Rms-retrieval errors and retrieval biases for soil moisture estimates of the Porvoo test area (in %-units).

	Worst case included		Worst case excluded	
	rms-error	bias	rms-error	bias
1st order iteration	9.35	2.2	6.56	3.8
2nd order iteration	8.76	-0.2	5.24	1.3

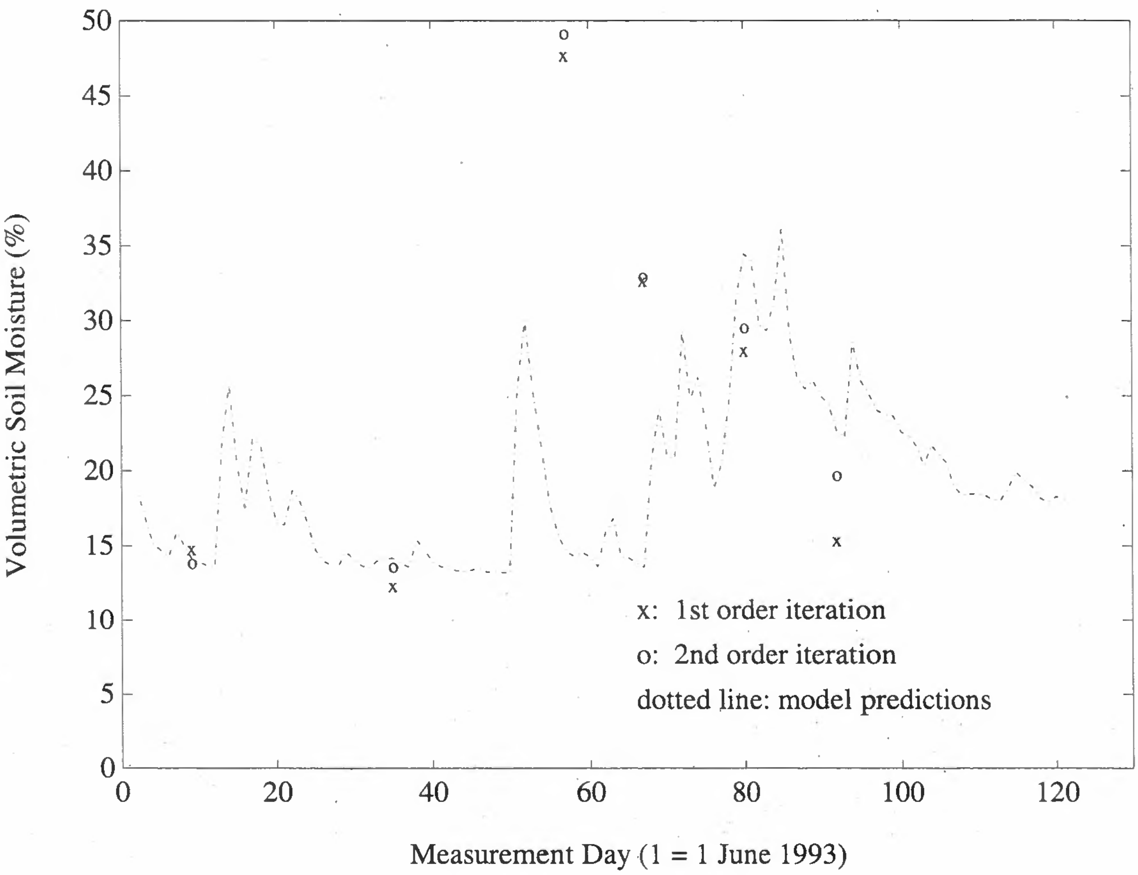

Figure 8.2. Temporal behavior of soil moisture in the Porvoo test area. Both the ERS-1 Wind Scatterometer-based soil moisture estimation results and the hydrological model-based predictions are shown (average values for different days).

<u>Testing of first order soil moisture retrieval algorithm and effects of weather conditions</u>

The first order iteration procedure was also tested for a more extensive data set. This is described on the following.

Figure 8.3 presents the comparison between the ERS-1 Wind Scatterometer-based soil moisture estimates and hydrological model-based reference soil moisture values. The results include values obtained for 323 cases on 18 different dates from a total of 32 fixed pixels (grid cells) of the South Finland test area (Eurajoki and Porvoo test sites). The results show that on dry conditions the soil moisture estimate is nearer the reference value than on wet conditions. Since the radar response to variations in the soil moisture is quite saturated at volumetric moistures higher than about 30%, the estimates disperse towards high values (i.e. the radar data does not allow the estimation of high moisture values). Moreover, the results indicate that on autumn the WS-based estimates tend to give systematically lower soil moisture values than the reference considerations. A possible explanation is that due to the withering of vegetation in autumn, the volume backscatter from vegetation can decrease the total level of backscatter compared to summer conditions.

Figures 8.4 and 8.5 show the relation between the two-day cumulative precipitation and the WS-based soil moisture estimate, and additionally, the combined effect of soil moisture and precipitation. These results clearly show that:

(1) It is possible to obtain good estimates for soil moisture in forested areas using ERS-1 Wind Scatterometer data when considerable precipitation has not occurred directly prior to image acquisition.

(2) The soil estimate obtained is actually related to the soil moisture and incident precipitation, probably due to the fact that precipitation increases the amount of loose water on surface vegetation or on ground which amplifies the backscatter from forest floor. As described above, the inversion method estimates the magnitudes of both the forest floor and forest canopy backscattering contributions. Since the forest floor backscattering contribution is assumed to be only related to the soil moisture in the estimation procedure, the possible loose water causes an overestimated soil moisture. Hence, the soil moisture estimate really estimates the total effective amount of water in top soil layer and on ground vegetation.

Figure 8.6 shows a soil moisture map obtained for Southern Finland for June 10, 1993. The Wind Scatterometer-based soil moisture estimates are interpolated into a 1 km by 1 km grid, and the estimation results are combined with water mask. Water and no-data areas are presented as black pixels. The soil moisture values are coded by a linear brightness scale: the lighter is the colour, the higher is the soil moisture (minimum 0% and maximum 32.4%).

The inversion method takes into account separately the backscattering contributions of water areas and land areas. The 25 km by 25 km sized grid cells into which the WS data were interpolated are typically mixed pixels with some water areas included. In the inversion algorithm, the level of backscatter from water areas is estimated from the backscattering values of open sea areas. Evidently, this method is not accurate, and higher errors in inversion are the more probable, the higher is the fraction of water areas in a pixel. This phenomenon is well observable in Figure 8.6 for some lake areas: the highest soil moisture estimate (32.4%) is obtained for a lake area in Eastern (rightmost) part of the image. This value is evidently a far too high soil moisture value.

(a)

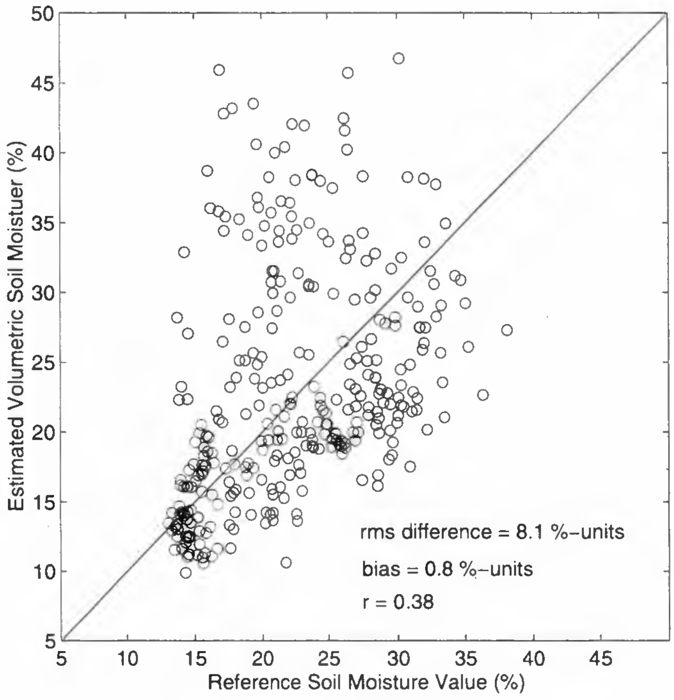

(b)

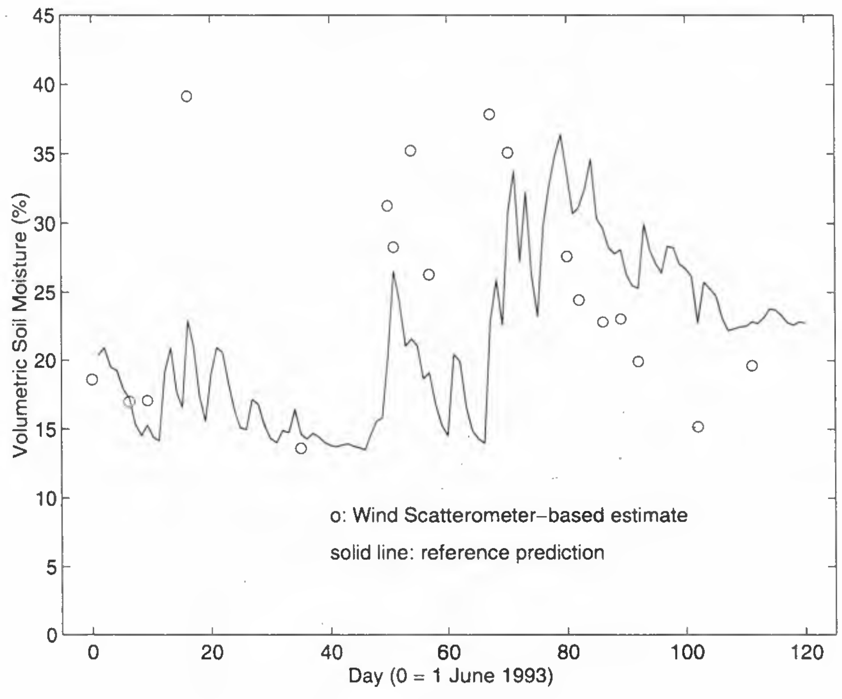

Figure 8.3. Soil moisture retrieval results for Porvoo and Eurajoki test areas (Southern Finland) for the time period from June to September 1993.
(a): Results for 323 pixel-wise measurements on 18 occasions. The test area includes 32 fixed grid cells for which the WS measurements were interpolated (each sized 25 km by 25 km).
(b): Comparison of average values of 18 measurement dates with the average reference moisture.

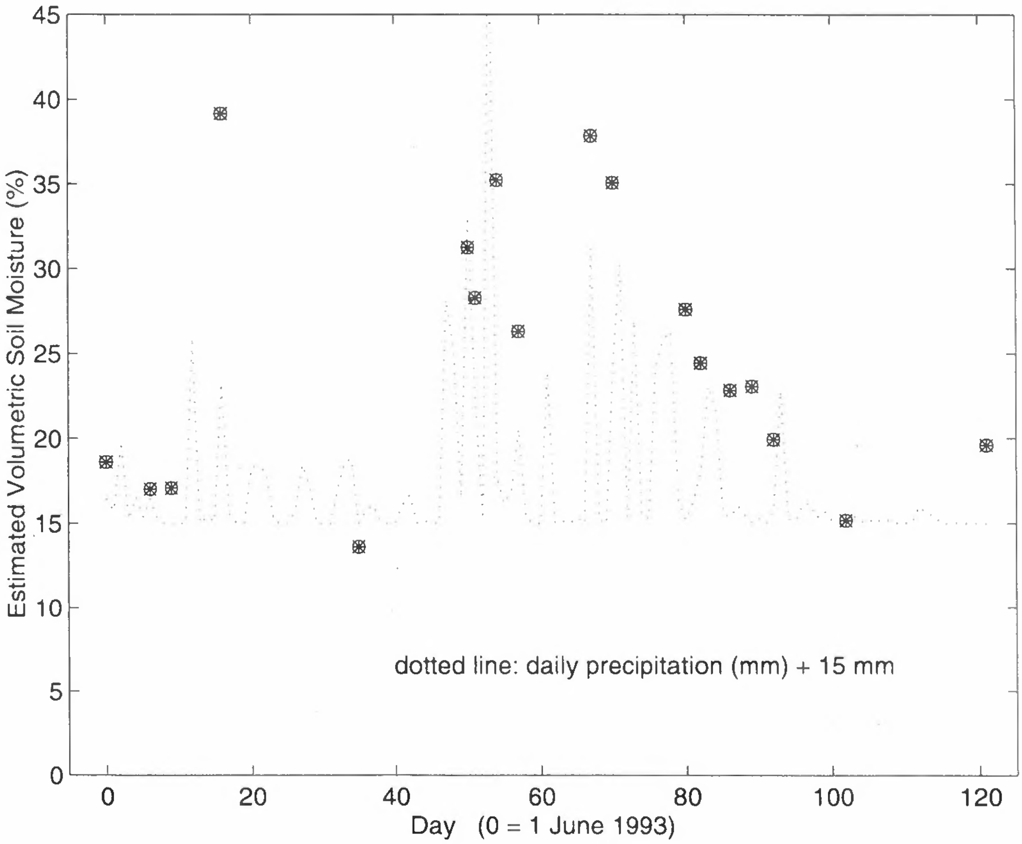

Figure 8.4. Comparison between the soil moisture estimate obtained and the two-day cumulative precipitation.

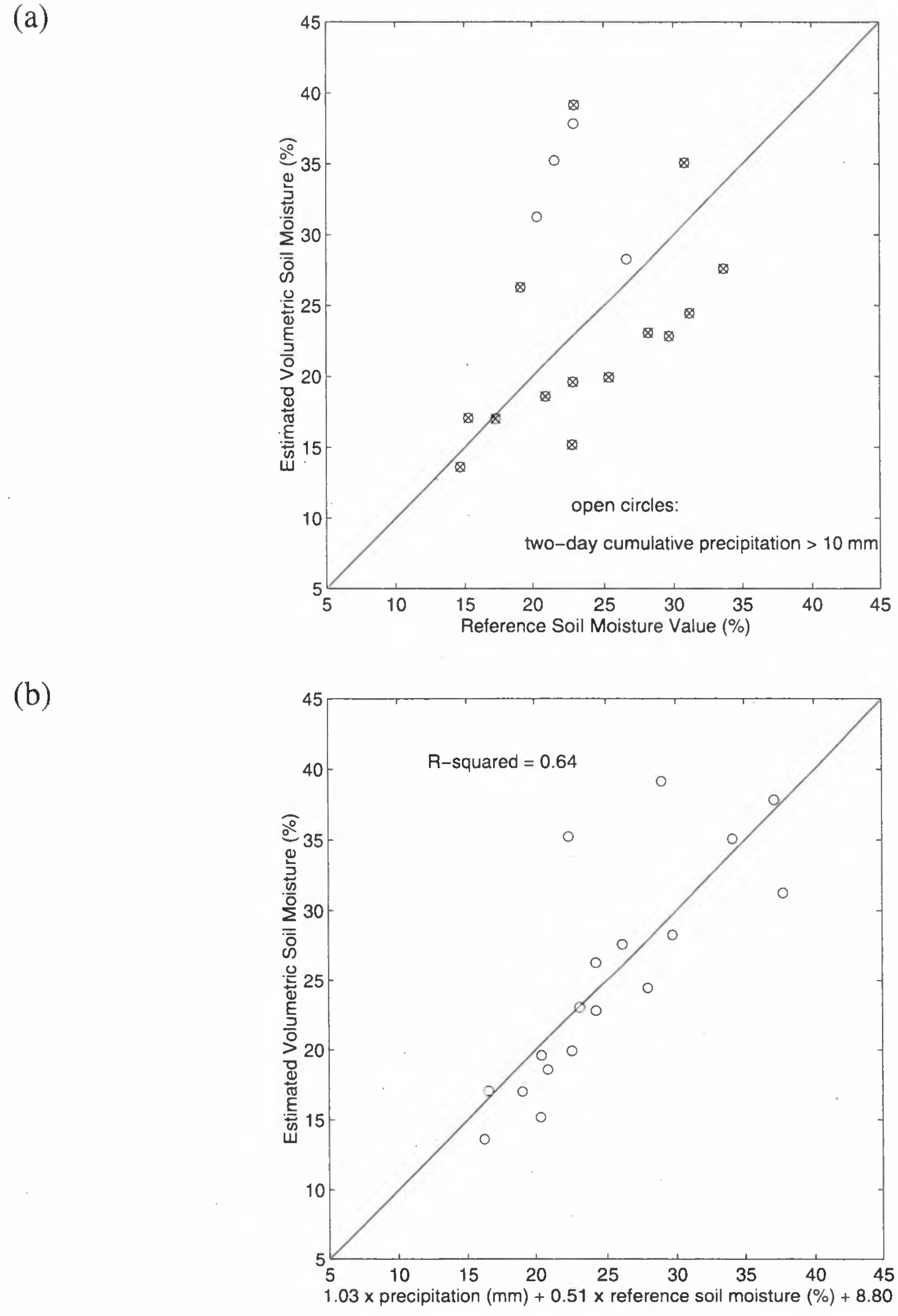

Figure 8.5. Comparison between the daily WS-based average soil moisture estimate against the reference soil moisture and two-day cumulative precipitation.
(a): Scattergram of daily measurements (refer to Figure 5.2 and 5.1). For measurement days with cumulative precipitation less than 10 mm the correlation coefficient with the soil moisture estimate and the reference soil moisture is 0.52 (0.34 for all dates).
(b) Regression relation between the soil moisture estimate and the sum of reference soil moisture and two-day cumulative precipitation.

ERS-1 Wind Scatterometer-Based Soil Moisture Estimate

Southern Finland, 10 June 1993

Figure 8.6. Soil moisture estimate for 10 June 1993. The results are interpolated into a 1 km by 1 km sized fixed grid (minimum value: 0% (lakes, sea and no-data), maximum value: 32.4%).

8.2 Detection of Soil Freezing

The detection of soil freezing was tested using ERS-1 Wind Scatterometer data of South Finland test area covering the time period from September to November 1993. The reference data employed were (1) daily weather statistics and (2) soil frost measurements for a set of ground stations. The soil frost information includes the depth of frost (in cm) separately for open areas and forests. These data were available for 19 locations in the South Finland test area for three dates per month. An average soil frost depth value for an individual 25 km by 25 km grid cell was calculated from this information using the grid cell-wise land use information on coverage fractions of open and forested areas. Since ERS-1 WS measurements were not available for exactly the same days as soil frost measurements for all cases, the WS data for close-by days were employed (the largest difference was two days).

The frost detection algorithm used is actually the first order soil moisture retrieval algorithm introduced in Section 8.1. The soil moisture retrieval algorithm estimates the soil moisture using a well validated relation between the soil dielectric constant and the volumetric soil moisture (*Hallikainen et Al. 1985*). When soil freezes, the soil dielectric constant decreases significantly and, as a consequence, the model predicts a low soil moisture (the model does not describe the frozen soil characteristics as a function of soil water (ice) content, and hence from the model point of view, a frozen soil behaves as a very dry soil). Therefore, when the inversion algorithm suggest an unrealistic low soil moisture value, it really detects a frozen area. Since the microwave backscatter is related to both vegetation and soil, the scatterometer-based soil estimate is also affected by the freezing of vegetation. However, the reference data employed in these investigation does not include any information on that matter. Hence, the results are only compared with air temperature and soil frost characteristics.

Figure 8.7 depicts the average behavior of soil frost depth and WS-based soil moisture estimate for the South Finland test area (and additionally the behavior of daily mean air temperature). The comparison is carried out for six occasions using soil moisture estimates and reference data values for a total of 19 locations scattered around the test area. The conclusion from the results is that under non-frost conditions the soil moisture estimates typically show values well above 10% (which can be also noticed in Figure 8.3), but in the case of frozen soil the estimates obtained are usually below 10%. Moreover, the soil moisture estimate appears to correlate with the depth of soil frost.

Figure 8.8 shows the behavior of the depth of soil frost as a function of WS-based soil moisture estimate for all 19 grid cells and for all 6 occasions. The results show that when the soil moisture estimate obtained is below 9.5%, the soil is either frozen or at least the mean air temperature is below freezing point (which may indicate that the forest/ground vegetation is partially frozen). Both Figure 8.8 and 8.7 indicate that ERS-1 Wind Scatterometer has considerable potential in mapping of soil/vegetation freezing. An WS-based image series on the evolution of soil frost in the South Finland test area for early November 1993 is shown in Appendix I.

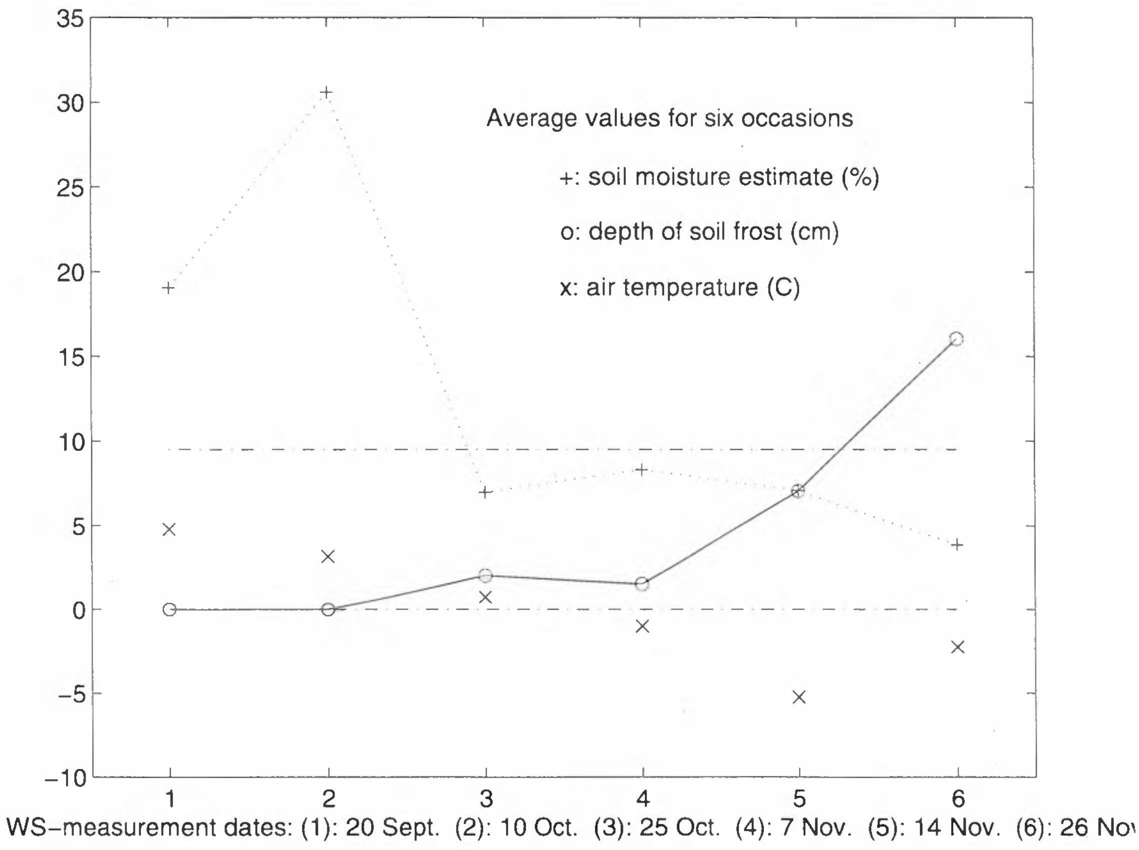

Figure 8.7. Behavior of WS-based soil moisture estimate (soil frost detector), depth of soil frost and daily mean air temperature in the South Finland test area for autumn 1993. The daily average values calculated from a total of 19 grid cells are presented (the measurements do not cover all grid cells on all occasions).
On y-axis is the soil moisture estimate (in %-units) and near surface air temperature (in C°). The upper dotted line shows the frost detection limit determined from individual grid cell-wise results (value of soil moisture estimate: 9.5%). The lower dotted line is the 0°C reference line.

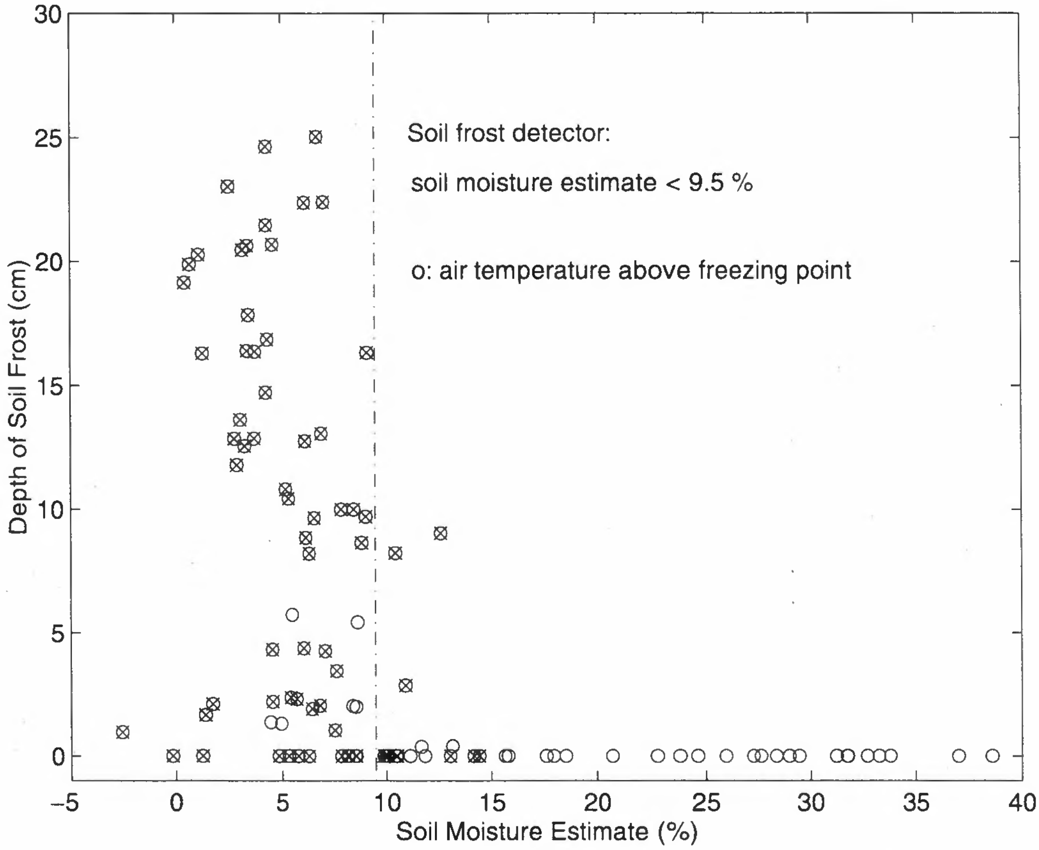

Figure 8.8. Relation between WS-based soil moisture estimate and the depth of soil frost. The grid cell-wise results for all six measurement occasions are shown. The cross-marked circles present the cases where mean air temperature has been below (or equal to) the freezing point.

8.3 Feasibility for Other Applications

The ERS-1 Wind Scatterometer data may have some applications not discussed in detail or tested in this study. According to the discussion in Section 4.5 the detection of snow melt can be feasible (similarly to detection of soil frost discussed in Section 8.2). Another area of application may be the mapping of total sea ice concentration.

Discussion in Section 6.2 indicates that WS data may have some limited potential in land use classification. However, in the case of forest biomass mapping its applicability is negligible, particularly due to the low spatial resolution.

9 Retrieval Algorithms for SSM/I Data

9.1 Retrieval of Surface Temperature from Summer-Time Data

Figures 7.42 and 7.43 show that the SSM/I data has a considerable potential in surface temperature estimation due to the fact that the surface emissivity of forested areas is relatively invariable with time during snow-free conditions. Hence, techniques for the retrieval of physical temperature (air temperature at the ground) using SSM/I data were developed and tested. The methods investigated include an inversion approach, similar to that discussed in Section 8 above, and additionally, two empirical approaches: (a) statistical multiple linear regression and (b) empirical polarization difference approach. The retrieval methods have been tested using the interpolated night/morning SSM/I results of some individual pixels of the Southern Finland test area covering the time period from July to September 1993 and June 1994.

Inversion approach

The inversion technique developed is based on the idea of taking an advantage of the invariable surface emissivity (invariable as a function time, but not spatially). The inversion approach is introduced here in the case of SSM/I but it applies to other space-borne microwave radiometers as well. The inversion method is a two-stage process that first estimates the average surface emissivity of a given location (fixed pixel) for each SSM/I channel using multi-temporal SSM/I data interpolated into that location. In the second stage, these emissivities are employed for the determination of the physical temperature (as Figures 7.42 and 7.43 show, once the target emissivities have been retrieved they can be considered to be invariant with time under snow-free conditions in the case of boreal forests).

First stage: estimation of target emissivity

The retrieval of target emissivity for a certain fixed location and for each SSM/I channel requires the employment of multi-temporal data. This is due to the fact that for a single measurement there are seven brightness temperature values available, but simultaneously there are seven unknown surface emissivities, an unknown surface temperature and unknown atmospheric conditions. The method developed overcomes this problem by using multi-temporal SSM/I data. The first stage of the algorithm estimates the surface emissivities, and additionally, the physical temperatures for a set of SSM/I measurements. The atmospheric effects can be treated using average atmospheric characteristics (the multi-temporal data set should cover a time period long enough that the mean atmospheric conditions are valid on average). The algorithm to estimate the surface emissivity (and simultaneously the physical temperatures for each measurement) can be written as:

$$\text{Minimize} \quad \sum_{j=1}^{N} \sum_{i=1}^{7} [(T_b)_{i,j} - g_{i,j}(e_i, (T_{phys})_j, \hat{\gamma})]^2, \tag{9.1}$$

where

$(T_b)_i$ = brightness temperature measured by the SSM/I instrument at ith channel and at jth measurement (19V: i=1, 19H: i:2, 22V: i=3, 37V: i=4, 37 H: i=5, 85V: i=6 and 85H: i=7)

N = total number of multi-temporal measurements

g = model for brightness temperature

e_i = surface emissivity at ith channel

$\hat{\gamma}$ = 0.0368, a constant that defines the mean atmospheric transmissivity (here corresponding to average Finnish conditions).

The model mapping g is

$$g_{i,j} = e_i (T_{phys})_j t_i(\gamma_j) + \alpha_{\uparrow}(T_{phys})_j (1 - t_i(\gamma_j)) + \alpha_{\downarrow}(T_{phys})_j (1 - e_i) t_i(\gamma_j)(1 - t_i(\gamma_j)), \tag{9.2}$$

where $\alpha_{\uparrow}$ and $\alpha_{\downarrow}$ are atmospheric profile factors related to atmospheric transmissivity t_i by a polynomial fit (*Aschbacher 1989*). t_i is given by a statistical principal component model (*Pulliainen et Al. 1993*):

$$t_i(\gamma) = \left[(t_P^0)_i + (t_P^1)_i \gamma\right]^{1.0681}, \tag{9.3}$$

where scalar variable $\gamma = \hat{\gamma} = 0.0368$ (average value for Finnish conditions). t_P^0 and t_P^1 are the zero-order and the first order principal components of atmospheric transmissivity for different SSM/I channels:

$$t_P^0 = (0.9211 \quad 0.9211 \quad 0.8326 \quad 0.8624 \quad 0.8624 \quad 0.6656 \quad 0.6656)^T \tag{9.4}$$

$$t_P^1 = (0.2069 \quad 0.2069 \quad 0.4642 \quad 0.2746 \quad 0.2746 \quad 0.8163 \quad 0.8163)^T \tag{9.5}$$

The exponent correction factor in Equation (9.3) arises from the fact that the principal component model (*Pulliainen et al. 1993*) is determined for the angle of incidence of 50°, whereas the angle of incidence in SSM/I measurements is 53.1°.

<u>*Second stage: estimation of surface temperature*</u>

Once the surface emissivities for a certain pixel have been determined, these values can be used for predicting the physical temperature for any measurement date. In this case, the atmospheric conditions do not have to be treated using a constant value for γ, instead it can be considered as a free parameter or as a Gaussian random variable with a known mean value and a known standard deviation. In this case the algorithm to estimate the physical temperature can be written as

$$\text{Minimize} \quad \sum_{i=1}^{7} \frac{1}{2\sigma_i^2}[(T_b)_i - g_i(e_i, (T_{phys}), \gamma)]^2 + \frac{1}{2\lambda^2}(\gamma - \hat{\gamma})^2, \tag{9.6}$$

where

σ_i = standard deviation of SSM/I measurement at ith channel (assumed to be 2 K at 19, 22 and 37 GHz channels and 5 K at 85.5 GHz channels)

λ_i = standard deviation of γ (0.05 used in these investigations)

$\hat{\gamma}$ = mean value of γ.

Inversion algorithm testing

Figure 9.1 shows the results obtained using the inversion method developed (Equations (9.1) and (9.6)). The results are determined covering the time period from July to September 1993 and June 1994 using interpolated data from pixel #131 of the North Finland test area. In this case, 30 first data points from July and August 1993 were used for the determination of surface emissivities for different SSM/I channels employing Equation (9.1). After that, the physical temperatures were estimated for the whole data set using these constant emissivity values. Figure 9.1b only depicts the results for a test data set of 49 dates in order to enable a direct comparison with the results obtained using empirical methods.

Figure 9.1b shows a 6.03 °C bias compared with the reference value. When the inversion method was tested for other pixels of the South and North Finland test areas, about the same bias emerged. The evident reason for the bias is that the absolute level of the temperature estimate is influenced by the accuracy of the atmospheric model. For example, when the atmospheric transmissivity is kept constant in the first stage of the inversion algorithm (Equation (9.1)), the physical surface level temperature is the only varying parameter that effects on the upwelling atmospheric brightness temperature (the second sum term in Equation (9.2)). However, the atmospheric contributions are quite insensitive to changes in the physical temperature, e.g. a 1 °C increase in the physical temperature only causes an increase of from 0.1 to 0.3 °C (depending on the frequency) in the upwelling atmospheric brightness temperature. Hence, a small inaccuracy in atmospheric model can cause a relatively large about constant bias in the physical temperature estimate. This is also demonstrated in Figure 9.2 which shows that an about constant bias emerges into the upwelling atmospheric brightness temperature if there exists a 2% inaccuracy in term $\alpha_{\uparrow}$. In the case of Figure 9.2, the 2% error in the atmospheric consideration causes a bias higher than 5 K in the physical temperature. In Figure 9.1a, as well as in most forthcoming figures, the average 6.03 °C bias is removed.

The pixel-wise behavior of the retrieval bias is shown in Figure 9.3a. These results are obtained for 48 grid cells and they indicate that the bias is fairly constant at different locations. The corresponding retrieval errors for all data points of the one year period are depicted in Figure 9.3b (5057 samples). These results, as well as Figure 9.4a, show that the rms retrieval error for all data points is about 2.2 °C. If the results for a single grid cell are investigated, the retrieval error can be significantly lower. This is shown in Figures 9.4b and 9.4c. Figure 9.4b depicts that for a single grid cell the retrieval error can be as small as 1.2 °C. The higher level of scatter evident in Figures 9.3b and 9.4a is mainly due to the varying bias between the different grid cells. Figure 9.4c shows the pixel-wise rms errors for all grid cells. These characteristics imply that the retrieval error is low (and r^2 is high) for most pixels. However, for some pixels poor values are observed. The evident reason is illustrated in Figure 9.5: the higher is the coverage fraction of water or agricultural areas, the higher is the retrieval error. The explanation is that the surface emissivity is the more constant, the higher is the coverage fraction of forests. In contrast to that, seasonal or wind conditions dependent variations are apparent in water and agricultural areas. Moreover, the physical temperature of the target is nearer to the air temperature at the height of 2 m for forested areas than for open areas.

As Chapter 7 indicates the temperature retrieval method should not work under snow cover conditions. This is also demonstrated in Figure 9.6 which shows the estimation results for a single pixel for the whole one year period. The surface emissivity decreases due to the snow cover, and hence, the inversion method tends to underestimate the physical temperature.

(a)

(b)

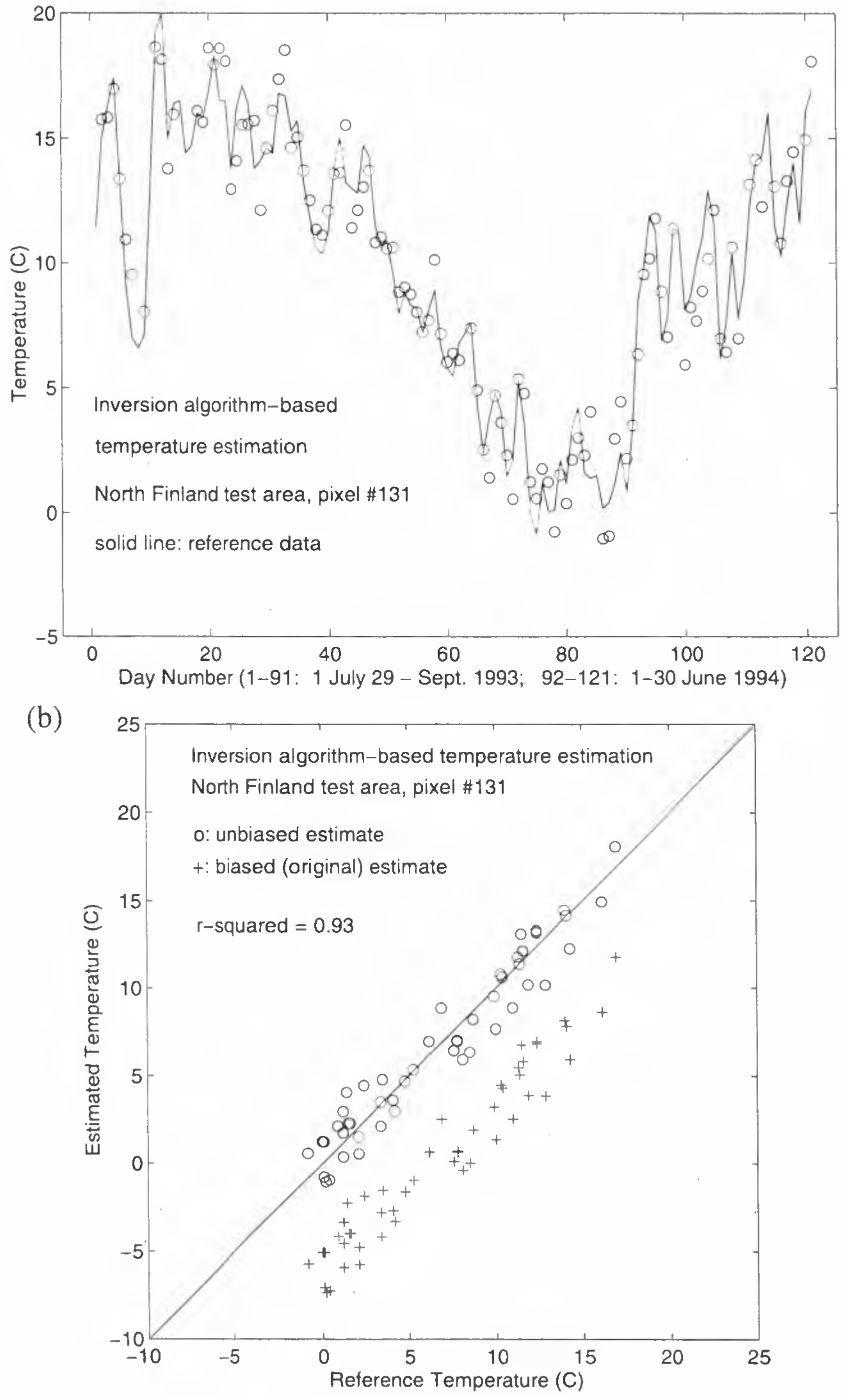

Figure 9.1. Inversion algorithm-based temperature estimation results for pixel #131 of the North Finland test area using a test data set of 49 SSM/I measurements from September 1993 and June 1994. The reference temperature is the ground-based average daily air temperature.
(a) Unbiased results for the whole four-month period.
(b) Estimation results for the 49 point test data set (September 1993 and June 1994). Both the biased and unbiased estimates are shown.

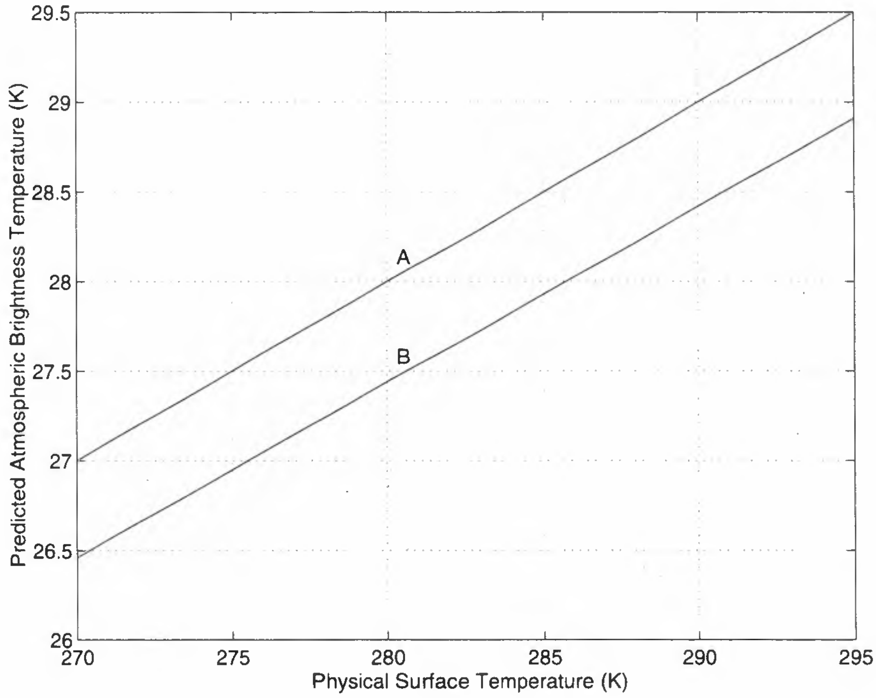

Figure 9.2. Effect of inaccuracy in atmospheric consideration ($\alpha_{\uparrow}$) on the upwelling atmospheric brightness temperature contribution $\alpha_{\uparrow}(1-t(\gamma))T_{phys}$ as a function surface temperature. For curve A: $\alpha_{\uparrow}(1-t(\gamma)) = 0.1$ and for curve B: $\alpha_{\uparrow}(1-t(\gamma)) = 0.098$.

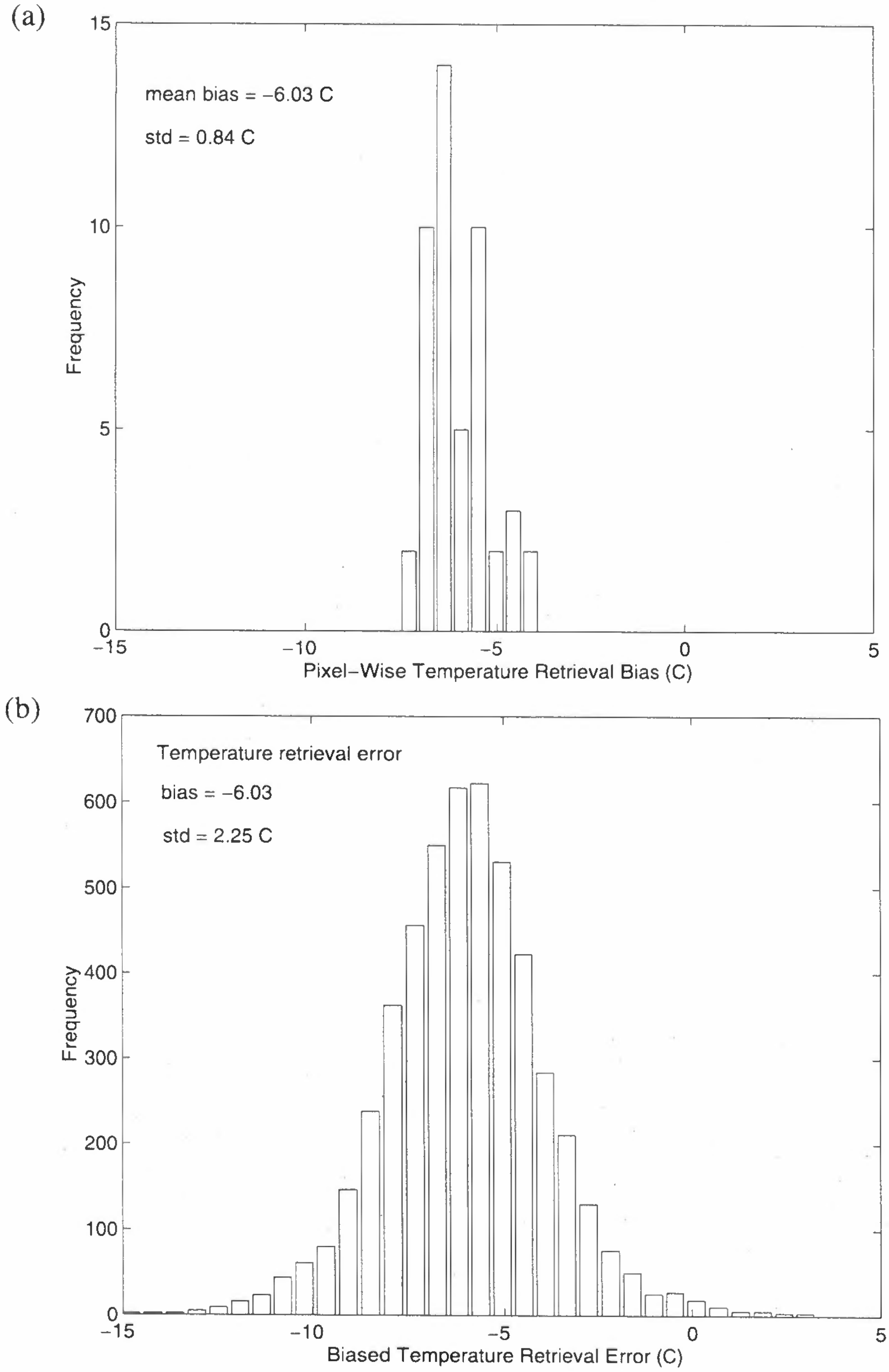

Figure 9.3. Behavior of inversion error for the set 48 grid cells.
(a) Behavior of pixel-wise bias (pixel wise average retrieval error).
(b) Retrieval error for all 5057 estimates.

(a)

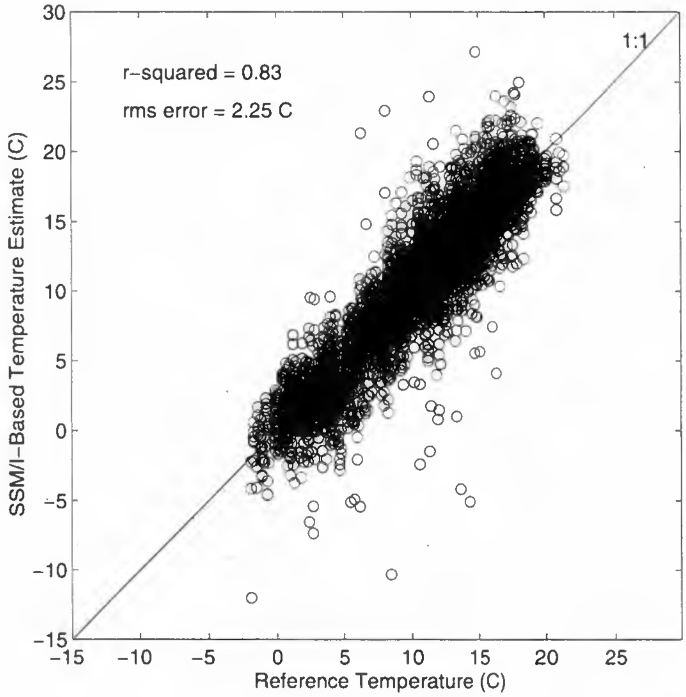

(b)

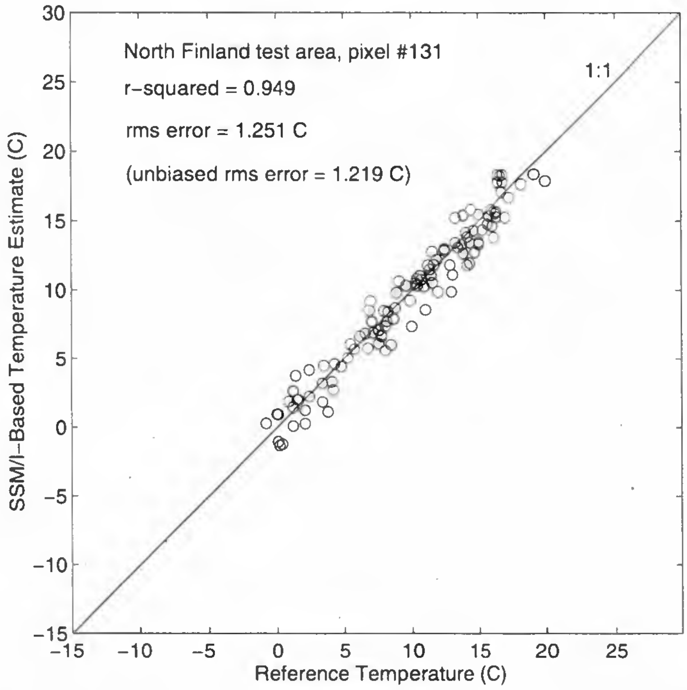

Figure 9.4. Inversion algorithm-based temperature retrieval results using SSM/I data from July to September 1993 and June 1994.
(a) All grid cells employing the mean bias correction (6.03 °C).
(b) A single pixel (#131 of North Finland test area).
(c) Pixel-wise unbiased retrieval error.

(c)

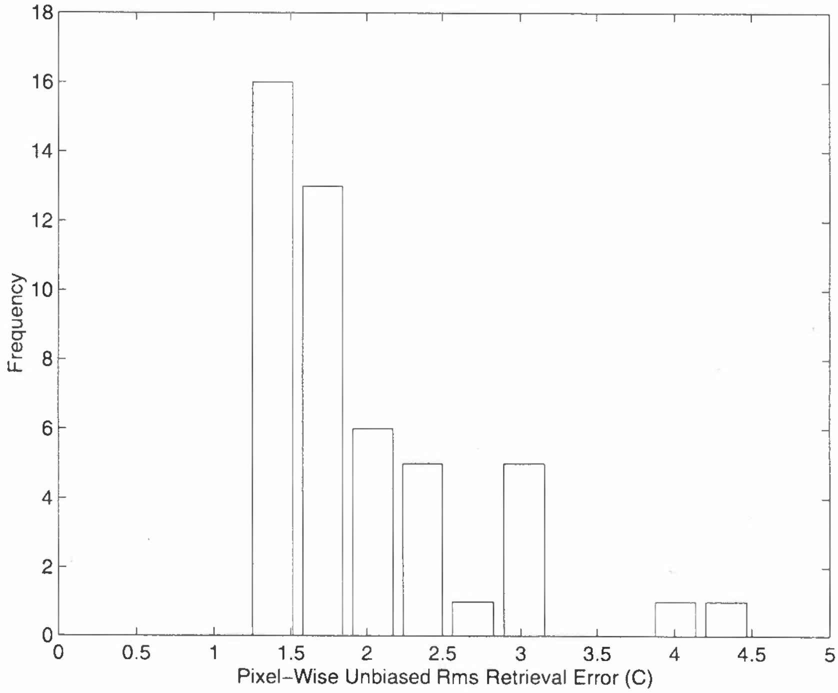

Figure 9.4 continued.

(a)

(b)

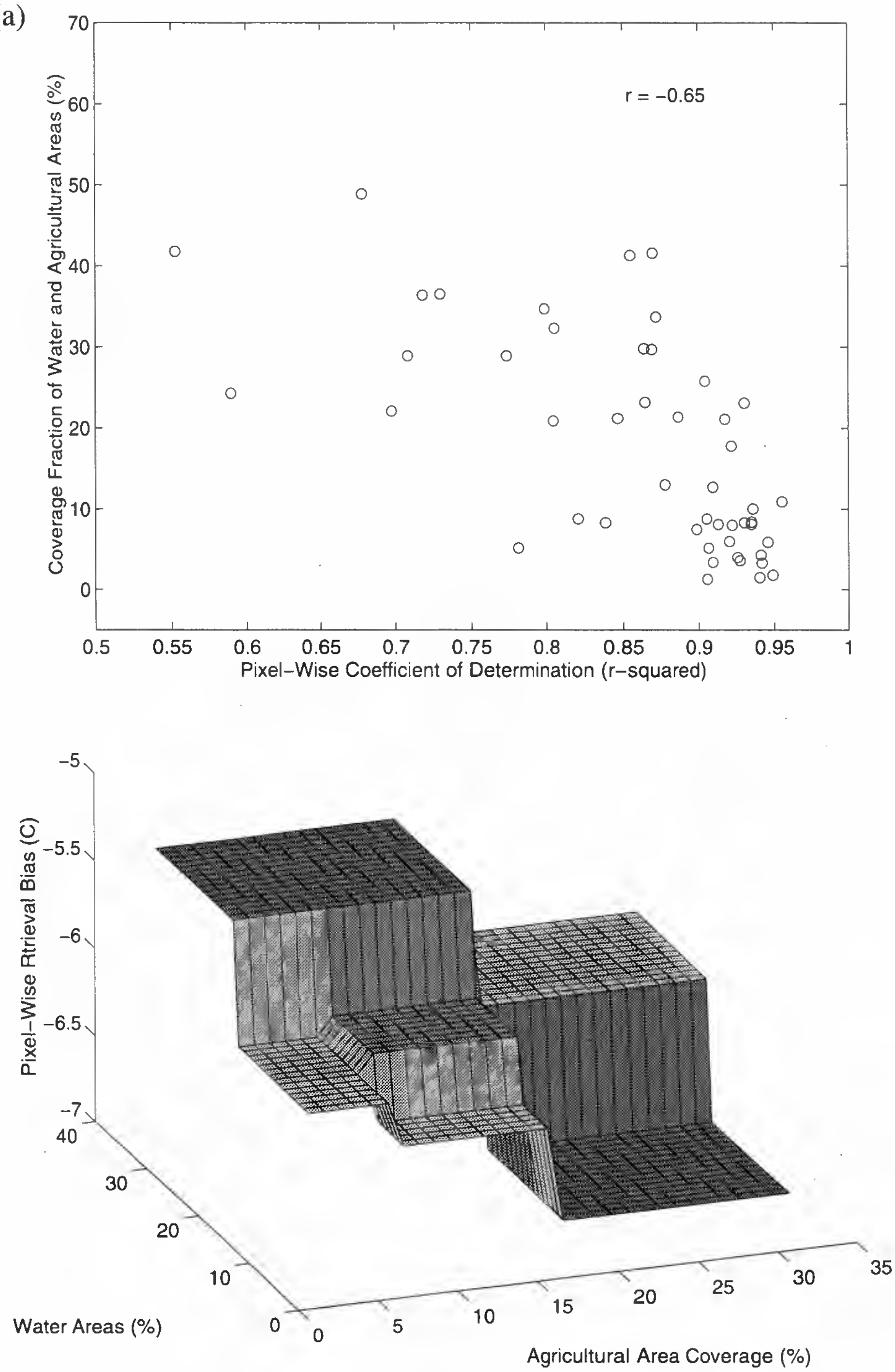

Figure 9.5. Effect of land use on retrieval accuracy (coefficient of determination) and pixel-wise retrieval bias.

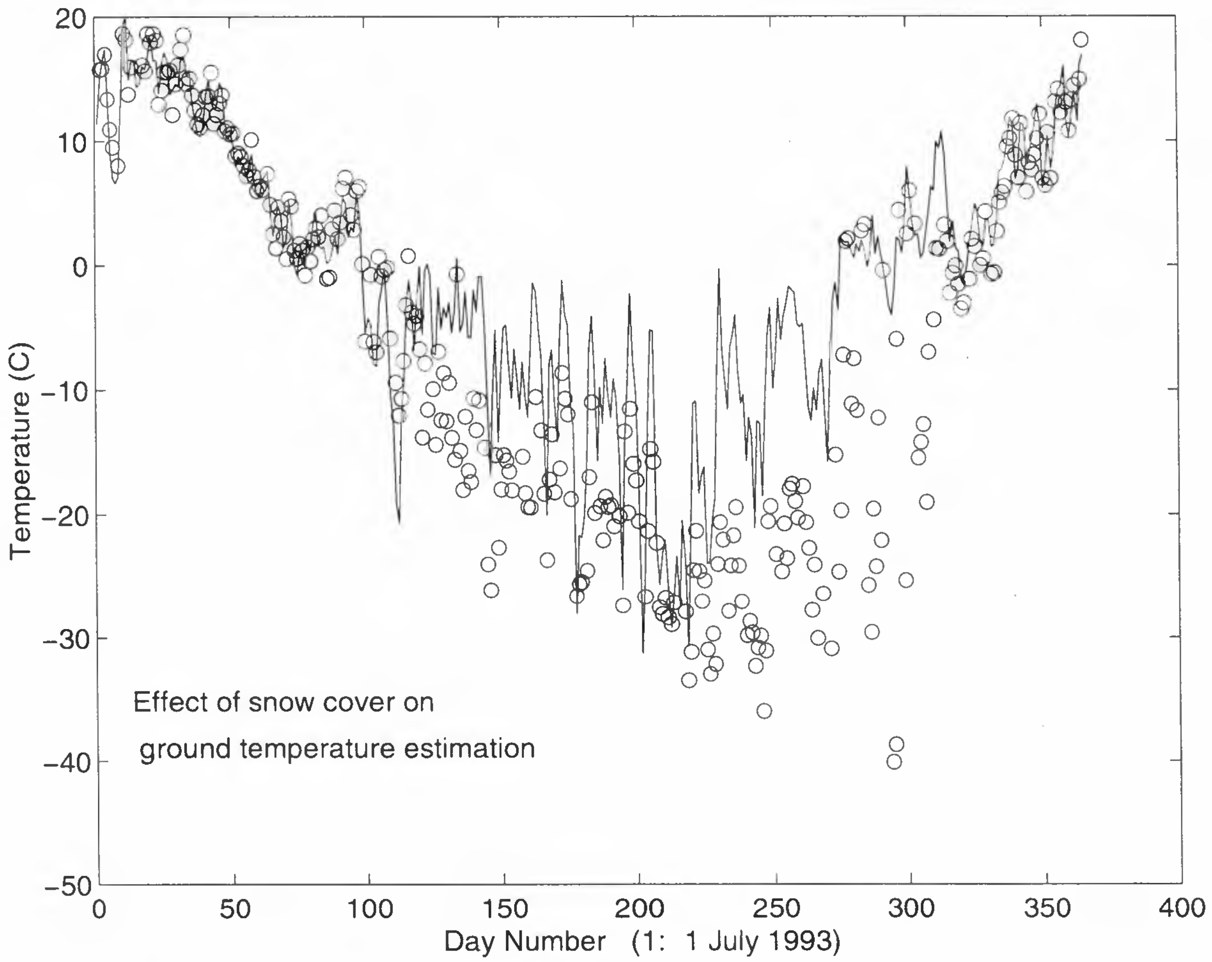

Figure 9.6. Inversion algorithm-based temperature estimation results for pixel #131 of the North Finland test for a one year period. The snow cover starts to evolve after day 100 and melts off after day 320, refer to Figure 7.44.

Empirical methods

The empirical methods were tested by applying formulas retrieved from the SSM/I data from all 48 test grid cells (for the South and North Finland test areas). A 60-day teaching data set was used in the determination of regression coefficients for the algorithms. The algorithms were tested using (a) all measurement dates and (b) a test data set that excluded the teaching data. Additionally, single grid cell-wise empirical formulas were retrieved for some grid cells.

Regression equation using data from all test sites

Figure 9.7 presents the results obtained for a single pixel (#131 of the North Finland test area) using multiple linear regression model that was developed using data from all 48 test grid cells. The results can be directly compared with the results of inversion algorithm shown in Figure 9.1. SSM/I results and reference air temperature values from 60 consecutive measurements (July, August and early September 1993) are employed in the determination of regression coefficients. The regression model obtained is then tested using 49 data points from September 1993 and June 1994. The regression algorithm obtained for the retrieval of the air temperature at the surface level T in °C is

$$T = 0.2769 \cdot T_{b,19V} - 0.5101 \cdot T_{b,19H} + 0.9758 \cdot T_{b,22} + 0.6959 \cdot T_{b,37V}$$
$$- 0.4244 \cdot T_{b,37H} - 0.03812 \cdot T_{b,85V} - 0.02716 \cdot T_{b,85H} - 243.3. \tag{9.7}$$

The results for test data from a single grid cell show that a small bias has emerged and the rms retrieval error is 1.96 °C. The coefficient of determination $r^2 = 0.94$. The corresponding figures with statistical approach depicted in Figure 9.1 show somewhat higher accuracies: a rms retrieval error of 1.34 °C and $r^2 = 0.93$. Grid cell #131 of the North Finland test area is a relatively homogeneous heavily forested area (having a forest cover fraction of about 80 %). The inversion approach works best for these kind of areas as Figure 9.5 indicates. When multiple linear regression algorithm was tested for more diversified grid cells, it gave significantly higher accuracies than the inversion technique. This is evident as the discussion in Section 7.2 states, since the surface emissivity varies temporally the more, the smaller is the forest cover coverage. This is not the case with the regression formula of Equation (9.8) since it was developed using teaching data from all grid cells. Hence, the multiple linear regression formula gave higher overall accuracies than the inversion approach when data from 48 grid cells covering all dates were used for testing. The performances obtained in this case are: $r^2 = 0.91$ and a rms error of 1.54 °C for the multiple linear regression, and $r^2 = 0.83$ and a rms error of 2.24 °C for the inversion approach.

Regression equation using data from a single test site

The multiple linear regression was also tested by retrieving a single pixel-wise regression formulas for some pixels. For example, when the regression model is determined for pixel #131 of the North Finland test area, the formula corresponding to Equation (9.8) (using again a 60-day teaching data) is

$$T = 0.2510 \cdot T_{b,19V} + 0.7492 \cdot T_{b,19H} + 0.2093 \cdot T_{b,22} - 0.4387 \cdot T_{b,37V}$$
$$+ 0.1079 \cdot T_{b,37H} + 0.1703 \cdot T_{b,85V} - 0.0254 \cdot T_{b,85H} - 254.8. \tag{9.8}$$

The retrieval performances obtained for this single grid cell algorithm show the following values (using a 49-day test data set): $r^2 = 0.90$ and a rms error of 1.68 °C which are slightly poorer characteristics than those obtained by the inversion method.

Regression equation using three SSM/I channels and data from all test sites

Multiple linear regression was also tested using channel subset regression formulas. These tests indicate that instead of employing all seven SSM/I channels almost as high performances can be obtained using only three channels: 22 GHz channel, and 19 Ghz V and H polarized channels (i.e. only three empirical coefficients and an intercept constant have to be determined from the teaching data). The regression equation for T (in C°) obtained similarly to Equation (9.7) is

$$T = 0.8315 \cdot T_{b,19V} - 0.9173 \cdot T_{b,19H} + 1.022 \cdot T_{b,22V} - 240.0. \tag{9.9}$$

The performances obtained using data from 48 test grid cells and all dates are: $r^2 = 0.90$ and an rms error of 1.58 °C.

Polarization difference approach

Hiltbrunner et al. (1994) suggested an empirical algorithm for the retrieval of physical temperature retrieval using SSM/I data. The algorithm is based on the employment of the polarization difference at 19 GHz and it can be represented as:

$$T_{phys} = \frac{kT_{b,19V} - (k-1)T_{b,19H}}{e_x}. \tag{9.10}$$

where k and e_x are empirical constants that have to be retrieved from a teaching data set. In (*Hiltbrunner et al. 1994*), the values for e_x were obtained from ground-based radiometer measurements of short vegetation and bare soil targets and the values for k were obtained by fitting Equation (9.10) into reference soil temperature measurements using actual SSM/I data. Since any *in situ* emissivity measurements on boreal forest were not available, both k and e_x had to be determined from the SSM/I data in this investigation.

The parameters k and e_x were determined from a teaching data set covering 60 dates in order to compare the polarization difference algorithm directly with the results obtained using inversion approach and multiple regression formulas. The mean values obtained for the 48 test grid cells are: $k = 2.275$ and $e_x = 0.9432$.

The algorithm was first tested for some individual grid cells. The results obtained for pixel #131 of the North Finland test area showed the following performances: $r^2 = 0.88$ and a rms error of 2.51 °C. These are significantly lower performances than those obtained by the inversion approach and the regression formula of Equation (9.7). When the polarization difference method was tested using all data from 48 grid cells covering all different dates, it gave accuracies lower than those obtained by the regression formula but slightly higher than those obtained by the inversion approach: $r^2 = 0.85$ and a rms error of 1.98 °C. Figure 9.8 shows the comparison of grid cell-wise performance between the polarization difference algorithm and the inversion approach. The histograms of pixel-wise coefficients of determination are depicted. The results clearly indicate that the inversion algorithm has a larger potential most cases, i.e. in the cases of heavily forested grid cells. In cases of mixed pixels the performance of polarization difference method is higher (refer to Figure 9.5).

The polarization difference approach requires the employment of two empirical coefficients that have to retrieved using satellite-borne teaching data (unless any experimental ground-based emissivity measurement data sets are available). However, the algorithm has some physical background, which probably increases its feasibility compared with the multiple linear regression formulas.

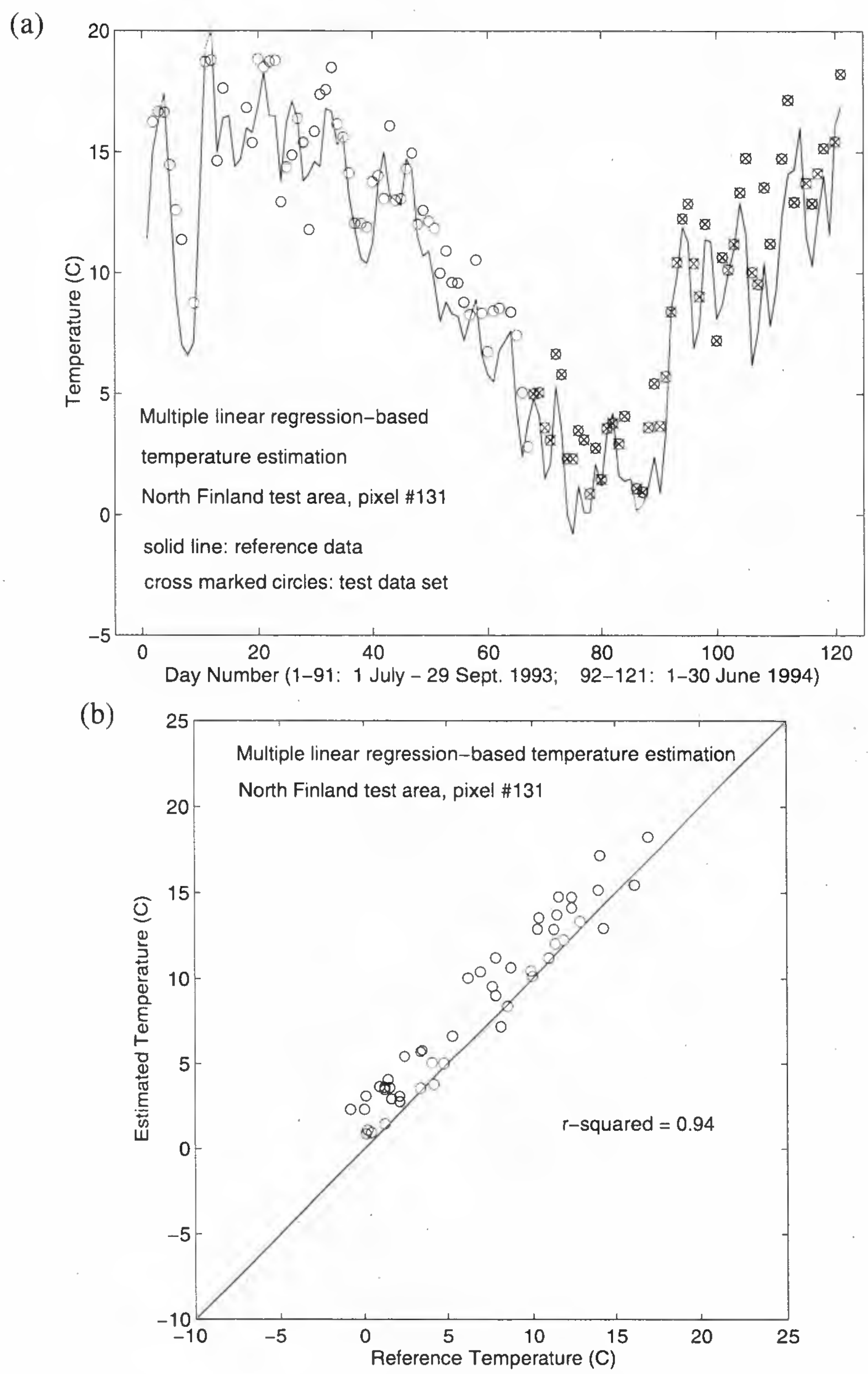

Figure 9.7. Multiple linear regression-based temperature estimation results for pixel #131 of the North Finland test area using a set of 109 SSM/I measurements from July to September 1993 and June 1994. The reference temperature is the ground-based average daily air temperature. The 60 consecutive data points from all test grid cells covering the time period from July to September 1993 are used for the determination of regression coefficients (algorithm teaching).
(a) Results for the whole four-month period.
(b) Estimation results for the 49 point test data set (September 1993 and June 1994), respectively to Figure 9.1b.

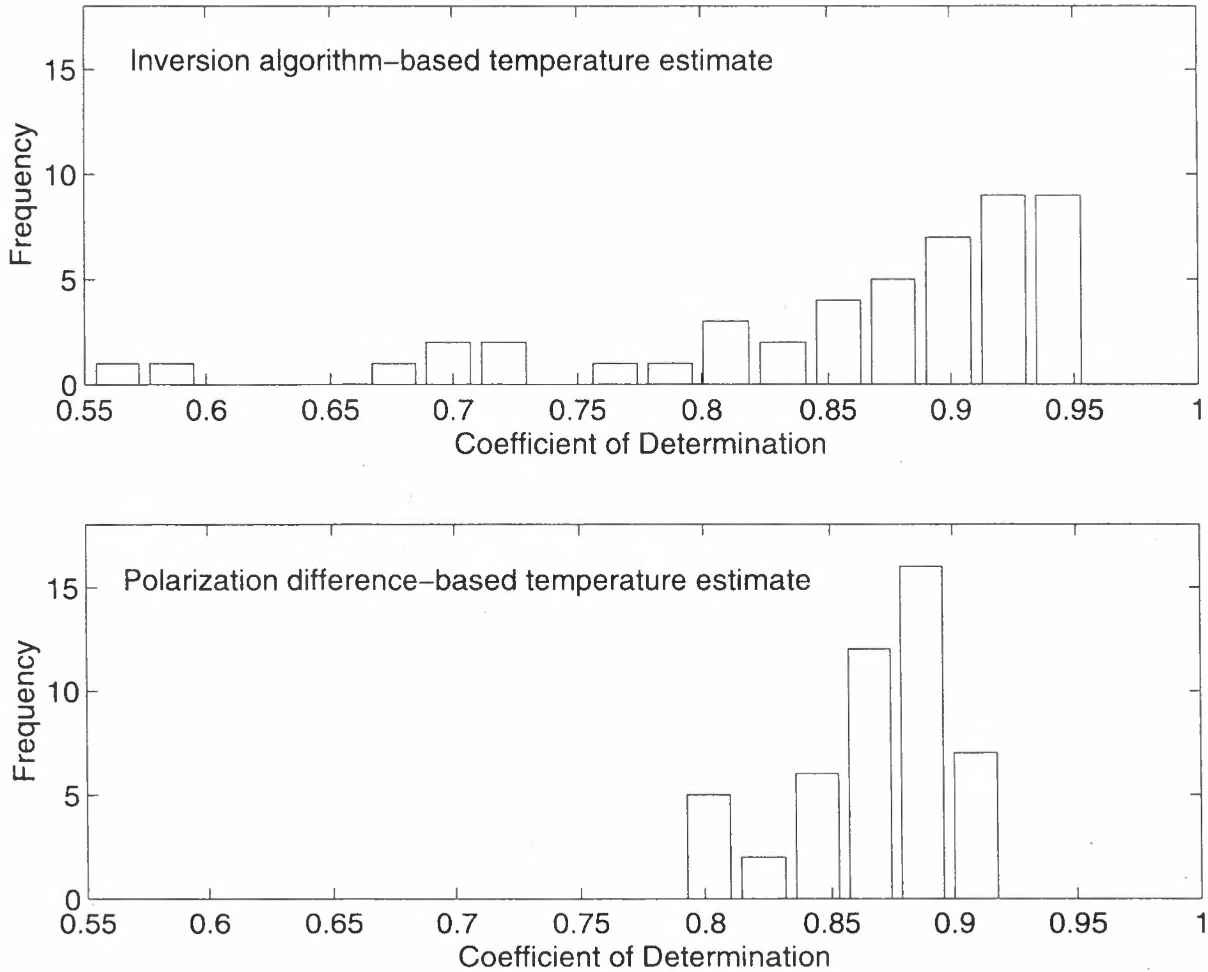

Figure 9.8. Behavior of pixel-wise coefficient of determination in cases of statistical inversion approach and polarization difference method.

Comparison of retrieval algorithms

When multiple linear regression formulas are compared with the inversion approach, one should note that the regression methods have some drawbacks that do not appear in the case of the inversion method. First, regression formulas require teaching data over long periods. Second, they employ several model coefficients that do not have any physical background. Since the physical background is lacking, the applicability of the method is restricted to conditions similar to those under which the algorithm was developed.

Also the polarization difference approach requires the employment of two empirical coefficients that have to retrieved using satellite-borne teaching data (unless experimental ground-based emissivity measurement data sets are available). However, the algorithm has some physical background, which probably increases its feasibility compared to the multiple linear regression formulas.

Table 9.1 presents a comparison of the three temperature retrieval approaches. The results were obtained using all test grid cells and all measurement dates. Additionally, the test results for some individual pixels are presented. The comparison shows that the multiple linear regression equations and the empirical polarization difference equation gave better overall performance than the inversion method. However, in the case of individual pixels the inversion approach may give better performance. Especially, this is the case for heavily forested pixels. In Table 9.1, grid cells #111 and #131 represent heavily forested areas, while grid cell #249 represents a mixed pixel. The same feature is also illustrated in Figure 9.8 which shows a comparison of grid cell-wise performances between the polarization difference algorithm and the inversion approach. Figure 9.8 depicts the histograms of pixel-wise coefficients of determination. The results clearly indicate that the inversion algorithm provides better results in most cases, including the cases of heavily forested grid cells. For mixed pixels the performance of polarization difference method is better (see Figure 9.5).

Table 9.1. Comparison of four temperature retrieval formulas (using all measurement dates from July - September 1993 and June 1994). The overall and single grid cell-wise rms retrieval errors and coefficients of determination are shown.

	All Grid Cells		Examples of Single Grid Cell-Wise Results					
Method	48 Pixels		Pixel North #111		Pixel North #131		Pixel South #249	
	rms (C°)	r^2	rms (C°)	r^2	rms (C°)	r^2	rms (C°)	r^2
Inversion Method (Eqs. (9.1) - (9.6))	2.25	0.83	1.37	0.94	1.25	0.95	2.11	0.87
7-Channel Multiple Regression (Eq. (9.7))	1.55	0.91	1.72	0.93	1.82	0.94	1.40	0.89
3-Channel Multiple Regression (Eq. (9.9))	1.58	0.90	1.67	0.93	1.75	0.93	1.52	0.88
Polarization Difference (Eq. (9.10))	1.98	0.85	2.19	0.90	2.39	0.88	2.00	0.80

Summary

The results obtained show that in the case of boreal forests the physical temperature at the surface level can be retrieved with an accuracy of from 1.2 to 2.5 °C using SSM/I data (space-borne microwave radiometer data) under snow free conditions. These performances are about the same or even higher than those reported for space-borne infrared instruments. Reported accuracies for NOAA AVHRR show values from 1.5 to 3.0°C (*Kerr et al. 1992, Vidal 1991*). Moreover, the usability of microwave data is not affected by weather conditions (cloud cover) as the employment of infrared/optical data. The results presented in this paper were determined without any data rejection. However, the SSM/I-based temperature retrieval is only possible under snow free conditions when the surface emissivity of forested areas remains in a constant value at a given location.

Three methods for interpreting SSM/I data were employed: (1) a novel inversion approach, (2) statistical multiple linear regression and (3) empirical polarization difference method. The physical temperature estimated was the air temperature at height of 2 m. The results showed that the inversion approach gives the highest accuracies in the case of pure forest targets. In these cases the rms retrieval accuracy is typically as high as from 1.2 to 1.8 °C (varying pixel-wise). However, the performance of the inversion method considerably declines as the coverage of water bodies or agricultural areas increases (the critical value is roughly 20 % of the total target area). Since the two empirical methods employed are developed using data from different kind of test areas, their accuracies did not vary considerably between the cases of heterogeneous and homogeneous targets. The observed variation in performances (rms retrieval error) was roughly from 1.4 °C to 2.0 °C for the multiple linear regression-based algorithm and from 1.9 °C to 2.5 °C for the polarization difference algorithm.

Since the empirical methods do not significantly suffer from the presence of water or agricultural areas, they gave overall accuracies higher than the inversion approach. The overall rms errors obtained were: 2.2 °C for the inversion approach, 1.5 °C for the multiple linear regression and 2.0 °C for the polarization difference algorithm (however, the empirical algorithm testing was conducted using the whole data set including the teaching data). Even though the empirical methods gave somewhat higher overall performances, they have some serious drawbacks, e.g. they include at least two empirical coefficients with no physical background which reduces their applicability to targets and conditions for which they were developed. The inversion algorithm only applies one empirical parameter (average retrieval bias).

The temperature retrieval algorithms were tested using point measurement values of daily average air temperature at the height of 2 m. As the SSM/I data was interpolated into 25 km by 25 km sized fixed grid cells, the reference data itself probably cause some unfavourable effects. The reference data does not represent the air temperature for the whole grid cell area and for the hour of imaging. Furthermore, the SSM/I measurements are not actually affected by the ground level air temperature, but the forest and forest floor physical temperature which can be slightly different from the air temperature (especially in open areas). Thus, the accuracy characteristics presented in this paper can give to a degree pessimistic view of the applicability of SSM/I instrument for the boreal forest temperature monitoring. The SSM/I-based temperature mapping is demonstrated in Figure 9.9 which shows the evolution of surface air temperature for early September 1993 in Northern Finland. The map is determined using the developed inversion algorithm for temperature retrieval.

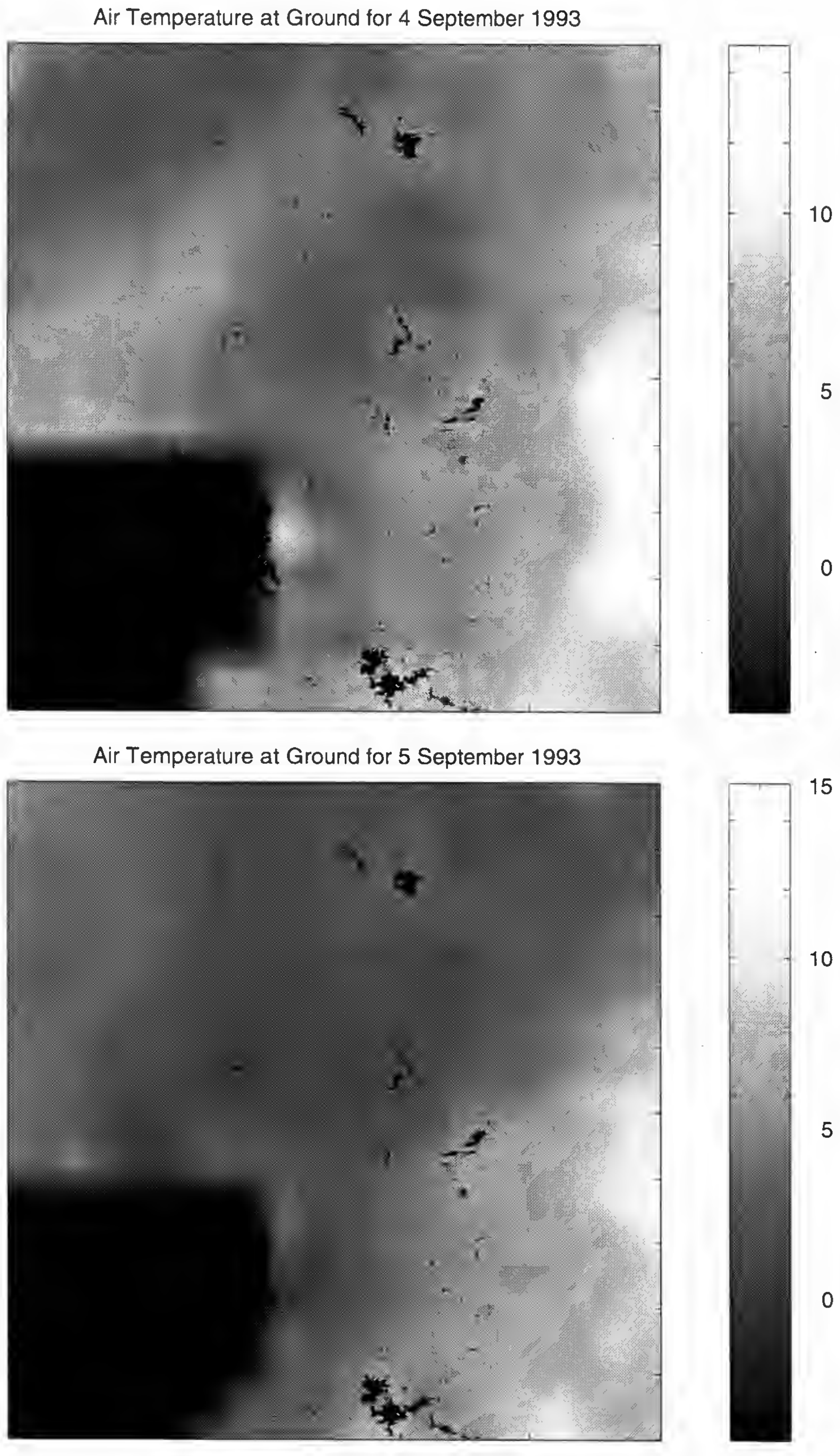

Figure 9.9. SSM/I-based evolution of surface air temperature at the North Finland test area for earl. September 1993.

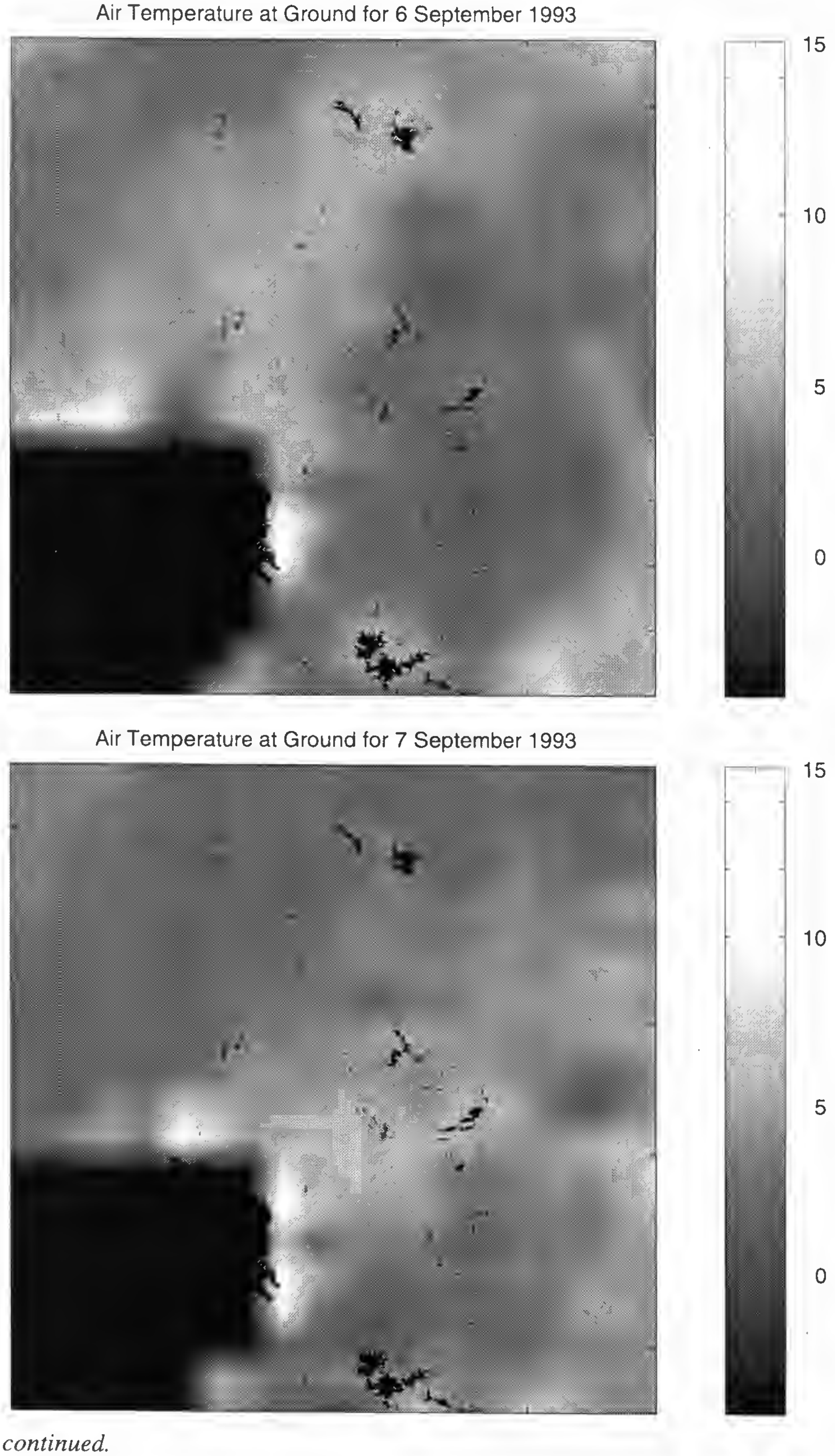

Figure 9.9 continued.

9.2 Retrieval of Snow Water Equivalent and Snow Density

The inversion method used is similar to those described in Sections 8.1 and 9.1. The method is based on a least squares minimizing equation. In order to fully understand the inversion results, the behavior of the main snow parameters for a typical winter has to be known. Therefore, measured snow water equivalent and snow density values are shown in Figures 9.10 and 9.11. The results have been obtained from about 100 line measurement sites throughout Finland. Most of the measurements have been conducted twice a month (around the 1st and the 15th day of the month), therefore the scatter plots have concentrated around certain days.

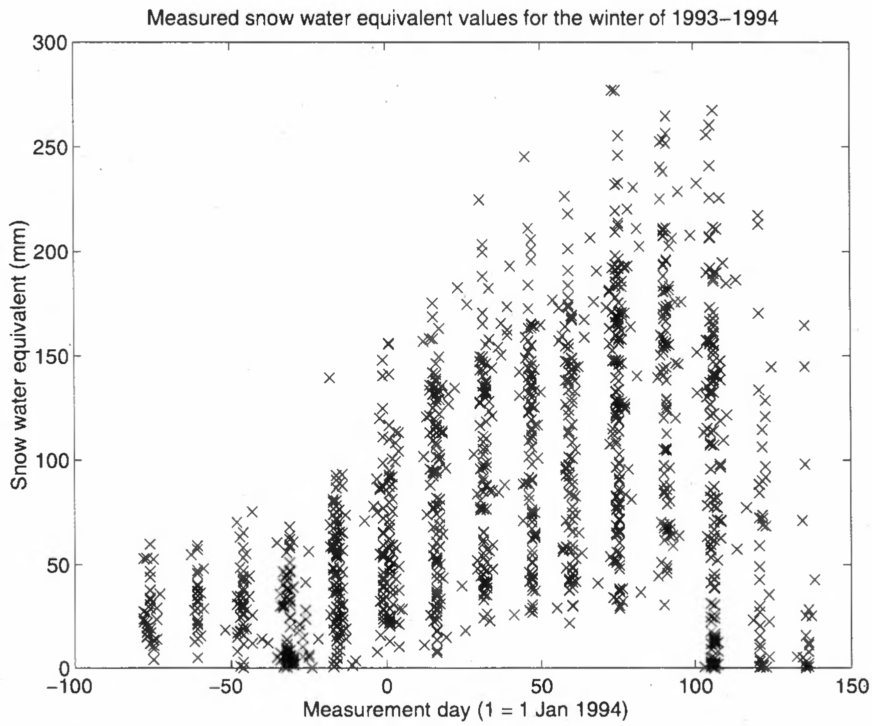

Figure 9.10. Measured snow water equivalent values (reference data) for the winter of 1993-1994 in Finland.

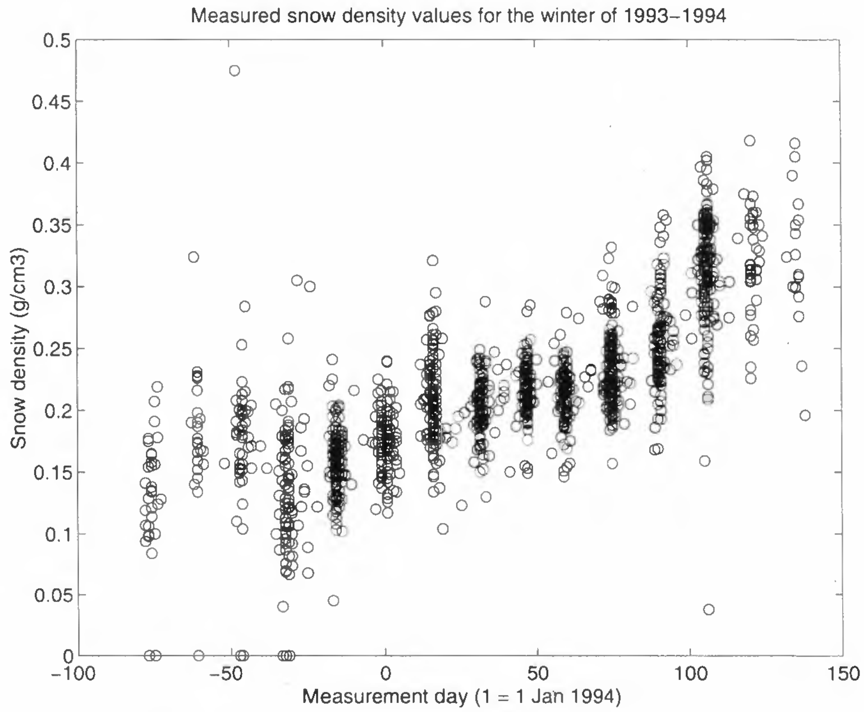

Figure 9.11. Measured snow density values (reference data) for the winter of 1993-1994 in Finland.

It is evident from the figures, that temporal and geographical variations are large both for snow water equivalent and snow density values during a typical winter in Finland. The snow water equivalent reaches peak values of >250 mm for northernmost parts of Finland, but in southern parts the snow water equivalent may saturate to even 50 mm or less. The density values tend to rise throughout the winter, due to the increased weight of the snow layer. The snow structure also changes towards spring, and especially grain sizes tend to grow. No exact measurement data similar to those depicted in Figures 9.10 and 9.11 exist, though.

The feasibility of the snow model for inversion purposes was studied for three main test periods, i.e. at the 1) beginning of the snow season, 2) in the middle of the snow season and 3) at the end of the snow season. Figures 9.12 to 9.21 show the results for the South Finland test area only. The comparison between the North and South Finland test areas is discussed later in this Section. The density values used as initial values for the inversion were obtained from the seasonal variation of the reference snow density.

The studied statistical parameters depicting the performance of the inversion were 1) correlation, 2) rms-difference and 3) bias. The correlation values were the main source of information, as e.g. bias is adjustable during later processing of the inversion results.

The results for a typical day during the beginning of the snow season are presented in Figures 9.12 to 9.14 for the 2 January, 1994. Figure 9.12 shows the inversion results when all channels have the same weighting coefficient during the inversion process. The estimated snow water equivalent values are clearly too low when compared to measured values. However, the grouping is tight and only few samples are clearly off the main group.

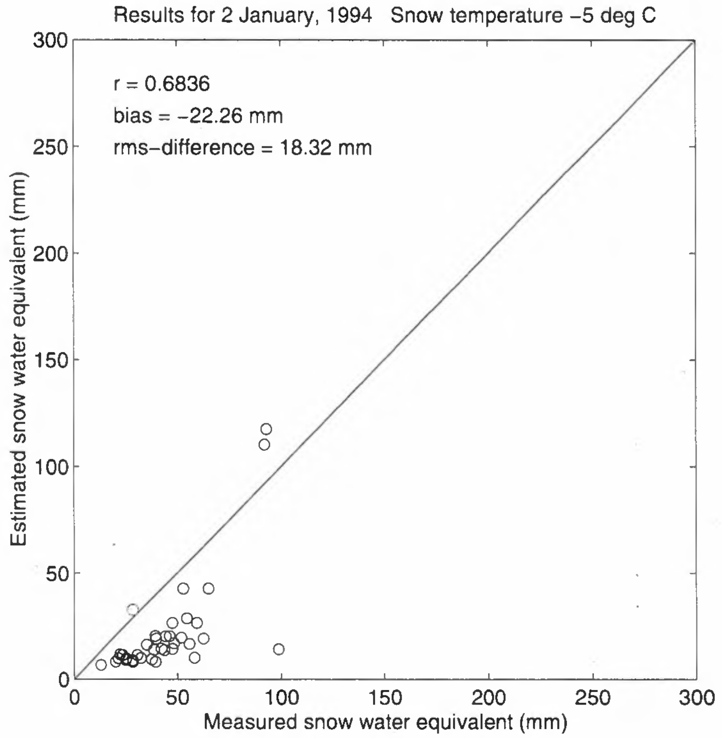

Figure 9.12. Inversion results for 2 January, 1994. All channels have the same weighting coefficients during the inversion process.

Figure 9.13. shows the inversion results for the same day (2 January, 1994) when the weighting coefficient of the 37 GHz channels have been put to approximately half of the value used in the original run and in Figure 9.14 both the 37 GHz and 85 GHz have lowered weighting coefficients. It is evident from the results shown in the figures that lowering the effect of the 37 GHz channels to the inversion increases the performance of the retrieval algorithm. Even if the correlation value is lower, the bias is smaller. As the sample size is also rather small, the correlation is very sensitive to the placement of individual samples on the scatter plot.

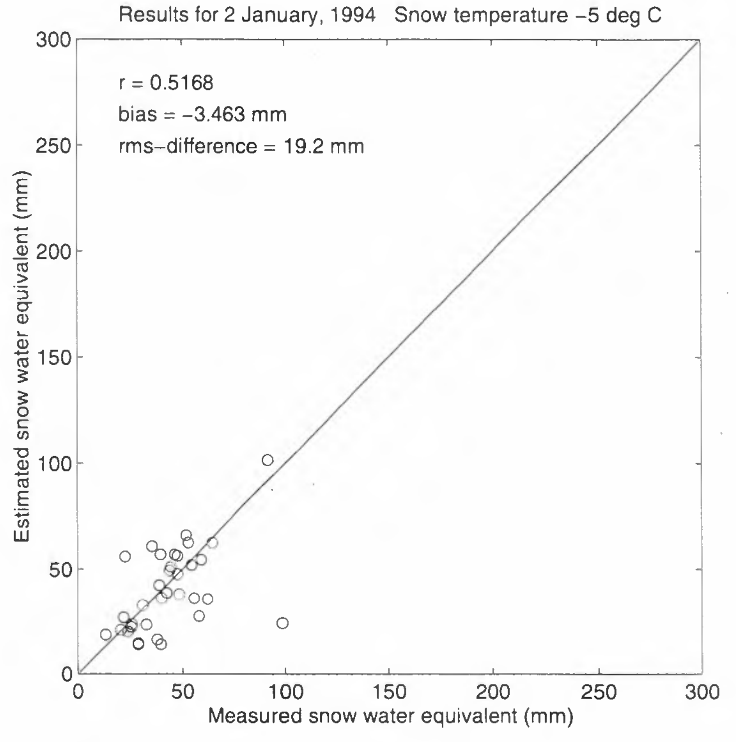

Figure 9.13. Inversion results for 2 January, 1994. The 37 GHz channels have a lower weighting coefficient than in Figure 9.12.

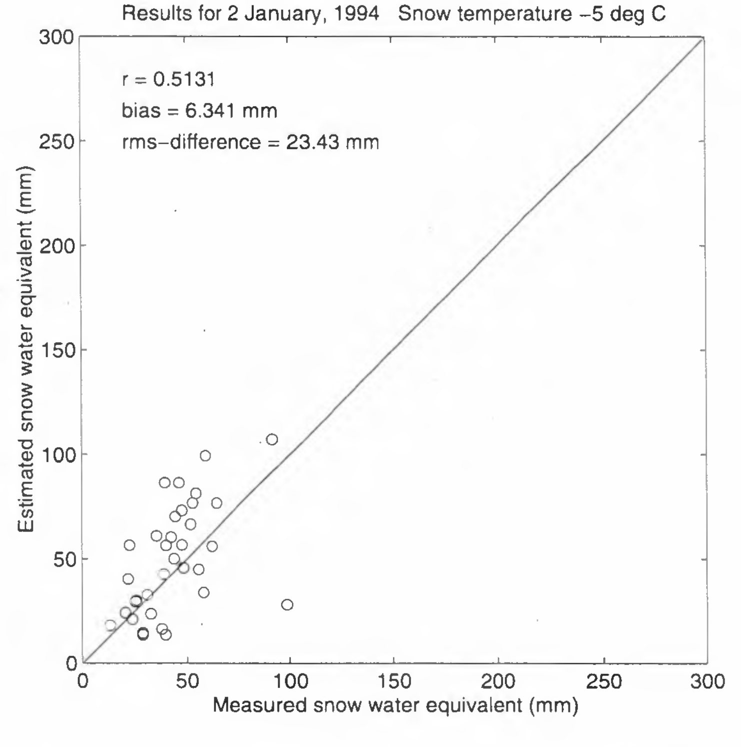

Figure 9.14. Inversion results for 2 January, 1994. Both the 37 GHz and 85 GHz channels have lower weighting coefficients than in Figure 9.12.

The results for the mid-snow season (1 March, 1994) are shown in Figures 9.15 to 9.17. The results have been obtained by using the same methods as described for the results of the 2 January, 1994. This includes lowering the weighting coefficients of the higher frequency channels (37 and 85 GHz). The correlation values are roughly the same for the results in Figures 9.15 to 9.17, but when the bias and rms-difference values are studied, it would implicate that best results are obtained when the same weighting coefficients are give for all channels (Figure 9.15).

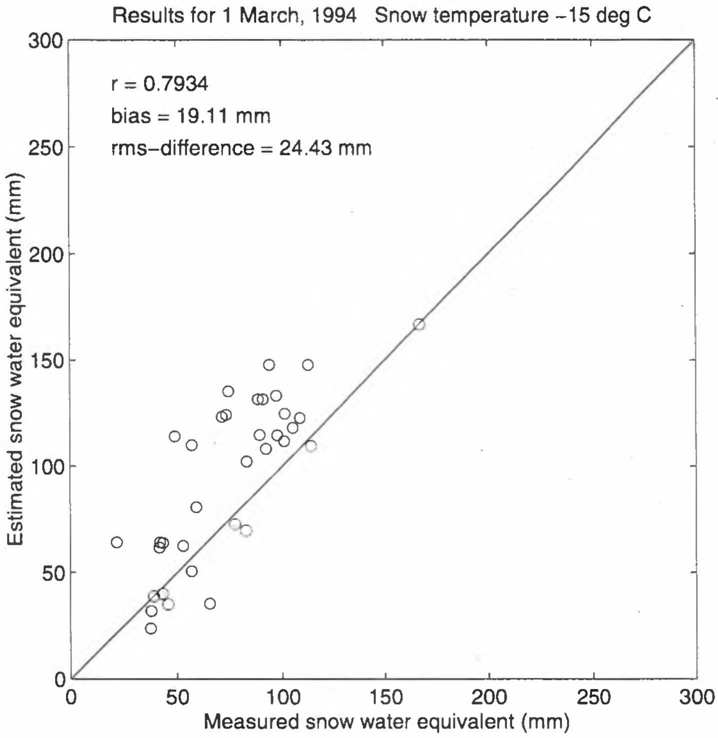

Figure 9.15. Inversion results for 1 March, 1994. All channels have the same weighting co-efficients during the inversion process.

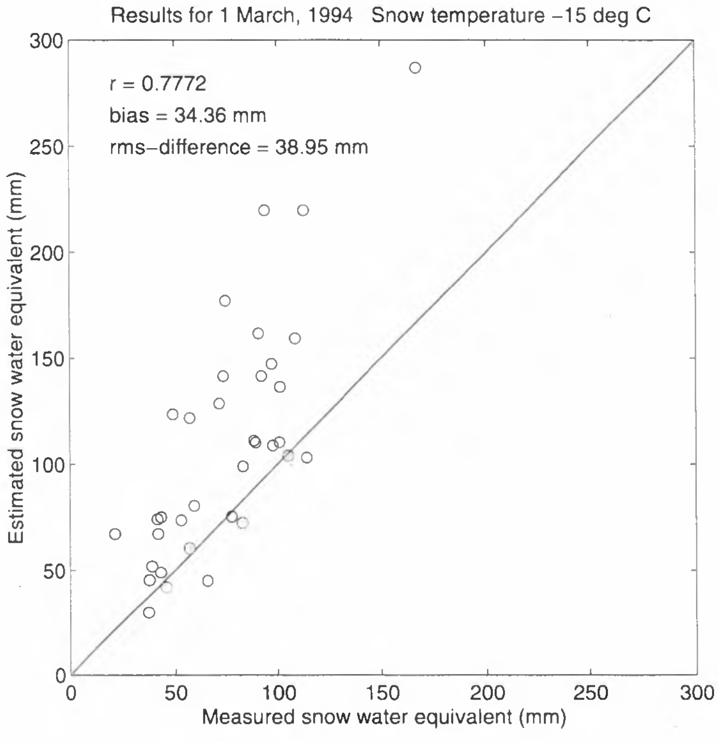

Figure 9.16. Inversion results for 1 March, 1994. The 37 GHz channels have a lower weighting coefficient than in Figure 9.15.

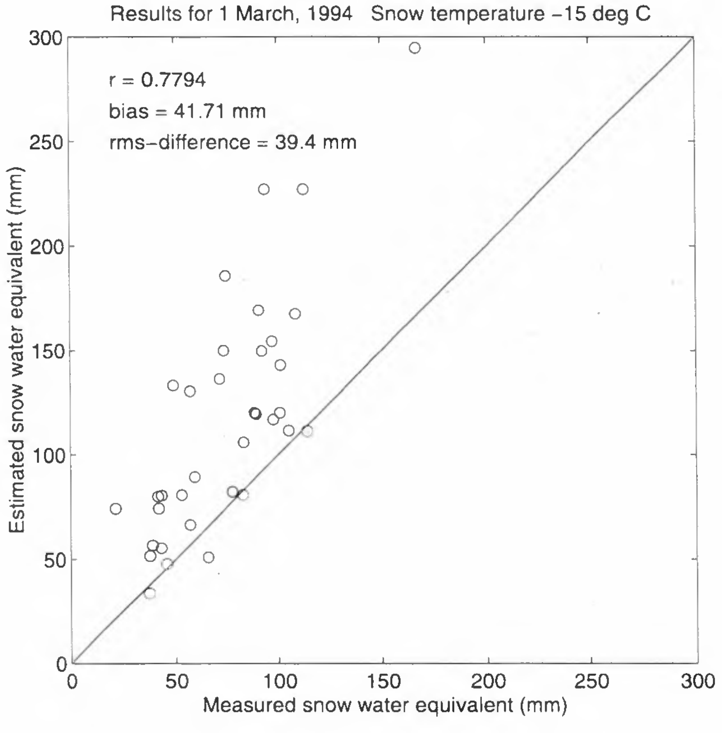

Figure 9.17. Inversion results for 1 March, 1994. Both the 37 GHz and 85 GHz channels have lower weighting coefficients than in Figure 9.15.

Figures 9.18 to 9.20 show the inversion results for a peak snow season (1 April, 1994) with and without lowered weighting coefficients for higher frequency channels. It is evident from the figures and the attached statistical data that the altering of the weighting coefficients results in a better performance. However, as the measured and estimated snow water equivalent values increase, the rms-error of the inversion also increase. Therefore, it may be assumed that the inversion algorithm does not function in a satisfactory manner for situations with a high (> 150 mm) snow water equivalent.

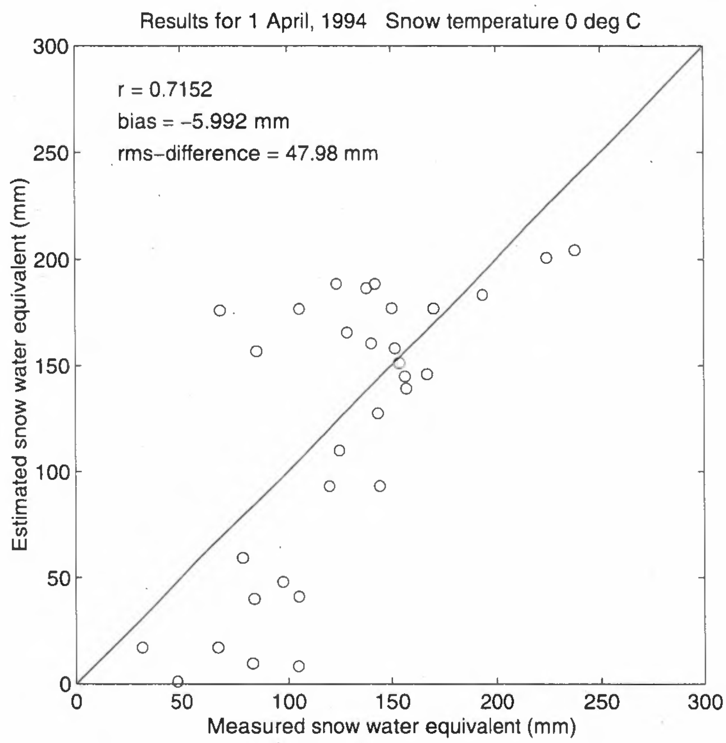

Figure 9.18. Inversion results for 1 April, 1994. All channels have the same weighting coefficients during the inversion process.

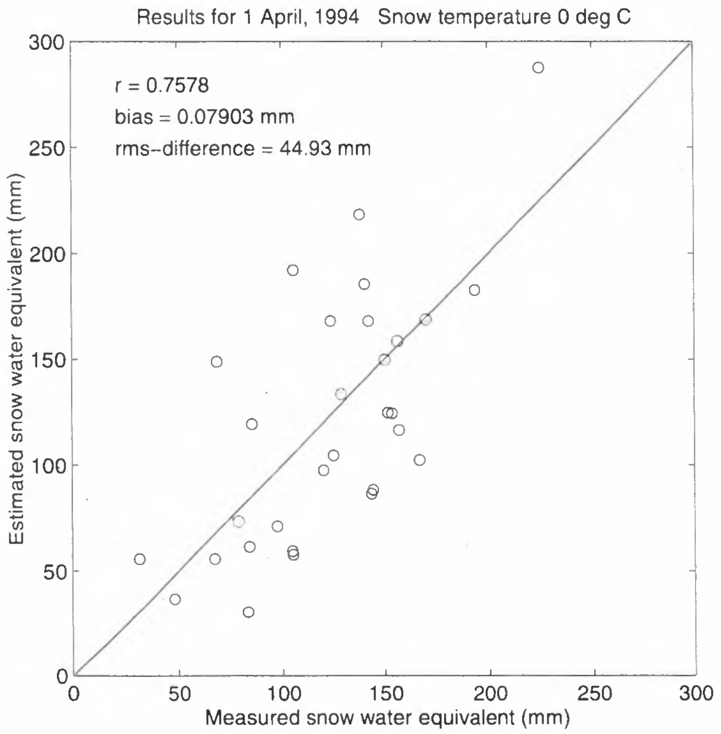

Figure 9.19. Inversion results for 1 April, 1994. The 37 GHz channels have a lower weighting coefficient than in Figure 9.18.

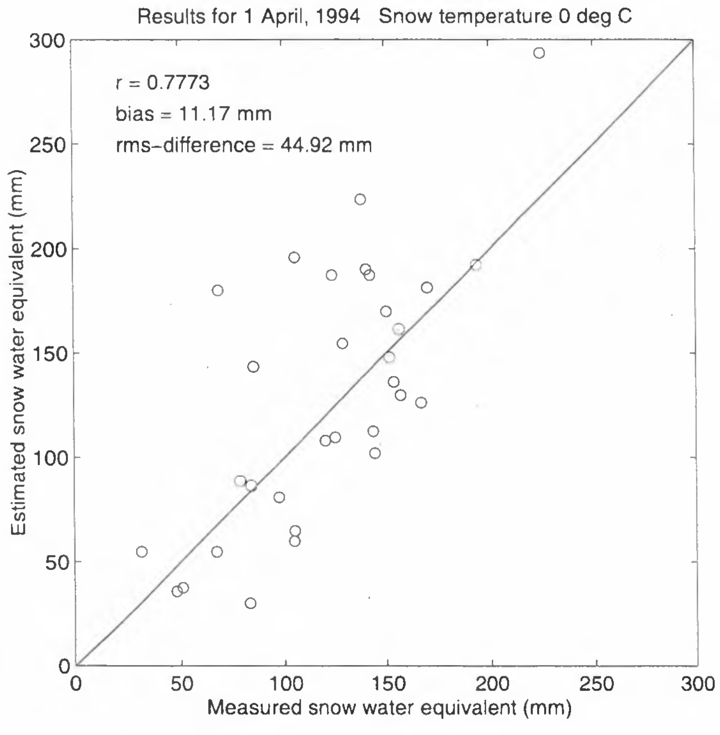

Figure 9.20. Inversion results for 1 April, 1994. Both the 37 GHz and 85 GHz channels have lower weighting coefficients than in Figure 9.18.

As a conclusion for the preliminary validation of the HUT snow model based inversion algorithm, figures with data from several measurement days are presented. Figure 9.21 shows the results when all channels are treated equally, and in Figure 9.22 the weighting coefficients for the 37 GHz channels have been decreased. The results seem to indicate that for lower snow water equivalent values the inversion algorithm seems to perform well, but for higher values the rms-error tends to increase to values not acceptable in practical applications.

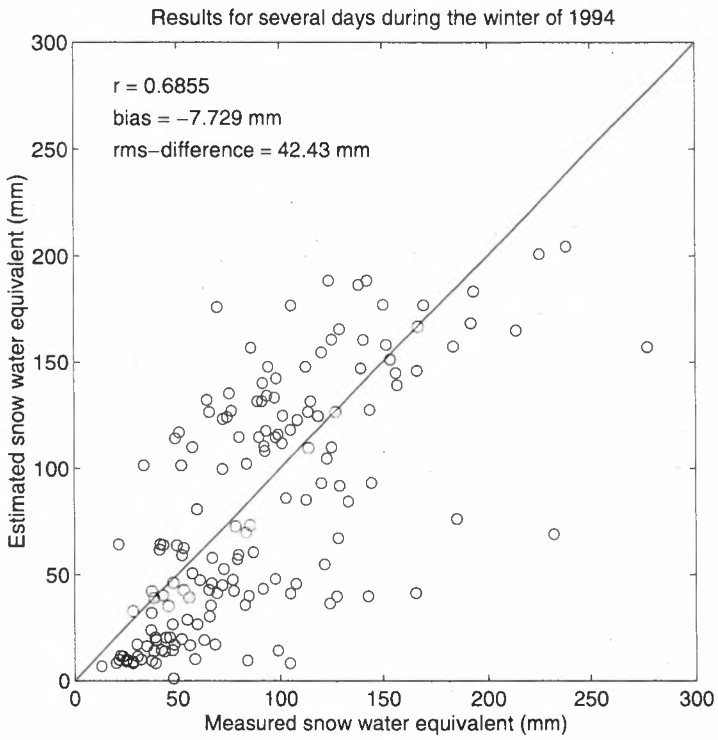

Figure 9.21. Inversion results for four measurement days during the winter of 1994 (January-April). All channels have the same weighting coefficients during the inversion process.

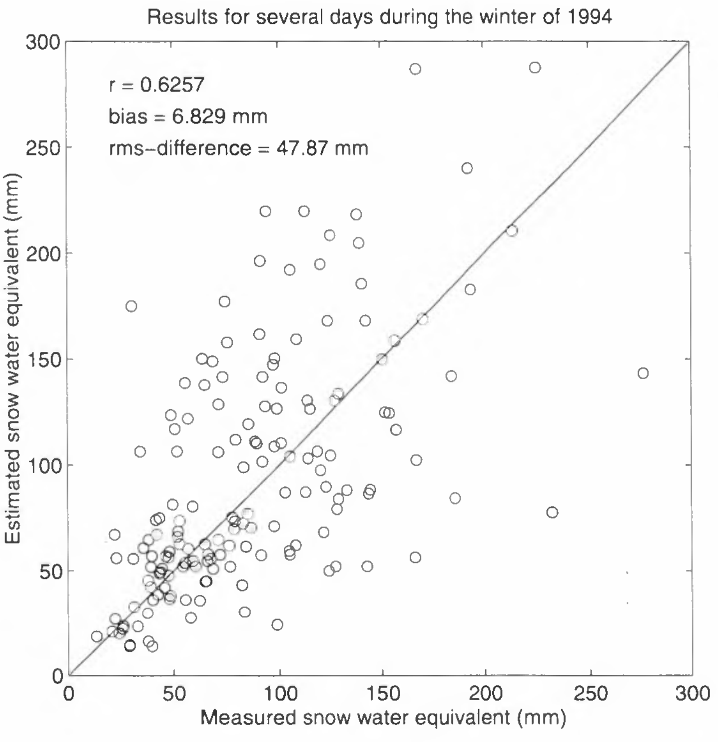

Figure 9.22. Inversion results for several measurement days during the winter of 1994. The 37 GHz channels have a lower weighting coefficient than in Figure 9.21.

Comparison between the results of the South and North Finland test areas

The snow model was tested for test sites located both in the South and North Finland test areas, although only results for South Finland test area are included in the report (Figure 9.12 to 9.22). It was shown by the results that the model performs well for southern areas, where snow water equivalents reach maximum values of 150-180 mm. For northern Finland, however, there is a constant bias in the results, as the model underestimates the snow water equivalents, and gives even results which would indicate that less snow is present in the north than in the south, which is of course a false estimate. This is due to the fact that the brightness temperatures of a snow covered ground reach minimum values in the vicinity of 200 mm snow water equivalent, after which the multiple scattering typically starts to increase the brightness temperatures with increasing snow water equivalent. This effect is however not included in the model. Thus, the range of applicability of the model is roughly 0-200 mm of snow water equivalents, or until the brightness temperature minimum is reached for each frequency.

9.3 Retrieval of Sea Ice Concentration

The total sea ice concentration retrieval algorithm was tested using SSM/I data from Northern Baltic sea and Gulf of Bothnia. The analysis was conducted for two dates, since the visible/infrared NOAA AVHRR reference data were only available for these occasions (due to poor imaging conditions).

In order to be able to verify the results obtained by the inversion algorithms, a set of reliable reference data has to be available. This is always difficult for sea ice applications, since usually large areas have to be covered and since the target conditions vary with time. There are currently a few ways to obtain this reference information:

- ground-based measurements on location,
- sea ice charts typically produced by national agencies,
- visible-band satellite images.

It is quite clear that the first alternative is impossible for anything else than some purely scientific field work connected with airborne or ground based (e.g. tower) microwave measurements. The second alternative including sea ice charts is more attempting due to the ease of covering a large area with reference information. However, the charts are mainly drafted from ship-based visual observations and, if weather and lighting conditions permit using visible range satellite images. These images are mentioned as the third alternative for obtaining reference data. The problem of this approach is that both lighting and weather conditions usually prevent the using of visible range images during winter-time (or summer-time in the southern hemisphere). However, we have chosen to use AVHRR images from two days from the spring of 1994, during which both the lighting and the cloud conditions are acceptable:

- February 27, 1994,
- March 31, 1994.

Using these visible range images of 1 km x 1 km resolution, it is possible to determine the feasibility of the sea ice emission model for inversion purposes. The inversion technique is a maximum likelihood method similar to those presented in Sections 8.1, 9.1 and 9.2.

The results obtained are shown in Figures 9.23 - 9.30. The SSM/I-based estimates and the visible range NOAA AVHRR reference images are presented as pairs of images. The results are determined for the open sea areas of both the North and South Finland test areas and for the two dates mentioned above. In order to be able to compare the result image to the reference image, the original 25 km x 25 km SSM/I pixels have been interpolated into a 1 km x 1 km grid. However, no real additional information is gained from this procedure. Land areas are masked off in the SSM/I ice concentration images.

Discussion on the images for February 27, 1994

The day of the measurement was in the middle of a very cold mid-winter period, when air temperatures as low as -30°C were measured. During this period, a lot of new ice was formed in the sea areas of South Finland test area, Figure 9.26. However, this ice is not covered by snow, and is therefore only weakly noticeable in the AVHRR image. It is therefore justified to presume that the estimated nearly 100% total sea ice concentration is close to reality. In the image from the northern test area, where the snow cover is older, the interpretation of AVHRR images are more clear to the eye even without any background information.

Discussion on the images for March 31, 1994

These images are more interesting as the melting season is in progress, and the southern parts of the test area are already free of ice. Most of the ice has started to drift, forming areas of open water of different sizes and shapes. Even if a precise estimation of the ice-water borderlines is impossible for a coarse resolution radiometer such as the SSM/I, an estimation of the total concentration within a 25 km x 25 km pixel seems to be possible. When the reference and estimation images are compared, it is evident that open water inclusions do lower the estimated total sea ice concentrations for these areas. This is notable e.g. in Figures 9.27 and 9.28, where the open water area in the southeastern part of the Gulf of Bothnia is clearly detectable in the SSM/I-based results.

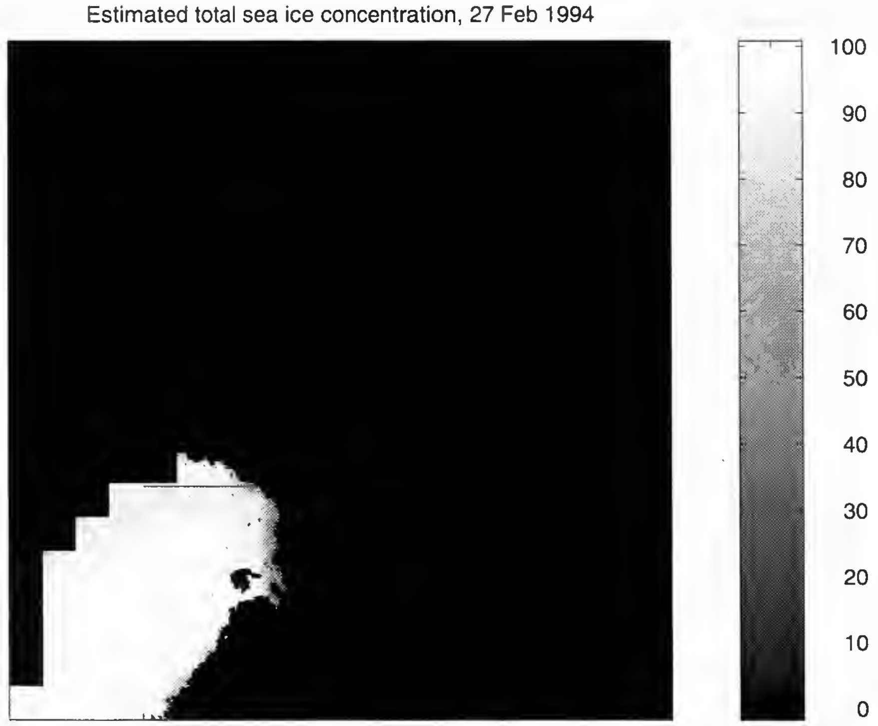

Figure 9.23. Inversion results for North Finland test area, interpolated into a 1 km x 1 km grid. The measurement day is 27 February 1994.

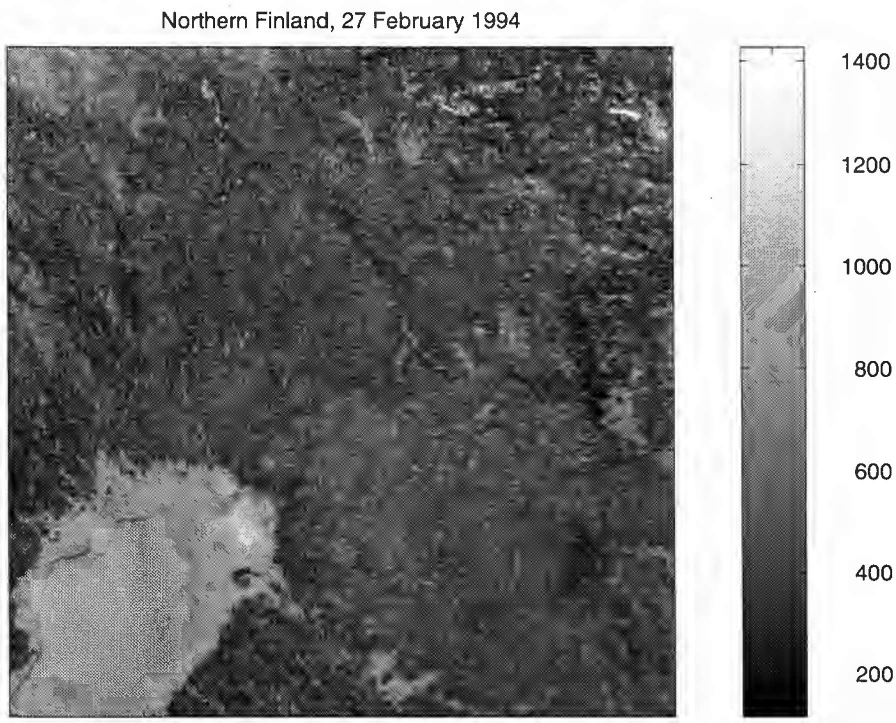

Figure 9.24. Reference AVHRR image for 27 February 1994 (North Finland test area).

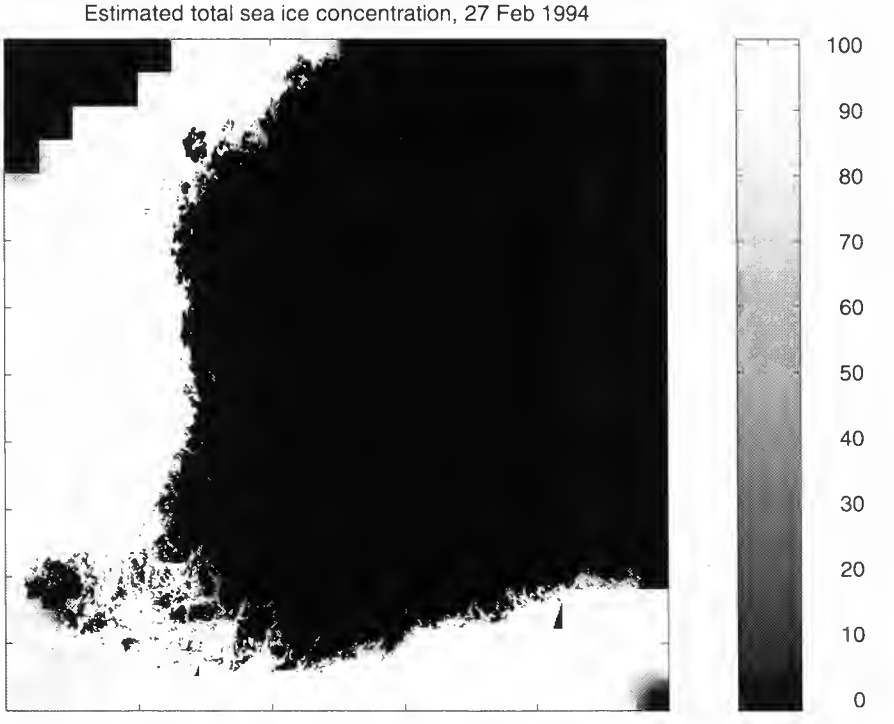

Figure 9.25. Inversion results for South Finland test area, interpolated into a 1 km x 1 km grid. The measurement day is 27 February 1994.

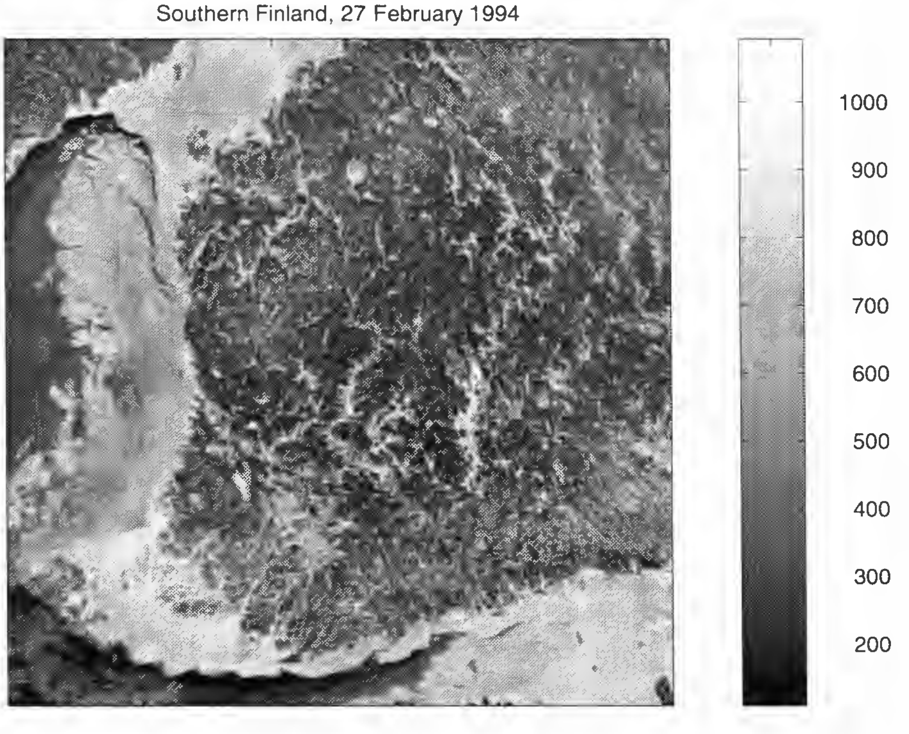

Figure 9.26. Reference AVHRR image for 27 February 1994 (South Finland test area).

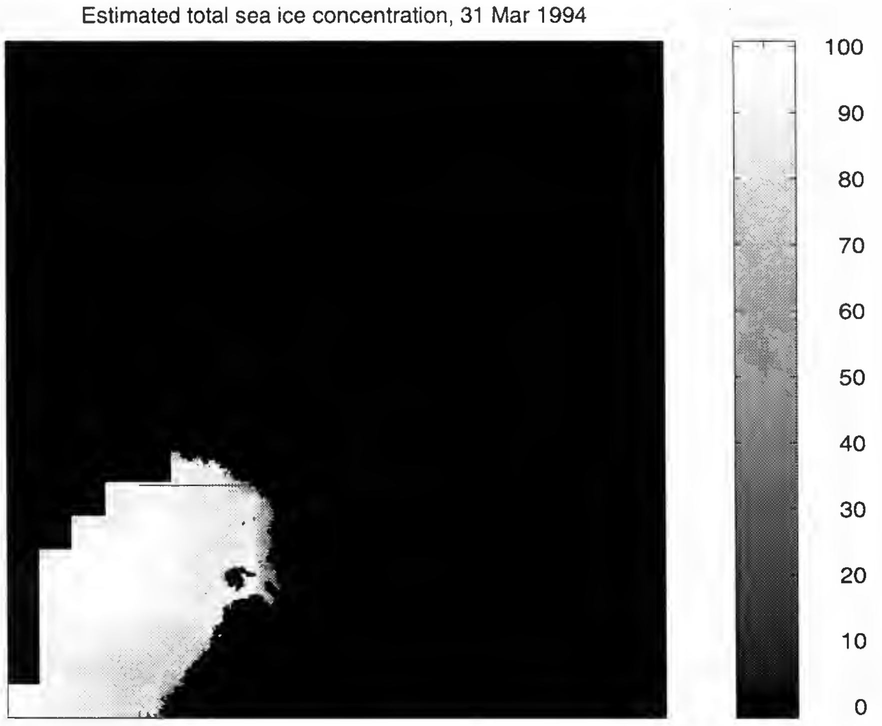

Figure 9.27. Inversion results for North Finland test area, interpolated into a 1 km x 1 km grid. The measurement day is 31 March 1994.

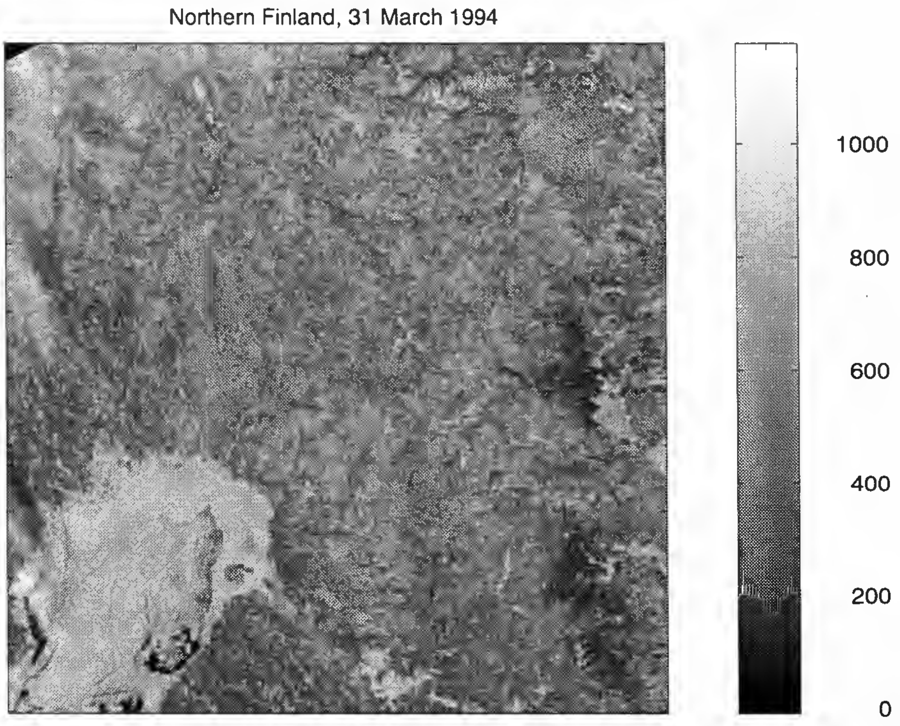

Figure 9.28. Reference AVHRR image for 31 March 1994 (North Finland test area).

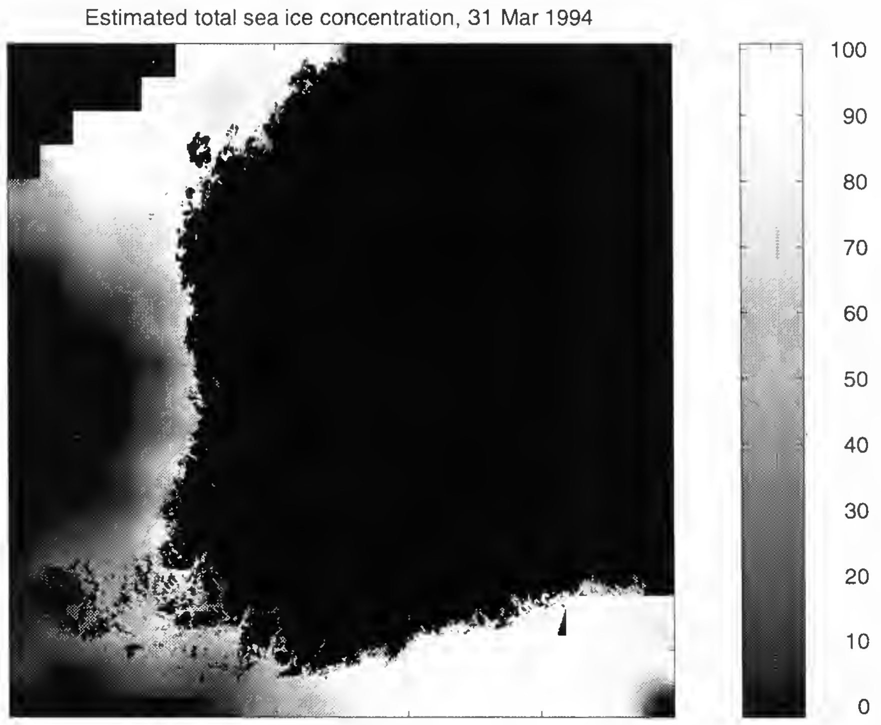

Figure 9.29. Inversion results for South Finland test area, interpolated into a 1 km x 1 km grid. The measurement day is 31 March 1994.

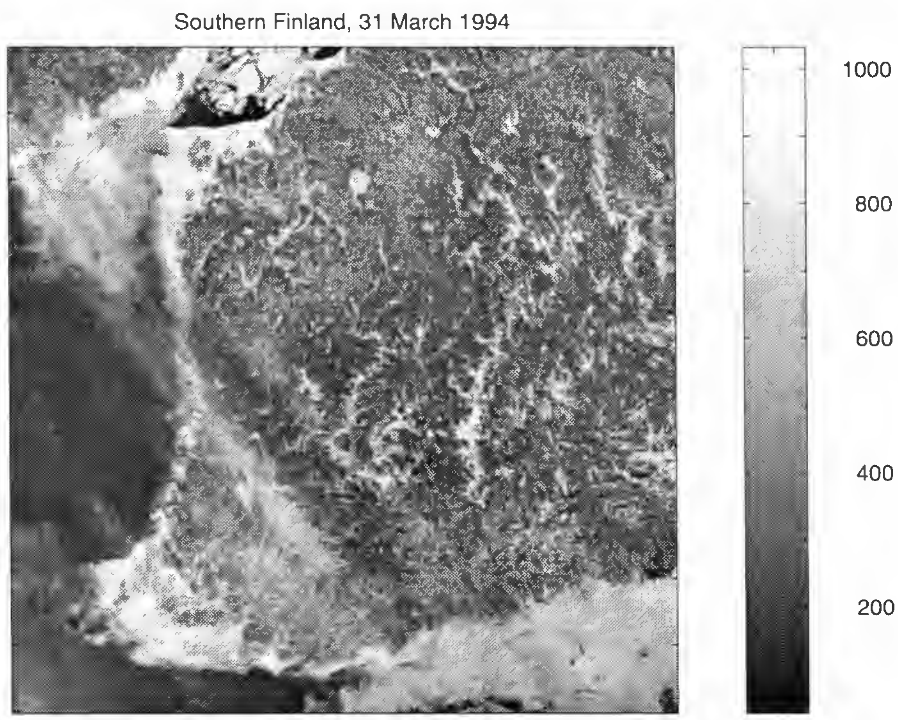

Figure 9.30. Reference AVHRR image for 31 March 1994 (South Finland test area).

Numerical comparisons

Figures 9.31 - 9.35 show the histograms of differences (in %-units) between AVHRR-based total sea ice concentration estimates and SSM/I-based estimates. Both results are calculated for 25 km by 25 km-sized grid cells. Figure 9.31 - 9.34 show the results for individual test areas and dates. In Figure 9.35, all cases are collected into same data set.

The results show that even if the obvious error pixels have not been removed, the inversion accuracy is satisfactory. However, AVHRR images can not be treated as precise reference data. For these images, it is clear that some of the AVHRR pixels can not be used for reliable estimation of the sea ice concentration. None of the obvious source of errors have been removed from the data. These sources of error are such as the cloudy area in southern Baltic Sea observable in the image from 31 March and the area covered by new ice (which is estimated to be open water in the AVHRR data classification). With these erroneous pixels removed, results would improve significantly, since the overestimation shown by the SSM/I inversion results would decrease. This is especially the case for the results of 27 February 1993.

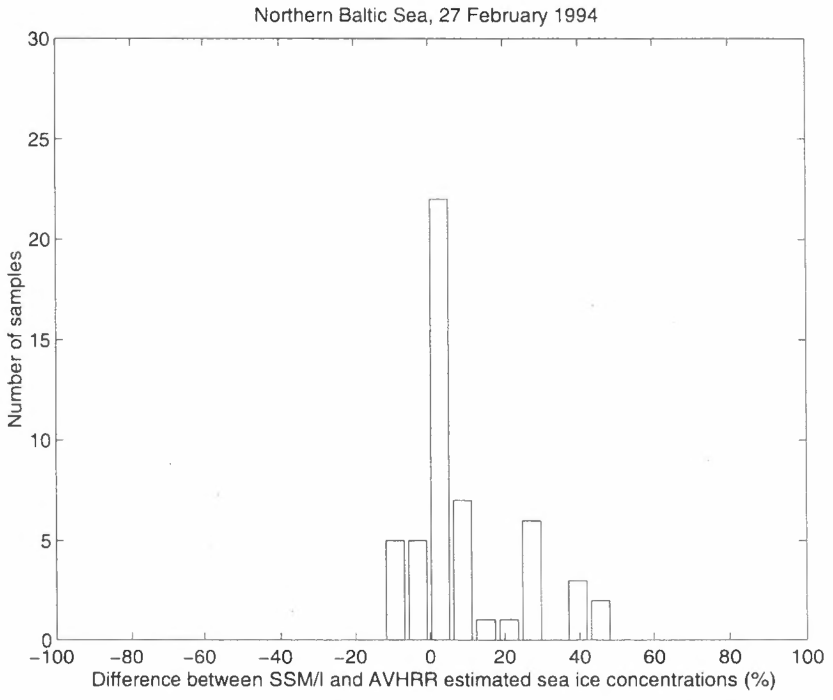

Figure 9.31. Distribution of the difference between SSM/I and AVHRR inversion results for sea ice concentration percentage (in %-units). The measurements day is February 27, and the test site is the North Finland test area (no erroneous data removed).

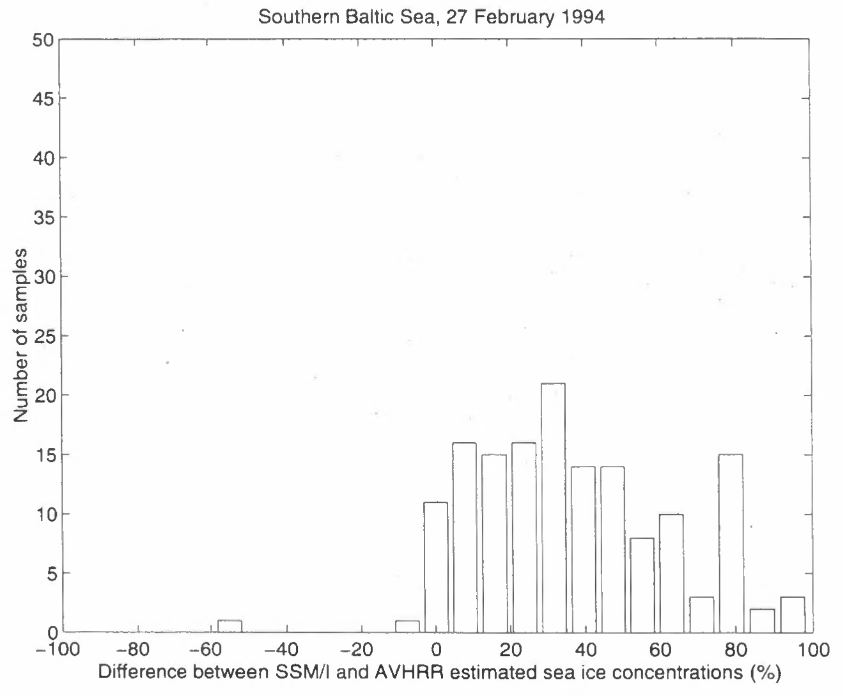

Figure 9.32. Distribution of the difference between SSM/I and AVHRR inversion results for sea ice concentration percentage (in %-units). The measurements day is February 27, and the test site is the South Finland test area (no erroneous data removed).

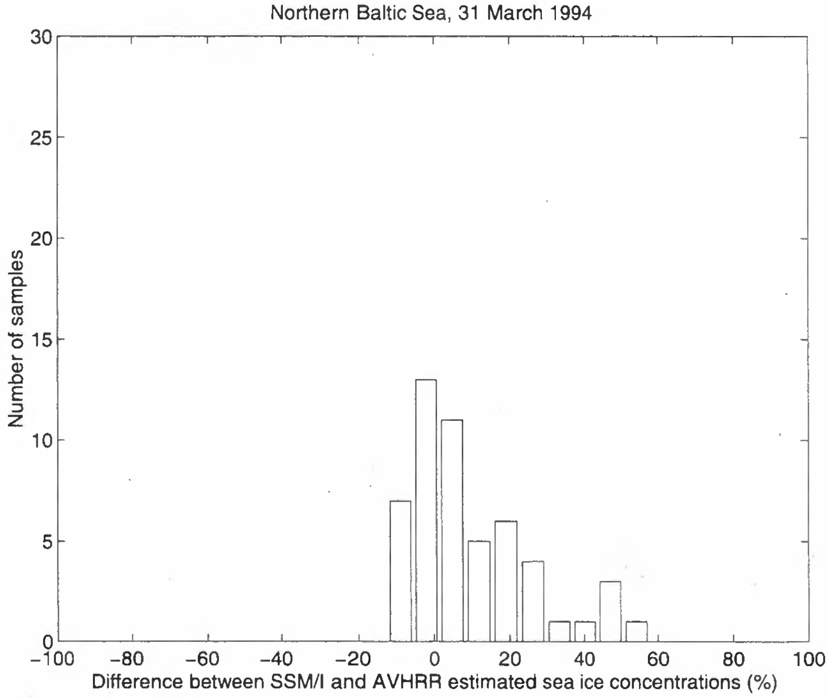

Figure 9.33. Distribution of the difference between SSM/I and AVHRR inversion results for sea ice concentration percentage (in %-units). The measurements day is March 31, and the test site is the North Finland test area (no erroneous data removed).

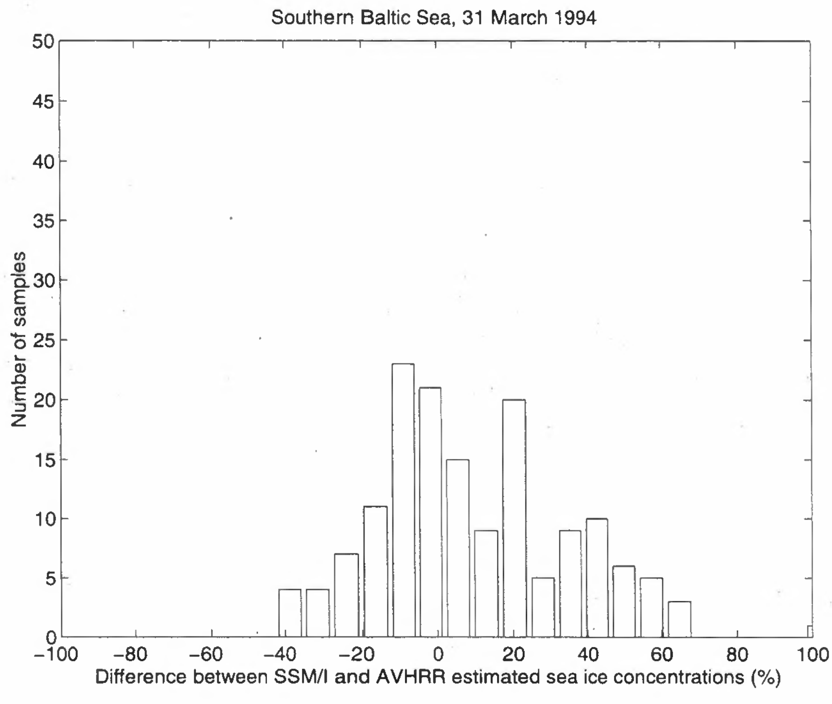

Figure 9.34. Distribution of the difference between SSM/I and AVHRR inversion results for sea ice concentration percentage (in %-units). The measurements day is March 31, and the test site is the South Finland test area (no erroneous data removed).

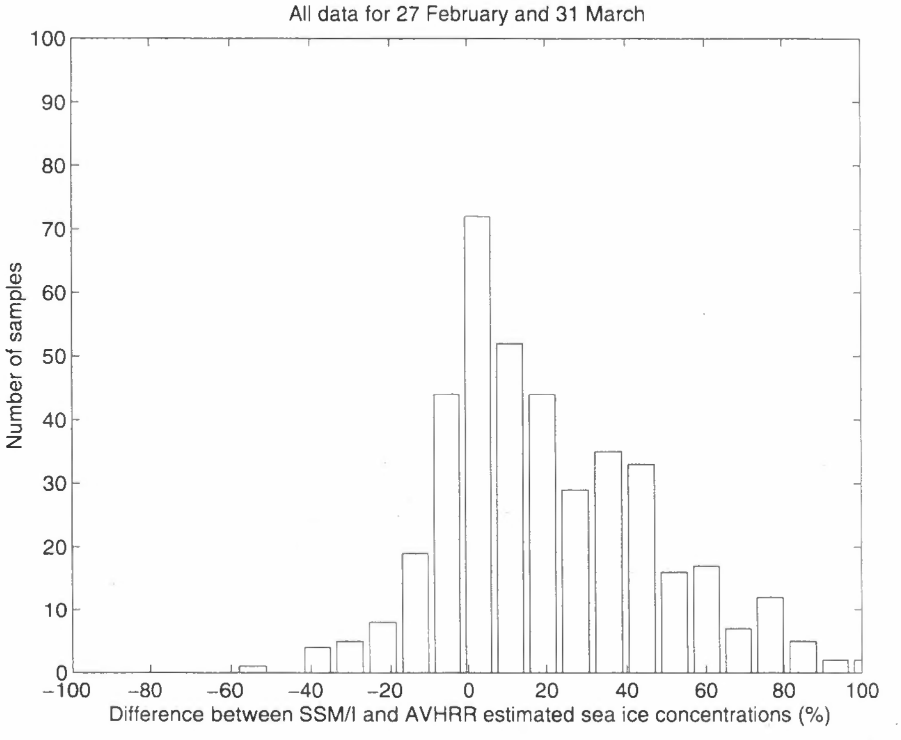

Figure 9.35. Distribution of the difference between SSM/I and AVHRR inversion results for sea ice concentration percentage (in %-units). For this figure, all data from 27 February 1994 and 31 March 1994 are included (no erroneous data removed).

9.4 Feasibility for Other Applications

It was shown previously that the brightness temperature measured by the SSM/I instrument does not show any correlation to forest stem volume (biomass). However, the land use category within the pixel (25 km x 25 km) seemed to have a great influence on the measured brightness temperatures. This is quite expected due to the large size of each test site (grid cell) when compared with stem volume variations within a typical area. This behavior suggests that a modeling and a retrieval approach for the application of land use category should be rewarding.

Empirical model for the retrieval of land use category

The reference data for land use category used for this study includes 70 categories for the 25 km x 25 km pixel. Due to the weak or non-existent sensitivity of microwave emission to forest biomass, the forest categories which include several sub-categories according to their stem volume, may be combined. As a general rule, observed emission from the ground can be divided into three components: 1) contribution from open water areas, 2) contribution from open land areas and 3) contribution from forested areas. The resulting model, after any possible simplifications in land use categories can be defined as

$$T_B = (C_{water}e_{water}(f,p) + C_{open}e_{open}(f,p) + C_{forest}e_{forest})T_{phys}, \tag{9.10}$$

where

C_{water} = fraction of open water within a pixel,

C_{open} = fraction of open land areas within a pixel,

C_{forest} = fraction of forested areas within a pixel,

$e_{water}(f,p)$ = emissivity of open water,

$e_{open}(f,p)$ = emissivity of open land areas,

$e_{forest}(f,p)$ = emissivity of forested areas,

T_{phys} = physical ground temperature (K),

f = frequency,

p = polarization.

In addition to the expression for ground emitted radiation in Equation (9.10), the effect of the atmosphere must be included for satellite applications. This procedure is explained in Section 9.1.

Inversion techniques explained in Section 9.1 are appropriate to determine values for the various emissivities for Finnish circumstances. The physical temperature values can be also obtained by using the inversion methods introduced in Section 9.1.

Semi-empirical model for the retrieval of land use category

In a semi-empirical approach all the contributing factors to the resulting total brightness temperature are modeled by physical or theoretical models, but some simplifications and assumptions must be made. Therefore the resulting model will be semi-empirical. This approach enables a more precise handling of the various land use categories, as e.g. open land areas may be divided into several groups, such as agricultural land and grass. Forested areas may also be divided into several sub-categories according to their dominant scattering and/or absorption properties.

10 ERS-1 Wind Scatterometer Resolution Enhancement

10.1 Introduction

Although the ERS-1 scatterometer was primarily designed for measuring ocean surface-wind velocities, the wide swath and global coverage offered by this instrument have also excited considerable interest for use in land and ice applications. Examples of land applications making use of the ERS-1 scatterometer are given by *Wismann et al. (1994)* and *Rott et al. (1994)*. However, the low resolution (~47 km) of ERS-1 scatterometer images means that it is only possible to observe and monitor large scale features. If it were possible to resolve a wider range of features then this would lead to a corresponding increase in the number of land applications for which scatterometer data would be appropriate.

This section will describe work conducted at the GEC-Marconi Research Centre which is concerned with improving the resolution of ERS-1 scatterometer imagery. This begins with re-assessment of earlier work conducted in this field and leads to the development of an enhanced resolution algorithm which has been applied to scatterometer data taken over Finland. This Chapter is structured as follows:

* Section 10.2 describes previous work in which an algorithm was developed for improving the resolution of Seasat scatterometer (SASS) data. The following Sections (10.3 to 10.5) explain why it is not appropriate to use this algorithm with ERS-1 scatterometer images.
* Section 10.3 describes the processing chain that is used to produce the scatterometer images.
* In Section 10.4 the frequency content of the impulse response function and some examples of scatterometer data is examined in order to confirm that the data is not under-sampled to any serious degree.
* Section 10.5 explains how the results obtained from Sections 10.3 to 10.4 can be used to establish a realistic limit on the degree of resolution enhancement that is possible with ERS-1 scatterometer data.
* Section 10.6 shows how it is possible to re-sample the scatterometer data without introducing ringing effects at the edges of the image which occur if a Fourier 'zero-padding' technique is used.
* In Section 10.7 a review is given of a wide range of image enhancement and super-resolution techniques.
* Section 10.8 assesses the suitability of the methods discussed in Section 10.7 for application to ERS-1 scatterometer data. This discussion leads to the definition of an

algorithm which involves a Wiener filter which is then followed by either the application of a median filter or the use of a land - water mask if this is available for the data under consideration.

* In Section 10.9 a technique is described which enables resolution enhancement algorithms to be used without producing serious edge 'ringing' effects which are caused by digital Fourier transforms.

* Section 10.10 demonstrates how the Wiener filter can be used with a median filter to produce enhanced resolution scatterometer images.

* In Section 10.11 it is shown how a land - water mask for Finland can be overlaid on the scatterometer images collected from this region. This allows *a priori* knowledge concerning the position of land and water areas to be incorporated in the image enhancing process.

* Section 10.12 summarises the work conducted during this study.

* Section 10.13 provides a brief review of Fourier sampling theory, which is relevant to the discussions in Sections 10.3 to 10.5.

10.2 Previous Scatterometer Resolution Enhancement Work

To date, work in the area of enhancing scatterometer data has been principally conducted by *Long et al. (1992), (1993)* and *Long and Hardin (1994)* using an algorithm which was developed for use with Seasat scatterometer (SASS) data.

The SASS σ^0 measurements made by a single antenna on a single beam during one orbit have no overlap, and only a small increase in the sampling is achieved by combining measurements from the forward and aft beams *(Hardin and Long 1994)*. If data is sampled at, or above the Nyquist limit (twice the highest frequency present in the data) then it is said to be adequately sampled and the original data can be reconstructed exactly using only the sampled data. The poor level of sampling used in the Seasat scatterometer means that its resultant data is substantially under-sampled.

The first step used by *Long et al.* to improve the resolution of the SASS scatterometer data involved taking advantage of the spatial overlap in scatterometer measurements made at different times. By combining the data from different antenna passes on a finer pixel grid it was possible to artificially synthesise an image with a less coarse tiling effect and therefore to build up a more complete picture of the ground scene. This process of combining data from different antenna passes will not, in itself, increase the resolution of the image beyond that determined by the instrument impulse response function. Instead it can be seen as essentially a method to overcome the fact that the data from a single SASS scatterometer antenna is inadequately sampled. The second stage used by *Long et al.* involved a technique referred to as multiplicative algebraic reconstruction which includes an edge preserving median filter.

More recently the enhanced resolution method due to *Long and Hardin (1993)* has also been adapted for use with ERS-1 data *(Long et al. 1994, Early et al. 1994)*. In order to assess whether it is appropriate to use the SASS resolution enhancement method on ERS-1 images it is instructive to review the processing chain used by the ERS-1 scatterometer (see Section 10.3). This review also makes it possible to establish what levels of enhanced resolution might be possible.

10.3 The ERS-1 Scatterometer Processing Chain

In order to enhance the resolution of ERS-1 scatterometer images it is important to understand the processing chain that has been used to create this product. In this Section an overview of the most important aspects of this processing chain are given. Further details are given in *P. Hans et al. (1986)* and *Pierschel (1987)*.

The ERS-1 wind scatterometer operates at C band with VV polarisation and uses 3 side-looking antennae, one of which points in a direction perpendicular to the direction of flight, the other two point at 45° in forward and backward directions. The illuminated swath is 500 km and provides radar backscatter measurements with a spatial resolution of ~47 km on a 25 km × 25 km pixel grid. The ERS-1 AMI system operates continuously in its scatterometer mode whenever the SAR is not being used. This provides a monitoring capability with nearly global coverage in 3 to 4 days.

A scatterometer image product contains 19 × 19 pixels and each of these pixels represents an area of approximately 25 × 25 km^2. The σ^o value at each pixel is an average formed by a two-dimensional weighted integration of a number of received echo signals.

In the across-track direction sampling is achieved by range gating and in the along-track direction the movement of the spacecraft between consecutive pulses is used. A non-chirped, range gating system will have a triangular impulse response function which will vary in width across the swath. An azimuth Doppler processing system will produce a *sinc* squared impulse response function. The final, total ERS-1 scatterometer image impulse response function will be given by the convolution between these 'raw' system impulse response functions and contributions due to the subsequent processing stages.

Groups of 32 pulses are transmitted cyclicly from each of the fore, mid and aft antennas. The pulse length for the fore and aft beams is 130 μsec and is 70 μsec for the mid beam. The pulse repetition time for the fore and aft beams is 10.21 msec and is 8.7 msec for the mid beam. In total, one complete cycle of 32 pulses from each of the fore, mid and aft beams takes 941 msec. During the time that it takes to make four of these cycles the satellite will travel approximately 25 km (this number will vary slightly depending on the altitude of the satellite).

The returned signals which have been scattered from the earth undergo a small amount of on-board processing before they are transmitted to the ground. A coarse Doppler shift is made to the fore and aft signals and a low pass filter is also applied.

Most of the scatterometer processing is completed on the ground. The main features are summarised under the following points.

1. Re-sampling of the data to avoid aliasing during the subsequent processing stages.
2. Fine Doppler compensation to shift the spectrum of the received signal into the receiver pass-band.
3. Low pass filtering to improve the signal to noise ratio.

4. Envelope detection to get a measure of the signal power (which is proportional to the σ^o values). It is useful to note that up until this point the data has been represented in I and Q form.

5. Noise subtraction to improve the measurement accuracy. The receiver noise power is measured separately and then subtracted from the sum of the target power and noise power.

6. Internal calibration to compensate for transmitter and receiver fluctuations.

7. Block averaging of target samples which have identical echo times to reduce the data throughput for the following processing stages.

8. Power to normalised σ^o conversion.

9. Spatial integration to increase the radiometric resolution and to give the desired impulse response function.

From the point of view of the resolution enhancement problem the most important stage in this processing chain is the last one. The spatial integration stage determines which pulses will be used to form the σ^o value at any given node. The integration takes place in an area which is centred on a node and is approximately 85 km square (it is 84.5 km square for the fore and aft beams and 86 km square for the mid beam, *Munz (1995)*). The contributions of the pulses from this area are weighted by a Hamming function. The Hamming window is widely used in signal processing *(Harris 1978)* and takes the following form,

$$w(n) \quad = \quad \alpha + (1-\alpha)\cos\left(\frac{2\pi}{N}n\right) \tag{10.1}$$

where,

$$|n| \quad = \quad \frac{N}{2}. \tag{10.2}$$

By using trigonometric relations it can be shown that this equation is a cosine squared function which sits on a pedestal above the zero level. In general the Hamming window is designed to have a Fourier transform with low sidelobes. The value of α (which can vary between 0 and 1) used in the scatterometer weighting function is set to 0.54. This value produces the optimum level of sidelobe suppression, such that the highest sidelobe is -43 dB below the peak value.

The Hamming function used in the spatial averaging process will dominate the form of the scatterometer impulse response function. The special properties of this function are important when considering whether the scatterometer data can be regarded as being adequately or inadequately sampled. If the data has been under-sampled it would become very difficult to apply deconvolution or super-resolution algorithms. In fact under these circumstances there might be some merit in using the techniques developed by *Long (1992)*, where data was taken at different dates or from different antennas and was combined in order to attempt to produce an adequately sampled image.

In the following Section (10.4) the frequency content of the ERS-1 scatterometer impulse response function is examined to evaluate how well the resultant scatterometer images are sampled.

10.4 Examining the Frequency Content of ERS-1 Scatterometer Data

Examining the impulse response function

In the previous Section (10.3) it was shown that the ERS-1 scatterometer impulse response function is dominated by a Hamming function used in a spatial averaging processing stage. By examining the frequency content of this function it is possible to ascertain whether the scatterometer data can be regarded as being adequately or inadequately sampled.

Figure 10.1 shows a one dimensional Hamming weighting function (Equation (10.1)). Figures 10.2 and 10.3 show the power spectrum of the Hamming function plotted on linear and logarithmic scales. Also shown in Figures 10.2 and 10.3 is the frequency corresponding to the pixel sampling rate for ERS-1 scatterometer data, i.e. 25 km. From Figure 10.2 it is clear that the vast majority of the energy in the power spectrum is contained within this limit.

In Figure 10.3 it can be seen that the power spectrum is a rapidly decreasing function which crosses the sampling rate at a level of approximately -32 dB and has sidelobe levels which are approximately -43 dB below the peak level. The high frequency components which lie outside of the region indicated by the sampling rate could be accessed by combining data sets together taken at different times or with different antennas. It can be seen that (in comparison to noise and possible mis-registration effects) there is virtually no information which can be obtained using this process.

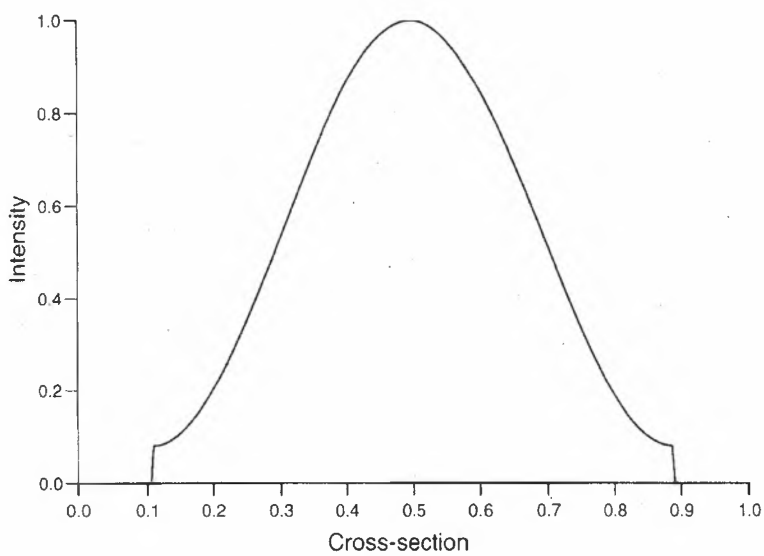

Figure 10.1. The Hamming window function.

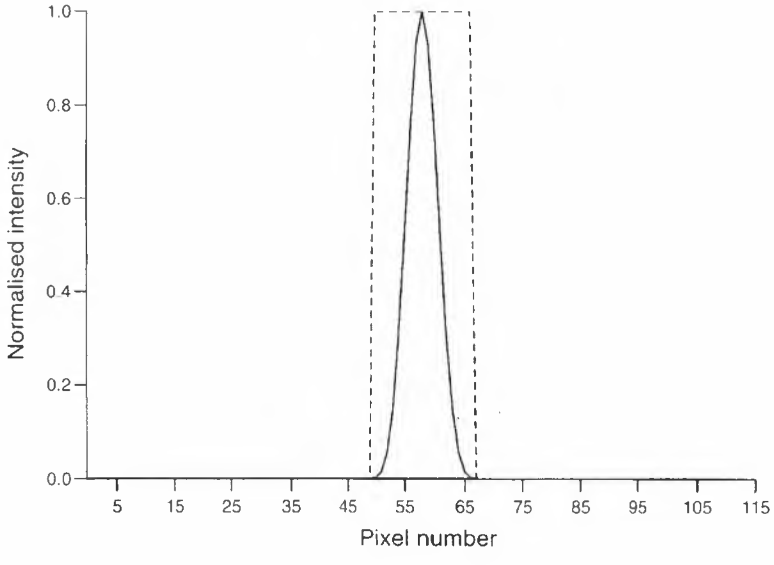

Figure 10.2. The power spectrum of the Hamming window function plotted on a linear scale. The dashed line indicates the sampling frequency for ERS-1 scatterometer images.

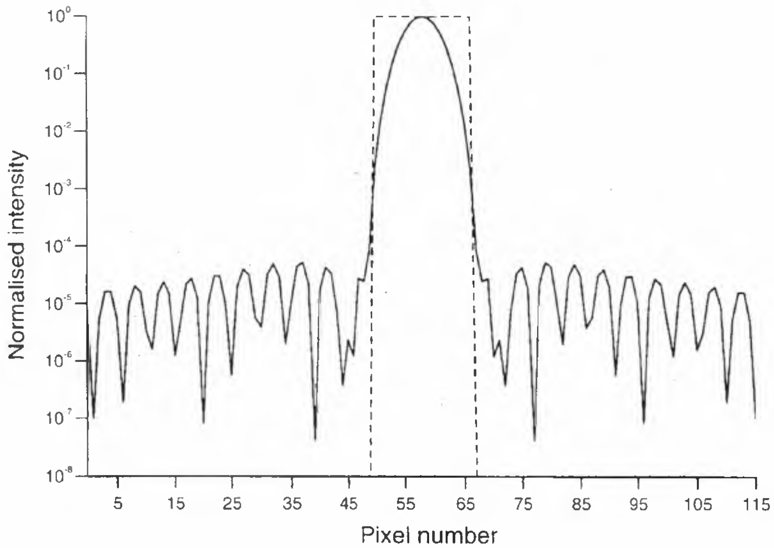

Figure 10.3. The power spectrum of the Hamming window function plotted on a logarithmic scale. The dashed line indicates the sampling frequency for ERS-1 scatterometer images.

Examining the data

In order to help confirm that ERS-1 scatterometer data is adequately sampled it is useful to examine the frequency spectrum of an image. An ERS-1 scatterometer image is shown in Figure 10.4 taken over the Gulf of Bothnia (west of Finland) on the 22nd June 1993 using the aft beam on a descending pass. (In order to make use of a simple Fourier transform algorithm the image in Figure 10.4 contains 16×16 pixels instead of the usual 19×19. The pixels have been removed from the right and bottom sides of the image.)

Figure 10.5 shows a contour plot of the power spectra of the image in Figure 10.4. The image mean was subtracted from the image so the power spectra does not contain a large DC term and the contours are plotted on a logarithmic scale. The solid line (towards the centre of the figure) represents the -10 dB level down from the peak in the data. The dashed, dotted and dash-dotted lines then show the -20 dB, -30 dB and -40 dB levels respectively.

It can be seen that along the vertical and horizontal axes there is energy (at the -30 dB level) which reaches the edge of Figure 10.5 (i.e. the sampling frequency), however in other directions the energy is very well confined within the figure. The energy along the x and y axes is almost certainly due to the image boundary effects. The discrete Fourier transform algorithm assumes that the data is circular and joined at the edges (ie. in the form of a torus). In general there will be significant discontinuities at these boundaries which result in high-frequency components extending along the x and y axes.

The image in Figure 10.4 contains a relatively high-contrast, linear structure (the Gulf of Bothnia) which is oriented in an 'off-vertical' direction. This is reflected by the 'off-horizontal' oval contours in Figure 10.5. If the data were under-sampled then the oval contours would show a significant contribution of energy reaching the sampling frequency at the boundary of the figure. This is not the case, showing that the data can be regarded as adequately sampled.

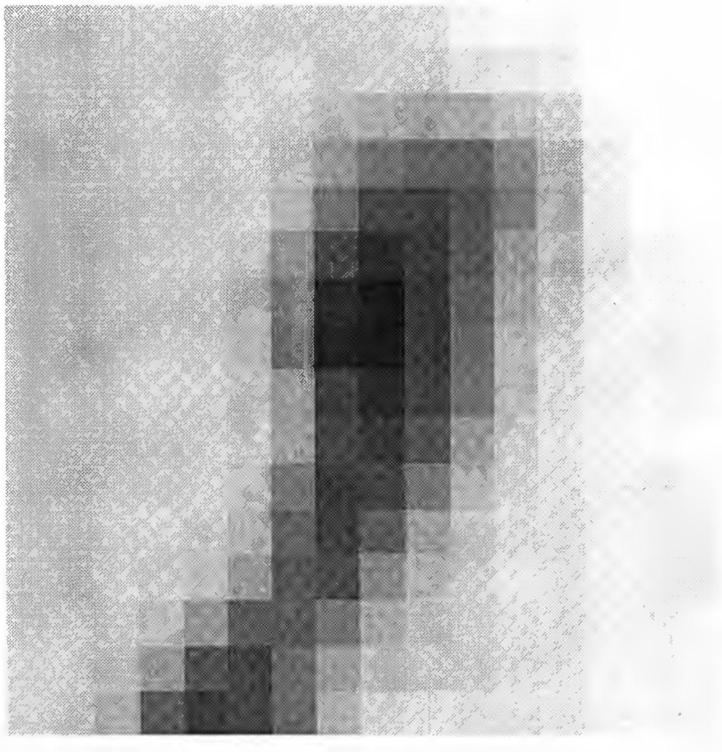

Figure 10.4. An ERS-1 scatterometer image taken over West Finland.

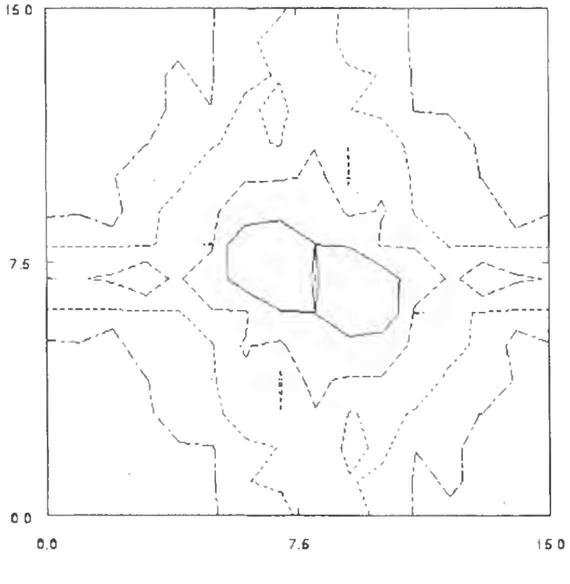

Figure 10.5. The power spectrum of an ERS-1 scatterometer image taken over West Finland.

10.5 What Level of Resolution Enhancement is Possible?

In Section 10.4 the frequency content of ERS-1 scatterometer data was examined. With the information gained from that Section it is possible to re-assess the earlier work by *Long et al. (1994)* and *Early et al. (1994)* and to establish a realistic limit on the degree of resolution enhancement that may be possible.

Once a data set has been adequately sampled then no amount of re-sampling or combining with other data sets taken of the same scene will improve the spatial resolution of the final image. It has been shown in Section 10.4 that the ERS-1 scatterometer data is adequately sampled and so the only possible advantage to be gained by combining different data sets will be to improve the signal to noise ratio of the image. However, whether this is possible will be dependant on the temporal stability of the scene and on the accuracy with which images of the same scene can be registered. In the case of ERS-1 scatterometer data, the signal to noise ratio is already very high *(Mougin et al. 1995)* and the most significant effect of combining different data sets together will probably be a degradation in the spatial resolution.

An image can be thought of as having been formed by the convolution of the imaging system's impulse response function with the actual scene being represented. Linear deconvolution methods such as the Weiner filter *(Sethmann et al. 1994)* are able to increase the resolution of an image by removing the effect of the 'tapered' impulse response function from the data. However, it is important to note that a restored image obtained using any linear technique will not have a greater bandwidth than the original data. If the frequency content of an image is zero above a certain 'cut-off' level then this range of high frequencies will remain zero after the operation of a linear filter. It can be seen from Figures 10.2 and 10.3 that there is virtually no information existing at frequencies above that corresponding to the sampling rate at 25 km. Therefore the use of linear deconvolution techniques will not increase the resolution of the data beyond this limit.

If the bandwidth of a restored image is no greater than the original image then no genuine super-resolution has occurred. In order to increase the bandwidth of the data beyond that which is possible using linear techniques it is necessary to have some form of *a priori* information about the scene under consideration. In Sections 10.7 and 10.8 a range of different super-resolution algorithms are reviewed and evaluated. Many of these techniques have been developed with specific problems such as identifying small targets within an image. In these cases the form of *a priori* knowledge that can be incorporated in the algorithm concerns the likely physical extent of the objects in question. This information is not available if an entire remotely sensed image is to be enhanced. A number of authors (see Section 10.8) have developed resolution enhancement techniques which are more appropriate for use with entire images than for identifying small targets. These methods generally aim to sharpen the edges within an image. This type of approach will increase the bandwidth of the data but these edge sharpening methods appear to have more in common with image segmentation techniques than genuine super-resolution algorithms.

An alternative means for improving the resolution of ERS-1 scatterometer data would be to avoid degrading it in the first place, during the ground processing stages. This is discussed more fully in the recommendations for further work in Section 10.12.

10.6 Re-sampling the Data

Introduction

In order to improve the resolution of the scatterometer data it will be necessary to extend its bandwidth beyond that imposed by the imaging function. Since the original data is sampled at a rate close to the Nyquist limit, in order to avoid aliasing effects, it will be necessary to re-sample the data at a higher rate. The simplest way of doing this is to 'zero pad' the Fourier transform of the original image. However, this has a tendency to produce ringing effects at the edges of the image which are particularly significant for relatively small images such as the scatterometer data.

During the course of this study two different techniques have been developed which enable a small image to be re-sampled with reduced levels of the problematic ringing effects. The first method is based on performing a convolution in the 'space' domain (as opposed to performing this operation in the Fourier domain). It was later found to be possible to reduce the ringing effects even further by re-sampling the data using a bicubic spline algorithm. Both of the methods are described below.

The convolution method

Figure 10.6 shows a scatterometer image (4B26N61B) taken on the 24th February 1994 with KKJ coordinates SW lat 6693232, SW long 3629383, NE lat 7093357, NE long 4124085. Figure 10.7 shows image 4B26N61B after it has been expanded by a factor of 8 in each dimension by having its Fourier transform zero padded. It can be seen that this new image contains significant ringing effects at the edges. The right hand image in Figure 10.7 is an edge detected version of the 'up-sampled' image, this is shown to demonstrate the edge effects more clearly. (The edge image was derived using a 3×3 Sobel mask.)

The ringing effects demonstrated in Figure 10.7 would completely spoil any attempts to improve the resolution of this data. Therefore, in order to re-sample the data without these effects an algorithm has been derived which allows the re-sampling to be carried out in the image space (as opposed to the Fourier space). This has been achieved by convolving the data with a two-dimensional *sinc* function. Before the convolution process was carried out each of the pixels in the original image were split into 8×8 sub-pixels. The *sinc* function used has its first zero point at a distance of 8 sub-pixels from the peak.

When performing a convolution in the image space there is always a problem in deciding what to do when the mask hangs over the edge of the image. Many algorithms simply avoid this problem by reducing the size of the resultant image by the width of the convolution mask (i.e. by half of the width of the mask at each edge). However, this is not a feasible option with the scatterometer data because there are very few pixels in the first place. The problem has been solved with an algorithm which only considers contributions from the convolution mask which lie within the image. This means that the pixels in the resultant image which lie at the edges and corners of the image have been formed with a smaller number of 'looks' than the central pixels, however the much improved results of the algorithm justify its use.

Figure 10.8 shows the result of re-sampling image 4B26N61B using the convolution method. It can be seen from this image and the corresponding edge image that the ringing effects are greatly reduced.

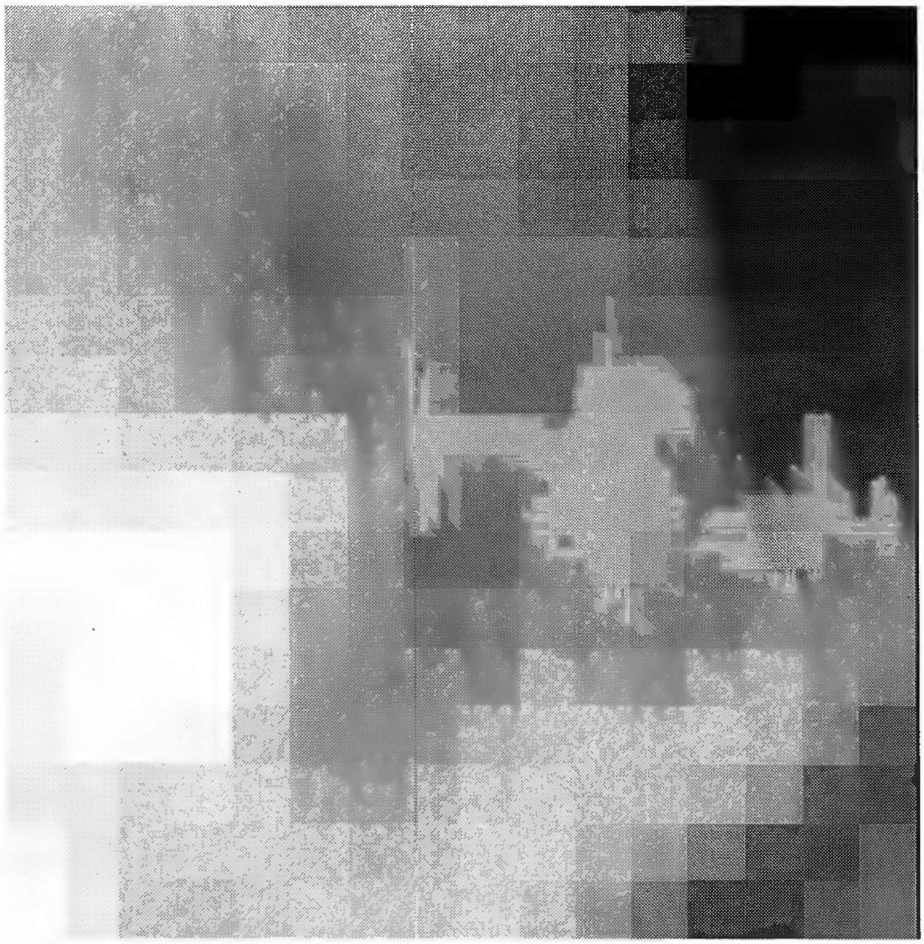

Figure 10.6. Scatterometer data 4B26N61B.

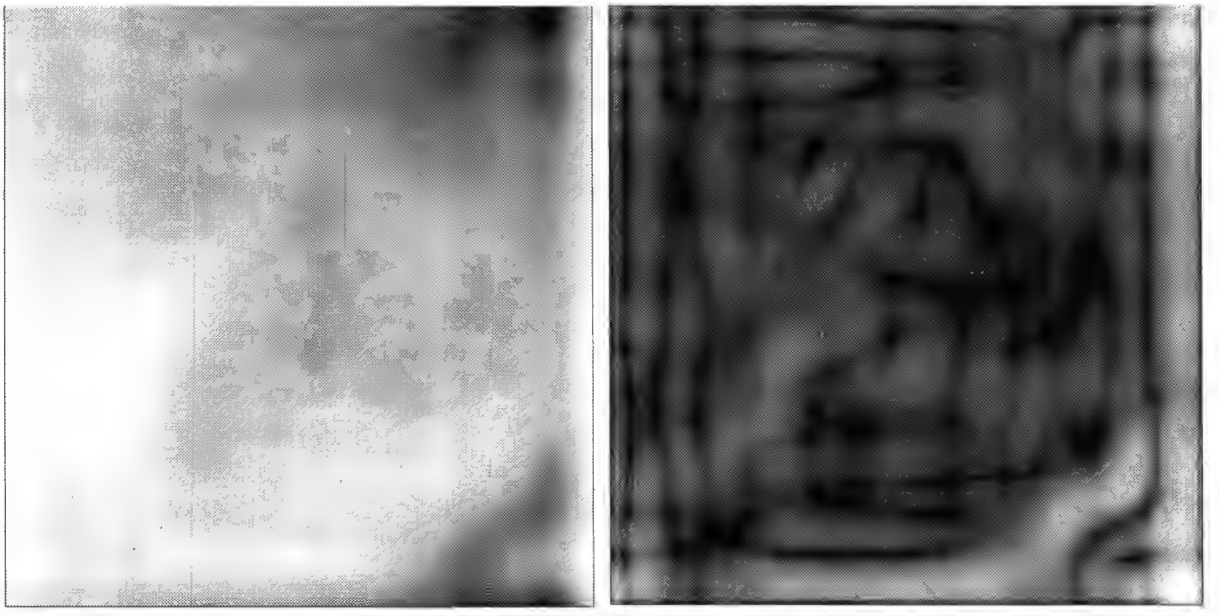

Figure 10.7. The image 4B26N61B 'up-sampled' by a factor of 8 showing ringing effects. The right hand image shows an edge image of the up-sampled image.

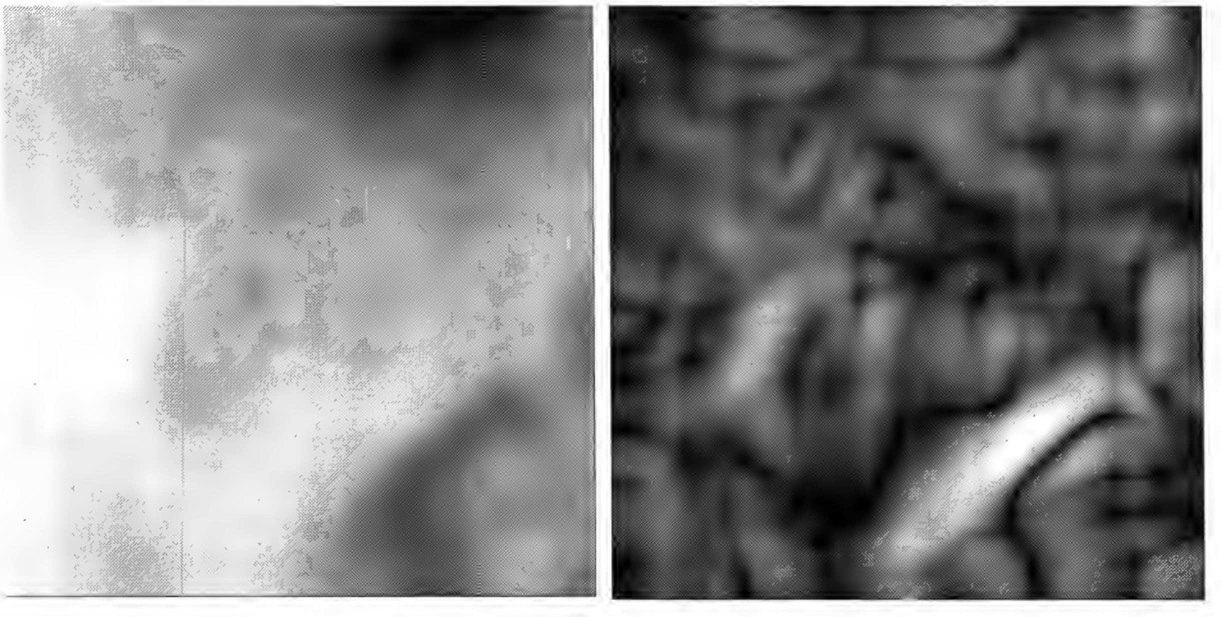

Figure 10.8. The image 4B26N61B 'up-sampled' by a factor of 8 with reduced ringing effects. The right hand image shows an edge image of the up-sampled image.

The bicubic spline method

Although the convolution method described above provided results which were substantially improved in comparison to the zero-padding approach there were still instances where ringing effects could be observed.

In order to re-sample the scatterometer images without introducing spurious ringing effects an algorithm has been written which makes use of bicubic splines. A NAG routine has been used to perform the bicubic spline operation; this is the routine E02DCF described in the NAG Fortran Library Manual, Mark 15. (The slowly varying nature of the scatterometer data has made it possible to set the "smoothness factor" used by this algorithm to zero in all instances.)

Figure 10.9 shows a scatterometer image of north east Finland taken on the 23rd June 1993. This figure also shows re-sampled versions using both the convolution technique and the bicubic spline. It can be seen that the bicubic spline version does not show the horizontal 'ringing lines' which are present in the image derived using the convolution technique.

A point which needs to be noted when using the bicubic spline method is that the interpolation excludes a small border around the edge of the image which has a thickness of one half of an original image pixel. This is because the interpolation extends between the centres of the pixels which leaves a missing edge of half a pixel at the boundary of the image. This effect is evident in Figure 10.9 where it can be seen that, for example, the dark area at the top of the image is narrower in the bicubic spline version than in that from the convolution.

The graph in Figure 10.10 helps to show more clearly the effects described above. Figure 10.10 shows a series of vertical cross-sections taken through the three images shown in Figure 10.9 (the slice is taken at approximately half-way across the image). It can be seen that the bicubic spline has provided a result without any ringing effects. The figure also shows the fact that the bicubic spline interpolation causes one half of a pixel to be lost at either end of the image. In order to plot these curves on the same axis the (effectively) smaller interpolation given by the bicubic spline has been stretched out slightly. This has caused, for example, the small dip in intensity at the right-hand side of the figure to be mis-aligned in the two interpolations.

Figure 10.9. The left-hand image shows scatterometer data collected over north east Finland. The centre image shows the result of re-sampling this image by a factor of 8 using the convolution method. The right-hand image shows the result of re-sampling using the bicubic spline technique.

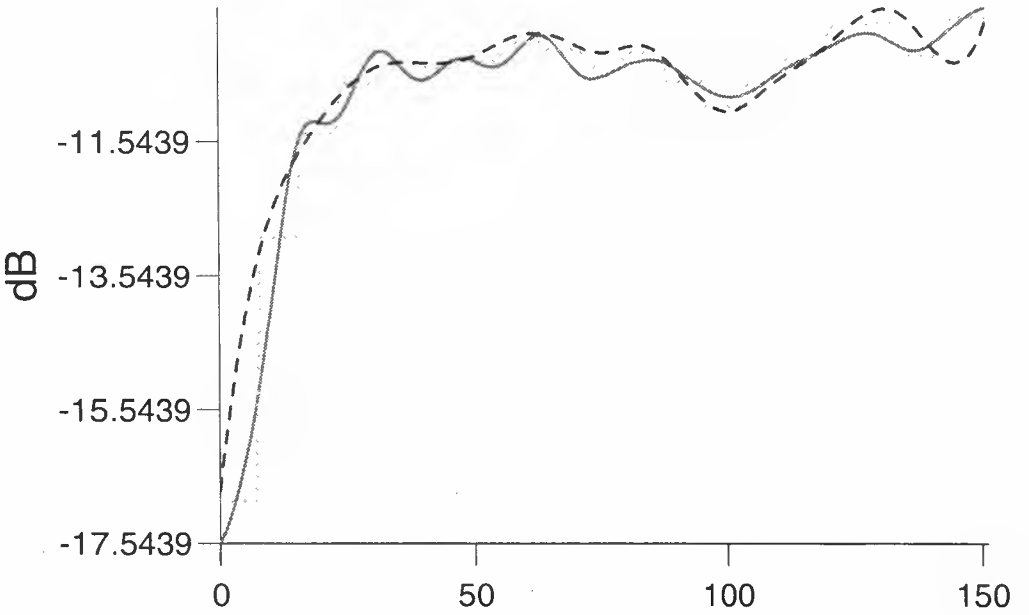

Figure 10.10. This graph shows a vertical cross-section through the images shown above. The dotted line shows the original image values. The solid line shows the ringing effects present in the convolution interpolation. The dashed line shows the bicubic spline interpolation. In this demonstration it can also be seen that the bicubic spline solution is slightly mis-aligned with respect to the other two lines.

10.7 A Review of Deconvolution and Enhanced Resolution Algorithms

Introduction

During this study a range of different deconvolution and enhanced resolution algorithms have been reviewed and tested. In this Section a review is given of the basic algorithms which were considered as possible candidate methods for use with the scatterometer data. In Section 10.8 the algorithms discussed here are assessed further and over Sections 10.9 and 10.10 a method is defined which is applied to data from the project test sites.

In the following discussion the topics and algorithms listed below are considered:

* A review of the image restoration problem.
* Linear deconvolution techniques.
* The Wiener filter.
* Constrained iterative deconvolution.
* Bayesian methodology.
* The maximum likelihood technique.
* The maximum a posteriori (MAP) technique.
* Maximum entropy.

A review of the image restoration problem

A digital image $s(i)$ can be thought of as having been formed by the convolution of the imaging system's impulse response function $h(i)$ with the actual object or scene being considered $f(i)$.

This can be represented by the equation:

$$s(i) \quad = \quad f(i) \otimes h(i) + n(i) \tag{10.3}$$

Where $\otimes$ represents the convolution operation and $n(i)$ is any noise inherent in the system. Deconvolution techniques aim to recover the scene $f(i)$ from the image assuming that something is known about the imaging function $h(i)$. The fundamental difficulty of image restoration is the ill-conditioned behaviour of an integral equation of this kind. This means that minor perturbations in the data can lead to major perturbations in the solution, ie. the presence of noise in the image can lead to major errors in attempts that are made to reconstruct the scene $f(i)$.

Linear deconvolution techniques

If we ignore the noise term in the convolution - image formation equation, then it initially appears that the original scene can be recovered from the blurred image by inverse filtering, ie if,

$$s(i) = f(i) \otimes h(i) \tag{10.4}$$

then

$$S = F \times H. \tag{10.5}$$

Where S, F and H denote the Fourier transforms of s, f and h. Therefore, an estimate of Fourier transform of original scene is given by;

$$F' = \frac{S}{H}. \tag{10.6}$$

However, in practice conventional inverse filtering does not work. In general H will be band-limited so that it will either become zero or will assume very low values for frequencies above a given cutoff frequency. At the high frequencies for which H is zero the inverse filter will be undefined and where it has very low values it will amplify high frequency noise components in the signal.

The Wiener filter

The inverse filter can be modified to help to prevent high-frequency gain and noise amplification. The Wiener filter is an example of such a modification. A commonly used version of the Wiener filter has the following form;

$$F' = \frac{H^*}{|H|^2 + 1/(SNR)^2} S \tag{10.7}$$

Where SNR is an estimate of the signal to noise ratio in the image and the symbol * denotes the complex conjugate.

The Wiener filter suppresses noise efficiently but at the same time it suppresses the weak signal components even more. These components often form the important edge details which help to define an image. As a result a Weiner filter restored image will often exhibit 'ringing' or undershoot/overshoot effects at the edges.

In addition, it is important to note that the estimate F' obtained using any linear technique, such as the Wiener or inverse filter, will not have a greater bandwidth than the original data S. If S is zero for a certain range of high frequencies then they will remain zero after the operation of a linear filter. If the bandwidth of the restored image is no greater than the original image then no genuine super-resolution is possible. (However, by using the Wiener filter in conjunction with edge sharpening and 'ringing' reduction methods it is possible to increase the bandwidth of the image. This is discussed further in Section 10.8.)

Constrained iterative deconvolution

Equation (10.6) shows how an estimate for F' can be obtained by a single application of the operator $1/H$ on the data H. It is also possible to obtain the same result using an indirect iterative method. This iterative result can be derived by first expanding $1/H$ in terms of a geometric series, ie.

$$F' = \alpha(\Sigma_{n=0}^{\infty}(1-\alpha H)^n)S \tag{10.8}$$

The term in brackets converges to $1/H$ provided,

$$\| 1-\alpha H \| < 1 \tag{10.9}$$

Where $\| . \|$ denotes the Euclidean norm. This condition can usually be met by a suitable choice of α. If F_k' is the approximation given by summing k terms in Equation (10.8), then the relationship between F_k' and F_{k+1}' is given by,

$$F_{k+1}' = \alpha F + (1-\alpha H)^n F_k' \tag{10.10}$$

At first sight this iterative solution only appears to provide a slow method for obtaining a result which offers no super-resolution and which is very sensitive to noise. However, the value of the iterative approach is that it allows non-linear constraints to be introduced which can help to reduce noise effects and to increase the bandwidth of an image.

The use of an inverse filter (whether implemented directly or iteratively) will generally produce ringing effects at boundaries or around point features. This ringing will typically result in negative pixel values. If it is known *a priori* from physical grounds that the required image must be entirely positive then this constraint can be enforced at each iteration, ie.

$$F_{k+1}' = F[\mathrm{P}[F^{-1}\alpha F + (1-\alpha H)^n F_k']] \tag{10.11}$$

Where P is a positivity operator which simply clips any negative values to zero, and where F and F^{-1} denote forward and inverse Fourier transform operators. This algorithm is known as a form of constrained iterative deconvolution and can be shown to converge under the same criteria expressed in Equation (10.9).

The positivity constraint used in Equation (10.11) is a non-linear operator and therefore tends to extend the bandwidth of the reconstructed image beyond that which exists in the original band-limited image. If high frequency information has been lost in the imaging process then this can potentially be recovered using the algorithm thus making genuine super-resolution possible.

If, in addition to positivity, there is other *a priori* knowledge about the required reconstructed image (in either the image or Fourier domains) then this can also be incorporated in the form of non-linear constraints in Equation (10.11)

Bayesian methodology

Bayesian probability theory has proved useful in a wide range of applications. In terms of the image reconstruction problem the basic Bayes equation can be written as;

$$p(f \mid s) \quad = \quad \frac{p(s \mid f)p(f)}{p(s)} \tag{10.12}$$

Where the notation $p(a \mid b)$ denotes the probability of a occurring given that b has occurred. Bayesian estimation attempts to recover the object f in such a way that the probability of getting f given the observed measurements in s is a maximum. The term $p(f \mid s)$ is known as the *a posteriori* probability and therefore finding the maximum of this distribution is known as the maximum *a posteriori* or MAP method. In practice the MAP method is implemented by making assumptions about the distributions of $p(s \mid f)$ and $p(f)$ which are consistent with what is known about the imaging system in which s was measured (the denominator term $p(s)$ will be a constant and does not affect the optimisation). The distribution of $p(s \mid f)$ is given by what is known about the statistics of the noise in the system. Assigning an *a posteriori* probability distribution to the object f is generally more difficult than that of $p(s \mid f)$. In cases where there is no reliable indication about the statistical behaviour of the object then $p(f)$ can be set to a constant. The problem of maximising $p(f \mid s)$ then reduces to one of maximising $p(s \mid f)$, this procedure is known as the maximum likelihood (ML) solution.

The maximum likelihood technique

In order to implement a maximum likelihood algorithm it is necessary to make some assumption about the probability distribution function of the noise that will affect the image. *Long at al. (1993)* suggest that for scatterometer data the variance of the intensity is likely to be proportional to the mean of the signal. This is consistent with the Poisson probability density which is known to govern the arrival of photons at a detector. The probability distribution function of a single Poisson random variable is given by the expression:

$$p(x) \quad = \quad \frac{\lambda^{x}\exp(-\lambda)}{x!} \tag{10.13}$$

Where λ is the rate parameter that governs the arrival of photons per unit time at a pixel. By making use of the fact that the probability distribution function of all of the image pixels is the product of the distributions for all of the pixels considered separately it is possible to write an expression for the conditional probability of the image s given the scene f,

$$p(s \mid f) \quad = \quad \prod_{i}\frac{(h(i)\otimes f(i))^{s(i)}\exp(-h(i)\otimes f(i))}{s(i)!} \tag{10.14}$$

Hunt (1994) has shown how this expression is maximised with respect to f under the condition that the following set (one for each j) of equations is met;

$$\left[\frac{s(i)}{h(i) \otimes f(j)} \right] \otimes h(i) \quad = \quad 1 \tag{10.15}$$

This set of non-linear equations and their solution using an iterative approach is known as the Richardson-Lucy maximum likelihood algorithm which has been derived independently by a number of authors, eg. *Holmes and Liu (1989)*;

$$f'_{k+1} \quad = \quad f'_k \left(\left(\frac{s}{h \otimes f'_k} \right) \otimes h \right) \tag{10.16}$$

The Richardson-Lucy maximum likelihood image restoration algorithm has been implemented and tested on simulated scatterometer data. The results of this algorithm have a tendency to produce a 'checker-board' effect on the final image. This has also been reported by other authors eg. *Levitan and Herman (1987)*.

The maximum a posteriori (MAP) technique

The MAP technique is similar to the Maximum Likelihood method. However, whilst in the Maximum Likelihood method it is assumed that there is no available information about the statistics of the underlying scene (sometimes referred to as the 'maximum ignorance' assumption) in the MAP method a probability distribution is assigned to the underlying object statistics. *Hunt (1994)* has derived an iterative algorithm which models the object statistics (as well as the noise) by a Poisson distribution, this is given by the following expression;

$$f'_{k+1} \quad = \quad f'_k \exp\left(\left(\frac{s}{h \otimes f'_k} - 1 \right) \otimes h \right) \tag{10.17}$$

This approach has been implemented and has produced some encouraging preliminary results. After a limited number of iterations the resultant restored images do not exhibit the 'checker-board' effect found using the maximum likelihood technique.

The Poisson model used to describe the object statistics does not take in to account any possible correlation that might exist between neighbouring pixels. In general there will be a high degree of correlation between the backscattering characteristics of the areas in a scene which represent neighbouring pixels in an image. This is desirable information to include, if possible, in a de-convolution algorithm. However, in practice this has proved difficult to achieve, and solutions have a high degree of complexity. *Levitan and Herman (1987)* have attempted to model neighbouring pixels as being related by a Gaussian model. *Herbert and Leahy (1989)* have used a gradient ascent technique to solve this problem in a model where neighbouring pixels are related to one another by a Markov process.

Maximum entropy

The reconstructed image which has the maximum entropy is the one which contains the least amount of information (subject to the image equation and the initial given image). The only structure that is present in the reconstruction is that which is necessary to fit the data, and the solution will therefore contain the minimum of artifacts.

Although the maximum entropy approach has remained popular amongst many authors the underlying rational of the technique has caused widespread controversy, *Gull (1989)*. For example, it has been argued that its use is more suited to the estimation of probability distributions rather than to image reconstruction problems (*Frieden 1985, Bedini and Tonazzini 1990*).

10.8 Assessment of Deconvolution and Enhanced Resolution Algorithms

Introduction

In the previous Section (10.7) a review was given of a range of different deconvolution and enhanced resolution algorithms which might be appropriate for use with scatterometer imagery. In this Section a number of the problems associated with some of these methods are discussed. This assessment has then led to the development of an algorithm (defined over Sections 10.9 and 10.10) which has been designed to take into account the characteristics which are particular to scatterometer data.

The image deconvolution methods reviewed for this study in Section 10.7 have included the constrained iterative deconvolution algorithm and the maximum likelihood and maximum a posteriori techniques. There are some problems associated with these methods:

* These techniques have all been implemented using iterative algorithms and as a consequence can take a long time to run (the maximum likelihood method described by Holmes and Liu 1989 typically requires between 1,000 and 10,000 iterations).

* These techniques all make (repeated) use of Fourier techniques. As is discussed in Section 10.9 this has a tendency to produce strong edge effects in the scatterometer data.

* The positivity constraint used in the constrained iterative deconvolution algorithm is more appropriate for problems involving the identification of point targets on a dark background.

Super resolution algorithms are most commonly used for identifying and classifying small targets (e.g. stars in astronomical images or military targets such as aircraft or tanks in radar images, *Delves et al. (1988)*). In these cases the form of *a priori* knowledge that can be incorporated in the algorithm concerns the positivity of the image or the likely physical extent of the objects in question. It is for use in circumstances such as these that methods such as the constrained iterative deconvolution algorithm and the maximum likelihood and maximum *a posteriori* techniques have been designed and most regularly tested. If the problem is to enhance the resolution of an entire remotely sensed image then it is much less clear how any *a priori* information can be incorporated into a resolution enhancing algorithm. The only real *a priori* information that exists is that, in general, different land use types change quite abruptly from one region to the next. The most obvious example of this phenomenon is the boundary between water and land. This will usually involve a sharp discontinuity rather than a smooth transition.

A number of different authors have sought to develop deconvolution techniques which are much less computationally expensive than the iterative methods discussed above and which are more suitable for the general problem of enhancing images rather than the specific task of identifying certain small targets within an image. All of these algorithms are similar in the sense that they use the simple Wiener filter solution and also recognise that this is liable to produce (Gibbs) ringing artifacts in the vicinity of edge structure within the image. Methods are then used to sharpen the edges and reduce any ringing effects.

Sethmann et al. (1991) have used a method combining maximum entropy and Wiener filtering (originally developed by *Gonsalves and Kao (1987)*) to enhance satellite microwave SSM/I data. The technique uses the Wiener filter to remove the effect of the impulse response function from the data and uses the maximum entropy approach to help to sharpen the edges within the image and to help to reduce any ringing effects which may have been introduced by Wiener filter at the edges in the image. In their later work in this same area *Sethmann et al. (1994)* no longer use the maximum entropy approach and have adapted their use of the Wiener filter to reflect the fact that the SSM/I instrument impulse response function varies across its swath.

A similar method to the maximum entropy and Wiener filter technique has been developed by *Lettington and Hong (1994a)*. In this algorithm the Wiener filter is combined with a maximum likelihood approach which assumes that the distribution of edges within an image follows a Lorentzian function. In the case of the scatterometer images, which only contain 19×19 pixels, it is probably not sensible to make this assumption about the distribution of edges. *Lettington and Hong (1994b)* have also developed an algorithm where a Wiener filter is followed by a stage where the edges within the image are identified and replaced by simple flat planer regions. This reduces any ringing effects and generally sharpens the image.

The algorithm due to *Lettington and Hong (1994b)* is similar to the method known as the theory of convex projections which is described by *Sezan and Tekalp (1990)*. In this method the Wiener filter solution is used in areas where it is believed that ringing artifacts will not be produced. In the vicinity of the problematic edge regions a solution is derived by making use of information gained by having previously segmented the image.

An alternative and simpler technique for removing ringing artifacts is to use a median filter. This approach was used in the algorithms designed by *Long et al.* for enhancing scatterometer data and has also been used in this current study following an initial Wiener filtering stage (Section 10.10).

Of the iterative techniques reviewed in Section 10.7 the maximum *a posteriori* (or MAP) method was judged to be the most promising. The arguments which have been presented above have have tended to show that for scatterometer data it might be more suitable to use a method based upon the Wiener filter which a subsequent post-processing stage to sharpen the edges and to remove any ringing effects. In the light of these facts it is instructive to compare the results of the MAP and the Wiener filtering approaches.

The MAP method can be implemented using an iterative algorithm (Equation (10.17)) which can produce results with less than 100 iterations. Figure 10.11 shows a comparison of the MAP and Wiener methods using data taken over South-East Finland on the 23rd July 1993. In order to produce these results the reflection algorithm was used in both cases (see Section 10.9, the MAP algorithm was run for 25 iterations, the Wiener reciprocal signal-to-noise parameter was set to 0.02 and no median filter was used. It can be seen that the resulting enhanced images are very similar. This visual impression is further confirmed by examining cross-sections taken through the images. In Figure 10.12 a horizontal cross-section is shown which is approximately 6% down from the top of the image.

There appears to be little (if any) advantage to using the MAP solution in favour of Wiener filter based approach. In addition the Wiener filter is much quicker to use and therefore in subsequent Sections it is the Wiener filter which forms the basis for the methods which are applied to scatterometer data.

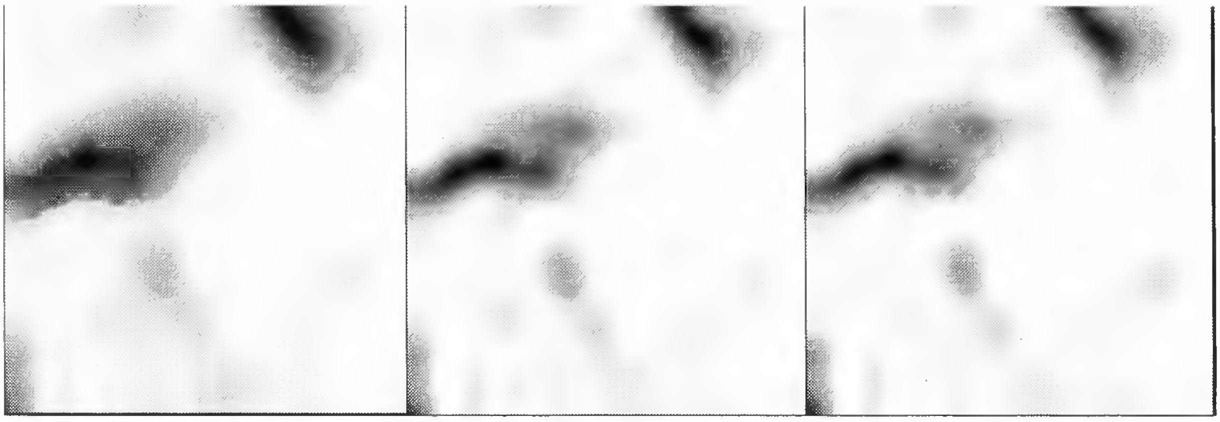

Figure 10.11. Left to right: Re-sampled data from scatterometer image from Eastern Finland 23rd July 1993. Wiener filtered image. MAP solution.

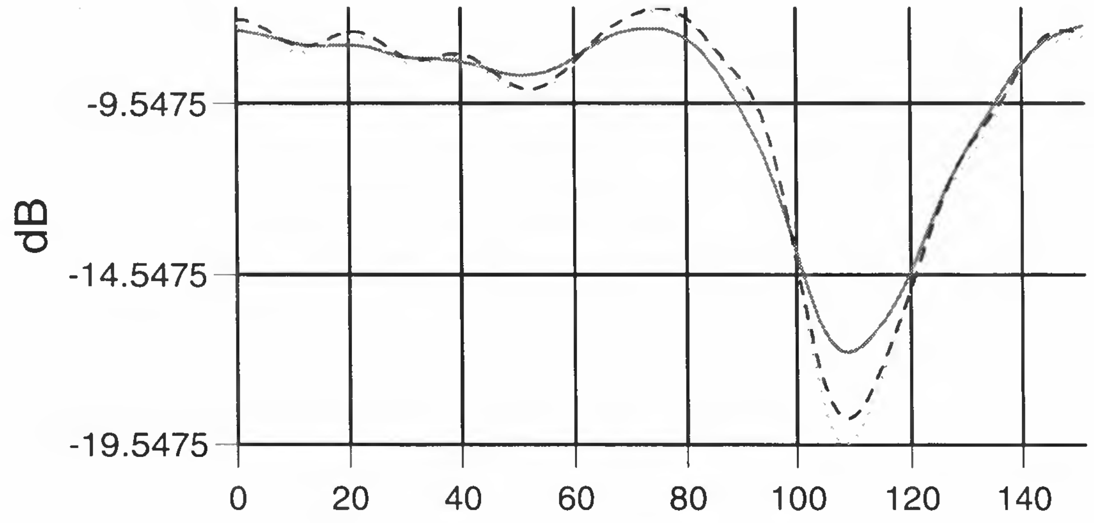

Figure 10.12. The solid line indicates the original re-sampled data, the dashed line represents the MAP solution and the dotted line shows the Wiener solution.

10.9 The Reflection Algorithm

In Section 10.6 the ringing effects were discussed which were caused when scatterometer images are re-sampled by zero padding a Fourier transform. Ringing effects are also caused when Fourier methods are employed in the enhanced resolution techniques which were reviewed in Sections 10.7 and 10.8. The discrete Fourier transform algorithm assumes that an image is circular and joined at the edges (ie. in the form of a torus). This 'wrap-around' effect can cause ringing effects at the edges of a resultant enhanced image.

In order to reduce the ringing effects in an enhanced image an algorithm has been written which reflects portions of the original image to form a larger image which has twice the dimensions of the original. Figure 10.13 shows an up-sampled scatterometer image taken over southern Finland on the 23rd July 1993. Figure 10.14 shows the image of Figure 10.13 after it has been reflected and expanded.

Figures 10.15 and 10.16 show the result of applying a Wiener filter to the original and reflected scatterometer data. (The reflected image has been 'cropped' so that only the relevant 'non-reflected' area of the image is shown and the reciprocal signal-to-noise factor (see Equation (10.7)) used in the Wiener filter was in each case 0.01.) It can be seen that the reflection algorithm has smoothed the boundaries at the edge of the image and has therefore helped to prevent the ringing effects. The extent of the ringing in the non-reflected image is also demonstrated in Figure 10.17 which shows a horizontal slice taken at approximately 45% of the way down each of the Wiener filtered images. It can be seen that the reflection algorithm has very substantially reduced the ringing effects which are prominent in the non-reflected version.

Figure 10.13. Scatterometer data from Southern Finland.

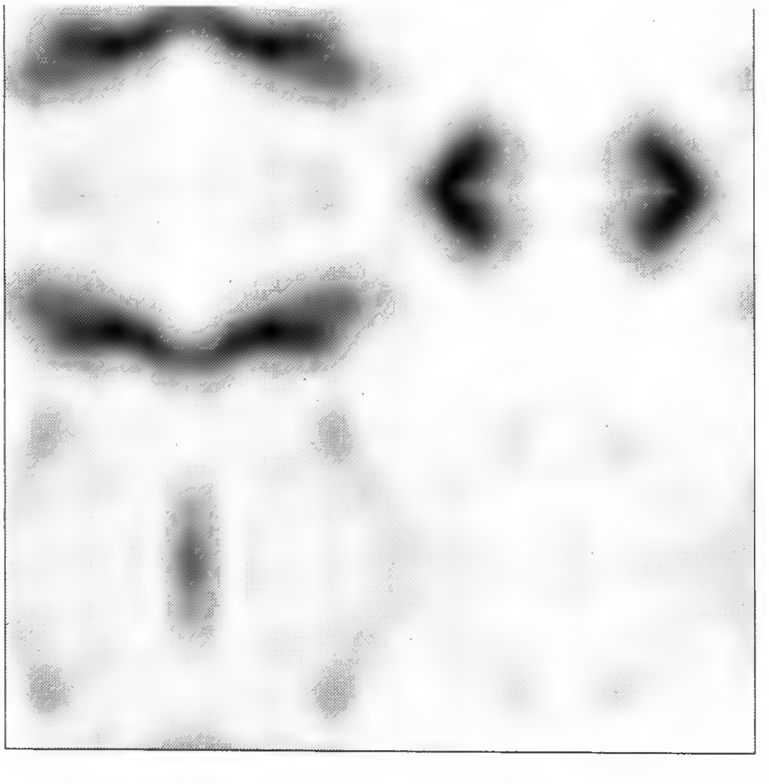

Figure 10.14. 'Reflected' scatterometer image from Southern Finland.

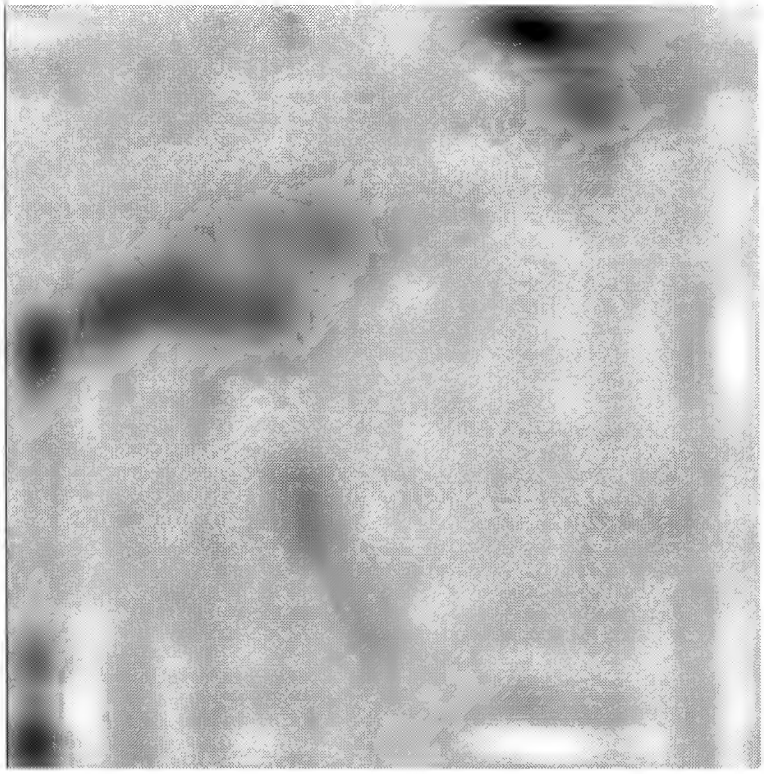

Figure 10.15. Wiener filtered version of the scatterometer data from Southern Finland (showing ringing effects).

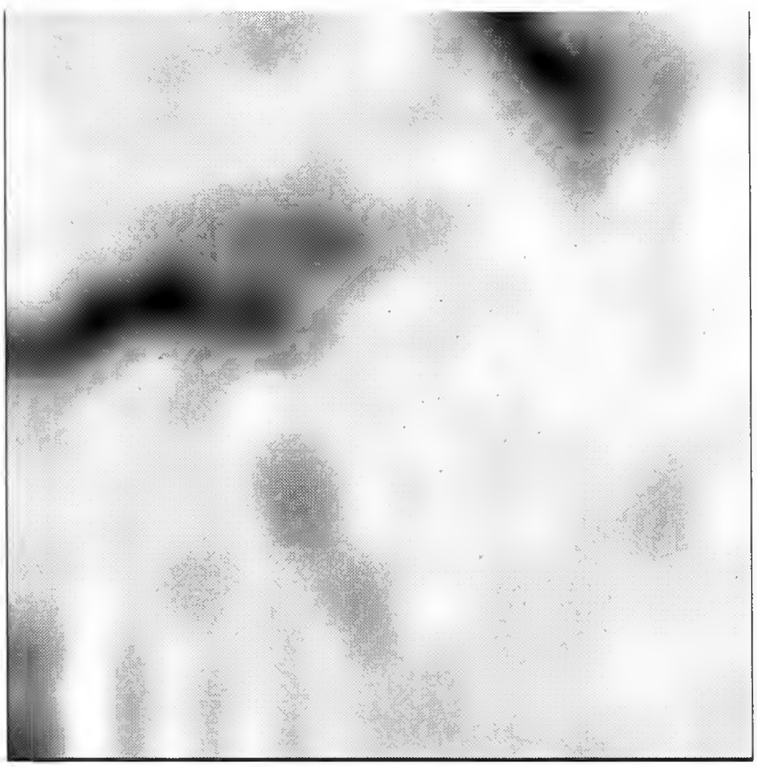

Figure 10.16. Wiener filtered version of the reflected scatterometer image from Southern Finland (with reduced ringing effects).

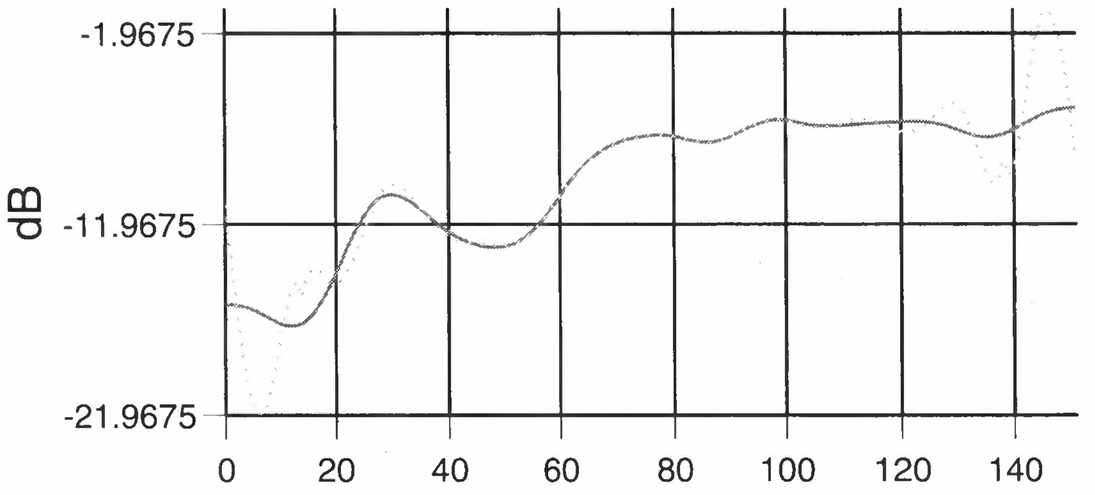

Figure 10.17. Graph showing a horizontal cross section through the Wiener filtered images. The solid line shows the reflected image and the dashed line the non-reflected image.

10.10 The Wiener Filter and Median Filter

The discussion in Section 10.8 presented arguments which suggested that an algorithm which included a Wiener filter and a edge sharpening method such as a median filter would be suitable for application with scatterometer data.

Figures 10.18 and 10.19 show a sequence of image enhancing processing stages applied to scatterometer data taken over East and West Finland on the 22nd and 23rd of July 1993. The steps shown are the re-sampling process, the application of a Wiener filter (with the reciprocal signal-to-noise parameter set to 0.02, see Equation (10.7)), and the application of two median filter steps using a window size of 8×8 sub-pixels (ie. 25×25 km). The median filter stages help to remove noise such as any unwanted ringing effects and, to an extent, can help to sharpen the edges between the boundaries in the image.

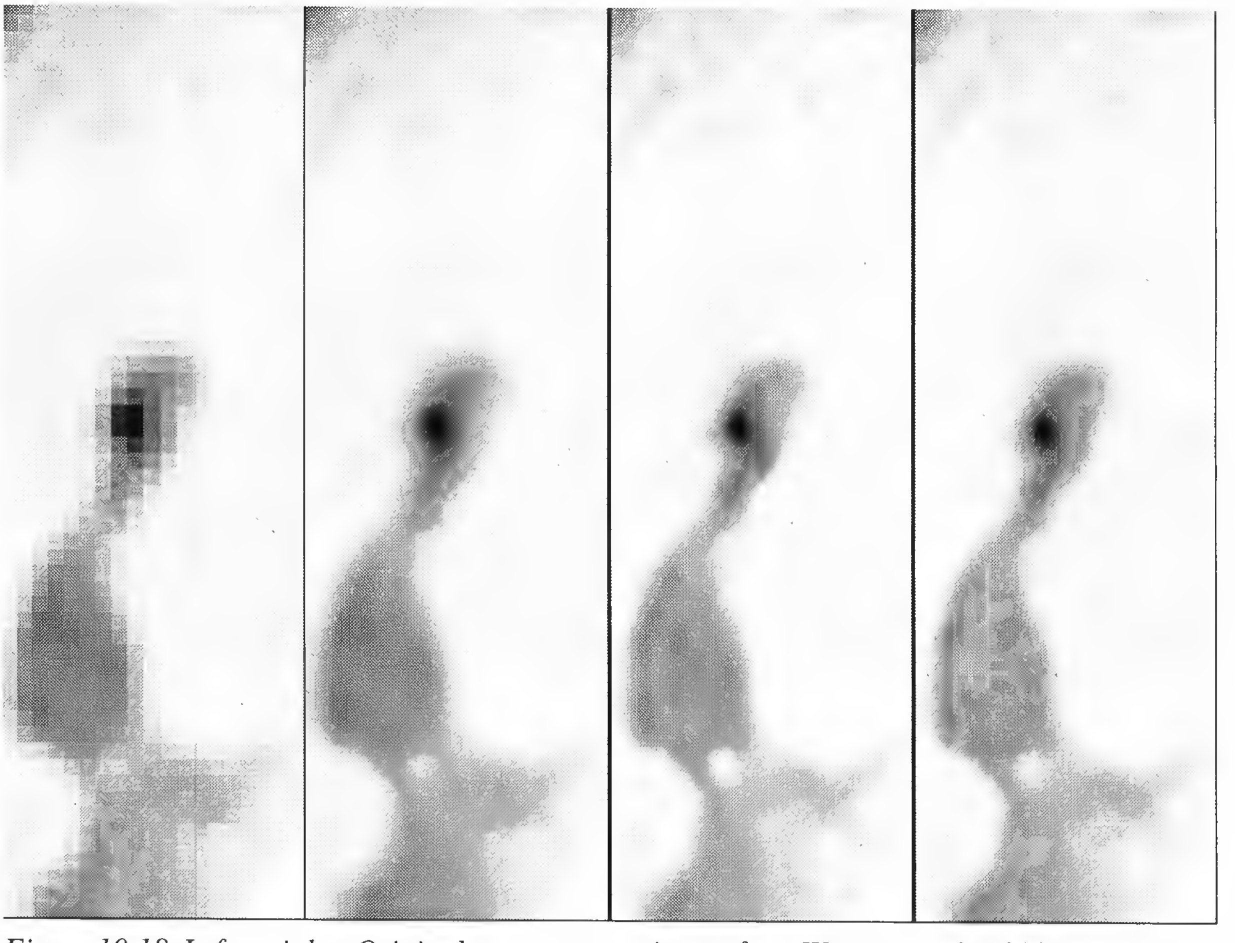

Figure 10.18. Left to right: Original scatterometer image from Western Finland 22nd July 1993. Re-sampled data. Wiener filtered image. Wiener and median filtered image.

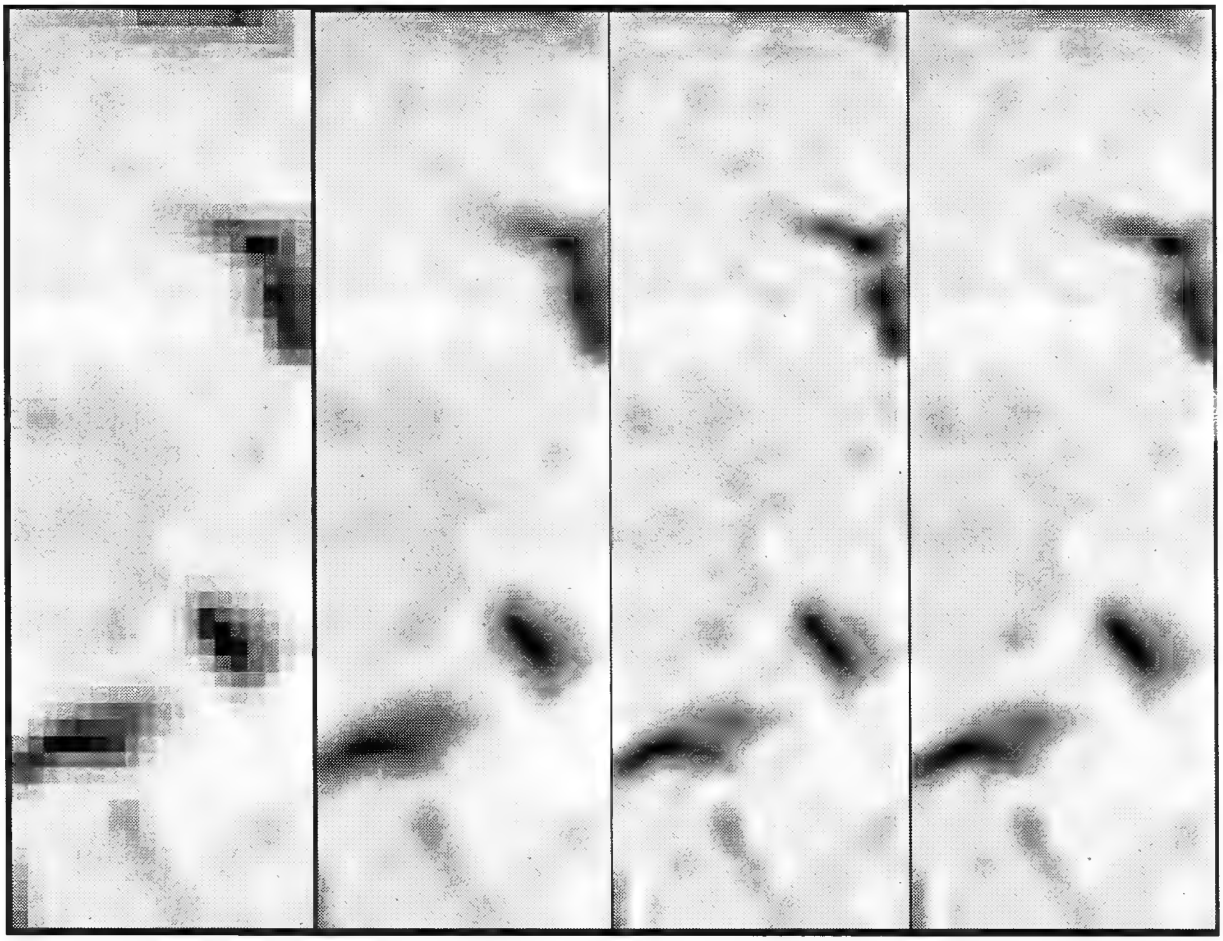

Figure 10.19. Left to right: Original scatterometer image from Eastern Finland 23rd July 1993. Re-sampled data. Wiener filtered image. Wiener and median filtered image.

10.11 The Finnish Land - Water Mask

A land - water mask for Finland is available which shows where the coast-line lies around Finland and where the major lakes are situated. In this Section simulated and real scatterometer data are used to demonstrate how this mask may be combined with the Wiener filter to enhance the resolution of images.

The 'header files' for the scatterometer images from Finland contain data which gives the position of each pixel in terms of the Finnish KKJ coordinate system. The Finnish land - water mask is also given in terms of the KKJ coordinate system so it is therefore possible to 'look-up' an appropriate land - water index value for each pixel in a scatterometer image. An algorithm has been written which performs this task.

Figure 10.20 shows a scatterometer image of western Finland taken on the 22nd June 1993 and a corresponding land - water mask for this particular region. The white areas in the mask represent the water, the grey areas represent the land and the black areas are those which correspond to regions not covered by the mask. It can also be seen that the mask is only valid for the regions in the close vicinity of Finland. A small area off the west coast of Finland is marked as water but most of the remainder of the Gulf of Bothnia is incorrectly shown as being land.

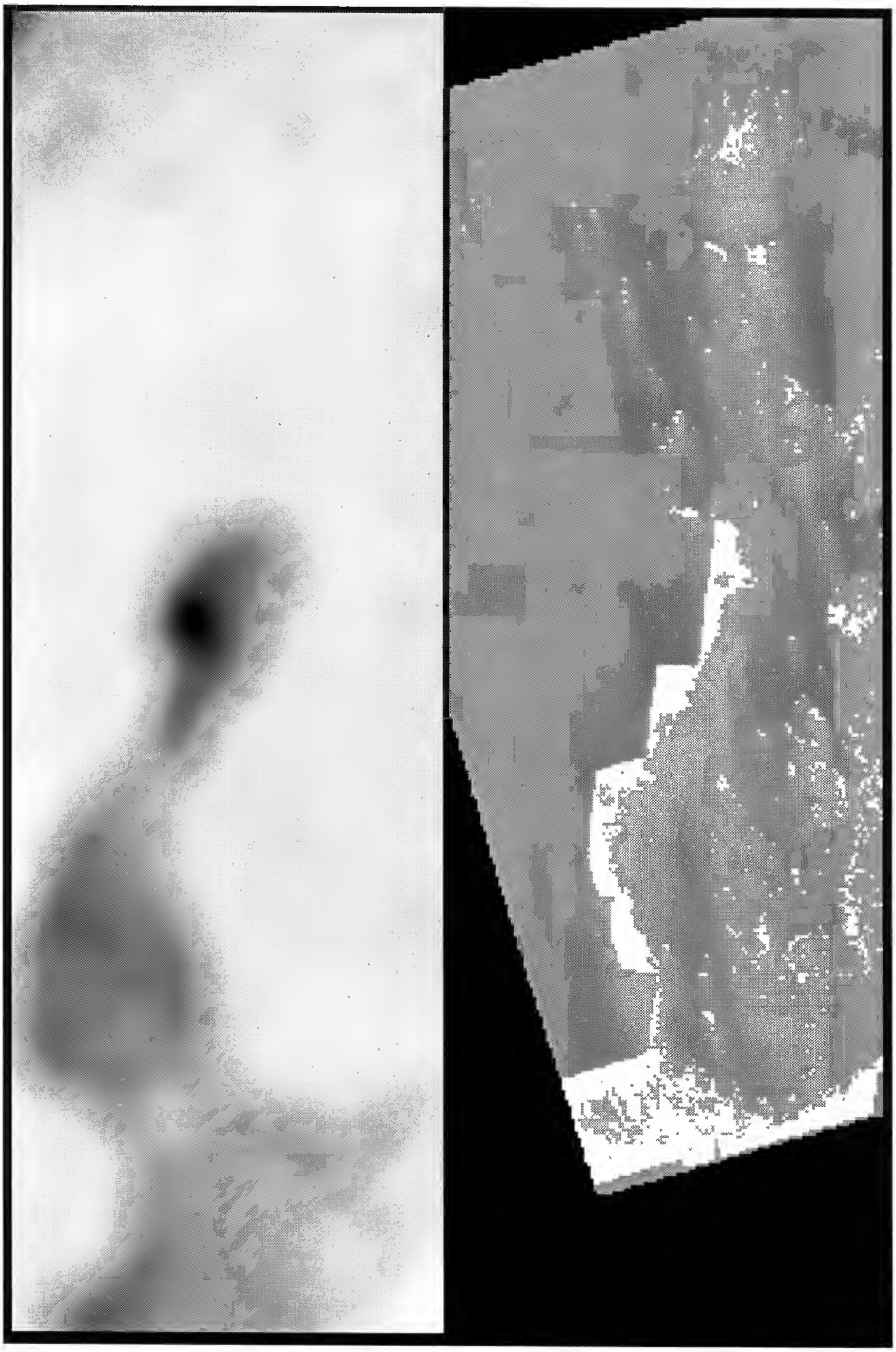

Figure 10.20. The left-hand side shows a scatterometer image of the west of Finland. The right-hand image shows the corresponding land - water mask for this same region.

Using a Land - Water Mask: Simulated Data

In order to make use of the land - water mask for enhancing the scatterometer data a simple algorithm has been written which can be applied to a Wiener filtered image. The algorithm essentially replaces each pixel in the Wiener solution by the mean of the values in a window (of user specified size) which surround the pixel. However, pixels from the window are only used in the mean calculation if they have land - water mask values which are the same as that for the centre pixel under consideration. Thus if the centre pixel has a mask value indicating it is from an area of land then only pixels within the window which are also designated as land are used to calculate the mean value.

A simple demonstration of this algorithm is shown in Figure 10.21. The figure shows an image of a rectangle before and after it has been blurred using a Hamming weighting function. The rectangle might represent, for example, an area of water surrounded by land (or visa versa). The figure also shows the result of applying a Wiener filter to the blurred image and the result of having twice applied the 'masked-mean' algorithm to the Wiener solution (the mask being the original rectangle image). The image contains 32×32 pixels and the Hamming function has a width of 11 pixels. The signal-to-noise ratio factor required by the Wiener filter was set to 0.001 (see Equation (10.7)) and the width of the masked-mean window was 7×7 pixels. It can be seen that the final reconstructed image is similar to that of the original.

The results from Figure 10.21 are more clearly demonstrated in the graph shown in Figure 10.22. This graph shows a horizontal cross section taken through each of the images shown in Figure 10.21. It can be seen that the Wiener solution manages to redistribute the energy in the image so that more of it returns to the rectangle region. However, in doing so this causes a degree of 'under-shooting' and 'over-shooting'. After the application of the masked-mean filter these ringing effects are flattened out. Also shown in Figure 10.22 is the result of applying the masked-mean filter directly to the blurred data, i.e. without the intermediate Wiener filter stage. It can be seen that although this solution has 'sharpened-up' the blurring effect it has not restored the intensity levels to their correct values.

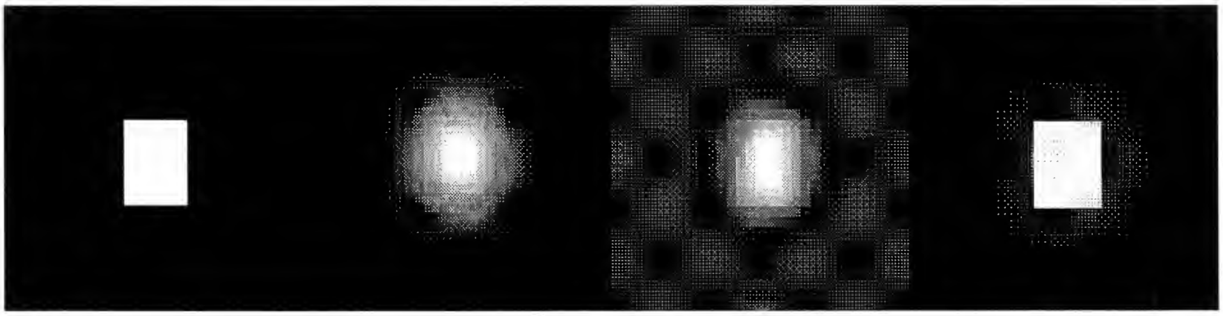

Figure 10.21. Left to right: Original image. Blurred image. Wiener restored image. Masked-mean image.

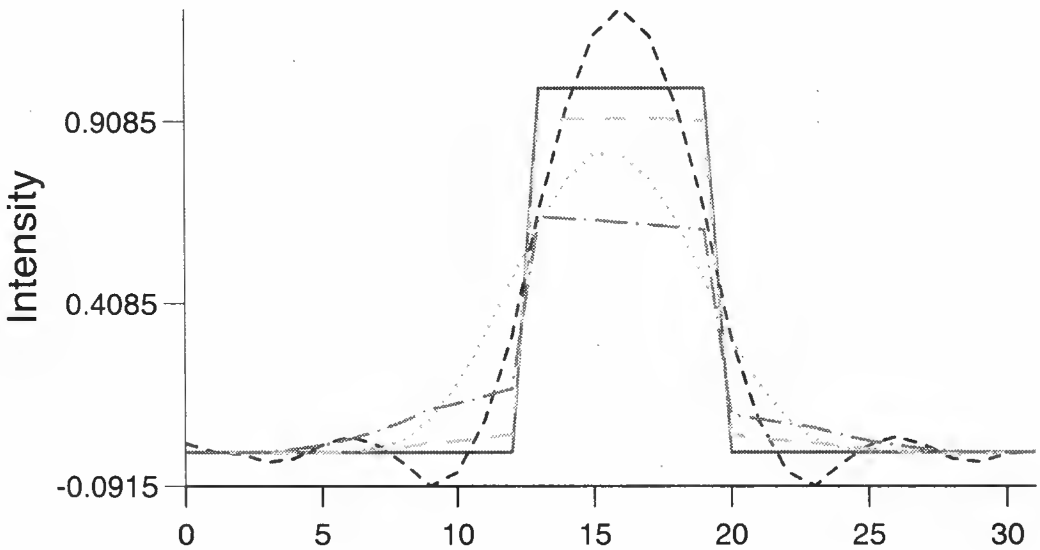

Figure 10.22. Graph key: Solid line = Original image. Dotted line = Blurred image. Short dashed line = Wiener restored image. Long dashed line = Masked-mean image applied to the Wiener solution. Combined dot and dashed line = Masked-mean applied directly to the blurred image.

Using a Land - Water Mask: Scatterometer Data

The masked-mean algorithm has been applied to scatterometer data from Finland. Figure 10.23 shows a scatterometer image from western Finland taken on the 22nd June 1993 together with the land - water mask which corresponds to this region. Also shown is the result of having applied the masked-mean algorithm to the output from the Wiener filtered version of the original image. The valid part of the land - water mask does not cover the whole of the region in the image and this has caused features, which are as prominent as the enhanced definition of the genuine coastline, which can be observed in this image. (The bicubic spline algorithm was used to up-sample the original image by a factor of 16, the signal-to-noise factor used in the Wiener filter was 0.05 and the window size of the masked-mean algorithm, which was applied twice, was 7×7.)

Figure 10.23. Images: left to right. Original re-sampled scatterometer image from west Finland. Land - water mask. Enhanced image using land mask.

10.12 Summary

This Chapter has given a comprehensive review of all of the important issues which need to be considered in order to address the problem of improving the resolution of ERS-1 scatterometer data. A wide range of potential super-resolution methods have been reviewed and assessed and an algorithm has then been defined which has been used to enhance the resolution of scatterometer data collected over Finland.

It has been shown that the form of the ERS-1 scatterometer data is very heavily influenced by the ground processing chain which essentially convolves the received pulses with a Hamming function. This ensures that the resulting images are not under-sampled so that averaging overlapping images (which was suggested in earlier work in this area) would not help to improve the resolution of the data. In fact any averaging process would inevitably introduce errors due to mis-registration and the fact that the ground scattering properties will change between images.

The relatively small size of the scatterometer images (in terms of pixels) means that edge effects can produce substantial ringing when using Fourier techniques for either re-sampling the data or attempting to enhance its resolution. A method has been described which allows the data to be re-sampled without incurring these problems. An algorithm has also been devised which reflects and expands an image so that the edge effects encountered when using Fourier techniques are substantially reduced.

Following an extensive review of deconvolution and super-resolution techniques a method involving a Wiener filter has been defined for application with ERS-1 scatterometer data. It has been shown how the linear Wiener filter can remove the 'tapering' shape of the system impulse response function from the data. Small ringing effects introduced by the Wiener filter can be removed by the use of a median filter. It is also possible to further enhance scatterometer images by incorporating *a priori* information in the form of a land -water mask which shows where we expect to find relatively sharp discontinuities in the radar backscatter levels.

The current scatterometer data processing chain has been developed to provide a very high degree of radiometric resolution for use in wind derivation and ocean applications. For land applications it would be useful and very interesting to examine the effect of sacrificing some of this radiometric resolution in favour of an improved spatial resolution.

10.13 Appendix to Chapter 10: Sampling Theory

Figure 10.24 is designed to illustrate some of the principals of Fourier sampling theory. Figure (a) shows a scene of interest, Figure (c) represents the impulse response function of an imaging system and Figure (e) shows the image of the scene after it has been convolved with the imaging function. Therefore, in the scatterometer problem in which we are interested, Figure (a) would represent the radar backscatter response at any given infinitesimal point on the ground, and Figure (c) would be the impulse response function of the scatterometer antenna.

In the example in Figure 10.24 the impulse response function has been chosen to be a *sinc* function. This is because a *sinc* function has nice mathematical properties which help to simplify the arguments. The actual scatterometer imaging system does not follow a *sinc* pattern but similar principals are still applicable. The aim of deconvolution techniques is to try and remove the effect of the imaging function from the blurred image in Figure (e) and, therefore, to recover the original scene.

However, in general, we do not have continuous images such as Figure (e) to work with, instead we have images which are sampled and divided into pixels. An important question is, therefore, how frequently should the image be sampled, or in other words, how many pixels should there be per unit length? Clearly if these samples are taken very infrequently important information might be lost, whilst on the other hand if samples are taken very frequently there will be a large degree of correlation, and therefore, redundancy between neighbouring pixels.

Fourier theory tells us that if we know the maximum frequency that is present in a signal then if we sample the signal at, at least, twice this rate then it is possible to completely recover the original signal solely from these samples.

The Fourier transform of the imaged function is shown in Figure (f). This is equal to the Fourier transform of the original scene (Figure (b)) multiplied by the Fourier transform of the imaging impulse response function (Figure (d)).

It can be seen that the Fourier transform of the *sinc* function has a box shape and has a maximum frequency content of $f_{\max}$. This means that the Fourier transform of the image will also be restricted (band-limited) to $f_{\max}$. Therefore, we know that if we sample the image at a rate which is at least twice $f_{\max}$ then all of the information present in the original image (i.e. Figure (c)) will be preserved in the sampled image. The sampling rate required to achieve this for an image formed using the *sinc* function in this example is shown in Figure (g). The Fourier transform of this sampled function is shown in Figure (h). It can be seen that this function is equal to the Fourier transform of the original image (i.e. Figure (f)) only repeated (indefinitely) at intervals of $2 \times f_{\max}$. In other words, all of the information that is contained in Figure (f) is also contained in Figure (h).

If the image is sampled at a rate which is lower than $2 \times f_{\max}$ then it will not be possible to recover the image from the samples. This is illustrated by Figure (i) which shows samples from the image which have been taken half as frequently as in Figure (g). Figure (j) shows the Fourier transform of the samples in Figure (i). It can be seen that the original band-limited Fourier transform of the image is now repeated with twice the frequency than was observed in Figure (h). This causes the repeated transforms to overlap, the portions which overlap are added together so that the original transform containing the information about the image is lost.

As was stated earlier the impulse response function of the ERS-1 scatterometer instrument is not a simple *sinc* function. (The actual form of the ERS-1 scatterometer impulse response function is discussed in Section 10.3.) This means that the Fourier spectrum of the impulse response function is not a simple box function with a clearly defined cut-off frequency. This situation is common to most other real radar systems. In practice, complex (I and Q channel) radar signals (images) are sampled at a rate corresponding to a distance equal to the 3-dB beam-width of its impulse response function. For detected images, it is necessary to sample at twice this rate. Thus, for the scatterometer instrument with a 3-dB beam-width of approximately 50 km, a sampling frequency which corresponds to 25 km meets the usual criteria necessary to satisfy the Nyquist theory. In a similar manner the ERS-1 SAR PRI images have a resolution of approximately 30 m and are sampled every 12.5 m.

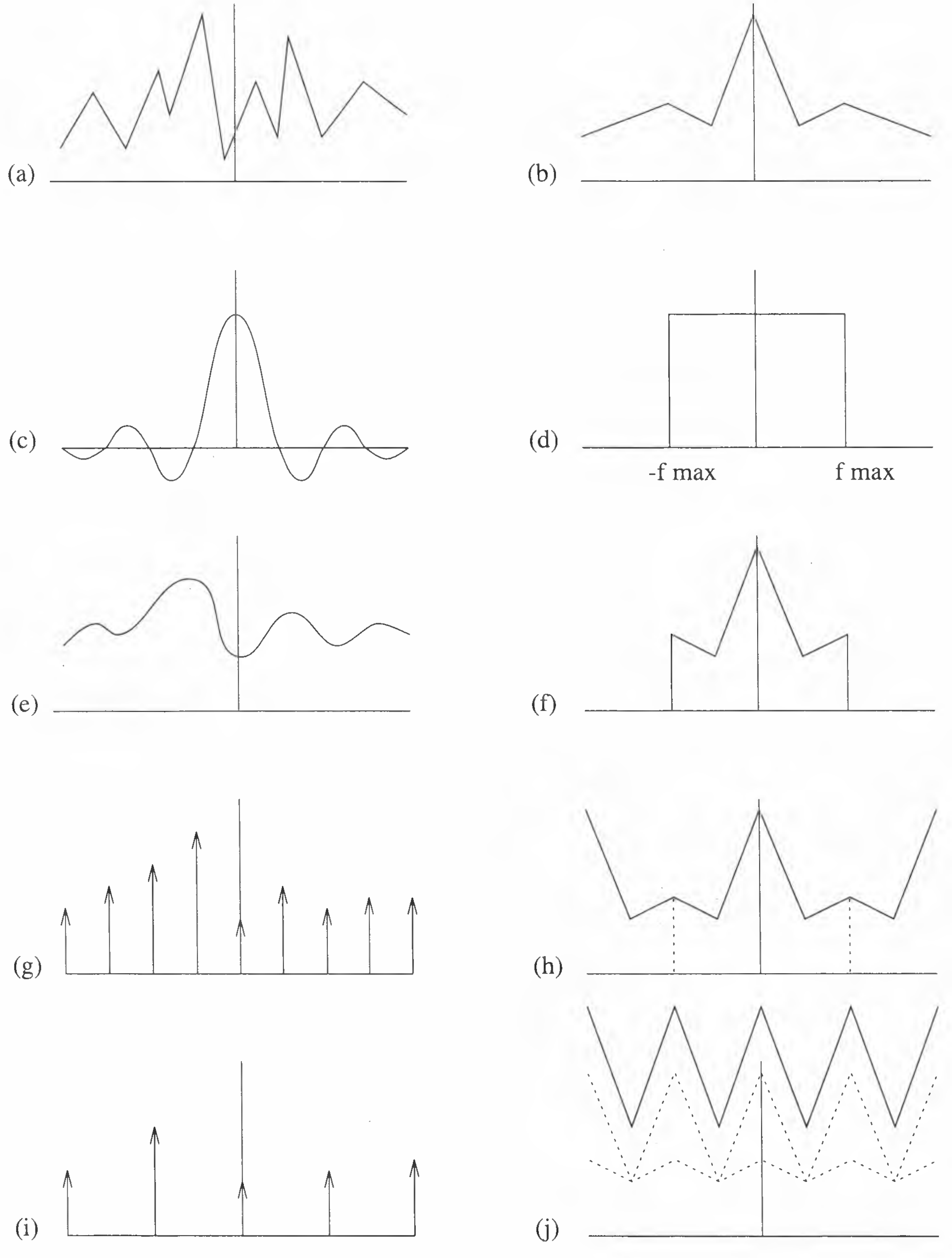

Figure 10.24. The diagrams on the right hand side show the Fourier transforms of the corresponding images in the left hand column.

11 Conclusions on the Feasibility of Wind Scatterometer and SSM/I Data

11.1 Applicability of ERS-1 Wind Scatterometer Data

The usability of ERS-1 Wind Scatterometer for land applications has been primarily tested using data from test areas in Finland. The investigations conducted show that WS data have considerable potential in the estimation soil/vegetation moisture (total amount of water). Additionally, the investigations indicate that the monitoring of seasonal changes such as freezing/thawing of soil and detection of wet snow may be appropriate applications. Particularly, the feasibility in soil frost detection was tested and the results obtained are very promising. They show that ERS-1 Wind Scatterometer can have potential for operative employment in this field.

The possibilities to map forest biomass using WS data appear to be negligible. This is due to the fact that the sensitivity of C-band radar's response to forest biomass is low. Moreover, since the spatial resolution of ERS-1 Wind Scatterometer is low, the range of forest biomass in WS data pixels of forested areas cannot be large, which enforces the unsuitability. In the case of land use category mapping, WS data may have some potential, especially in the case of distinguishing the fraction of water areas in a WS pixel.

Effect of incidence angle and possibilities in land/water fraction retrieval

When using ERS-1 wind scatterometer data, the first thing to decide is, whether to use image data or individual pixels. If one is interested mainly in relative changes, it is possible to work with image data, but when it comes to monitoring absolute backscattering values, one should rather deal with individual pixels, if no angular corrections are carried out. Applications of short duration involve mostly so limited a number of data, that then one has put up with images. Yet the effect of the incidence angle variation can not be overlooked.

When one works with individual pixels, the incidence angle should be chosen according to whether the water or land area is of interest. Incidence angle of about 25° is good for land applications, if there is no special reason to use a large incidence angle. The biomass studies seem to be rather insensitive to the incidence angle, but large incidence angles produce a slightly larger variation of the backscattered intensity, when the biomass value is very low (refer to Figures 6.14-6.17 and 4.2). In general the intensity level varies with incidence angle, but the relationship between the intensity and biomass is qualitatively about the same for all incidence angle values. The intensity saturates in such low values of biomass, that only the observation of areas of very low biomass values seems possible. One example could be the detection of clearcutting and regrowth of a clearcutting. However, the resolution of ERS-1 is not high enough for practical inventory usage, if not in very large almost uninhabited areas like Siberia. Large scale change detection in polar areas could be a suitable application. This would be motivated from the environmental point of view. For example the northern border of forested areas in Europe, Asia and North America will be one indicator of large scale climatic changes.

Although the backscattered intensity is very sensitive to water area percentage in the scatterometer pixel, the scatter of the points is too large to permit a reliable estimation of the water area using the intensity values. Only a rough estimate of the majority type of target (water or land) can be obtained from the scatterometer data using large incidence angles. Since the resolution of the ERS-1 wind scatterometer is so coarse, it is not probable that this classification possibility finds any practical use. However, if the resolution were markedly better, it could be used for example for estimation of the extent of flooded areas or perhaps the concentration estimation of sea ice. Scatterometer data has the advantage to SAR data that its using does not require complicated image analysis algorithms that have to overcome the problem of speckle. Therefore applications requiring large numbers of data in real time very frequently, such as winter shipping, would benefit from a high resolution scatterometer despite of the development of new advanced SARs.

11.2 Applicability of SSM/I Data

The SSM/I data seem to suitable for following applications: (1) estimation of snow water equivalent of dry snow, (2) estimation of physical temperature at forested areas during summer conditions and (3) sea ice mapping. Additionally, the SSM/I instrument may have some potential in land use classification. In the case of temperature estimation the results obtained show surprisingly high accuracies, as high or even higher than those obtained using NOAA AVHRR infrared channels. Moreover, in all applications, the use of microwave radiometer is not restricted to cloud-free conditions as the employment of infrared radiometers. Especially if space-borne measurements were used for monitoring purposes this matter reduces the use of optical/infrared instruments severely.

The results obtained in snow water equivalent retrieval are still somewhat poor to most hydrological applications. However, the novel inversion approach introduced in Section 9.2 appears to give higher retrieval accuracies than traditional methods, such as the SPD algorithm (*Aschbacher 1989*). In order to improve the accuracy of SSM/I-based estimates to fulfil the requirements of more operative use, two methods can be applied: (1) the employment of *in situ* measurements together with SSM/I data (which is possible with the developed inversion approach) and (2) the employment of ancillary space-borne data (e.g. NOAA AVHRR data) to correct SSM/I-based estimates. The latter aspect is discussed in Section 11.4 below.

11.3 Combined Use of Wind Scatterometer and SSM/I Data

The possibilities to use combined ERS-1 Wind Scatterometer and SSM/I data for inversion appear to be quite limited. On contrary to that, SSM/I and ERS-1 WS seem to be complementary to each other (especially in the case of boreal forests):

(1) During summer, the WS measurements of forested areas are highly effected by the variations in soil and vegetation moisture and by the precipitation, but the SSM/I data appear to be almost insensitive to these factors. Instead, the SSM/I data is highly correlated with the physical temperature, whereas the correlation of WS data to temperature is negligible.

(2) During winter, the SSM/I measurements are highly effected by the snow cover characteristics in the case of dry snow conditions. Under wet snow conditions, microwave radiometer data does not allow the discrimination of snow covered areas from snow-free areas. In the case of WS measurements the behaviour is opposite.

However, some possibilities to utilise combined SSM/I and WS data can be noticed in the land use classification, since both the SSM/I and WS data appear to be effected by the land use category.

11.4 Combination of Microwave Data with Other Space-Borne Remote Sensing Data

The combination of microwave data with optical/infrared data was investigated in the case of SSM/I-based snow water equivalent estimation (presented in Section 9.2). This was carried out by combining SSM/I data with NOAA AVHRR data in order to find out correction formulas for estimates obtained using solely SSM/I measurements.

In these investigations, three AVHRR brightness temperature bands were employed together with seven SSM/I channels. Due to the difference in resolution (25km x 25km for SSM/I data and 1km x 1km for AVHRR data), the AVHRR images were averaged within 25km by 25km-sized squares. As a result, two imagery types of equal resolution and geo-location were obtained. The data set for the study includes also the original snow water equivalent (SWE) estimates produced by the inversion method (refer to section 9.2), and the original ground truth data.

Data sets from two dates of winter 1994 were used: February 11 and February 27. The data was collected from both the South and North Finland test areas. Hence, four separate data sets were obtained. Those observations having *in situ* SWE more than 150 mm were excluded from the analysis (teaching data set). This was due to the fact that the brightness temperature at SSM/I channels saturates as SWE exceeds 150 mm. Also those observations with the estimation error more than ±150 mm were excluded. For these restrictions, a total of 70 observations (29+25+11+5) was employed in further analyses (see Table 11.1).

Table 11.1. Description of the combined data set (teaching data set).

	Minimum	Maximum
Estimation Error (mm)	-112.21	105.54
In Situ SWE (mm)	21.99	149.06
Total Number of Samples (N)	70	

The basic idea of using the NOAA AVHRR data was to find out whether it has some potential to improve the SWE estimates obtained by the inversion method. From a correlation analysis it was noticed that the use of the AVHRR itself cannot be successfully utilized in SWE estimation. Instead, it was found out that the AVHRR works well when it is used as an explanatory factor for estimation errors. This was detected by calculating several terms including both the AVHRR and the SSM/I data (like differences and ratios of the individual channels of these two instruments) and by investigating the correlation between these terms and the estimation errors (of original SSM/I-based SWE estimates).

The correlation analysis showed that difference terms S1-A4, S2-A4 and S3-A4 (S*n* denoting the *n*th channel of SSM/I and A*n* denoting the *n*th channel of the AVHRR) remarkably correlate with the estimation error (of SSM/I-based estimates). This was the case within each separate data set and within the combination of all of them. Due to the small differences in the correlation factors within each data set, a multiplicative term (S1-A4)x(S2-A4)x(S3-A4) was taken into use. This term gave the best correlation coefficient ($r = -0.72$) with the original SSM/I-based SWE estimation error (see Figure 11.1). For further analyses this term was modified to have an average value of zero (these modified values are depicted in Figure 11.1). Let Z be the multiplicative term

$$Z_i \;=\; ((S1_i - A4_i)\cdot(S2_i - A4_i)\cdot(S3_i - A4_i)) \qquad i = 1\ldots N. \tag{11.1}$$

The modified (zero mean) term $Z\varnothing$ is then:

$$Z\varnothing_i \;=\; Z_i \;-\; \overline{Z}, \tag{11.2}$$

where $\overline{Z}$ is the ensemble average of Z.

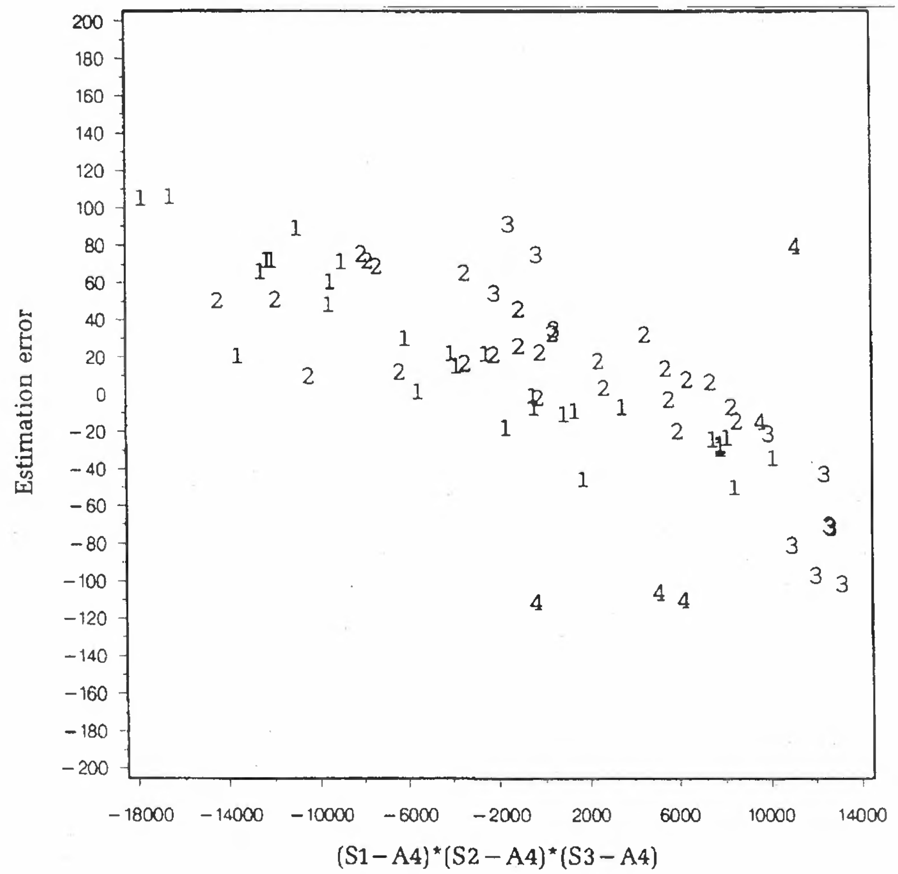

Figure 11.1. Scatter plot of the term Z∅ (zero mean (S1-A4)x(S2-A4)x(S3-A4)) and the SWE estimation error obtained using the inversion procedure of Section 9.2. The data set (N = 70) covers two dates and test areas:
1 = data for February 11, South Finland test area,
2 = data for February 27, South Finland test area,
3 = data for February 11, North Finland test area,
4 = data for February 27, North Finland test area.

A variety of terms including the SSMI/I-measured brightness temperatures only was also tested. Some of them seemed to work well within individual data sets. However, this was the case barely due to systematic properties of each data set, such as the strong (negative or positive) correlation between the *in situ* SWE and the estimation error, and a strong concurrent correlation between the *in situ* SWE and the SSM/I brightness temperature (this may happen e.g. if the inversion algorithm presumes a totally wrong value for a certain emission model parameter, such as snow grain size or surface roughness). This judgement was verified with the combined data set, as correlations between SSM/I channels and the estimation error remarkably deteriorated.

Considering the results above, the employment of AVHRR is likely to correct the estimation errors caused e.g. by the use of inappropriate ground temperatures as input for the inversion procedure. This conclusion led to an attempt to correct the SWE estimates by means of regression analysis. A simple linear regression was used with estimation error e being the dependent variable and $Z\varnothing$ being the descriptive variable:

$$e_i \quad = \quad a \cdot Z\varnothing_i, \qquad i = 1...70 \tag{11.3}$$

where

a = model parameter to be estimated and

e_i = (original) estimated SWE - *in situ* SWE.

Results from the regression analysis are shown in Table 11.2.

Table 11.2. Results of the regression analysis (using teaching data set).

$\hat{a}$	-0.0047
Coefficient of Determination (r^2)	0.511
RMSE (mm)	37.634
Total Number of Samples (N)	70

The new (corrected) SWE estimates were determined using the regression model of Equation (11.3) with $\hat{a}$ (estimate of a):

$$SWE_{new} \quad = \quad SWE_{old} \quad - \quad \hat{a} \cdot Z\varnothing, \tag{11.4}$$

where

SWE_{old} = (original) estimated SWE obtained using the SSM/I inversion algorithm of Section 9.2 and

SWE_{new} = new corrected SWE estimate.

The testing of this algorithm (Equation (11.4)) was conducted using all data (also those observations having the *in situ* SWE higher than 150 mm and estimation error larger than ±150 mm). This led to the total number of 81 observations (with a minimum SWE of 21.99 mm, and maximum SWE of 201.27 mm).

The comparison between the new and the old SWE estimates is presented in Table 11.3 and in Figure 11.2. Table 11.3 presents the mean and standard deviation, as well as the standard deviation around zero (std0), of the estimation errors determined from the original SSM/I-based estimates and from the AVHRR-corrected estimates. The results indicate that AVHRR data have potential to improve the SWE estimates obtained using solely SSM/I data. This is clearly detectable in Figure 11.2, where both the original SSM/I-based SWE estimates and AVHRR-corrected new SWE estimates are depicted. However, the results presented here were obtained using a quite limited data set (due to the fact that applicable AVHRR data can only be obtained in cloud free conditions which are quite occasional). Hence, further investigations in this field are needed, in order to evaluate the practical feasibility of combined microwave/infrared data in snow water equivalent retrieval.

Table 11.3. Characteristics for the SWE estimation errors before and after the AVHRR-aided correction.

	Before Correction	After Correction
Minimum (mm)	-139.52	-139.35
Maximum (mm)	299.52	157.53
Mean (mm)	8.754	8.754
Std (mm)	76.208	49.787
Std0 (mm)	76.241	50.247

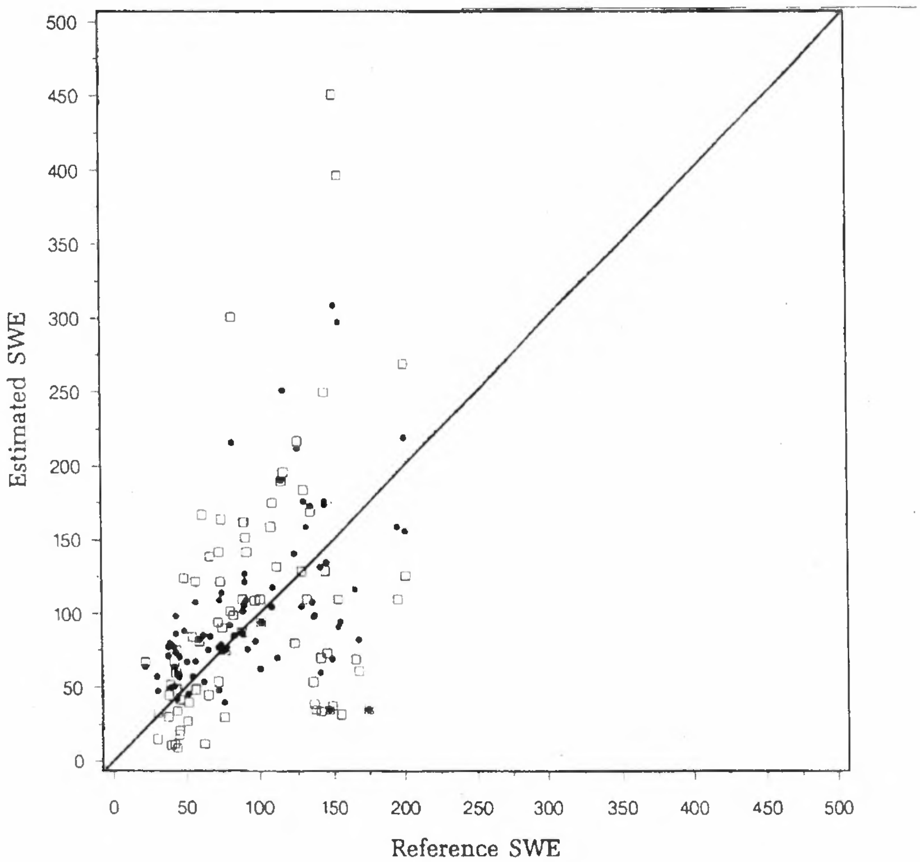

Figure 11.2. The SWE estimates before (squares) and after (dots) AVHRR-aided correction.

12 Recommendations for Future Work

Instrument characteristics

The present space-borne scatterometers and radiometers have some constraints which limit application development. These matters are discussed next.

The basic handicap of both the ERS-1 Wind Scatterometer and the SSM/I radiometer is the relatively poor spatial resolution (about 50 km for the WS and the low-frequency SSM/I channels). The analyses conducted in this study show that especially open water areas (lakes) inside a measurement cell may significantly disturb scatterometer and radiometer data interpretation.

Both the ERS-1 WS and the SSM/I instrument produce multi-channel data: multi-angular in the case of the WS instrument and multi-frequency/polarization in the case of the SSM/I instrument. This characteristic was found to be highly beneficial for all applications. However, the Wind Scatterometer instrument operates only at a single frequency band using a single polarization (C-band, VV polarization). The applicability of other frequencies and polarizations was not investigated in this study. Based on literature, the use of a lower frequency channel (L- or P-band) together with C-band would significantly improve the feasibility of SAR in land use classification and vegetation biomass retrieval.

In the case of SSM/I data the highest frequency channels (85 GHz) were found to have a marginal usability in all applications investigated. Based on literature, radiometer channels operating at frequencies below the lowest SSM/I frequency (19 GHz) should have a much higher potential for land applications than the 85 GHz SSM/I channels.

Scatterometer resolution enhancement

The investigations conducted showed that the ERS-1 Wind Scatterometer image resolution cannot be improved that much as suggested in the previous work in this area, not even by overlapping images. Moreover, the justification of overlapping (over-sampling) data from several satellite overpasses is questionable in general. This is due to the fact that, typically in land areas, target characteristics can change rapidly (e.g. due to precipitation). Instead, the data processing chain of future scatterometer systems could be changed to enable a higher spatial resolution (with some sacrifices in radiometric resolution).

Application development

Scatterometer is more suitable than SAR for monitoring large areas over long periods of time due to the simplicity of the data processing, the coarse resolution, the small size of the data files and the large aerial coverage. The radiometric sensitivity of scatterometer is also better than that of SAR. The effect of mixed pixel (e.g. open water areas) can be taken into account using map information to obtain the water area percentages. Thus, scatterometer data can be used also for fragmented land areas. Then a global monitoring system could be made for change detection for example in the Northern hemisphere land areas.

In this study, detection of soil frost was found to be the most prominent land application of the ERS-1 Wind Scatterometer. Other potential applications are retrieval of soil moisture and effect of precipitation (i.e. monitoring of changes in total water content of the target) and monitoring of snow melt. These applications require further work.

Most of the retrieval algorithms developed and tested in this study were inversion techniques that require the use of *a priori* land use information. The algorithms were tested using, additonally, LANDSAT TM- and ground-based land use reference data for test sites in Finland. In large area applications, these reference data can be probably obtained using NOAA AVHRR data.

The SSM/I radiometer data were found to be very suitable for some applications, especially for the retrieval of surface (air) temperature in the boreal forest zone. Retrieval of the snow water equivalent and sea ice concentration are promising candidates for operational use in large area applications. The results of this study suggest that the combined use of SSM/I data with NOAA AVHRR data in snow water equivalent retrieval may be useful, although this was only briefly demonstrated in this study.

As a conclusion, it is proposed that future work will be carried out in the following fields:

1. *Application development using presently available satellite data*

* Soil frost monitoring using ERS-1 WS data.
* Snow melt detection using ERS-1 WS data.
* Monitoring of changes in soil moisture and vegetation water content using ERS-1 WS data.
* Change detection (vegetation extent, land use) using ERS-1 WS data.
* Surface temperature mapping using SSM/I data.
* Sea ice concentration retrieval using SSM/I data,
* Snow water equivalent retrieval using SSM/I and NOAA AVHRR data,
* Monitoring of snow season using combined SSM/I and ERS-1 WS data, including the monitoring of soil frost, snow cover evolution (snow water equivalent) and snow melt.

2. *Airborne remote sensing campaigns for the above applications using the following sensors*

* Microwave radiometers covering the 6 to 90 GHz frequency range.
* Scatterometers operating at P, L, C and X band.
* Synthetic aperture radars operating at P, L, C and X band.

Funding of airborne campaigns by ESA should cover a centralized effort to collect the necessary ground truth data. Past experiences show that relying on local organizers to collect these data without proper funding does not work out. The value of an airborne data set is determined by the quality of ground truth data.

3. *Tower-based measurements on the above applications using the following sensors*

* Microwave radiometers covering the 6 to 90 GHz frequency range.

* Scatterometers operating at P, L, C and X band.

Tower-based measurements allow collection of long time series with detailed ground truth for understanding the behaviour of the target. This is not possible when satellite data and airborne data are used.

4. *Development of airborne sensors to optimize the feasibility of future spaceborne sensors*

* Microwave radiometers in the 1 to 90 GHz range with advanced features (interferometry, polarimetry)

* Scatterometers operating simultaneously at P, L, C and X band.

The technical characteristics of future spaceborne sensors can be optimized with airborne sensors that cover a wide frequency range, employ multiple polarization and have an in-flight capability to change the incidence angle.

5. *Theoretical modeling on the above applications, using high-quality experimental data (satellite data, airborne data, tower-based data and ground truth) to test the models*

All models should be tested using the same set of experimental data.

References

Amans, V., "*Wind Scatterometer Monthly Report: September 1994*," Document DEX/EM/VA/94/006, Issue 1.0, 22 p., 1994.

Attema, E.P.W., Ulaby, F.T., "Vegetation modeled as a water cloud", *Radio Science*, vol. 13, no. 2, pp. 357-364, 1978.

Aschbacher, J., "*Land Surface Studies and Atmospheric Effects by Satellite Microwave Radiometry*," Ph.D. dissertation, University of Innsbruck, 1989.

Bahar, E., "Physical interpretation of the full wave solutions for the electromagnetic fields scattered from irregular stratified media", *Radio Sci.*, vol. 23, no. 5, pp. 749-759, 1988.

Bedini, L., Tonazzini, A., "Neural network use in maximum entropy image restoration", *Image and Vision Computing*, vol. 8, no. 2, May 1990.

Bernard, R., *Radiometer Performances for Tropospheric Path Correction for an Advanced Terrain Mapping Altimeter*, Document de Travail DT/CRPE/1156, Centre National d'Etudes des Telecommunications, 1988.

Borgeaud, M., Kong, J.A., Lin, F.C., "Microwave remote sensing of snow-covered sea ice", *Proc. IGARSS'86*, Zurich, 8-11 Sep, Ref. ESA SP-254, pp. 133-138, 1986.

Carlström, A., Ulander L.M.H., "C-Band backscatter signatures of old sea ice in the central Arctic during freeze-up", *IEEE Trans. Geosci. Remote Sensing*, vol. 31, No. 4, pp. 819-829, 1993.

Chauhan, N.S., Lang, R.H., Ranson, K.J., "Radar modeling of boreal forest", *IEEE Trans. Geosci. Remote Sensing*, vol. 29, no. 4, pp. 627-638, 1991.

Chang, A., Foster, J., Hall, D., "Nimbus-7 SMMR derived global snow parameters", *Annals of Glaciology*, vol. 9, pp. 39-44, 1987.

Choudhury, B., Schmugge, T., Newton, R., Chang, A., Effect of surface roughness on the microwave emission from soils, *J. Geophys. Res.*, vol. 84, pp. 5699-5706, 1979.

Delves, L.M., G.C. Pryde, S.P. Luttrell, "A super-resolution algorithm for SAR images", *Inverse Problems*, vol. 4, pp. 681-703, 1988.

Dobson, M.C., Ulaby, F.T., Hallikainen, M.T., El-Rayes, M.A., "Microwave dielectric behavior of wet soil - part II: dielectric mixing models", *IEEE Trans. Geosci. Remote Sensing*, vol. 23, no. 1, pp. 35-46, 1985.

Drinkwater, M.R., Crocker, G.B., "Modeling changes in the dielectric and scattering properties of young snow-covered sea ice at GHz frequencies", *J. Glaciol.*, vol. 34, No. 118, pp. 274-282, 1988.

Durden, S.L., Van Zyl, J.J., Zebker, H.A., "Modeling and observation of the radar polarization signature of forested areas", *IEEE Trans. Geosci. Remote Sensing*, vol. 27, no. 3, pp. 290-301, 1989.

Early, D.S., D.G. Long, M.R. Drinkwater, "Comparison of enhanced resolution images of Greenland from ERS-1 and Seasat scatterometers", *Proceedings of the International Geoscience and Remote Sensing Symposium*, pp. 2382-2384, Pasadena, 8-12 Aug. 1994.

Eppler, D., Farmer, D., Lohanick, A., Anderson, M., Cavalieri, D., Comiso, J., Gloersen, P., Garrity, G., Grenfell, T., Hallikainen, M., Maslanik, J., Mätzler, C., Melloh, R., Rubinstein, I., Swift, C., Passive Microwave signatures of sea ice, *Microwave remote sensing of sea ice*, Geophysical Monograph 68, American Geophysical Union, 1992.

Frieden, B.R., "Dice, entropy, and likelihood", *Proc. of the IEEE*, vol. 73, no. 12, Dec. 1985.

Fung, A., *Microwave Scattering and Emission Models and Their Applications*, Artech House, 573 p., 1994.

Grandell, K.J., Hallikainen, M.T., "Modeling and retrieval of snow and sea ice characteristics in the frequency range 6 to 90 GHz", *ESA/ESTEC Purchase order* 123775, 1994.

Gull, S.F., "Developments in maximum entropy data analysis", Published in *Maximum Entropy and Bayesian Methods*, J. Skilling (ed.), Kluwer Academic Publishers, 1989.

Hallikainen, M.T., "Retrieval of snow water equivalent from Nimbus 7 SMMR: effect of land-cover categories and weather conditions", *IEEE J. Oceanic Engineering*, vol. 9, No. 5, pp. 372-376, 1984.

Hallikainen, M.T., Ulaby, F.T, Dobson, M.C., El-Rayes, M.A., Wu, L.K., "Microwave dielectric behavior of wet soil Part I: empirical equations and experimental observations", *IEEE Trans. Geosci. Remote Sensing*, vol. 23, pp. 25-34, 1985.

Hallikainen, M.T., Ulaby, F.T., Abdelrazik, M., "Dielectric properties of snow in the 3 to 37 GHz range", *IEEE Trans. on Antennas and Propagation*, vol. AP-34, no. 11, pp. 1329-1340, 1986.

Hallikainen, M.T., Ulaby, F.T., Deventer, T.E., "Extinction behavior of dry snow in the 18- to 90-GHz range", *IEEE Trans. Geosci. Remote Sensing*, vol. GE-25, pp. 737-745, 1987.

Hallikainen, M.T., Jääskeläinen, V.I., "Microwave emission behaviour of snow", *Proc. IGARSS'88*, Edinburgh, 13-16 Sept., 1988.

Hallikainen, M., Hyyppä, J., Haapanen, J., Tares, T., Ahola, P., Pulliainen, J., Toikka, M., "A helicopter-borne eight-channel ranging scatterometer for remote sensing: part I: system description", *IEEE Trans. Geosci. Remote Sensing*, vol. 31, pp. 161-169, 1993.

Hans, P., H. Munz, R. Kremer, "Quasi real time conversion of the ERS-1 scatterometer raw data to σ^o-triplets", *Proceedings of IGARSS'86*, pgs. 389-394, Zurich, 8-11 Sept., 1986.

Harris, F., "On the use of windows for harmonic analysis with the discrete Fourier transform", *Proceedings of the IEEE*, Vol. 66, No. 1, pgs. 51-83, Jan. 1978.

Herbert, T., R. Leahy "A generalised EM algorithm for 3-D Bayesian reconstruction from Poisson data using Gibbs priors", *IEEE Trans. Med. Imaging*, Vol. 8, No. 2, pgs. 194-202, June 1989.

Hiltbrunner, D., C. Mätzler, A. Wiesmann, "Monitoring land surfaces with combined DMSP-SSM/I and ERS-1 scatterometer data," *Proc. IGARSS'94 Symp.*, pp. 1945-1947, Pasadena, 1994.

Hoekman, D.H., van der Sanden, J.J., Rijckenberg, G.-J., "Analysis of forest backscatter using airborne polarimetric data and multi-temporal ERS-1 SAR data", *Proc. IGARSS'92*, Houston, IEEE 92CH3041-1, pp. 1209-1211, 1992.

Holmes, T.J., Liu, Y-H., "Richardson-Lucy/maximum likelihood image restoration algorithm for fluorescence microscopy: further testing", *Applied Optics*, vol. 28, no. 22, pp. 4930-4938, Nov 1989.

Hsu, C.C., Han, H.C., Shin, R.T., Kong J.A., "Radiative transfer theory for polarimetric remote sensing of pine forest", *Proc. IGARSS'92*, Houston, IEEE 92CH3041-1, pp. 1129-1131, 1992.

Hunt, B.R., "Prospects for image restoration", *International Journal of Modern Physics C*, vol. 5, no. 1, pp. 151-178, 1994.

Hyyppä, J., *Development and Feasibility of Airborne Ranging Radar for Forest Assessment*, Doctoral dissertation, Helsinki University of Technology, Laboratory of Space Technology, 109 p., 1993.

Häme, T., Salli, A., Lahti, K., "Estimation of carbon storage in boreal forests using remote sensing data", in Kanninen, M., Anttila, P., (editors), *The Finnish Research Programme on Climate Change, Progress Report*, Publications of the Academy of Finland 3/92, pp. 250-252, Helsinki, 1992.

Häme, T., Salli, A., Andersson, K., Lohi, A., Rauste, Y., "Estimation of biomass and other characteristics of boreal forest over extensive areas using NOAA AVHRR data", *Proc. of EU-ROPTO Symposium*, Rome, Italy, September 26-30, 12 p., 1994.

Jääskeläinen, V., *Remote Sensing of Snow by Microwave Radar* (in Finnish), Licentiate's Thesis, Department of Electrical Engineering, Helsinki University of Technology, 110 pp., 1993.

Jääskeläinen, V., Kurvonen, L., Hallikainen, M., "Effect of land-cover type and season in microwave remote sensing of snow", *Proc. IGARSS'93 Symposium*, Tokyo, IEEE 93-77594, pp. 1046-1049, 1993.

Karam, M.A., Fung, A.K., Amar, F., Mougin, E., Lopes, A., Beaudoin, A., "Polarimetric signatures of a coniferous forest canopy based on vector radiative transfer theory", *Proc. IGARSS'92*, Houston, IEEE 92CH3041-1, pp. 773-775, 1992a

Karam, M.A., Fung, A.K., Lang, R.H., Chauhan, N.S., "A microwave scattering model for layered vegetation". *IEEE Trans. Geosci. Remote Sensing*, vol. 30, no. 4, pp. 767-784, 1992b

Kasischke, E.S., Christensen, N.L., "Connecting forest ecosystem and microwave backscatter models", *Int. J. Remote Sensing*, vol 11, no. 7, pp. 1277-1298, 1990.

Kerr, Y., Njoku, E., "A semiempirical model for interpreting microwave emission from semiarid land surfaces as seen from space", *IEEE Trans. Geosci. Remote Sensing*, vol. 28, no. 3, pp. 384-393, 1990.

Kerr, Y., Lagouarde, J., Imbernon, J., "Accurate land surface temperature retrieval from AVHRR data with use of an improved split window algorithm," *Remote Sens. Environ.*, vol. 41, pp. 197-209, 1992.

Kim, Y.S., Moore, R.K., Onstott, R.G., Gogineni, S., "Towards identification of optimum radar parameters for sea-ice monitoring", *J. Glaciol.*, vol. 31, pp. 214-219, 1985.

Kong, J.A., Shin, R., "Theory and experimental results for passive microwave remote sensing of snowpacks", *J. of Geophysical Research*, vol. 84, pp. 5669-5673, 1979.

Kramer, P., Kozlowski, T., *Physiology of Woody Plants*, Academic Press, pp. 474-493, 1979.

Kurvonen, L., *Radiometer measurements of snow in Sodankylä 1991-93*, Helsinki University of Technology, Laboratory of Space Technology, Report 16, September, 1994a.

Kurvonen, L., Radiometer measurements of sea ice in the Gulf of Bothnia 1992, Helsinki University of Technology, Laboratory of Space Technology, Report 17, 1994b.

Le Toan, T., Beaudoin, A., Chong, D.L.S., Kong, J.A., Nghiem, S.V., Han, H.C., *Study of Microwave Interaction with the Earth's Surface, Volume II*, ESA Rep., ESTEC/No. 8447/89/NL/PB(SC), 1990.

Lee, J.K., Kong, J.A., "Active microwave remote sensing of an anisotropic random medium layer", *IEEE Trans. Geosci. Remote Sensing*, vol. 23, no. 6, pp. 910-923, 1985.

Lettington, A.H., Q.H. Hong, "A non-linear image restoration algorithm with artifact reduction", *SPIE, Applications of Digital Image Processing XVII*, 24-29 July, 1994.

Levitan, E., Herman, G.T., "A maximum a posteriori probability expectation maximisation algorithm for image reconstruction in emission tomography", *IEEE Trans. on Medical Imaging*, vol. MI-6, no. 3, pp. 185-192, Sept. 1987.

Liebe, H., "MPM - An atmospheric millimetre-wave propagation model", *International J. Infrared and Millimeter Waves*, vol 10, no. 4, 1989.

Lin, F.C., Kong, J.A., Shin, R.T., "Theoretical models for microwave remote sensing of snow covered sea ice", *Proc. IGARSS'87*, Ann Arbor, 18-21 May, pp. 1121-1125, 1987.

Long, D.G., P.T. Whiting, P.J. Hardin, "High-resolution land/ice imaging using Seasat scatterometer measurements", *Proceedings of the International Geoscience and Remote Sensing Symposium*, Houston, TX, May 1992.

Long, D.G., P.J. Hardin, P.T. Whiting, "Resolution enhancement of spaceborne scatterometer data", *IEEE Trans. Geoscience and Remote Sensing*, Vol. 31, No.3, May 1993.

Long, D.G., P.J. Hardin, "Vegetation studies of the Amazon Basin using enhanced resolution Seasat scatterometer data", *IEEE Trans. Geoscience and Remote Sensing*, Vol. 32. No. 4, March 1994.

Long, D.G., D.S. Early, M.R. Drinkwater, "Enhanced resolution ERS-1 scatterometer imaging of Southern Hemisphere Polar Ice", *Proc. IGARSS 1994*.

Long, D.G., Hardin, P.J., "Vegetation studies of the Amazon Basin using enhanced resolution Seasat scatterometer data", *IEEE Trans. Geoscience and Remote Sensing*, vol. 32. no. 4, March 1994.

Manninen, T., "Problematic calculation of surface backscattering of sea ice", *Proc. of PIERS'94 Conference*, the Netherlands, 4 p., 1994.

McDonald, K.C., Dobson, M.C., Ulaby, F.T., "Using MIMICS to model L-band multiangle and multi-temporal backscatter from a walnut orchard", *IEEE Trans. Geosci. Remote Sensing*, vol. 28, no. 4, pp. 477-491, 1990.

McDonald, K.C., Dobson, M.C., Ulaby, F.T., "Modeling multi-frequency diurnal backscatter from a walnut orchard", *IEEE Trans. Geosci. Remote Sensing*, vol. 29, no. 6, pp. 852-863, 1991.

McDonald, K.C., Ulaby, F.T., "Radiative transfer modelling of discontinuous tree canopies at microwave frequencies", *Int. J. Remote Sensing*, vol 14, no. 11, pp. 2097-2128, 1993.

Mougin, E., Lopes, A., Karam, M., Fung, A., "Effect of tree structure on X-band microwave signature of conifers", *IEEE Trans. Geosci. Remote Sensing*, vol. 31, no. 3, pp. 655-667, 1993.

Mätzler, C., "Applications of the interaction of microwaves with the natural snow cover", *Remote Sensing Reviews*, no. 2, pp. 259-387, 1987.

Mätzler, C., "Passive microwave signatures of landscapes in winter", *Meteorology and Atmospheric Physics*, vol. 54, pp. 241-260, 1994a.

Mätzler, C., "Microwave (1-100 GHz) dielectric model of leaves", *IEEE Trans. Geosci. Remote Sensing*, vol. 32, no. 5, pp. 947-949, 1994b.

Oh, Y., Sarabandi, K., Ulaby, F.T., "An empirical model and inversion technique for radar scattering from bare soil surfaces", *IEEE Trans. Geosci. Remote Sensing*, vol. 30, no. 2, pp. 370-381, 1992.

Pierschel, D. + AMI Team, "Active microwave instrument requirements specification", *Dornier System Document ER-RS-DSF-AM-0001*, May 1987.

Pulliainen, J., Hallikainen, M., Somersalo, E., Kärnä, J-P., Jääskeläinen, V., Hyyppä, J., Talvela, J., Luntama, J-P., *Study of microwave interaction with the earth's surface, Volume I*, ESA Rep., ESTEC No. 8447/89/NL/PB(SC), 1990.

Pulliainen, J.T., Hallikainen, M.T., *Microwave Signatures of Defoliating Spruce Canopies*, Rep. 9, Laboratory of Space Technology, Helsinki University of Technology, 1992.

Pulliainen, J., Kärnä, J-P., Hallikainen, M., "Development of geophysical retrieval algorithms for the MIMR," *IEEE Trans. Geosci. Remote Sensing*, vol. 31, no. 1, pp. 268-277, 1993.

Pulliainen, J., Heiska, K., Hyyppä, J., Hallikainen, M., "Backscattering properties of boreal forests at C- and X-bands", *Proc. IGARSS'93*, Tokyo, pp. 388-390, 1993.

Pulliainen, J., "*Investigation on the backscattering properties of Finnish boreal forests at C- and X-band: a semi-empirical modeling approach*", Thesis for the degree of Doctor of Technology, Helsinki University of Technology, Report 19, 119 p., May 1994.

Pulliainen, J., Heiska, K., Hyyppä, J., Hallikainen, M, "Backscattering properties of boreal forests at the C- and X-bands", *IEEE Trans. Geosci. Remote Sensing*, vol. 32, no. 5, pp. 1041-1050, 1994.

Pulliainen, J., Grandell, J., Hallikainen, M., Virtanen, M., Walker, N., Metsämäki, S., Ikonen, J-P., Sucksdorff, Y., Manninen, T., *Sudy of Scatterometer and Radiometer Land Applications*, 1st Interim Report, ESRIN Contract No. 11122/94/I-HGE(SC), 48 pp., 1995a.

Pulliainen, J., Grandell, J., Hallikainen, M., Virtanen, M., Walker, N., *Study of Scatterometer and Radiometer Land Applications*, 2nd Interim Report, ESRIN Contract No. 11122/94/I-HGE(SC), 97 pp., 1995b.

Richards, J.A., Sun, G.-Q., Simonett, D.S., "L-band radar backscattering modeling of forest stands", *IEEE Trans. Geosci. Remote Sensing*, vol. 25, no. 4, pp. 487-498, 1987.

Rosenkrantz, P., "Rough-Sea Microwave Emissivities Measured with the SSM/I", *IEEE Trans. Geosci. Remote Sensing*, Vol. 30, No. 5, 1992.

Ruck, G.T., Barrick, D.E., Stuart, W.D., Krichbaum, C.K., *Radar Cross Section Handbook, Volume II*, Plenum Press, New York - London, pp. 671-728, 1970.

Schluessel, P., Luthardt, H., "Surface wind speeds over the North Sea from Special Sensor Microwave/Imager observations, *J. of Geophys. Res.*, vol. 96, No. C3, pp. 4845-4853, 1991.

Schmugge, T.J., Jackson, T.J., "A dielectric model of the vegetation effects on the microwave emission from soils", *IEEE Trans. Geosci. Remote Sensing*, vol. 30, pp. 757-760, 1992.

Sezan, M.I., A.M. Tekalp, "Adaptive image restoration with artifact suppression using the theory of convex projections", *IEEE Trans. on Acoustics, Speech and Signal Processing*, Vol. 38, No. 1, Jan. 1990.

Sethmann, R., G.C. Heygster, B.A. Burns, "Image deconvolution techniques for reconstruction of SSM/I data", *Proceedings of IGARSS*, pgs. 2377-2380, 1991.

Sethmann, R., B.A. Burns, G.C. Heygster, "Spatial resolution improvement of SSM/I data with image restoration techniques", *IEEE Trans. on Geoscience and Remote Sensing*, Vol. 32, No. 6, pgs. 1144-1151, Nov. 1994.

Stiles, W.H., F.T. Ulaby, "Microwave remote sensing of snowpacks", *NASA Contractor Report* 3263, 1980.

Stogryn. A., "Equations for calculating the dielectric constant of saline water", *IEEE Trans. Microwave Theory and Techniques*, Vol. 19, pp. 733-736, 1971.

Stogryn, A., "A study of the microwave brightness temperature of snow from the point of view of strong fluctuation theory", *IEEE Trans. Geosci. Remote Sensing*, vol. 24, no. 2, pp. 220-231, 1986.

Sucksdorff, Y., S. Tattari, M. Heikinheimo, J.-P. Ikonen, C. Ottlé, B. Mehrez, "The development of soil/plant/atmosphere model", in *The Finnish Research Programme on Climate Change, Progress Report*. Helsinki, Publ. Acad. Finland, pp. 43-47, March 1992.

Sun, G., Simonett, D.S., Strahler, A.H., "A radar backscatter model for discontinuous coniferous forests", *IEEE Trans. Geosci. Remote Sensing*, vol. 29, no. 4, pp. 639-650, 1991.

Tjuatja, S., Fung, A.K., Bredow, J., "A scattering model for snow-covered sea ice", *IEEE Trans. Geosci. Remote Sensing*, vol. 40, no. 4, pp. 804-810, 1992.

Tsang, L., Kong, J.A., Shin, R.T., *Theory of Microwave Remote Sensing*, John Wiley & Sons, 456 p., New York 1985.

Tsang, L., "Passive remote sensing of dense nonteneous media", *J. Electromagnetic Waves and Applications*, vol. 1, no. 2, pp. 159-173, 1987.

Ulaby, F.T., Moore, R.K., Fung A.K., *Microwave Remote Sensing, Vol. I*, Addison-Wesley, 1981.

Ulaby, F.T., Moore, R.K., Fung A.K., *Microwave Remote Sensing, Vol. II*, Addison-Wesley, pp.457-1064, 1982.

Ulaby, F., Moore, R., Fung, A., "Microwave remote sensing, Active and Passive, Volume III", Artech House Inc., pp. 1412-1467, 1986.

Ulaby, F.T., El-Rayes, A., "Microwave dielectric spectrum of vegetation - part II: dual-dispersion model", *IEEE Trans. Geosci. Remote Sensing*, vol. GE-25, no. 5, pp. 550-556, 1987.

Ulaby, F.T., Sarabandi, K., McDonald, K., Whitt, M., Dobson, M.C., "Michigan microwave canopy scattering model", *Int. J. Remote Sensing*, vol 11, no. 7, pp. 1223-1253, 1990.

Ulaby, F.T., *Modeling Radar Backscatter from Vegetation*. Short Course Notes, DLR, Oberpfaffenhofen, December 1992.

Wang, Y., Davis, F., Melack, J., "Simulated and observed backscatter at P-, L-, and C-bands from Ponderosa pine stands", *IEEE Trans. Geosci. Remote Sensing*, vol. 31, no. 4, pp. 871-879, 1993.

Weise, T., *Radiometric and Structural Measurements of Snow*, PhD Thesis, University of Bern, 159 p., February 1996.

Wentz, F., "A model function for ocean microwave brightness temperatures", *J. Geophys. Res.*, Vol. 88, No. C3, pp. 1892-1908, 1983.

Wentz, F.J., "User's Manual: SSM/I antenna temperature tapes", *RSS Technical Report* 120191, 1991.

Vidal, A., "Atmospheric and emissivity correction of land surface temperature measured from satellite using ground measurements or satellite data," *Int. J. Remote Sensing*, vol. 12., pp. 2449-2460, 1991.

Appendices

APPENDIX I Evolution of Soil Frost in Southern Finland in November 1993

Soil Freezing, 4 November 1993

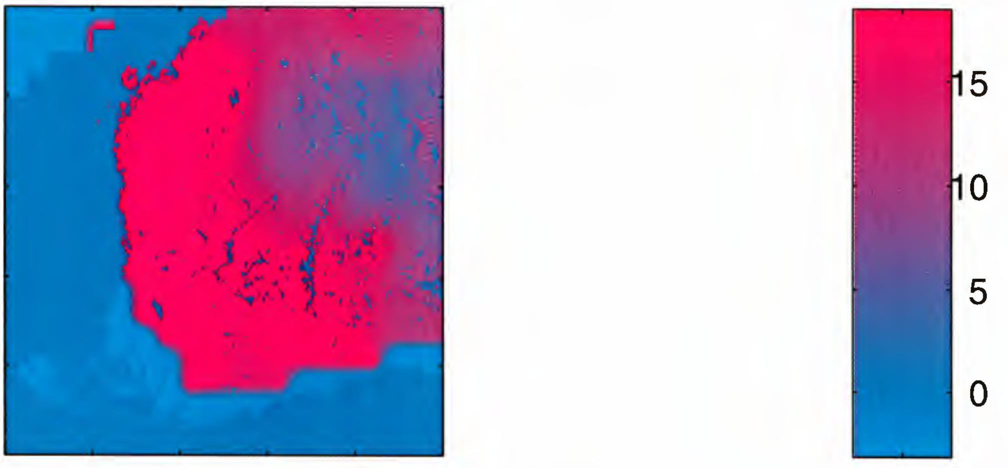

Soil Frost Detector: Soil Moisture Estimate < 9.5%

Soil Freezing, 10 November 1993

Soil Frost Detector: Soil Moisture Estimate < 9.5%